

ALEXANDER JANZ

Structure-preserving space-  
time discretization in a mixed  
framework for multi-field  
problems in large strain elasticity



Alexander Janz

**Structure-preserving space-time discretization in a mixed  
framework for multi-field problems in large strain elasticity**

**Schriftenreihe des Instituts für Mechanik  
Karlsruher Institut für Technologie (KIT)**

**Band 6**

Herausgeber:

Prof. Dr.-Ing. habil. Peter Betsch

Prof. Dr.-Ing. habil. Thomas Seelig

Eine Übersicht aller bisher in dieser Schriftenreihe erschienenen Bände  
finden Sie am Ende des Buches.

# **Structure-preserving space-time discretization in a mixed framework for multi-field problems in large strain elasticity**

by  
Alexander Janz

Karlsruher Institut für Technologie  
Institut für Mechanik

Structure-preserving space-time discretization in a mixed  
framework for multi-field problems in large strain elasticity

Zur Erlangung des akademischen Grades eines Doktor-Ingenieurs von  
der KIT-Fakultät für Bauingenieur-, Geo- und Umweltwissenschaften  
des Karlsruher Instituts für Technologie (KIT) genehmigte Dissertation

von M. Sc. Alexander Janz aus Kirchen (Sieg)

Tag der mündlichen Prüfung: 14. Mai 2019  
Hauptreferent: Prof. Dr.-Ing. habil. Peter Betsch  
Korreferent : Prof. Dr.-Ing. habil. Sigrid Leyendecker

## Impressum



Karlsruher Institut für Technologie (KIT)  
KIT Scientific Publishing  
Straße am Forum 2  
D-76131 Karlsruhe

KIT Scientific Publishing is a registered trademark  
of Karlsruhe Institute of Technology.  
Reprint using the book cover is not allowed.

[www.ksp.kit.edu](http://www.ksp.kit.edu)



*This document – excluding the cover, pictures and graphs – is licensed  
under a Creative Commons Attribution-Share Alike 4.0 International License  
(CC BY-SA 4.0): <https://creativecommons.org/licenses/by-sa/4.0/deed.en>*



*The cover page is licensed under a Creative Commons  
Attribution-No Derivatives 4.0 International License (CC BY-ND 4.0):  
<https://creativecommons.org/licenses/by-nd/4.0/deed.en>*

Print on Demand 2019 – Gedruckt auf FSC-zertifiziertem Papier

ISSN 2363-4936

ISBN 978-3-7315-0926-4

DOI 10.5445/KSP/1000093768





This thesis is dedicated to my grandfather Alois Link.



# Abstract

The present thesis deals with the design of structure-preserving numerical methods in the field of nonlinear elastodynamics with an extension to multi-field problems. First, a new approach to the design of energy-momentum (EM) consistent time-stepping schemes for nonlinear elastodynamics is proposed. The underlying mixed variational formulation is motivated by the structure of polyconvex stored energy functions and benefits from the notion of a tensor cross product for second-order tensors. The structure-preserving discretization in time of the mixed variational formulation yields an EM consistent semi-discrete formulation. The semi-discrete formulation offers several options for the discretization in space. In the special case of a purely displacement-based method, a new form of the algorithmic stress formula is obtained. Afterwards, we introduce a new algorithmic stress formula in its eigenvalue representation to model the transient behavior of hyperelastic bodies of Ogden-type materials. Moreover, we extend the formalism to multi-field problems. Therefore, we provide a new approach to the design of energy momentum consistent integration schemes in the field of non-linear thermo-elastodynamics and nonlinear electro-elastodynamics. Finally, several numerical investigations show the superior performance of the proposed EM consistent time-stepping schemes in terms of numerical accuracy, stability, validity, and robustness.

**Keywords:** Finite element methods; Nonlinear elastodynamics; Nonlinear thermo-elasto dynamics; Nonlinear electro-elastodynamics; Hu-Washizu functional; Mixed finite elements; Implicit time-stepping schemes; Structure-preserving discretization; Tensor cross product; Electroactive polymer.



# Kurzfassung

Die vorliegende Dissertation behandelt die Entwicklung strukturerhaltender numerischer Methoden für die nichtlineare Elastodynamik und deren Erweiterung auf Mehrfeld-Probleme. Im ersten Schritt wird eine neue Herangehensweise zur Entwicklung von energie- und drehimpulskonsistenten Zeitschrittverfahren für die nichtlineare Elastodynamik vorgestellt. Die zugrundeliegende gemischte Variationsformulierung ist hierbei motiviert durch die polykonvexe Form der Formänderungsenergiefunktion und wird durch die Einführung eines Tensorprodukt für Tensoren zweiter Stufe begünstigt. Die strukturerhaltende Diskretisierung in der Zeit der gemischten Variationsformulierung resultiert in einer energie- und drehimpulskonsistenten semidiskreten Formulierung. Diese vorgestellte semidiskrete Formulierung erlaubt dann verschiedene Möglichkeiten für die räumliche Diskretisierung. Die Verwendung einer rein verschiebungsbasierten Formulierung als Spezialfall resultiert dann in einer neuen algorithmischen Spannungsformel für die nichtlineare Elastodynamik. Im Anschluss wird eine weitere algorithmische Spannungsformel eingeführt. Diese unterscheidet sich durch die Beschreibung in den Eigenwerten des Verzerrungstensors und erlaubt die Simulation transienten Verhaltens von hyperelastischen Körpern bestehend aus Material vom Ogden-Typ. Darüber hinaus erfolgt die Erweiterung der bestehenden Formulierung auf Mehrfeld-Probleme. Hierfür wird ein neuer Ansatz für die Entwicklung energie- und drehimpulskonsistenter Zeitschrittverfahren der nichtlinearen Thermo-Elastodynamik und Elektro-Elastodynamik vorgestellt. Zur Demonstration aller vorgestellten Formulierungen werden numerische Beispiele herangezogen, um die hervorragenden Eigenschaften der energie- und drehimpulskonsistenten Zeitschrittverfahren im Hinblick auf die numerische Genauigkeit, Stabilität, Validität und Robustheit aufzuzeigen.

**Schlüsselwörter:** Finite Elemente Methode, Nichtlineare Elastodynamik; Nichtlineare Elektro-Elastodynamik; Nichtlineare Thermo-Elastodynamik; Hu-Washizu Funktional; Gemischte finite Elemente; Implizite Zeitschrittverfahren; Strukturhaltende Diskretisierung; Tensorprodukt; Elektroaktive Polymere.

# Acknowledgements

The work presented in this thesis was carried out during my time as a research assistant at the Institute of Mechanics (IfM) at Karlsruhe Institute of Technology (KIT) from May 2014 to May 2019. The support of the DFG (Deutsche Forschungsgemeinschaft) within the Project BE 2285/9 entitled 'Gemischte Verfahren für die strukturerhaltende Integration in der nichtlinearen Struktur- und Elastodynamik' is gratefully acknowledged.

First and foremost, I want to express my deepest gratitude to my supervisor Prof. Peter Betsch for offering me the great opportunity to work in the field of computational mechanics. His vast knowledge of mechanics and numerical methods inspired me from the first course in mechanics during my bachelor's degree till today. Throughout the years, he has always been patient, understanding and motivating to me. Without all the discussions, his guidance and encouragement, this work would not have been possible. I will be forever grateful to that.

My special thank also goes to Prof. Sigrid Leyendecker for acting as the external examiner of this thesis.

The last few years of intensive and successful work in both research and teaching, have been supported by all my colleagues, co-workers and friends at the institute. Therefore, I would like to express my gratitude to all of them. In particular, I would like to thank Dr. Marlon Franke for hiring me as a student staff member, approximately eight years ago. I am very thankful for his technical support, the fruitful collaborations and all of his help during my time at the institute. A very special thank you goes to Mark Schiebl. I am grateful for his thorough understanding of computational mechanics, for sharing his knowledge, shell scripts and kitchen sink. Furthermore, I would like to thank Jonas Hund for sharing the office with me during many hours of exhausting work and also for sharing his power-bars on exhausting roadbike tours. Moreover, a special thank you goes to Tobias Laschütza for all the

very important discussions about life and science during our countless after work runs. Additionally, I like to thank Timo Ströhle for sharing coffee and French pastry during our lunch-extensions. But I also would like to thank my other colleagues at the IfM: Julian Bauer, Robin Pfefferkorn, Simeon Schneider, Michael Strobl, as well as my former colleagues, Christian Becker and Yinping Yang for their support and contributing to the excellent working atmosphere in our institute. In addition, I would like to thank all the student staff and tutors at the IfM. I am grateful to my student assistant, Philipp Kinon, for all of his help over the past few years.

Also, many thanks to the working group at the Chair of Computational Mechanics, University of Siegen. In particular, I would like to thank Prof. Christian Hesch for the helpful discussions, the technical support and for providing the computational environment 'ESRA'. Moreover, I would like to thank Dr. Maik Dittmann, Dr. Melanie Krüger, Stefan Schuß and Jonathan Schulte for the successful collaboration on the ESRA project during the last few years.

Acknowledgement is also given to Antonio Gil, Professor at Zienkiewicz Centre for computational Engineering, Swansea, UK. I highly appreciate having had the chance to work with him and Dr. Rogelio Ortigosa for a period of three months, during my stay in Swansea. I enjoyed all the discussions regarding my work and I am glad that the collaboration was a success both in Swansea and ongoing. Many people helped to make my time in Swansea most enjoyable. My friends, Dr. Mai Abdul Latif, Dr. Nidhal Jamia and Dr. Germán Martínez Ayuso made this period of time very special, not only from the research point of view.

Regarding this thesis, I express my special thanks to my Canadian sister, Danielle den Admirant, for stylistic and linguistic suggestions.

I am very thankful to all of my friends for their support, not only during my time as a PhD candidate, but over the course of my life.

Finally, and most importantly, I would like to express my deepest gratitude and acknowledgement to my entire family. I must thank my mother Gabriele Janz, my father Klaus Janz, my sister Katharina Schulz and my grandparents Alois Link and Johanna Link. They all encouraged me to find what I love, to work hard at it and achieve great heights. While showing me constant support and unconditional love throughout my lifetime.

Karlsruhe, 2019

Alexander Janz

# Contents

<b>List of Figures</b> . . . . .	<b>xi</b>
<b>List of Tables</b> . . . . .	<b>xv</b>
<b>1 Introduction</b> . . . . .	<b>1</b>
1.1 Objectives . . . . .	3
1.2 Organization of the work . . . . .	7
<b>2 Continuum mechanics</b> . . . . .	<b>9</b>
2.1 Cofactor and tensor cross product . . . . .	9
2.2 Kinematics . . . . .	11
2.2.1 Polyconvex large strain elasticity . . . . .	13
2.2.2 Frame-indifferent material formulation . . . . .	15
<b>3 A mixed variational framework for the design of EM schemes</b> . . . . .	<b>19</b>
3.1 Variational formulation . . . . .	19
3.1.1 Extension to elastodynamics . . . . .	22
3.1.2 Balance laws . . . . .	24
3.2 Discretization in time . . . . .	27
3.2.1 Structure-preserving integration scheme . . . . .	28
3.2.2 Semi-discrete balance laws . . . . .	31
3.3 Discretization in space . . . . .	34
3.3.1 Displacement formulation . . . . .	34
3.3.2 Mixed formulation . . . . .	37
3.4 Numerical Investigations . . . . .	38
3.4.1 Patch test . . . . .	39
3.4.2 Cooks membrane . . . . .	41
3.4.3 L-shaped block . . . . .	43

<b>4</b>	<b>EM schemes for quasi-incompressible elasticity in principal stretches . . .</b>	<b>49</b>
4.1	Multiplicative and spectral decomposition . . . . .	49
4.1.1	Eigenvalue representation . . . . .	49
4.1.2	Spectral decomposition . . . . .	51
4.1.3	Multiplicative decomposition . . . . .	51
4.2	Constitutive equations for large strain elasticity . . . . .	52
4.2.1	Hyperelastic model using principal stretches . . . . .	54
4.2.2	Ogden-type material model . . . . .	55
4.3	Variational formulation . . . . .	56
4.3.1	Displacement based variational formulation . . . . .	56
4.3.2	Mixed formulation for quasi-incompressibility . . . . .	57
4.3.3	Extension to elastodynamics . . . . .	58
4.3.4	Balance laws . . . . .	58
4.4	Discretization in time . . . . .	60
4.4.1	Structure-preserving integration scheme . . . . .	61
4.4.2	Semi-discrete balance laws . . . . .	63
4.5	Discretization in space . . . . .	65
4.6	Numerical Investigations . . . . .	66
4.6.1	Static convergence analysis . . . . .	66
4.6.2	Compressed block . . . . .	68
4.6.3	Twisting column . . . . .	73
<b>5</b>	<b>EM scheme for nonlinear thermo-elastodynamics . . . . .</b>	<b>77</b>
5.1	Finite strain thermo-elastodynamics . . . . .	77
5.2	Constitutive equations for large strain thermo-elasticity . . . . .	80
5.3	Temperature-based governing equations . . . . .	82
5.3.1	Temperature-based strong form . . . . .	82
5.3.2	Temperature-based weak form . . . . .	83
5.3.3	Balance laws . . . . .	84
5.4	Discretization in time . . . . .	86
5.4.1	Structure-preserving integration scheme . . . . .	87
5.4.2	Semi-discrete balance laws . . . . .	89
5.5	Discretization in space . . . . .	91
5.6	Numerical Investigations . . . . .	92
5.6.1	L-shaped block . . . . .	93
5.6.2	Rotating disc . . . . .	97
5.6.3	Moving disc . . . . .	99

---

<b>6</b>	<b>EM scheme for nonlinear electro-elastodynamics</b>	<b>103</b>
6.1	Finite strain electrostatic-elastodynamics	103
6.2	Constitutive equations for large strain electro-elasticity	104
6.3	Variational formulation	106
6.3.1	Three-field mixed formulation for electro-mechanics	106
6.3.2	Extension to electro-elastodynamics	108
6.3.3	Balance laws	109
6.4	Discretization in time	111
6.4.1	Structure-preserving integration scheme	111
6.4.2	Semi-discrete balance laws	114
6.5	Discretization in space	117
6.6	Numerical Investigations	118
6.6.1	Rotating actuator	118
6.6.2	Bending actuator	121
6.6.3	Rotating cross	125
6.6.4	Twisting actuator	129
6.6.5	Clamped membrane	133
<b>7</b>	<b>Summary and outlook</b>	<b>137</b>
7.1	Summary	137
7.2	Outlook	139
<b>Appendix A</b>	<b>Appendix to Chapter 2</b>	<b>141</b>
A.1	Relations for the tensor cross product	141
<b>Appendix B</b>	<b>Appendix to Chapter 3</b>	<b>143</b>
B.1	Implementation details of the displacement formulation	143
B.2	Implementation details of the mixed formulation	145
<b>Appendix C</b>	<b>Appendix to Chapter 4</b>	<b>151</b>
C.1	Spectral decomposition of a symmetric tensor and its cofactor	151
C.2	Relationship between the eigenvalue of a tensor and its derivative	152
C.3	Remarks on the numerical implementation	153
C.3.1	Time discrete eigenvalues	153
C.3.2	Perturbation technique	153
<b>Appendix D</b>	<b>Appendix to Chapter 5</b>	<b>155</b>
D.1	Energy termination	155

D.2 Classical mid-point discretization . . . . . 155

D.3 Linearisation of the material model . . . . . 156

**Appendix E Appendix to Chapter 6 . . . . . 159**

    E.1 Proof of directionality property . . . . . 159

    E.2 Definition of the discrete derivatives in the limit . . . . . 160

**Declaration of Authorship . . . . . 165**

**Publications and talks . . . . . 167**

**Bibliography . . . . . 171**

# List of Figures

1.1	Sketch of the aim of the present work . . . . .	3
2.1	Sketch of the reference and the deformed configuration of a continuum body. 11	
3.1	Nodal points for the displacements and mixed fields. . . . .	39
3.2	Patch test: Boundary conditions, initial regular mesh and distorted mesh. . 40	
3.3	Patch test: Stress distribution of the regular and distorted mesh (disp. form.). 40	
3.4	Patch test: Stress distribution of the regular and distorted mesh (mix. form.). 41	
3.5	Cooks membrane: Boundary conditions, initial mesh and final stress distribution. . . . .	42
3.6	Cooks membrane: Convergence with mesh refinement. . . . .	43
3.7	Cooks membrane: Comparison of the Newton iterations in a typical load step. . . . .	43
3.8	L-shaped block: Initial configuration. . . . .	44
3.9	L-shaped block: Snapshots of configurations and von Mises stress distribution. . . . .	46
3.10	L-shaped block: Total energy versus time (disp. formulation). . . . .	47
3.11	L-shaped block: Incremental change of total energy (disp. formulation). . . 47	
3.12	L-shaped block: Total energy versus time (mixed formulation). . . . .	47
3.13	L-shaped block: Incremental change of total energy (mixed formulation). . 47	
3.14	L-shaped block: Incremental change of angular momentum (disp. formulation). . . . .	48
3.15	L-shaped block: Incremental change of angular momentum (mixed formulation). . . . .	48
4.1	Nodal points for the Q1 finite element and the Q1P0 finite element. . . . .	66
4.2	Convergence analysis: Boundary conditions and stress distribution. . . . .	68
4.3	Convergence analysis: Mesh refinement convergency. . . . .	69
4.4	Convergence analysis: Newton iterations. . . . .	69

4.5	Compressed block: Boundary conditions, mesh and final stress distribution. . . . .	70
4.6	Compressed block: Convergence with mesh refinement (compressible). . . . .	71
4.7	Compressed block: Convergence with mesh refinement (quasi incomp.). . . . .	71
4.8	Compressed block: Evolution of total energy. . . . .	72
4.9	Compressed block: Incremental change of total energy. . . . .	72
4.10	Compressed block: Snapshots of configurations with stress distribution. . . . .	72
4.11	Column: Boundary conditions, mesh, nodal velocity and stress distribution. . . . .	73
4.12	Column: Evolution of total energy. . . . .	75
4.13	Column: Incremental change of total energy. . . . .	75
4.14	Column: Evolution of total angular momentum. . . . .	75
4.15	Column: Incremental change of total angular momentum. . . . .	75
4.16	Column: Error in the displacements. . . . .	76
4.17	Column: Snapshots of configurations with stress distribution. . . . .	76
5.1	L-shaped block: Boundary and temperature conditions and discretized model. . . . .	93
5.2	L-shaped block: Total energy evolution. . . . .	95
5.3	L-shaped block: Incremental change of energy. . . . .	95
5.4	L-shaped block: Total angular momentum evolution. . . . .	95
5.5	L-shaped block: Incremental change of angular momentum. . . . .	95
5.6	L-shaped block: Study of convergence of the error in displacements. . . . .	96
5.7	L-shaped block: Snapshots of configurations with temperature distribution. . . . .	96
5.8	Rotating disc: Initialized motion, boundary conditions and discretized model. . . . .	97
5.9	Rotating disc: Total energy evolution. . . . .	98
5.10	Rotating disc: Incremental change of energy. . . . .	98
5.11	Rotating disc: Snapshots and temperature plots. . . . .	99
5.12	Moving disc: Initialized motion, boundary conditions and discretized model. . . . .	100
5.13	Moving disc: Total energy evolution. . . . .	101
5.14	Moving disc: Temperature distribution. . . . .	101
5.15	Moving disc: Snapshots of configurations and temperature plots. . . . .	102
6.1	Nodal points for finite elements considered . . . . .	118
6.2	Rotating actuator: Configuration, boundary conditions and discretizations. . . . .	119
6.3	Rotating actuator: Second order accuracy of proposed EM scheme. . . . .	120
6.4	Bending actuator: Configuration, boundary conditions and discretizations. . . . .	122
6.6	Bending actuator: Evolution of Hamiltonian. . . . .	123
6.7	Bending actuator: Incremental change of Hamiltonian. . . . .	123

---

6.5	Bending actuator: Contour plot of von Mises stress. . . . .	124
6.8	Rotating cross: Configuration, boundary conditions and discretization. . .	125
6.9	Rotating cross: Evolution of Hamiltonian. . . . .	127
6.10	Rotating cross: Incremental change of Hamiltonian. . . . .	127
6.11	Rotating cross: Incremental change of Hamiltonian (detail). . . . .	128
6.12	Rotating cross: Evolution of angular momentum. . . . .	128
6.13	Rotating cross: Incremental change of angular momentum . . . . .	128
6.14	Rotating cross: Contour plot of electric potential. . . . .	129
6.15	Twisting actuator: Configuration, boundary conditions and discretization.	130
6.16	Twisting actuator: Evolution of Hamiltonian. . . . .	132
6.17	Twisting actuator: Incremental change of Hamiltonian. . . . .	132
6.18	Twisting actuator: Contour plot of the von Mises stress. . . . .	132
6.19	Clamped membrane: Configuration, boundary conditions and discretization.	133
6.20	Clamped membrane: Evolution of Hamiltonian. . . . .	135
6.21	Clamped membrane: Incremental change of Hamiltonian. . . . .	135
6.22	Clamped membrane: Contour plot of the von Mises stress. . . . .	135



# List of Tables

- 3.1 Patch test: Material data, simulation parameters and geometry. . . . . 40
- 3.2 Cooks membrane: Material data, simulation parameters and geometry. . . 42
- 3.3 Cooks membrane: Investigation on the robustness . . . . . 43
- 3.4 L-shaped block: Investigation on the robustness . . . . . 45
- 3.5 L-shaped block: Material data, simulation parameters and geometry. . . . . 46
  
- 4.1 Convergence analysis: Material data, simulation parameters and geometry. 68
- 4.2 Compressed block: Material data, simulation parameters and geometry. . . 71
- 4.3 Column: Material data, simulation parameters and geometry. . . . . 74
  
- 5.1 L-shaped block: Material data, simulation parameters and geometry. . . . . 94
- 5.2 Rotating disc: Material data, simulation parameters and geometry . . . . . 98
- 5.3 Moving disc: Material data, simulation parameters and geometry . . . . . 100
  
- 6.1 Rotating actuator: Material and simulation parameters and geometry. . . . 120
- 6.2 Bending actuator: Discretization spaces for finite elements considered. . . . 121
- 6.3 Bending actuator: Material and simulation parameters and geometry. . . . 123
- 6.4 Rotating cross: Material and simulation parameters and geometry. . . . . 126
- 6.5 Twisting actuator: Material and simulation parameters and geometry. . . . 131
- 6.6 Clamped membrane: Material and simulation parameters and geometry. . 134



# 1 Introduction

In the last three decades, energy-momentum (EM) consistent integrators have been developed mainly in the field of structural and solid mechanics for the simulation of time-dependent non-linear problems. Because the consistent approximation of linear momentum, angular momentum, and total energy are desirable for those transient simulations, EM schemes seem to be the method of choice. Moreover, this class of second-order accurate time-stepping schemes yield an enhanced performance in terms of robustness and stability. The origin of this method can be found in [72, 55]. Especially during the nineties, EM consistent schemes made a breakthrough due to the works of [156, 159, 153, 50]. From that point until now, ongoing research on EM consistent time-integrators for non-linear structural dynamics and non-linear solid dynamics can be observed; see e.g., [158, 154, 92, 37, 49, 146, 147, 30, 54, 100, 10, 88, 118, 145, 46, 23, 80, 81].

Due to their desirable properties and improved performance, EM consistent schemes have also been successfully applied in different fields of computational mechanics, such as in non-linear visco-elastodynamics [57], anisotropic material behavior [59], finite deformation contact problems [94, 3, 63, 64], flexible multibody dynamics [11, 74, 29, 18, 19, 97, 16, 101, 22], optimal control problems [28, 21, 85, 14], non-linear elasto-thermodynamics [143, 58, 144, 65, 36, 44, 17] and electro-elastodynamics [83, 82, 133, 45].

In contrast to EM schemes, many important members of second-order implicit time integrators show numerical dissipation; see e.g., [70, 123, 136, 173, 67, 34]. However, by reason of the consistent energy approximation, EM schemes seem to be the perfect starting point when dealing with energy-decaying time-stepping schemes. Recent developments for energy-decaying time-stepping schemes can be found in [11, 91, 93, 4, 5, 146, 96].

Another elegant class of structure-preserving numerical methods are variational integrators, which follow an alternative path compared to EM schemes. The discrete Euler-Lagrange equations are obtained by the direct discretization of the variational functional. This yields a symplectic time-stepping scheme, and therefore the symmetries of the mechanical system are consistently approximated. A drawback of variational integrators is the lack of consistent energy approximation, although the error of the energy is bounded. See [109, 172, 98, 99, 102, 103, 20, 124, 148, 86, 171, 9] for detailed introductions and more recent developments on variational integrators.

We direct readers to the book of [13] for more background on structure-preserving numerical methods in general and on EM schemes (with their energy-dacaying variants) as well as variational integrators in particular.

For the space discretization of the semi-discrete equations of motion of the underlying mechanical system, the Finite Element Method (FEM) is widely used. A drawback of the FEM is that standard finite elements behave poorly under certain circumstances. Historically, the development of the FEM was influenced by the search for a finite element, suitable for all conceivable applications (see e.g., [71, 12, 174] for an overview of different approaches to improve the behavior of finite elements). A well-established approach for the formulation of high-performance finite elements is based on a mixed variational formulation originating from Hu-Washizu-type variational principles [170]. A large variety of mixed and enhanced finite elements for finite strain elasticity have been envisaged from these variational functionals (see e.g., [157, 152, 160, 48, 1, 84, 169, 149, 26, 23]). In non-linear applications, these elements often perform very well compared to classical displacement-based elements. Depending on which mixed finite element is used, one can observe a locking-free response, high coarse mesh accuracy, and very robust behavior in Newton-type solution processes (see numerical examples in the cited references).

Interestingly, previous EM consistent schemes have been mainly developed in the framework of displacement-based finite elements. As shown in [2], the use of mixed finite elements do not inherit the consistent approximation of energy and momentum balances in general. Only specific mixed finite elements have been successfully applied to EM schemes such as in [92, 115, 30], to name but a few.

# 1.1 Objectives<sup>1</sup>

In this work we aim to create a mixed variational framework for the design of EM schemes inspired by the structure of polyconvex stored energy functions. The combination of both, mixed finite elements and EM consistent time stepping schemes, gives rise to an improved performance in terms of accuracy, stability, and robustness within transient simulations. Moreover, with this framework at hand, we also focus on more involved problems of solid mechanics, such as modeling quasi-incompressible material behavior or the simulation of multi-field problems. To be precise, we focus on the intersections of these topics of computational mechanics, as illustrated in Fig. 1.1.

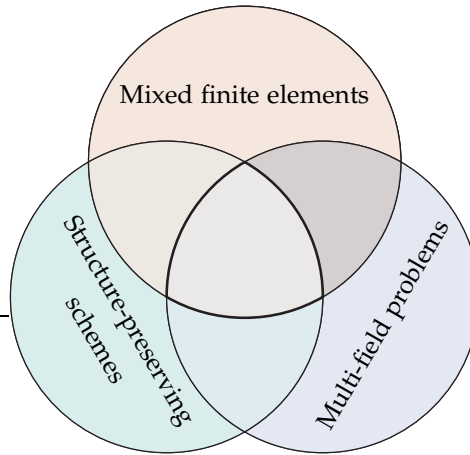


Figure 1.1: Sketch of the aim of the present work

## Design of EM schemes

In the last few years, the important notion of polyconvexity [7] inspired the design of new classes of mixed finite elements in the field of finite-strain solid mechanics. These types of finite elements rely on the independent approximation of the deformation map and an additional approximation of further kinematic fields entering the polyconvexity-inspired strain energy function. Starting from a Hu-Washizu-type variational functional [170], a large variety of alternative mixed finite element formulations can be envisaged. The novel mixed element formulation introduced by

<sup>1</sup> This section is based on the introductions given in [23, 81, 44, 133].

[26, 27], which builds upon the ideas of [149], particularly shows great advantages in terms of stability and robustness. Moreover, this formulation has been used in different fields of computational mechanics; for example in electro-mechanics [47, 131], phase-field models [66], beam and shell formulations [132, 130], and smooth particle hydrodynamic algorithms for large strain solid mechanics [95], to name but a few. In addition to the polyconvexity-based framework, the present work relies on the cross product between second-order tensors as introduced in [38]; see also [39, App. B 4.9.3]. This so-called tensor cross product has been used in the context of large-strain hyperelasticity in [26, 27] and remarkably simplifies the algebraic manipulation of the large-strain continuum formulation. In connection to EM schemes based on a mixed variational functional [77, 15, 78, 79, 23], we present a new cascade of kinematic relationships that make possible the EM consistent space-time discretization of hyperelastic continuum bodies. In particular, the newly proposed mixed variational formulation facilitates the design of new EM consistent discretizations in time. In addition to this, the mixed variational framework makes a wide variety of finite element discretizations in space possible. In the special case of a purely displacement-based discretization, we obtain a new form of the algorithmic stress formula which is a typical feature of EM consistent methods [145]. In particular, the new stress formula assumes a remarkably simple form, when compared to previously proposed alternative formulations [52, 60, 6].

## Quasi-incompressible elasticity in principal stretches

One aim of the present work is to extend the existing formulation [26, 27] to the class of Ogden-type materials [125, 126] defined in the principal stretches. To this end, we make use of a spectral decomposition of the strain tensor; see e.g., [162]. Ogden-type materials are known to yield a good relation between numerical simulations and experiments in finite strain elasticity problems of rubber-like solids [125]. Moreover, the Mooney-Rivlin material [120] is contained as a special case in the more general class of Ogden-type material; see e.g., [35]. In the present work we use a multiplicative decomposition of the deformation gradient to decouple the deformation into an isochoric part and a volumetric part, as proposed by [43]. This kinematic split is known to be advantageous in computational mechanics when dealing with nearly incompressible material behavior [157, 155]. Furthermore, we use a three-field Hu-Washizu variational principle to define our mixed framework motivated by the work of [157, 155], where next to the deformation map, the hydrostatic pressure and the

volumetric dilatation enter the mixed variational functional. Concerning the extension to nonlinear dynamics, we introduce a new algorithmic stress formula based on [23], now defined in terms of the principal stretches. This leads to a consistent energy and momentum approximation in time.

## Non-linear thermo-elastodynamics

Another objective of this work is the consistent discretization of nonlinear thermo-elastodynamics. In recent decades thermo-mechanical constitutive models have been addressed in numerous works (see e.g. [113, 69, 142] and textbooks [68, 53]). Classically, the hyperelastic Helmholtz free energy density function depends only on the deformation gradient and the temperature. Furthermore, the weak form is deduced from its strong form. Depending on the chosen material model, e.g., for a Mooney-Rivlin model, the consistent linearisation may lead to cumbersome expressions. In contrast to the classical approach, the present work is inspired by the concept of polyconvexity [7, 35]. The Helmholtz free energy is a convex function of the deformation gradient, its co-factor, its determinant, and is concave with respect to the absolute temperature. It is the main goal of this part of the thesis to apply the concept of EM consistent integrators to the regime of thermo-elastodynamical problems. The energy balance equation is commonly stated in entropy form [41, 65, 58, 69, 73] for this class of problems where the absolute temperature is chosen as the state variable. The construction of EM consistent integrators within such a framework relies on cumbersome discrete gradient operators [65] that feature artificial contributions for the algorithmic stress formula to restore energy consistency in the discrete setting. An alternative approach is based on the general equation for non-equilibrium reversible-irreversible coupling (GENERIC) framework [56, 134, 135]. Previously developed GENERIC-based formulations of nonlinear thermo-elastodynamics rely on the entropy density as the thermodynamical state variable (see e.g. [143, 144, 89, 90, 36]). In these works, EM consistent integrators have been successfully implemented. The main drawback of the entropy form is that the absolute temperature is preferred as the thermodynamical state variable in terms of material modeling [69, 142, 105, 122] because it can be measured directly. A Legendre transformation would be necessary to gain entropy-based thermodynamical potentials, which may involve a Newton procedure when the expression for the temperature can not be inverted analytically, but rather would need to be performed at each Gauss point. Furthermore, temperature Dirichlet boundary conditions cannot be applied directly, leading to the introduction

of Lagrange multipliers [89, 90], extending the system of equations to be solved. We therefore rephrase the energy balance into temperature form to be able to use the absolute temperature as the state variable [36] using the polyconvexity-based framework. In the semi-discrete setting, [36] makes use of the discrete derivative in the sense of [52] to construct EM integrators resulting in a complex algebraic formulation and implementation. In contrast, we present an algorithmic stress formula developed within the polyconvexity-based framework that avoids the use of the discrete derivative for the presented material model and instead uses an energy-conserving formula introduced in [55], which results in a remarkably simple form. In addition, we show that the algorithm presented herein is numerically stable for different types of initial and boundary conditions and correctly reproduces the physical behavior of the thermo-mechanical model.

## Non-linear electro-elastodynamics

Another objective is to derive an EM consistent scheme tailor-made for non-linear electro-elastodynamics to model the transient behavior of Electro Active Polymers (EAPs). EAPs [137, 138, 139, 87] represent an important family of smart materials, where dielectric elastomers and piezoelectric polymers are some of their most iconic integrants. Dielectric elastomers are very well known for their outstanding actuation capabilities and low stiffness properties, which makes them ideal for their use as soft robots [127]. For instance, electrically induced area expansions of over 380% on dielectric elastomer thin films placed on the verge of snap-through configurations have been reported in [104]. Other applications for dielectric elastomers include Braille displays, deformable lenses, haptic devices and energy generators, to name but a few [33]. Piezoelectric polymers have similar dielectric properties to dielectric elastomers, but, in contrast, have much larger stiffness. As a result, piezoelectric polymers cannot, in principle, exhibit large, electrically induced deformations. Instead, they can be used as moderately deformable actuators. Other important types of applications for these materials include tactile sensors, energy harvesters, acoustic transducers, and inertial sensors [127, 33]. The variational formulation of the governing equations of these materials is well established. In the most standard formulation, displacements and the scalar electric potential [165, 166, 167, 76, 163, 42, 148] are modelled as the unknown fields. In this formulation, the constitutive information is encapsulated in the Helmholtz energy functional via its invariant-based representation, depending upon kinematic strain measures and the electric field [32, 31]. However, for more complex

constitutive models than that of an ideal dielectric elastomer, the saddle point nature of the Helmholtz functional (convex with respect to the deformation gradient tensor and concave with respect to the electric field in the small strain/small electric field regime), makes it impossible to define *a priori* constitutive models that satisfy the ellipticity condition [108, 151, 150] in general. This is a necessary condition that ensures the well-posedness of the problem. Motivated by the possible loss of ellipticity of the Helmholtz functional, Gil and Ortigosa [47, 129, 128] advocated for the use of the internal energy functional for the definition of constitutive models in nonlinear electro-mechanics. In essence, the authors postulated a definition of the internal energy convex with respect to an extended set of arguments and proved that this definition satisfies the ellipticity condition unconditionally.

## 1.2 Organization of the work

The outline of this thesis is as follows:

**Chapter 2:** This chapter provides a summary of classical continuum mechanics as a basis for the present work. In Sec. 2.1 we introduce the tensor cross product of second-order tensors along with further algebraic relationships needed. Kinematic relations and the governing equations for finite strain elasticity, focusing on hyperelastic materials with polyconvex stored energy functions, are outlined in Sec. 2.2.

**Chapter 3:** A new approach to the design of EM consistent algorithms is proposed in this chapter. In Sec. 3.1 the newly proposed mixed variational formulation is presented and subsequently extended to the dynamic regime. The structure-preserving discretization in time and the semi-discrete balance laws of the mixed variational formulation are then dealt with in Sec. 3.2. The resulting semi-discrete variational formulation is further discretized in space in Sec. 3.3. The results of numerical investigations are then presented in Sec. 3.4.

**Chapter 4:** In this chapter we propose an EM consistent time stepping scheme where the stress response is defined in its eigenvalue representation. In Sec. 4.1 the eigenvalue representation of symmetric second-order tensors is outlined. Moreover, the

spectral decomposition and the multiplicative decomposition of the right Cauchy-Green strain tensor are introduced. Sec. 4.2 deals with hyperelastic material models with polyconvex stored energy functions using principal stretches. In Sec. 4.3 a displacement-based and a mixed variational formulation for elasto-statics are introduced and subsequently extended to the dynamic regime. In Sec. 4.4 we deal with the structure-preserving discretization in time of the underlying variational formulation and investigate the semi-discrete balance laws. The semi-discrete variational formulation is then discretized in space in Sec. 4.5 by using mixed finite elements. Finally, representative numerical examples are presented in Sec. 4.6.

**Chapter 5:** In this chapter we provide an EM consistent time stepping scheme for thermo elastodynamics. The equations of classical continuum thermo-elastodynamics are briefly summarized in Sec. 5.1. The polyconvexity-based formulation of the Helmholtz free-energy is introduced in Sec. 5.2. In Sec. 5.3 the weak form of the thermo-mechanically coupled problem at hand is deduced, where the temperature-based framework is employed. Furthermore, the strong form of the newly proposed polyconvexity-based framework is compared with the classical formulation. In addition, balance laws are investigated for the new framework. In Sec. 5.4 an EM consistent time-stepping scheme is newly proposed, where the balance laws for the semi-discrete system are demonstrated. The semi-discrete system is discretized in space in Sec. 5.5 by using finite elements. Eventually, representative numerical examples are outlined in Sec. 5.6.

**Chapter 6:** A new EM consistent time-stepping scheme for reversible electro-elastodynamics is proposed in this chapter. The governing equations in nonlinear electro-elastodynamics are presented in Sec. 6.1. The concept of multi-variable convexity and its importance from a material stability standpoint is presented in Sec. 6.2. Sec. 6.3 starts with a three-field mixed formulation in the context of static electromechanics. Its extension to electro-elastodynamics is then carried out. After derivation of the stationary conditions, Sec. 6.4 introduces a new EM time-stepping scheme for electro-elastodynamics. Sec. 6.5 briefly describes the finite element implementation of the new time integrator scheme and Section 6.6 presents some numerical examples in order to validate the conservation properties and robustness of the new scheme.

**Chapter 7:** Finally, the discussed topics are briefly summarized, conclusions are drawn, and an outlook on further research will be given in this chapter.

## 2 Continuum mechanics<sup>1</sup>

In this chapter we introduce the tensor cross product of second-order tensors along with further algebraic relationships needed in the sequel. Moreover, a summary of large strain solid mechanics focusing on hyperelastic materials with polyconvex stored energy function is given.

### 2.1 Cofactor and tensor cross product

In this section we introduce the cross product of two second-order tensors and provide a summary of important algebraic relations needed in the sequel. The present work deals with continuum bodies occupying three-dimensional Euclidean space. Vectors are typically denoted by lower case bold-face letters such as  $\mathbf{a} \in \mathbb{R}^3$ , with components  $a_i$  relative to a Cartesian coordinate frame. Second-order tensors are typically denoted by upper case bold-face letters such as  $\mathbf{A}$ , with associated Cartesian components  $A_{ij} = (\mathbf{A})_{ij}$ , ( $1 \leq i, j \leq 3$ ). The cofactor  $\text{cof}(\mathbf{A})$  of a second-order tensor  $\mathbf{A}$  is given by (see, for example, [35, Ch. 1])

$$(\text{cof}\mathbf{A})_{ij} = \frac{1}{2} \varepsilon_{imn} \varepsilon_{jpq} A_{mp} A_{nq}. \quad (2.1)$$

Here,  $\varepsilon_{ijk}$  denotes the permutation symbol and the summation convention applies to pairs of repeated indices. The determinant  $\det(\mathbf{A})$  can now be written in the form

$$\det(\mathbf{A}) = \frac{1}{3} (\text{cof}\mathbf{A})_{ij} A_{ij}. \quad (2.2)$$

---

<sup>1</sup> This chapter is based on [23].

The last equation directly gives rise to the well-known relationship

$$\det(\mathbf{A}) \mathbf{A}^{-\text{T}} = \text{cof}(\mathbf{A}), \quad (2.3)$$

provided that  $\mathbf{A}$  is invertible. Moreover, (2.1) directly leads to the familiar relationship

$$\text{cof}(\mathbf{A}) (\mathbf{a} \times \mathbf{b}) = (\mathbf{A}\mathbf{a}) \times (\mathbf{A}\mathbf{b}), \quad (2.4)$$

where the cross product of two vectors  $\mathbf{a}, \mathbf{b} \in \mathbb{R}^3$  is given by

$$(\mathbf{a} \times \mathbf{b})_i = \varepsilon_{ijk} a_j b_k. \quad (2.5)$$

Scalar multiplication of (2.4) by the vector  $\mathbf{A}\mathbf{c}$  and taking into account (2.3) leads to the expression

$$\det(\mathbf{A}) = \frac{((\mathbf{A}\mathbf{a}) \times (\mathbf{A}\mathbf{b})) \cdot (\mathbf{A}\mathbf{c})}{(\mathbf{a} \times \mathbf{b}) \cdot \mathbf{c}}. \quad (2.6)$$

Similarly, it is straightforward to show that the following relations hold:

$$\begin{aligned} (\text{cof} \mathbf{A})^{\text{T}} &= \text{cof}(\mathbf{A}^{\text{T}}), \\ \text{cof}(\mathbf{A}\mathbf{B}) &= \text{cof}(\mathbf{A}) \text{cof}(\mathbf{B}). \end{aligned} \quad (2.7)$$

Next, the cross product of two second-order tensors  $\mathbf{A}$  and  $\mathbf{B}$  is introduced as (see also [27])

$$(\mathbf{A} \star \mathbf{B})_{ij} = \varepsilon_{i\alpha\beta} \varepsilon_{jab} \mathbf{A}_{\alpha a} \mathbf{B}_{\beta b}. \quad (2.8)$$

An equivalent definition of the tensor cross product is given by (see [38] or [39, Appendix B 4.9.3])

$$(\mathbf{A} \star \mathbf{B}) (\mathbf{a} \times \mathbf{b}) = (\mathbf{A}\mathbf{a}) \times (\mathbf{B}\mathbf{b}) - (\mathbf{A}\mathbf{b}) \times (\mathbf{B}\mathbf{a}), \quad \forall \mathbf{a}, \mathbf{b} \in \mathbb{R}^3. \quad (2.9)$$

Now it is straightforward to rewrite  $\text{cof}(\mathbf{A})$  and  $\det(\mathbf{A})$  introduced in (2.1) and (2.2), respectively, by using the tensor cross product:

$$\begin{aligned} \text{cof}(\mathbf{A}) &= \frac{1}{2} (\mathbf{A} \star \mathbf{A}), \\ \det(\mathbf{A}) &= \frac{1}{6} (\mathbf{A} \star \mathbf{A}) : \mathbf{A}. \end{aligned} \quad (2.10)$$

In the last equation the scalar product of two second-order tensors is given by

$$\mathbf{A} : \mathbf{B} = \text{tr}(\mathbf{A}^{\text{T}}\mathbf{B}) = A_{ij} B_{ij}. \quad (2.11)$$

Next we summarize some important relations involving the tensor cross product that will be needed in the sequel:

$$\begin{aligned}
 \mathbf{A} \ast \mathbf{B} &= \mathbf{B} \ast \mathbf{A}, \\
 (\mathbf{A} \ast \mathbf{B})^T &= \mathbf{A}^T \ast \mathbf{B}^T, \\
 (\mathbf{A} \ast \mathbf{B}) : \mathbf{C} &= (\mathbf{A} \ast \mathbf{C}) : \mathbf{B} = (\mathbf{B} \ast \mathbf{C}) : \mathbf{A}, \\
 (\mathbf{A} \ast \mathbf{B})(\mathbf{C} \ast \mathbf{D}) &= (\mathbf{A}\mathbf{C}) \ast (\mathbf{B}\mathbf{D}) + (\mathbf{B}\mathbf{C}) \ast (\mathbf{A}\mathbf{D}), \\
 \mathbf{A} \ast (\mathbf{B} + \mathbf{C}) &= \mathbf{A} \ast \mathbf{B} + \mathbf{A} \ast \mathbf{C}, \\
 \mathbf{A} \ast \mathbf{I} &= \text{tr}(\mathbf{A})\mathbf{I} - \mathbf{A}^T, \\
 \mathbf{I} \ast \mathbf{I} &= 2\mathbf{I},
 \end{aligned} \tag{2.12}$$

where  $\mathbf{I} \in \mathbb{R}^{3 \times 3}$  is the unit tensor of second-order. For the sake of completeness, the above relations are verified in Appendix A.1.

## 2.2 Kinematics

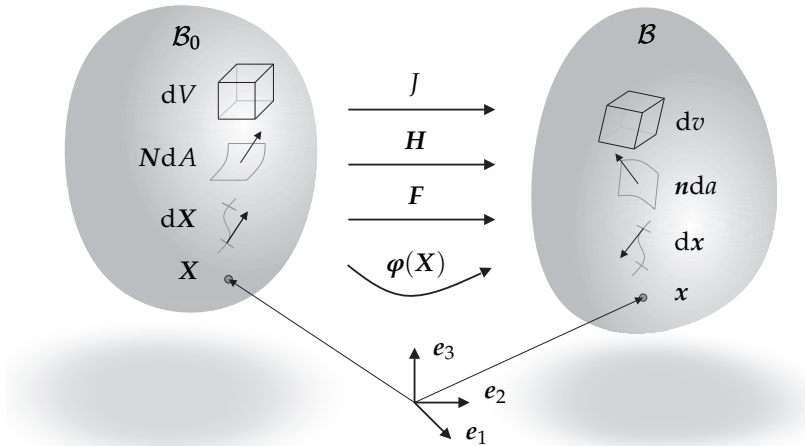


Figure 2.1: Sketch of the reference configuration  $\mathcal{B}_0$  and the deformed configuration  $\mathcal{B}$  of a continuum body

Consider a deformable body with reference configuration  $\mathcal{B}_0 \subset \mathbb{R}^3$  and sufficiently smooth boundary  $\partial\mathcal{B}_0$  as depicted in Fig. 2.1. The deformation map  $\varphi : \mathcal{B}_0 \rightarrow \mathbb{R}^3$  maps material points  $X \in \mathcal{B}_0$  to their placement  $x = \varphi(X)$  in the deformed configuration  $\mathcal{B} = \varphi(\mathcal{B}_0)$ . Assuming that on a portion  $\partial\mathcal{B}_0^\varphi$  of the boundary  $\partial\mathcal{B}_0$

the deformations are prescribed by  $\bar{\boldsymbol{\varphi}} : \partial\mathcal{B}_0^{\varrho} \rightarrow \mathbb{R}^3$ , the configuration space of the deformable body is defined by

$$\mathcal{Q} = \{\boldsymbol{\varphi} : \mathcal{B}_0 \rightarrow \mathbb{R}^3 \mid \det(\mathbf{F}) > 0, \boldsymbol{\varphi} = \bar{\boldsymbol{\varphi}} \forall \mathbf{X} \in \partial\mathcal{B}_0^{\varrho}\}. \quad (2.13)$$

The deformation gradient is a second-order tensor field  $\mathbf{F} : \mathcal{B}_0 \rightarrow \mathbb{R}^{3 \times 3}$  defined by

$$\mathbf{F} = \partial_{\mathbf{X}}\boldsymbol{\varphi}. \quad (2.14)$$

The deformation gradient maps infinitesimal vectors  $d\mathbf{X}$  based at  $\mathbf{X} \in \mathcal{B}_0$  to the corresponding infinitesimal vectors  $d\mathbf{x}$  at  $\mathbf{x} = \boldsymbol{\varphi}(\mathbf{X})$  in the deformed configuration

$$d\mathbf{x} = \mathbf{F} d\mathbf{X}. \quad (2.15)$$

Let two linearly independent infinitesimal vectors  $d\mathbf{X}^{(1)}$  and  $d\mathbf{X}^{(2)}$  span an infinitesimal oriented area element located at  $\mathbf{X} \in \mathcal{B}_0$  such that the relation

$$\mathbf{N} dA = d\mathbf{X}^{(1)} \times d\mathbf{X}^{(2)}, \quad (2.16)$$

holds, where  $\mathbf{N}$  is a unit normal vector at  $\mathbf{X} \in \mathcal{B}_0$ . The corresponding infinitesimal oriented area element at  $\mathbf{x} = \boldsymbol{\varphi}$  in the deformed configuration is given by

$$\mathbf{n} da = d\mathbf{x}^{(1)} \times d\mathbf{x}^{(2)}, \quad (2.17)$$

where  $\mathbf{n}$  is a unit normal vector at  $\mathbf{x} = \boldsymbol{\varphi}$ . Making use of (2.15), (2.17) can be recast in the form

$$\begin{aligned} \mathbf{n} da &= (\mathbf{F} d\mathbf{X}^{(1)}) \times (\mathbf{F} d\mathbf{X}^{(2)}) \\ &= \frac{1}{2} (\mathbf{F} \star \mathbf{F}) (d\mathbf{X}^{(1)} \times d\mathbf{X}^{(2)}) \\ &= \text{cof}(\mathbf{F}) \mathbf{N} dA, \end{aligned} \quad (2.18)$$

for  $\mathbf{x} = \boldsymbol{\varphi}$ . In the above equation use has been made of (2.9). Relationship (2.18) is often called Nanson's formula [126]. Next consider three non-coplanar infinitesimal vectors  $d\mathbf{X}^{(1)}$ ,  $d\mathbf{X}^{(2)}$ ,  $d\mathbf{X}^{(3)}$  at  $\mathbf{X} \in \mathcal{B}_0$ , which form a positively oriented triad (i.e.  $(d\mathbf{X}^{(1)} \times d\mathbf{X}^{(2)}) \cdot d\mathbf{X}^{(3)} > 0$ ). Then the infinitesimal volume element formed by these vectors at  $\mathbf{X} \in \mathcal{B}_0$  is given by

$$dV = (d\mathbf{X}^{(1)} \times d\mathbf{X}^{(2)}) \cdot d\mathbf{X}^{(3)}. \quad (2.19)$$

The corresponding infinitesimal volume element in the deformed configuration at  $\mathbf{x} = \boldsymbol{\varphi}(\mathbf{X})$  is given by

$$\begin{aligned} dv &= (d\mathbf{x}^{(1)} \times d\mathbf{x}^{(2)}) \cdot d\mathbf{x}^{(3)} \\ &= (\mathbf{F} d\mathbf{X}^{(1)} \times \mathbf{F} d\mathbf{X}^{(2)}) \cdot \mathbf{F} d\mathbf{X}^{(3)} \\ &= \det(\mathbf{F}) (d\mathbf{X}^{(1)} \times d\mathbf{X}^{(2)}) \cdot d\mathbf{X}^{(3)} \\ &= \det(\mathbf{F}) dV. \end{aligned} \quad (2.20)$$

In the last equation use has been made of (2.6). The fundamental kinematic relationships outlined above are also illustrated in Fig. 2.1.

## 2.2.1 Polyconvex large strain elasticity

We focus on hyperelastic material behavior with polyconvex stored energy functions of the form

$$\hat{\Psi}(\mathbf{F}) = \check{\Psi}(\mathbf{F}, \text{cof}(\mathbf{F}), \det(\mathbf{F})), \quad (2.21)$$

where  $\check{\Psi} : \mathbb{R}^{3 \times 3} \times \mathbb{R}^{3 \times 3} \times \mathbb{R}^+ \rightarrow \mathbb{R}$  is a convex function. Using the notion of a tensor cross product introduced in Sec. 2.1,  $\text{cof}(\mathbf{F})$  and  $\det(\mathbf{F})$  are recast in the form

$$\begin{aligned} \mathbf{H} &= \text{cof}(\mathbf{F}) = \frac{1}{2} \mathbf{F} \ast \mathbf{F}, \\ J &= \det(\mathbf{F}) = \frac{1}{6} (\mathbf{F} \ast \mathbf{F}) : \mathbf{F}, \end{aligned} \quad (2.22)$$

where  $\mathbf{H} : \mathcal{B}_0 \rightarrow \mathbb{R}^{3 \times 3}$  and  $J : \mathcal{B}_0 \rightarrow \mathbb{R}^+$ . In what follows we will use the expression

$$\hat{\Psi}(\mathbf{F}) = \check{\Psi}(\mathbf{F}, \mathbf{H}, J), \quad (2.23)$$

for the polyconvex stored energy function. Using (2.23), the total strain energy of the elastic body under consideration can be written as

$$\hat{\Gamma}^{\text{int}}(\boldsymbol{\varphi}) = \int_{\mathcal{B}_0} \check{\Psi}(\mathbf{F}, \mathbf{H}, J) \, dV. \quad (2.24)$$

For simplicity we assume that dead loads are acting on the body with associated potential energy of the form

$$\Pi_m^{\text{ext}}(\boldsymbol{\varphi}) = - \int_{\mathcal{B}_0} \bar{\mathbf{B}} \cdot \boldsymbol{\varphi} \, dV - \int_{\partial \mathcal{B}_0^p} \bar{\mathbf{T}} \cdot \boldsymbol{\varphi} \, dA. \quad (2.25)$$

Here  $\bar{\mathbf{B}} : \mathcal{B}_0 \rightarrow \mathbb{R}^3$  are prescribed body forces and  $\bar{\mathbf{T}} : \partial \mathcal{B}_0^p \rightarrow \mathbb{R}^3$  are prescribed stresses on  $\partial \mathcal{B}_0^p \subset \partial \mathcal{B}_0$ . As usual, we have the standard relationships  $\partial \mathcal{B}_0 = \partial \mathcal{B}_0^p \cup \partial \mathcal{B}_0^q$  and  $\partial \mathcal{B}_0^p \cap \partial \mathcal{B}_0^q = \emptyset$ . Now the total potential energy of the mechanical system at hand is given by

$$\hat{\Gamma}(\boldsymbol{\varphi}) = \hat{\Gamma}^{\text{int}}(\boldsymbol{\varphi}) + \Pi_m^{\text{ext}}(\boldsymbol{\varphi}). \quad (2.26)$$

The principle of stationary potential energy (see, for example, [170]) requires the satisfaction of the stationary condition

$$D\hat{\Pi}[\delta\boldsymbol{\varphi}] = \left. \frac{d}{d\varepsilon} \right|_{\varepsilon=0} \hat{\Pi}(\boldsymbol{\varphi}_\varepsilon) = 0, \quad (2.27)$$

where

$$\boldsymbol{\varphi}_\varepsilon = \boldsymbol{\varphi} + \varepsilon \delta\boldsymbol{\varphi}, \quad (2.28)$$

and  $\delta\boldsymbol{\varphi} \in \mathcal{V}$  denote admissible material variations of  $\boldsymbol{\varphi} \in \mathcal{Q}$  defined by the set

$$\mathcal{V} = \{ \delta\boldsymbol{\varphi} : \mathcal{B}_0 \rightarrow \mathbb{R}^3 \mid \delta\boldsymbol{\varphi} = \mathbf{0} \text{ for } \mathbf{X} \in \partial\mathcal{B}_0^q \}. \quad (2.29)$$

Now condition (2.27) along with (2.26) and (2.24) give rise to

$$\begin{aligned} D\hat{\Pi}^{\text{int}}[\delta\boldsymbol{\varphi}] &= \int_{\mathcal{B}_0} \left. \frac{d}{d\varepsilon} \right|_{\varepsilon=0} \tilde{\Psi}(\mathbf{F}_\varepsilon, \mathbf{H}_\varepsilon, J_\varepsilon) dV \\ &= \int_{\mathcal{B}_0} (\partial_{\mathbf{F}} \tilde{\Psi}(\mathbf{F}, \mathbf{H}, J) : D\mathbf{F}[\delta\boldsymbol{\varphi}] + \partial_{\mathbf{H}} \tilde{\Psi}(\mathbf{F}, \mathbf{H}, J) : D\mathbf{H}[\delta\boldsymbol{\varphi}] \\ &\quad + \partial_J \tilde{\Psi}(\mathbf{F}, \mathbf{H}, J) DJ[\delta\boldsymbol{\varphi}]) dV, \end{aligned} \quad (2.30)$$

where

$$\begin{aligned} D\mathbf{F}[\delta\boldsymbol{\varphi}] &= \left. \frac{d}{d\varepsilon} \right|_{\varepsilon=0} \mathbf{F}_\varepsilon = \partial_{\mathbf{X}} \delta\boldsymbol{\varphi}, \\ D\mathbf{H}[\delta\boldsymbol{\varphi}] &= \left. \frac{d}{d\varepsilon} \right|_{\varepsilon=0} \mathbf{H}_\varepsilon = \mathbf{F} * D\mathbf{F}[\delta\boldsymbol{\varphi}], \\ DJ[\delta\boldsymbol{\varphi}] &= \left. \frac{d}{d\varepsilon} \right|_{\varepsilon=0} J_\varepsilon = \frac{1}{2} (\mathbf{F} * \mathbf{F}) : D\mathbf{F}[\delta\boldsymbol{\varphi}]. \end{aligned} \quad (2.31)$$

Consequently,

$$D\hat{\Pi}^{\text{int}}[\delta\boldsymbol{\varphi}] = \int_{\mathcal{B}_0} D\mathbf{F}[\delta\boldsymbol{\varphi}] : (\partial_{\mathbf{F}} \tilde{\Psi} + \partial_{\mathbf{H}} \tilde{\Psi} * \mathbf{F} + \partial_J \tilde{\Psi} \mathbf{H}) dV, \quad (2.32)$$

and the stationary condition (2.27) yields the variational equation

$$D\hat{\Pi}[\delta\boldsymbol{\varphi}] = \int_{\mathcal{B}_0} D\mathbf{F}[\delta\boldsymbol{\varphi}] : \mathbf{P} dV + D\Pi_m^{\text{ext}}[\delta\boldsymbol{\varphi}] = 0, \quad (2.33)$$

which corresponds to the principle of virtual work for elastostatics. In the last equation

$$\mathbf{P} = \partial_{\mathbf{F}} \tilde{\Psi} + \partial_{\mathbf{H}} \tilde{\Psi} * \mathbf{F} + \partial_J \tilde{\Psi} \mathbf{H}, \quad (2.34)$$

is the first Piola-Kirchhoff stress-tensor.

## 2.2.2 Frame-indifferent material formulation

The axiom of frame-indifference requires that the stored energy function be invariant under superposed rigid motions of the form

$$\boldsymbol{\varphi}^\# = \mathbf{Q}\boldsymbol{\varphi} + \mathbf{c}, \quad (2.35)$$

for arbitrary  $\mathbf{c} \in \mathbb{R}^3$  and  $\mathbf{Q} \in SO(3)$ , the special orthogonal group. The arguments  $\{\mathbf{F}, \mathbf{H}, J\}$  of the stored energy function (2.23) transform under (2.35) as follows:

$$\begin{aligned} \mathbf{F}^\# &= \mathbf{Q}\mathbf{F}, \\ \mathbf{H}^\# &= \frac{1}{2}\mathbf{F}^\# \star \mathbf{F}^\# \\ &= \frac{1}{2}(\mathbf{Q}\mathbf{F}) \star (\mathbf{Q}\mathbf{F}) \\ &= \frac{1}{2}(\mathbf{Q} \star \mathbf{Q}) \frac{1}{2}(\mathbf{F} \star \mathbf{F}). \end{aligned} \quad (2.36)$$

In the last equation use has been made of relation (2.12)<sub>4</sub> (for  $\mathbf{A} = \mathbf{B} = \mathbf{Q}$  and  $\mathbf{C} = \mathbf{D} = \mathbf{F}$ ). Moreover, since  $\det(\mathbf{Q}) = 1$  and  $\mathbf{Q}^\top = \mathbf{Q}^{-1}$  for  $\mathbf{Q} \in SO(3)$ ,

$$\frac{1}{2}\mathbf{Q} \star \mathbf{Q} = \text{cof}(\mathbf{Q}) = \det(\mathbf{Q})\mathbf{Q}^{-\top} = \mathbf{Q}. \quad (2.37)$$

Accordingly, we obtain

$$\mathbf{H}^\# = \mathbf{Q}\mathbf{H}. \quad (2.38)$$

Furthermore,

$$J^\# = \det(\mathbf{F}^\#) = \det(\mathbf{Q}\mathbf{F}) = \det(\mathbf{Q})\det(\mathbf{F}) = \det(\mathbf{F}) = J. \quad (2.39)$$

A frame-indifferent stored energy function needs to satisfy the condition  $\hat{\Psi}(\mathbf{F}^\#) = \hat{\Psi}(\mathbf{F})$ , or

$$\tilde{\Psi}(\mathbf{F}^\#, \mathbf{H}^\#, J^\#) = \tilde{\Psi}(\mathbf{F}, \mathbf{H}, J). \quad (2.40)$$

To fulfill that condition the right Cauchy-Green deformation tensor  $\mathbf{C} : \mathcal{B}_0 \rightarrow \mathbb{R}^{3 \times 3}$  is introduced as

$$\mathbf{C} = \mathbf{F}^\top \mathbf{F}. \quad (2.41)$$

Additionally, we introduce

$$\mathbf{G} = \text{cof}(\mathbf{C}) = \mathbf{H}^\top \mathbf{H} = \frac{1}{2}\mathbf{C} \star \mathbf{C}, \quad (2.42)$$

where  $\mathbf{G} : \mathcal{B}_0 \rightarrow \mathbb{R}^{3 \times 3}$  is the co-factor of  $\mathbf{C}$ . Furthermore, the determinant of  $\mathbf{C}$  is introduced as

$$\mathbf{C} = \det(\mathbf{C}) = J^2 = \frac{1}{6} (\mathbf{C} \star \mathbf{C}) : \mathbf{C}, \quad (2.43)$$

where  $\mathbf{C} : \mathcal{B}_0 \rightarrow \mathbb{R}^+$ . Both  $\mathbf{C}$  and  $\mathbf{G}$  are symmetric second-order tensors. It can be easily seen that

$$\begin{aligned} \mathbf{C}^\# &= (\mathbf{F}^\#)^\top \mathbf{F}^\# = (\mathbf{Q}\mathbf{F})^\top \mathbf{Q}\mathbf{F} \\ &= \mathbf{F}^\top \mathbf{Q}^\top \mathbf{Q}\mathbf{F} = \mathbf{F}^\top \mathbf{F} \\ &= \mathbf{C}, \end{aligned} \quad (2.44)$$

and

$$\begin{aligned} \mathbf{G}^\# &= \frac{1}{2} (\mathbf{F}^\#)^\top \mathbf{F}^\# \star (\mathbf{F}^\#)^\top \mathbf{F}^\# \\ &= \frac{1}{2} (\mathbf{Q}\mathbf{F})^\top \mathbf{Q}\mathbf{F} \star (\mathbf{Q}\mathbf{F})^\top \mathbf{Q}\mathbf{F} \\ &= \frac{1}{2} \mathbf{F}^\top \mathbf{Q}^\top \mathbf{Q}\mathbf{F} \star \mathbf{F}^\top \mathbf{Q}^\top \mathbf{Q}\mathbf{F} \\ &= \mathbf{G}. \end{aligned} \quad (2.45)$$

Moreover, for  $\mathbf{C}$  we obtain

$$\begin{aligned} \mathbf{C}^\# &= \det((\mathbf{F}^\#)^\top \mathbf{F}^\#) = \det((\mathbf{Q}\mathbf{F})^\top \mathbf{Q}\mathbf{F}) \\ &= \det(\mathbf{F}^\top \mathbf{Q}^\top \mathbf{Q}\mathbf{F}) = \mathbf{C}. \end{aligned} \quad (2.46)$$

Consequently, a frame-indifferent stored energy function resulting from the function  $\hat{\Psi}(\mathbf{F}, \mathbf{H}, J)$  is given by

$$\hat{\Psi}(\mathbf{F}) = \hat{\Psi}(\mathbf{C}) = \Psi(\mathbf{C}, \mathbf{G}, C). \quad (2.47)$$

**Example (Mooney-Rivlin material):** The compressible Mooney-Rivlin material is based on a polyconvex stored energy function with

$$\hat{\Psi}(\mathbf{F}, \mathbf{H}, J) = \tilde{\Psi}^{\text{mech},1}(\mathbf{F}, \mathbf{H}) + \tilde{\Psi}^{\text{mech},2}(J), \quad (2.48)$$

where

$$\tilde{\Psi}^{\text{mech},1}(\mathbf{F}, \mathbf{H}) = a(\mathbf{F} : \mathbf{F} - 3) + b(\mathbf{H} : \mathbf{H} - 3), \quad (2.49)$$

and

$$\tilde{\Psi}^{\text{mech},2}(J) = \Gamma^1(J). \quad (2.50)$$

Here  $a > 0$ ,  $b > 0$  and  $\Gamma^1 : ]0, +\infty[ \rightarrow \mathbb{R}$  is a suitable convex function. For example,  $\Gamma^1(\delta) = c\delta^2 - d \log \delta$ ,  $c > 0, d > 0$ . The stored energy function (2.48) can be recast in the form

$$\Psi(\mathbf{C}, \mathbf{G}, C) = \Psi^{\text{mech},1}(\mathbf{C}, \mathbf{G}) + \Psi^{\text{mech},2}(C), \quad (2.51)$$

where

$$\Psi^{\text{mech},1}(\mathbf{C}, \mathbf{G}) = a(\text{tr } \mathbf{C} - 3) + b(\text{tr } \mathbf{G} - 3), \quad (2.52)$$

and

$$\Psi^{\text{mech},2}(\mathbf{C}) = \Gamma^1(\mathbf{C}^{1/2}). \quad (2.53)$$

We may now rewrite the internal energy functional (2.24) by using the stored energy function  $\Psi$  leading to

$$\hat{\Pi}^{\text{int}}(\boldsymbol{\varphi}) = \int_{\hat{\mathcal{B}}_0} \Psi(\mathbf{C}, \mathbf{G}, \mathbf{C}) \, dV. \quad (2.54)$$

Repeating the calculation of the stationary condition within the framework of the principle of stationary potential energy, we obtain

$$\begin{aligned} D\hat{\Pi}^{\text{int}}[\delta\boldsymbol{\varphi}] &= \left. \frac{d}{d\varepsilon} \right|_{\varepsilon=0} \hat{\Pi}^{\text{int}}(\boldsymbol{\varphi}_\varepsilon) \\ &= \int_{\hat{\mathcal{B}}_0} \left. \frac{d}{d\varepsilon} \right|_{\varepsilon=0} \Psi(\mathbf{C}_\varepsilon, \mathbf{G}_\varepsilon, \mathbf{C}_\varepsilon) \, dV \\ &= \int_{\hat{\mathcal{B}}_0} (\partial_{\mathbf{C}}\Psi : D\mathbf{C}[\delta\boldsymbol{\varphi}] + \partial_{\mathbf{G}}\Psi : D\mathbf{G}[\delta\boldsymbol{\varphi}] + \partial_{\mathbf{C}}\Psi D_{\mathbf{C}}[\delta\boldsymbol{\varphi}]) \, dV, \end{aligned} \quad (2.55)$$

where

$$\begin{aligned} D\mathbf{C}[\delta\boldsymbol{\varphi}] &= \left. \frac{d}{d\varepsilon} \right|_{\varepsilon=0} \mathbf{C}_\varepsilon = \left. \frac{d}{d\varepsilon} \right|_{\varepsilon=0} (\mathbf{F}_\varepsilon)^T \mathbf{F}_\varepsilon \\ &= (D\mathbf{F}[\delta\boldsymbol{\varphi}])^T \mathbf{F} + \mathbf{F}^T D\mathbf{F}[\delta\boldsymbol{\varphi}]. \end{aligned} \quad (2.56)$$

Moreover,

$$\begin{aligned} D\mathbf{G}[\delta\boldsymbol{\varphi}] &= \left. \frac{d}{d\varepsilon} \right|_{\varepsilon=0} \mathbf{G}_\varepsilon = \left. \frac{d}{d\varepsilon} \right|_{\varepsilon=0} \frac{1}{2} \mathbf{C}_\varepsilon * \mathbf{C}_\varepsilon \\ &= \frac{1}{2} (D\mathbf{C}[\delta\boldsymbol{\varphi}] * \mathbf{C} + \mathbf{C} * D\mathbf{C}[\delta\boldsymbol{\varphi}]) \\ &= \mathbf{C} * D\mathbf{C}[\delta\boldsymbol{\varphi}]. \end{aligned} \quad (2.57)$$

Note that in the last equation use has been made of relation (2.12)<sub>1</sub>. We further get

$$\begin{aligned} D\mathbf{C}[\delta\boldsymbol{\varphi}] &= \left. \frac{d}{d\varepsilon} \right|_{\varepsilon=0} \mathbf{C}_\varepsilon = \left. \frac{d}{d\varepsilon} \right|_{\varepsilon=0} \det(\mathbf{C}_\varepsilon) \\ &= \text{cof}(\mathbf{C}) : \left. \frac{d}{d\varepsilon} \right|_{\varepsilon=0} \mathbf{C}_\varepsilon \\ &= \mathbf{G} : D\mathbf{C}[\delta\boldsymbol{\varphi}]. \end{aligned} \quad (2.58)$$

Consequently, we obtain

$$\begin{aligned} \text{D}\hat{\Pi}^{\text{int}}[\delta\boldsymbol{\varphi}] &= \int_{\mathcal{B}_0} (\partial_{\mathbf{C}}\Psi : \text{DC}[\delta\boldsymbol{\varphi}] + \partial_{\mathbf{G}}\Psi : (\mathbf{C} \star \text{DC}[\delta\boldsymbol{\varphi}]) + \partial_{\mathbf{C}}\Psi \mathbf{G} : \text{DC}[\delta\boldsymbol{\varphi}]) \, dV \\ &= \int_{\mathcal{B}_0} \frac{1}{2} \mathbf{S} : \text{DC}[\delta\boldsymbol{\varphi}] \, dV. \end{aligned} \quad (2.59)$$

In the last equation the second Piola-Kirchhoff stress tensor

$$\mathbf{S} = 2 (\partial_{\mathbf{C}}\Psi + \partial_{\mathbf{G}}\Psi \star \mathbf{C} + \partial_{\mathbf{C}}\Psi \mathbf{G}), \quad (2.60)$$

has been introduced. In this connection, relation (2.12)<sub>3</sub> has been used. Note that expression (2.60) yields a symmetric tensor. In particular, the symmetry of (2.60) follows from the symmetry of  $\mathbf{C}$  and  $\mathbf{G}$  along with property (2.12)<sub>2</sub>. Eventually, the principle of stationary potential energy yields

$$\text{D}\hat{\Pi}[\delta\boldsymbol{\varphi}] = \int_{\mathcal{B}_0} \text{DF}[\delta\boldsymbol{\varphi}] : (\mathbf{F} \mathbf{S}) \, dV + \text{D}\Pi_m^{\text{ext}}[\delta\boldsymbol{\varphi}] = 0. \quad (2.61)$$

Note that in the last equation the symmetry of the second Piola-Kirchhoff stress tensor has been taken into account.

# 3 A mixed variational framework for the design of EM schemes<sup>1</sup>

In this chapter, a new approach to the design of EM consistent algorithms for non-linear elastodynamics is proposed. The method is inspired by the structure of polyconvex energy density functions and benefits from a tensor cross product for second-order tensors as introduced in Sec. 2.1. The structure-preserving discretization in time of the mixed variational formulation yields an EM consistent semi-discrete formulation. In addition, we introduce a new form of the algorithmic stress formula in the special case of a purely displacement-based formulation. Finally, several numerical examples are presented to evaluate the performance of the newly developed schemes.

## 3.1 Variational formulation

In this section we present a new mixed variational formulation that lays the foundation for the energy-momentum consistent discretization approach developed in the sequel. In our approach we introduce the fields  $\mathcal{C}(X)$ ,  $\mathcal{G}(X)$  and  $\mathcal{C}(X)$  as independent quantities. See (2.41), (2.42) and (2.43) for their deformation depending counterparts.

---

<sup>1</sup> This chapter is based on [23].

In particular, consider the cascade of kinematic relationships

$$\begin{aligned}
 \mathbf{C} &= \mathbf{C}, \\
 \mathbf{G} &= \frac{1}{2} \mathbf{C} * \mathbf{C}, \\
 \mathcal{C} &= \frac{1}{3} \mathbf{C} : \mathbf{G}.
 \end{aligned} \tag{3.1}$$

The above relations can be viewed as kinematic constraints that link the strain-type quantities  $\mathbf{C} \in \mathbb{V}_{\mathbf{C}}$ ,  $\mathbf{G} \in \mathbb{V}_{\mathbf{G}}$  and  $\mathcal{C} \in \mathbb{V}_{\mathcal{C}}$  to the deformation  $\boldsymbol{\varphi} \in \mathcal{Q}$ . In this connection,

$$\begin{aligned}
 \mathbb{V}_{\mathbf{C}} &= \{ \mathbf{C} : \mathcal{B}_0 \rightarrow \mathbb{S} \mid \text{for } C_{ij} \in \mathbb{L}_2(\mathcal{B}_0) \}, \\
 \mathbb{V}_{\mathbf{G}} &= \{ \mathbf{G} : \mathcal{B}_0 \rightarrow \mathbb{S} \mid \text{for } G_{ij} \in \mathbb{L}_2(\mathcal{B}_0) \}, \\
 \mathbb{V}_{\mathcal{C}} &= \{ \mathcal{C} : \mathcal{B}_0 \rightarrow \mathbb{R} \mid \text{for } \mathcal{C} \in \mathbb{L}_2(\mathcal{B}_0) \}.
 \end{aligned} \tag{3.2}$$

Here,  $\mathbb{L}_2$  denotes the space of square integrable functions and  $\mathbb{S}$  is the vector space of symmetric second-order tensors. Note that the symmetry condition implies that  $\dim(\mathbb{S}) = 6$ . Correspondingly, the constraints (3.1) comprise 13 independent algebraic equations. The newly proposed variational formulation relies on the following 7-field functional of the Hu-Washizu type:

$$\begin{aligned}
 \Pi(\boldsymbol{\varphi}, \boldsymbol{\Xi}, \boldsymbol{\Lambda}) &= \int_{\mathcal{B}_0} \left( \Psi(\mathbf{C}, \mathbf{G}, \mathcal{C}) + \boldsymbol{\Lambda}^{\mathbf{C}} : (\mathbf{C} - \mathbf{C}) \right. \\
 &\quad \left. + \boldsymbol{\Lambda}^{\mathbf{G}} : \left( \frac{1}{2} \mathbf{C} * \mathbf{C} - \mathbf{G} \right) \right. \\
 &\quad \left. + \boldsymbol{\Lambda}^{\mathcal{C}} \left( \frac{1}{3} \mathbf{C} : \mathbf{G} - \mathcal{C} \right) \right) dV + \Pi_m^{\text{ext}}(\boldsymbol{\varphi}).
 \end{aligned} \tag{3.3}$$

For convenience of notation the following abbreviations have been used on the left-hand side of the last equation:

$$\begin{aligned}
 \boldsymbol{\Xi} &= \{ \mathbf{C}, \mathbf{G}, \mathcal{C} \}, \\
 \boldsymbol{\Lambda} &= \{ \boldsymbol{\Lambda}^{\mathbf{C}}, \boldsymbol{\Lambda}^{\mathbf{G}}, \boldsymbol{\Lambda}^{\mathcal{C}} \}.
 \end{aligned} \tag{3.4}$$

As can be observed from the variational functional (3.3), the three kinematic constraints (3.1) are enforced by means of Lagrange multipliers  $\boldsymbol{\Lambda}^{\mathbf{C}} \in \mathbb{V}_{\mathbf{C}}$ ,  $\boldsymbol{\Lambda}^{\mathbf{G}} \in \mathbb{V}_{\mathbf{G}}$ , and  $\boldsymbol{\Lambda}^{\mathcal{C}} \in \mathbb{V}_{\mathcal{C}}$ . Imposing the stationary conditions on the functional (3.3) we obtain the

Euler-Lagrange equations

$$\begin{aligned}
 D_{\boldsymbol{\varphi}}\Pi(\boldsymbol{\varphi}, \boldsymbol{\Xi}, \boldsymbol{\Lambda})[\delta\boldsymbol{\varphi}] &= \int_{B_0} \boldsymbol{\Lambda}^c : \text{DC}[\delta\boldsymbol{\varphi}] \, dV + \text{D}\Pi_m^{\text{ext}}[\delta\boldsymbol{\varphi}] = 0, \\
 D_{\boldsymbol{C}}\Pi(\boldsymbol{\varphi}, \boldsymbol{\Xi}, \boldsymbol{\Lambda})[\delta\boldsymbol{C}] &= \int_{B_0} \delta\boldsymbol{C} : \left( \partial_{\boldsymbol{C}}\Psi - \boldsymbol{\Lambda}^c + \boldsymbol{\Lambda}^g \ast \boldsymbol{C} + \frac{1}{3} \boldsymbol{\Lambda}^c \boldsymbol{G} \right) \, dV = 0, \\
 D_{\boldsymbol{G}}\Pi(\boldsymbol{\varphi}, \boldsymbol{\Xi}, \boldsymbol{\Lambda})[\delta\boldsymbol{G}] &= \int_{B_0} \delta\boldsymbol{G} : \left( \partial_{\boldsymbol{G}}\Psi - \boldsymbol{\Lambda}^g + \frac{1}{3} \boldsymbol{\Lambda}^c \boldsymbol{C} \right) \, dV = 0, \\
 D_{\boldsymbol{C}}\Pi(\boldsymbol{\varphi}, \boldsymbol{\Xi}, \boldsymbol{\Lambda})[\delta\boldsymbol{C}] &= \int_{B_0} \delta\boldsymbol{C} (\partial_{\boldsymbol{C}}\Psi - \boldsymbol{\Lambda}^c) \, dV = 0, \\
 D_{\boldsymbol{\Lambda}^c}\Pi(\boldsymbol{\varphi}, \boldsymbol{\Xi}, \boldsymbol{\Lambda})[\delta\boldsymbol{\Lambda}^c] &= \int_{B_0} \delta\boldsymbol{\Lambda}^c : (\boldsymbol{C} - \boldsymbol{C}) \, dV = 0, \\
 D_{\boldsymbol{\Lambda}^g}\Pi(\boldsymbol{\varphi}, \boldsymbol{\Xi}, \boldsymbol{\Lambda})[\delta\boldsymbol{\Lambda}^g] &= \int_{B_0} \delta\boldsymbol{\Lambda}^g : \left( \frac{1}{2} \boldsymbol{C} \ast \boldsymbol{C} - \boldsymbol{G} \right) \, dV = 0, \\
 D_{\boldsymbol{\Lambda}^c}\Pi(\boldsymbol{\varphi}, \boldsymbol{\Xi}, \boldsymbol{\Lambda})[\delta\boldsymbol{\Lambda}^c] &= \int_{B_0} \delta\boldsymbol{\Lambda}^c \left( \frac{1}{3} \boldsymbol{G} : \boldsymbol{C} - \boldsymbol{C} \right) \, dV = 0.
 \end{aligned} \tag{3.5}$$

The above equations have to hold for any  $\delta\boldsymbol{\varphi} \in \mathcal{V}$  and arbitrary  $\delta\boldsymbol{C} \in \mathbb{V}_{\boldsymbol{C}}$ ,  $\delta\boldsymbol{G} \in \mathbb{V}_{\boldsymbol{G}}$ ,  $\delta\boldsymbol{C} \in \mathbb{V}_{\boldsymbol{C}}$  and  $\delta\boldsymbol{\Lambda}^c \in \mathbb{V}_{\boldsymbol{C}}$ ,  $\delta\boldsymbol{\Lambda}^g \in \mathbb{V}_{\boldsymbol{G}}$ ,  $\delta\boldsymbol{\Lambda}^c \in \mathbb{V}_{\boldsymbol{C}}$ . Note that (3.5)<sub>5–7</sub> recover the kinematic constraints (3.1) while (3.5)<sub>2–4</sub> yield the Lagrange multipliers

$$\begin{aligned}
 \boldsymbol{\Lambda}^c &= \partial_{\boldsymbol{C}}\Psi, \\
 \boldsymbol{\Lambda}^g &= \partial_{\boldsymbol{G}}\Psi + \frac{1}{3} \boldsymbol{\Lambda}^c \boldsymbol{C}, \\
 \boldsymbol{\Lambda}^c &= \partial_{\boldsymbol{C}}\Psi + \boldsymbol{\Lambda}^g \ast \boldsymbol{C} + \frac{1}{3} \boldsymbol{\Lambda}^c \boldsymbol{G}.
 \end{aligned} \tag{3.6}$$

Inserting these relations into (3.5)<sub>1</sub>, we recover the principle of virtual work in the form (2.61).

**Remark 3.1.** *The reduction of the mixed formulation (3.5) to the original ('displacement-based') form (2.61) can also be achieved by eliminating the Lagrange multipliers via the following consistency conditions emanating from the constraints (3.1):*

$$\begin{aligned}
 \delta\boldsymbol{C} &= \text{DC}[\delta\boldsymbol{\varphi}], \\
 \delta\boldsymbol{G} &= \boldsymbol{C} \ast \delta\boldsymbol{C}, \\
 \delta\boldsymbol{C} &= \frac{1}{3} (\boldsymbol{C} : \delta\boldsymbol{G} + \boldsymbol{G} : \delta\boldsymbol{C}).
 \end{aligned} \tag{3.7}$$

**Remark 3.2.** *The alternative mixed 7-field variational formulation in [26, Sec. 4.2] is based on the kinematic constraints*

$$\begin{aligned}\mathcal{F} &= \mathbf{F}, \\ \mathcal{H} &= \frac{1}{2} \mathbf{F} \star \mathbf{F}, \\ \mathcal{J} &= \det(\mathbf{F}),\end{aligned}\tag{3.8}$$

along with the stored energy in the form  $\hat{\Psi}(\mathcal{F}, \mathcal{H}, \mathcal{J})$ . Yet another mixed 5-field formulation has been proposed in [149] based on the kinematic constraints

$$\begin{aligned}\mathcal{G} &= \text{cof}(\mathbf{F}^T \mathbf{F}), \\ \mathcal{J} &= \det(\mathbf{F}),\end{aligned}\tag{3.9}$$

and the stored energy in the form  $\Psi(\mathbf{C}, \mathcal{G}, \mathcal{J}^2)$ . It can be observed from (3.8) as well as (3.9) that the new strain-type variables are directly linked to the deformation  $\boldsymbol{\varphi} \in \mathcal{Q}$ . This is in sharp contrast to the cascade form of the constraints (3.1) used in the present work.

### 3.1.1 Extension to elastodynamics

Next, we deal with the extension of the mixed formulation introduced above to the dynamic regime. Let  $\mathcal{I} = [0, T]$  where  $\mathcal{I} \subset \mathbb{R}_+$  is the time interval of interest. The motion of the continuum body is described by  $\boldsymbol{\varphi} : \mathcal{B}_0 \times \mathcal{I} \rightarrow \mathbb{R}^3$ , where  $\mathbf{x} = \boldsymbol{\varphi} := \boldsymbol{\varphi}(\mathbf{X}, t)$  characterizes the position of the material point  $\mathbf{X} \in \mathcal{B}_0$  at time  $t \in [0, T]$ . The material velocity field at time  $t$  is denoted by  $\mathbf{V} : \mathcal{B}_0 \times \mathcal{I} \rightarrow \mathbb{R}^3$  and defined by

$$\mathbf{V} = \dot{\boldsymbol{\varphi}},\tag{3.10}$$

where the superposed dot denotes time differentiation. Upon introduction of the reference mass density field  $\rho_0 : \mathcal{B}_0 \rightarrow \mathbb{R}^+$ , the mixed formulation governing the motion of the continuum body is given by

$$\begin{aligned}\int_{\mathcal{B}_0} \delta \mathbf{V} \cdot (\dot{\boldsymbol{\varphi}} - \mathbf{V}) \rho_0 \, dV &= 0, \\ \int_{\mathcal{B}_0} (\delta \boldsymbol{\varphi} \cdot \rho_0 \dot{\mathbf{V}} + \boldsymbol{\Lambda}^c : \text{DC}[\delta \boldsymbol{\varphi}]) \, dV + \text{DII}_m^{\text{ext}}[\delta \boldsymbol{\varphi}] &= 0,\end{aligned}\tag{3.11}$$

which has to be satisfied for arbitrary  $\delta\boldsymbol{\varphi}, \delta\mathbf{V} \in \mathcal{V}$ , together with

$$\begin{aligned} \int_{\tilde{\mathcal{B}}_0} \delta\boldsymbol{\mathcal{C}} : \left( \partial_{\boldsymbol{\mathcal{C}}} \Psi - \boldsymbol{\Lambda}^{\boldsymbol{\mathcal{C}}} + \boldsymbol{\Lambda}^{\boldsymbol{\mathcal{G}}} * \boldsymbol{\mathcal{C}} + \frac{1}{3} \boldsymbol{\Lambda}^{\boldsymbol{\mathcal{C}}} \boldsymbol{\mathcal{G}} \right) dV &= 0, \\ \int_{\tilde{\mathcal{B}}_0} \delta\boldsymbol{\mathcal{G}} : \left( \partial_{\boldsymbol{\mathcal{G}}} \Psi - \boldsymbol{\Lambda}^{\boldsymbol{\mathcal{G}}} + \frac{1}{3} \boldsymbol{\Lambda}^{\boldsymbol{\mathcal{C}}} \boldsymbol{\mathcal{C}} \right) dV &= 0, \\ \int_{\tilde{\mathcal{B}}_0} \delta\boldsymbol{\mathcal{C}} (\partial_{\boldsymbol{\mathcal{C}}} \Psi - \boldsymbol{\Lambda}^{\boldsymbol{\mathcal{C}}}) dV &= 0, \end{aligned} \quad (3.12)$$

for arbitrary  $\delta\boldsymbol{\mathcal{C}} \in \mathbb{V}_{\boldsymbol{\mathcal{C}}}$ ,  $\delta\boldsymbol{\mathcal{G}} \in \mathbb{V}_{\boldsymbol{\mathcal{G}}}$ ,  $\delta\boldsymbol{\mathcal{C}} \in \mathbb{V}_{\boldsymbol{\mathcal{C}}}$ , and

$$\begin{aligned} \int_{\tilde{\mathcal{B}}_0} \delta\boldsymbol{\Lambda}^{\boldsymbol{\mathcal{C}}} : (\boldsymbol{\mathcal{C}} - \boldsymbol{\mathcal{C}}) dV &= 0, \\ \int_{\tilde{\mathcal{B}}_0} \delta\boldsymbol{\Lambda}^{\boldsymbol{\mathcal{G}}} : \left( \frac{1}{2} \boldsymbol{\mathcal{C}} * \boldsymbol{\mathcal{C}} - \boldsymbol{\mathcal{G}} \right) dV &= 0, \\ \int_{\tilde{\mathcal{B}}_0} \delta\boldsymbol{\Lambda}^{\boldsymbol{\mathcal{C}}} \left( \frac{1}{3} \boldsymbol{\mathcal{G}} : \boldsymbol{\mathcal{C}} - \boldsymbol{\mathcal{C}} \right) dV &= 0, \end{aligned} \quad (3.13)$$

for arbitrary  $\delta\boldsymbol{\Lambda}^{\boldsymbol{\mathcal{C}}} \in \mathbb{V}_{\boldsymbol{\mathcal{C}}}$ ,  $\delta\boldsymbol{\Lambda}^{\boldsymbol{\mathcal{G}}} \in \mathbb{V}_{\boldsymbol{\mathcal{G}}}$ , and  $\delta\boldsymbol{\Lambda}^{\boldsymbol{\mathcal{C}}} \in \mathbb{V}_{\boldsymbol{\mathcal{C}}}$ . The above variational equations have to be supplemented by prescribed initial values  $\boldsymbol{\varphi}_0 \in \mathcal{Q}$  and  $\mathbf{V}_0 \in \mathcal{V}$  at time  $t = 0$ . Consistent initial values for the mixed strain fields,  $\{\boldsymbol{\mathcal{C}}_0, \boldsymbol{\mathcal{G}}_0, \boldsymbol{\mathcal{C}}_0\}$ , can be calculated by employing the kinematic constraints (3.1).

**Remark 3.3.** *The kinematic constraints (3.1) are enforced by the variational equations (3.13). Differentiation of (3.13) with respect to time yields the consistency conditions*

$$\begin{aligned} \int_{\tilde{\mathcal{B}}_0} \delta\boldsymbol{\Lambda}^{\boldsymbol{\mathcal{C}}} : (\dot{\boldsymbol{\mathcal{C}}} - \dot{\boldsymbol{\mathcal{C}}}) dV &= 0, \\ \int_{\tilde{\mathcal{B}}_0} \delta\boldsymbol{\Lambda}^{\boldsymbol{\mathcal{G}}} : (\boldsymbol{\mathcal{C}} * \dot{\boldsymbol{\mathcal{C}}} - \dot{\boldsymbol{\mathcal{G}}}) dV &= 0, \\ \int_{\tilde{\mathcal{B}}_0} \delta\boldsymbol{\Lambda}^{\boldsymbol{\mathcal{C}}} \left( \frac{1}{3} \boldsymbol{\mathcal{C}} : \dot{\boldsymbol{\mathcal{G}}} + \frac{1}{3} \boldsymbol{\mathcal{G}} : \dot{\boldsymbol{\mathcal{C}}} - \dot{\boldsymbol{\mathcal{C}}} \right) dV &= 0. \end{aligned} \quad (3.14)$$

*The above equations have to hold for arbitrary  $\delta\boldsymbol{\Lambda}^{\boldsymbol{\mathcal{C}}} \in \mathbb{V}_{\boldsymbol{\mathcal{C}}}$ ,  $\delta\boldsymbol{\Lambda}^{\boldsymbol{\mathcal{G}}} \in \mathbb{V}_{\boldsymbol{\mathcal{G}}}$ ,  $\delta\boldsymbol{\Lambda}^{\boldsymbol{\mathcal{C}}} \in \mathbb{V}_{\boldsymbol{\mathcal{C}}}$ , and can be viewed as constraints on the velocity level corresponding to the original constraints (3.13) on the position level.*

**Remark 3.4.** *In the continuous setting the variational equation (3.11)<sub>1</sub> implies  $\dot{\boldsymbol{\varphi}} = \mathbf{V}$  while the consistency conditions in (3.14) imply*

$$\begin{aligned}\dot{\mathbf{C}} &= \mathbf{D}\mathbf{V}^T \mathbf{F} + \mathbf{F}^T \mathbf{D}\mathbf{V}, \\ \dot{\mathbf{G}} &= \mathbf{C} \ast \dot{\mathbf{C}}, \\ \dot{\mathbf{C}} &= \frac{1}{3} (\mathbf{C} : \dot{\mathbf{G}} + \mathbf{G} : \dot{\mathbf{C}}).\end{aligned}\tag{3.15}$$

*As mentioned in Remark 3.2, an alternative mixed formulation relies on the introduction of the variables  $\{\mathbf{F}, \mathbf{H}, \mathbf{J}\}$  through the kinematic constraints (3.8). Differentiating (3.8) with respect to time yields the associated consistency conditions (or constraints on the velocity level)*

$$\begin{aligned}\dot{\mathbf{F}} &= \mathbf{D}\mathbf{V}, \\ \dot{\mathbf{H}} &= \mathbf{F} \ast \mathbf{D}\mathbf{V}, \\ \dot{\mathbf{J}} &= \frac{1}{2} (\mathbf{F} \ast \dot{\mathbf{F}}) : \mathbf{D}\mathbf{V}.\end{aligned}\tag{3.16}$$

*These equations can be recast in the so-called conservation form, see [40] and [26] for more details.*

**Remark 3.5.** *The mixed variational formulation developed above can be linked to an extended version of Hamilton's principle. In particular, consider the extended 8-field action functional given by*

$$S(\boldsymbol{\varphi}, \mathbf{V}, \boldsymbol{\Xi}, \boldsymbol{\Lambda}) = \int_0^T \left( \int_{\mathcal{B}_0} \left( \dot{\boldsymbol{\varphi}} - \frac{1}{2} \mathbf{V} \right) \cdot \mathbf{V} \rho_0 \, dV - \Pi(\boldsymbol{\varphi}, \boldsymbol{\Xi}, \boldsymbol{\Lambda}) \, dV \right) dt.\tag{3.17}$$

*The condition for stationarity of the above functional yields Euler-Lagrange equations that correspond to the variational equations (3.11)–(3.13) (see also [15] for similar considerations in the framework of a standard Hu-Washizu type functional).*

### 3.1.2 Balance laws

The dynamics of the hyperelastic body under consideration falls into the class of Hamiltonian systems with symmetry (see, for example, [108]). In the present work we focus on the corresponding balance laws for linear momentum, angular momentum and energy.

### 3.1.2.1 Balance of linear momentum

For verification of the balance of total linear momentum we assume that  $\delta\boldsymbol{\varphi} = \boldsymbol{\zeta}$  and  $\delta\mathbf{V} = \mathbf{0}$  are admissible variations, where  $\boldsymbol{\zeta} \in \mathbb{R}^3$  is arbitrary but constant. From (3.11) we get

$$\boldsymbol{\zeta} \cdot \left( \frac{d}{dt} \mathbf{L} - \mathbf{F}^{\text{ext}} \right) = 0, \quad (3.18)$$

where the total linear momentum is defined by

$$\mathbf{L} = \int_{\mathcal{B}_0} \rho_0 \mathbf{V} dV, \quad (3.19)$$

and the total external mechanical load is given by

$$\mathbf{F}^{\text{ext}} = \int_{\mathcal{B}_0} \bar{\mathbf{B}} dV + \int_{\partial\mathcal{B}_0^p} \bar{\mathbf{T}} dA, \quad (3.20)$$

containing bulk and boundary contributions. Therefore, for vanishing external mechanical loads the total linear momentum is a constant of motion of the continuous system.

### 3.1.2.2 Balance of angular momentum

To verify the balance law for angular momentum we assume that  $\delta\boldsymbol{\varphi} = \boldsymbol{\zeta} \times \boldsymbol{\varphi}$  and  $\delta\mathbf{V} = \boldsymbol{\zeta} \times \dot{\boldsymbol{\varphi}}$  are admissible variations, where  $\boldsymbol{\zeta} \in \mathbb{R}^3$  is constant. The specific choice of  $\delta\boldsymbol{\varphi}$  leads to the relationship  $D\mathbf{F}[\boldsymbol{\zeta} \times \boldsymbol{\varphi}] = \hat{\boldsymbol{\zeta}} \mathbf{F}$ , where  $\hat{\boldsymbol{\zeta}}$  is a skew-symmetric tensor such that  $\hat{\boldsymbol{\zeta}} \mathbf{a} = \boldsymbol{\zeta} \times \mathbf{a}$  for any  $\mathbf{a} \in \mathbb{R}^3$ . From (3.11) we get

$$\begin{aligned} \int_{\mathcal{B}_0} (\boldsymbol{\zeta} \times \dot{\boldsymbol{\varphi}}) \cdot \mathbf{V} \rho_0 dV &= 0, \\ \int_{\mathcal{B}_0} (\boldsymbol{\zeta} \times \boldsymbol{\varphi} \cdot \rho_0 \dot{\mathbf{V}} + \boldsymbol{\Lambda}^c : DC[\boldsymbol{\zeta} \times \boldsymbol{\varphi}]) dV + D\Pi^{\text{ext}}[\boldsymbol{\zeta} \times \boldsymbol{\varphi}] &= 0, \end{aligned} \quad (3.21)$$

where  $\hat{\boldsymbol{\zeta}} \boldsymbol{\varphi} \cdot \boldsymbol{\varphi} \rho_0 = 0$  has been taken into account. In addition, the admissible choice of the variation in conjunction with (2.56) leads to

$$DC[\boldsymbol{\zeta} \times \boldsymbol{\varphi}] = \frac{1}{2} (\text{sym}(\mathbf{F}^T \hat{\boldsymbol{\zeta}}^T \mathbf{F}) + \text{skw}(\mathbf{F}^T \hat{\boldsymbol{\zeta}}^T \mathbf{F})), \quad (3.22)$$

where

$$\begin{aligned} \text{sym}(\mathbf{F}^T \hat{\boldsymbol{\zeta}}^T \mathbf{F}) &= \frac{1}{2} (\mathbf{F}^T (\hat{\boldsymbol{\zeta}}^T + \hat{\boldsymbol{\zeta}}) \mathbf{F}) = \mathbf{0}, \\ \text{skw}(\mathbf{F}^T \hat{\boldsymbol{\zeta}}^T \mathbf{F}) &= \frac{1}{2} (\mathbf{F}^T (\hat{\boldsymbol{\zeta}}^T - \hat{\boldsymbol{\zeta}}) \mathbf{F}). \end{aligned} \quad (3.23)$$

Accordingly, the inner bracket term in (3.21)<sub>2</sub> vanishes due to the symmetry of  $\Lambda^{\mathcal{C}}$  and the double contraction with the skew symmetric tensor. Next we introduce the total angular momentum with respect to the origin of the inertial frame

$$\mathbf{J} = \int_{\mathcal{B}_0} \boldsymbol{\varphi} \times \mathbf{V} \rho_0 \, dV, \quad (3.24)$$

and the total torque about a corresponding axis  $\boldsymbol{\zeta} \cdot \mathbf{M}^{\text{ext}} = -\text{D}\Pi_m^{\text{ext}}[\boldsymbol{\varphi} \times \boldsymbol{\zeta}]$  exerted by the external (dead) loads on the elastic body, relative to the origin of the inertial frame given as

$$\boldsymbol{\zeta} \cdot \mathbf{M}^{\text{ext}} = \boldsymbol{\zeta} \cdot \left( \int_{\mathcal{B}_0} \boldsymbol{\varphi} \times \bar{\mathbf{B}} \, dV + \int_{\partial \mathcal{B}_0^p} \boldsymbol{\varphi} \times \bar{\mathbf{T}} \, dV \right). \quad (3.25)$$

Eventually, summation of (3.21)<sub>1</sub> and (3.21)<sub>2</sub> leads to the balance of angular momentum as

$$\boldsymbol{\zeta} \cdot \left( \frac{d}{dt} \mathbf{J} - \mathbf{M}^{\text{ext}} \right) = 0. \quad (3.26)$$

Equation (3.26) shows that components of the angular momentum,  $J^{\zeta} = \boldsymbol{\zeta} \cdot \mathbf{J}$  are conserved along solutions of equations of motions when the external torque about the corresponding axes,  $\boldsymbol{\zeta} \cdot \mathbf{M}^{\text{ext}}$  vanishes.

### 3.1.2.3 Balance of energy

We start from the mixed variational equations (3.11)-(3.13) and choose admissible variations of the form  $\delta \boldsymbol{\varphi} = \dot{\boldsymbol{\varphi}} \in \mathcal{V}$ ,  $\delta \mathbf{V} = \dot{\mathbf{V}} \in \mathcal{V}$  along with  $\{\delta \mathcal{C}, \delta \mathcal{G}, \delta \mathcal{C}\} = \{\dot{\mathcal{C}}, \dot{\mathcal{G}}, \dot{\mathcal{C}}\} \in \mathbb{V}_{\mathcal{C}} \times \mathbb{V}_{\mathcal{G}} \times \mathbb{V}_{\mathcal{C}}$  and  $\{\delta \Lambda^{\mathcal{C}}, \delta \Lambda^{\mathcal{G}}, \delta \Lambda^{\mathcal{C}}\} = \{\Lambda^{\mathcal{C}}, \Lambda^{\mathcal{G}}, \Lambda^{\mathcal{C}}\} \in \mathbb{V}_{\mathcal{C}} \times \mathbb{V}_{\mathcal{G}} \times \mathbb{V}_{\mathcal{C}}$ . Accordingly, (3.11)<sub>1</sub> yields

$$\int_{\mathcal{B}_0} \dot{\boldsymbol{\varphi}} \cdot \dot{\mathbf{V}} \rho_0 \, dV = \int_{\mathcal{B}_0} \mathbf{V} \cdot \dot{\mathbf{V}} \rho_0 \, dV = \frac{d}{dt} \left( \frac{1}{2} \int_{\mathcal{B}_0} \mathbf{V} \cdot \mathbf{V} \rho_0 \, dV \right) = \dot{T}, \quad (3.27)$$

where the kinetic energy of the continuum body is defined by

$$T = \frac{1}{2} \int_{\mathcal{B}_0} \mathbf{V} \cdot \mathbf{V} \rho_0 \, dV. \quad (3.28)$$

We further consider the time derivative of the total strain energy (2.24) leading to

$$\begin{aligned}
\frac{d}{dt}\Pi^{\text{int}} &= \frac{d}{dt} \int_{\mathcal{B}_0} \Psi(\mathbf{C}, \mathbf{G}, \mathcal{C}) dV \\
&= \int_{\mathcal{B}_0} (\partial_{\mathcal{C}} \Psi : \dot{\mathcal{C}} + \partial_{\mathbf{G}} \Psi : \dot{\mathbf{G}} + \partial_{\mathbf{C}} \Psi \dot{\mathcal{C}}) dV \\
&= \int_{\mathcal{B}_0} \left( \Lambda^{\mathcal{C}} : \dot{\mathcal{C}} - \Lambda^{\mathbf{G}} : (\mathbf{C} * \dot{\mathcal{C}} - \dot{\mathbf{G}}) - \Lambda^{\mathcal{C}} \left( \frac{1}{3} \mathbf{C} : \dot{\mathbf{G}} + \frac{1}{3} \mathbf{G} : \dot{\mathcal{C}} - \dot{\mathcal{C}} \right) \right) dV \\
&= \int_{\mathcal{B}_0} \Lambda^{\mathcal{C}} : \dot{\mathcal{C}} dV.
\end{aligned} \tag{3.29}$$

Here, use has been made of (3.12) and the consistency conditions (3.14). Substituting (3.27) and (3.29) into (3.11)<sub>2</sub> leads to the balance of energy along solutions of equations of motions in the form

$$\frac{d}{dt}(T + \Pi^{\text{int}}) = P^{\text{ext}}. \tag{3.30}$$

On the right-hand side of the last equation,

$$P^{\text{ext}} = \int_{\mathcal{B}_0} \dot{\boldsymbol{\varphi}} \cdot \bar{\mathbf{B}} dV + \int_{\partial \mathcal{B}_0^f} \dot{\boldsymbol{\varphi}} \cdot \bar{\mathbf{T}} dA = -\Pi_m^{\text{ext}}(\dot{\boldsymbol{\varphi}}), \tag{3.31}$$

corresponds to the power of the external loads. In the case of dead loads the balance law (3.30) corresponds to the conservation of the total energy defined by

$$E = T + \Pi, \tag{3.32}$$

where  $\Pi = \Pi^{\text{int}} + \Pi_m^{\text{ext}}$  is the total potential energy previously defined in (2.26).

## 3.2 Discretization in time

In this section we deal with the structure-preserving discretization in time of the mixed variational formulation presented in the previous section.

We define a partition of the time integration interval  $\mathcal{I}$  by introducing  $n$ -equidistant subintervals of the form  $\mathcal{I}_n = [t_n, t_{n+1}]$  with  $0 = t_0 < t_1 < \dots < t_n = T$  which correspond to a time-step size  $\Delta t = |\mathcal{I}_n|$ . The discrete approximations at times  $t_n$  and  $t_{n+1}$  of the continuous variable  $(\bullet)$  will be denoted by  $(\bullet)_n$  and  $(\bullet)_{n+1}$ , respectively.

### 3.2.1 Structure-preserving integration scheme

Assume that the state variables  $\{\boldsymbol{\varphi}_n, \mathbf{V}_n\} \in \mathcal{Q} \times \mathcal{V}$  along with consistent strain variables  $\{\mathbf{C}_n, \mathbf{G}_n, \mathcal{C}_n\}$  are given. Note that this implies that the strain variables  $\{\mathbf{C}_n, \mathbf{G}_n, \mathcal{C}_n\}$  satisfy the constraints (3.13) at time  $t_n$ . Now the semi-discrete version of the variational equations (3.11), (3.12) and (3.13) is introduced as

$$\begin{aligned} \int_{\mathcal{B}_0} \delta \mathbf{V} \cdot \frac{1}{\Delta t} (\boldsymbol{\varphi}_{n+1} - \boldsymbol{\varphi}_n) \rho_0 \, dV &= \int_{\mathcal{B}_0} \delta \mathbf{V} \cdot \mathbf{V}_{n+\frac{1}{2}} \rho_0 \, dV, \\ \int_{\mathcal{B}_0} \delta \boldsymbol{\varphi} \cdot \frac{1}{\Delta t} \rho_0 (\mathbf{V}_{n+1} - \mathbf{V}_n) \, dV &= - \int_{\mathcal{B}_0} \boldsymbol{\Lambda}_{n+1}^{\mathcal{C}} : \text{DC}[\delta \boldsymbol{\varphi}]|_{n+\frac{1}{2}} \, dV - \text{D}\Pi_m^{\text{ext}}[\delta \boldsymbol{\varphi}]|_{n+\frac{1}{2}}, \end{aligned} \quad (3.33)$$

for arbitrary  $\delta \boldsymbol{\varphi}, \delta \mathbf{V} \in \mathcal{V}$ , together with

$$\begin{aligned} \int_{\mathcal{B}_0} \delta \mathcal{C} : \left( \text{D}_{\mathcal{C}} \Psi - \boldsymbol{\Lambda}_{n+1}^{\mathcal{C}} + \boldsymbol{\Lambda}_{n+1}^{\mathcal{G}} * \mathbf{C}_{n+\frac{1}{2}} + \frac{1}{3} \boldsymbol{\Lambda}_{n+1}^{\mathcal{C}} \mathbf{G}_{n+\frac{1}{2}} \right) \, dV &= 0, \\ \int_{\mathcal{B}_0} \delta \mathbf{G} : \left( \text{D}_{\mathcal{G}} \Psi - \boldsymbol{\Lambda}_{n+1}^{\mathcal{G}} + \frac{1}{3} \boldsymbol{\Lambda}_{n+1}^{\mathcal{C}} \mathbf{C}_{n+\frac{1}{2}} \right) \, dV &= 0, \\ \int_{\mathcal{B}_0} \delta \mathcal{C} (\text{D}_{\mathcal{C}} \Psi - \boldsymbol{\Lambda}_{n+1}^{\mathcal{C}}) \, dV &= 0, \end{aligned} \quad (3.34)$$

for arbitrary  $\delta \mathcal{C} \in \mathbb{V}_{\mathcal{C}}$ ,  $\delta \mathbf{G} \in \mathbb{V}_{\mathcal{G}}$ , and  $\delta \mathcal{C} \in \mathbb{V}_{\mathcal{C}}$ , along with

$$\begin{aligned} \int_{\mathcal{B}_0} \delta \boldsymbol{\Lambda}^{\mathcal{C}} : (\mathbf{C}_{n+1} - \mathbf{C}_{n+1}) \, dV &= 0, \\ \int_{\mathcal{B}_0} \delta \boldsymbol{\Lambda}^{\mathcal{G}} : \left( \frac{1}{2} \mathbf{C}_{n+1} * \mathbf{C}_{n+1} - \mathbf{G}_{n+1} \right) \, dV &= 0, \\ \int_{\mathcal{B}_0} \delta \boldsymbol{\Lambda}^{\mathcal{C}} \left( \frac{1}{3} \mathbf{G}_{n+1} : \mathbf{C}_{n+1} - \mathcal{C}_{n+1} \right) \, dV &= 0, \end{aligned} \quad (3.35)$$

for arbitrary  $\delta \boldsymbol{\Lambda}^{\mathcal{C}} \in \mathbb{V}_{\mathcal{C}}$ ,  $\delta \boldsymbol{\Lambda}^{\mathcal{G}} \in \mathbb{V}_{\mathcal{G}}$ , and  $\delta \boldsymbol{\Lambda}^{\mathcal{C}} \in \mathbb{V}_{\mathcal{C}}$ . In (3.33) and (3.34),

$$(\bullet)_{n+\frac{1}{2}} = \frac{1}{2} ((\bullet)_n + (\bullet)_{n+1}), \quad (3.36)$$

denotes the average value of  $(\bullet)$  in the time interval  $[t_n, t_{n+1}]$ . Moreover, the time-discrete version of (2.56) is given by

$$\text{DC}[\delta \boldsymbol{\varphi}]|_{n+\frac{1}{2}} = (\text{DF}[\delta \boldsymbol{\varphi}])^{\text{T}} \mathbf{F}_{n+\frac{1}{2}} + \mathbf{F}_{n+\frac{1}{2}}^{\text{T}} \text{DF}[\delta \boldsymbol{\varphi}]. \quad (3.37)$$

Furthermore, in (3.34),  $\{D_{\mathcal{C}}\Psi, D_{\mathcal{G}}\Psi, D_{\mathcal{C}}\Psi\}$  denote time-discrete versions of the partial derivatives  $\{\partial_{\mathcal{C}}\Psi, \partial_{\mathcal{G}}\Psi, \partial_{\mathcal{C}}\Psi\}$ . In particular, we assume that  $\{D_{\mathcal{C}}\Psi, D_{\mathcal{G}}\Psi, D_{\mathcal{C}}\Psi\}$  are partitioned discrete derivatives in the sense of [51] for the stored energy function  $\Psi\{\mathcal{C}, \mathcal{G}, \mathcal{C}\}$ . Accordingly, the following relationship is assumed to be satisfied by definition of the discrete derivatives for the stored energy function:

$$\begin{aligned} D_{\mathcal{C}}\Psi : (\mathcal{C}_{n+1} - \mathcal{C}_n) + D_{\mathcal{G}}\Psi : (\mathcal{G}_{n+1} - \mathcal{G}_n) + D_{\mathcal{C}}\Psi (\mathcal{C}_{n+1} - \mathcal{C}_n) \\ = \Psi(\mathcal{C}_{n+1}, \mathcal{G}_{n+1}, \mathcal{C}_{n+1}) - \Psi(\mathcal{C}_n, \mathcal{G}_n, \mathcal{C}_n). \end{aligned} \quad (3.38)$$

Note that the relationship in (3.38) is known as the so-called directionality property which is a sufficient condition for algorithmic energy conservation (see [145]). See the examples below for particular expressions of the discrete derivatives.

**Example (Mooney-Rivlin material cont'd):** To illustrate the calculation of the discrete derivatives  $\{D_{\mathcal{C}}\Psi, D_{\mathcal{G}}\Psi, D_{\mathcal{C}}\Psi\}$  for the stored energy function we again consider the example of the compressible Mooney-Rivlin material (cf. example in Sec. 2.2.2). With regard to (2.51) the stored energy function is given by

$$\Psi(\mathcal{C}, \mathcal{G}, \mathcal{C}) = a(\text{tr}\mathcal{C} - 3) + b(\text{tr}\mathcal{G} - 3) + f(\mathcal{C}), \quad (3.39)$$

where  $f(\mathcal{C}) = \Gamma^1(\mathcal{C}^{1/2})$ . The discrete derivatives assume the simple form

$$\begin{aligned} D_{\mathcal{C}}\Psi &= \partial_{\mathcal{C}}\Psi = a \mathbf{I}, \\ D_{\mathcal{G}}\Psi &= \partial_{\mathcal{G}}\Psi = b \mathbf{I}, \end{aligned} \quad (3.40)$$

along with the Greenspan formula [55]

$$D_{\mathcal{C}}\Psi = \frac{f(\mathcal{C}_{n+1}) - f(\mathcal{C}_n)}{\mathcal{C}_{n+1} - \mathcal{C}_n}. \quad (3.41)$$

In the limit  $\mathcal{C}_{n+1} \rightarrow \mathcal{C}_n$ , the above formula should be replaced with  $f'(\mathcal{C}_{n+\frac{1}{2}})$ . It can be easily verified that property (3.38) is satisfied by the above formula.

**Example (Transversely isotropic material):** The calculation of the discrete derivatives  $\{D_{\mathcal{C}}\Psi, D_{\mathcal{G}}\Psi, D_{\mathcal{C}}\Psi\}$  is further illustrated with a more involved stored energy function characterizing transversely isotropic material. The specific stored energy function has been taken from [149]. Accordingly, the stored energy function relies on an additive decomposition into an isotropic and anisotropic part:

$$\Psi(\mathcal{C}, \mathcal{G}, \mathcal{C}) = \Psi_{\text{iso}}(\mathcal{C}, \mathcal{G}, \mathcal{C}) + \Psi_{\text{aniso}}(\mathcal{C}, \mathcal{G}, \mathcal{C}). \quad (3.42)$$

The isotropic part can be viewed as a modification of the Mooney-Rivlin model (3.39) and is given by

$$\Psi_{\text{iso}}(\mathbf{C}, \mathbf{G}, C) = \frac{a}{2} (\text{tr} \mathbf{C})^2 + \frac{b}{2} (\text{tr} \mathbf{G})^2 - d \ln(\sqrt{C}) + e_1 (C^{e_2} + C^{-e_2} - 2), \quad (3.43)$$

where  $a > 0$ ,  $b > 0$ ,  $d > 0$ ,  $e_1 > 0$  and  $e_2 > 2$ . The anisotropic part of the stored energy reads

$$\Psi_{\text{aniso}}(\mathbf{C}, \mathbf{G}, C) = \frac{g_0}{g_C + 1} (\text{tr}(\mathbf{C} \mathbf{M}))^{g_C + 1} + \frac{g_0}{g_G + 1} (\text{tr}(\mathbf{G} \mathbf{M}))^{g_G + 1} + \frac{g_0}{g_C} C^{-g_C}, \quad (3.44)$$

where  $g_0 > 0$ ,  $g_C > 0$ ,  $g_G > 0$  and  $g_C \geq 1$ . The local fiber direction in the undeformed configuration is characterized by a unit vector  $\mathbf{a}_0 \in \mathbb{R}^3$  that enters the structural tensor defined by

$$\mathbf{M} = \mathbf{a}_0 \otimes \mathbf{a}_0.$$

The discrete derivatives  $\{D_C \Psi, D_G \Psi, D_C \Psi\}$  are now introduced as

$$\begin{aligned} D_C \Psi &= a \text{tr}(\mathbf{C}_{n+\frac{1}{2}}) \mathbf{I} + G_{W_1}(\zeta_n, \zeta_{n+1}) \mathbf{M}, \\ D_G \Psi &= b \text{tr}(\mathbf{G}_{n+\frac{1}{2}}) \mathbf{I} + G_{W_2}(\gamma_n, \gamma_{n+1}) \mathbf{M}, \\ D_C \Psi &= G_{W_3}(C_n, C_{n+1}), \end{aligned} \quad (3.45)$$

where the Greenspan formula (3.41) is now written in the form

$$G_W(x, y) = \frac{W(y) - W(x)}{y - x}, \quad (3.46)$$

with a prescribed function  $W : \mathbb{R} \rightarrow \mathbb{R}$ . In the limit  $y \rightarrow x$ , the above formula should be replaced with  $W'(\frac{x+y}{2})$ . The functions  $W_1(\zeta)$ ,  $W_2(\gamma)$  and  $W_3(C)$  used in (3.45) are given by

$$\begin{aligned} W_1(\zeta) &= \frac{g_0}{g_C + 1} \zeta^{g_C + 1}, \quad \zeta = \text{tr}(\mathbf{C} \mathbf{M}), \\ W_2(\gamma) &= \frac{g_0}{g_G + 1} \gamma^{g_G + 1}, \quad \gamma = \text{tr}(\mathbf{G} \mathbf{M}), \\ W_3(C) &= -d \ln(\sqrt{C}) + e_1 (C^{e_2} + C^{-e_2} - 2) + \frac{g_0}{g_C} C^{-g_C}. \end{aligned} \quad (3.47)$$

It can be verified by a straightforward calculation that property (3.38) is satisfied by the discrete derivatives in (3.45).

Next, we show that there exists a time-discrete counterpart of the constraints on velocity level (3.14). In analogy to the continuous case, the discrete constraints on velocity level play an important role in the discrete balance laws as will be shown below.

**Proposition.** Let  $\{\mathbf{C}_n, \mathbf{G}_n, \mathcal{C}_n\}$  be consistent strain variables. Then the semi-discrete formulation at hand satisfies

$$\begin{aligned}
 \int_{\mathcal{B}_0} \delta \Lambda^{\mathcal{C}} : (\text{DC}[\boldsymbol{\varphi}_{n+1} - \boldsymbol{\varphi}_n]|_{n+\frac{1}{2}} - (\mathbf{C}_{n+1} - \mathbf{C}_n)) \, dV &= 0, \\
 \int_{\mathcal{B}_0} \delta \Lambda^{\mathcal{G}} : (\mathbf{C}_{n+\frac{1}{2}} * (\mathbf{C}_{n+1} - \mathbf{C}_n) - (\mathbf{G}_{n+1} - \mathbf{G}_n)) \, dV &= 0, \\
 \int_{\mathcal{B}_0} \delta \Lambda^{\mathcal{C}} \left( \frac{1}{3} \mathbf{C}_{n+\frac{1}{2}} : (\mathbf{G}_{n+1} - \mathbf{G}_n) + \frac{1}{3} \mathbf{G}_{n+\frac{1}{2}} : (\mathbf{C}_{n+1} - \mathbf{C}_n) - (\mathbf{C}_{n+1} - \mathbf{C}_n) \right) \, dV &= 0.
 \end{aligned} \tag{3.48}$$

**Proof.** Consistent strain variables  $\{\mathbf{C}_n, \mathbf{G}_n, \mathcal{C}_n\}$  satisfy the constraints (3.13) at time  $t_n$ . Similarly, (3.35) enforce the constraints (3.13) at time  $t_{n+1}$ . Accordingly, the following relations hold:

$$\begin{aligned}
 \int_{\mathcal{B}_0} \delta \Lambda^{\mathcal{C}} : (\mathbf{C}_{n+1} - \mathbf{C}_n - (\mathbf{C}_{n+1} - \mathbf{C}_n)) \, dV &= 0, \\
 \int_{\mathcal{B}_0} \delta \Lambda^{\mathcal{G}} : \left( \frac{1}{2} \mathbf{C}_{n+1} * \mathbf{C}_{n+1} - \frac{1}{2} \mathbf{C}_n * \mathbf{C}_n - (\mathbf{G}_{n+1} - \mathbf{G}_n) \right) \, dV &= 0, \\
 \int_{\mathcal{B}_0} \delta \Lambda^{\mathcal{C}} \left( \frac{1}{3} \mathbf{G}_{n+1} : \mathbf{C}_{n+1} - \frac{1}{3} \mathbf{G}_n : \mathbf{C}_n - (\mathbf{C}_{n+1} - \mathbf{C}_n) \right) \, dV &= 0.
 \end{aligned} \tag{3.49}$$

A straightforward calculation shows that the above equations are equivalent to (3.48).  $\square$

## 3.2.2 Semi-discrete balance laws

Next we show that the semi-discrete formulation at hand inherits the balance laws from the underlying continuous formulation for any time-step size.

### 3.2.2.1 Balance of linear momentum

We follow the procedure in Sec. 3.1.2.1 for the verification of the balance of total linear momentum. Assume that  $\delta \boldsymbol{\varphi} = \boldsymbol{\zeta}$  and  $\delta V = \mathbf{0}$  are admissible variations, where  $\boldsymbol{\zeta} \in \mathbb{R}^3$

is arbitrary but constant. Then (3.33) yields

$$\zeta \cdot \left( \frac{1}{\Delta t} (L_{n+1} - L_n) - F^{\text{ext}} \right) = 0. \quad (3.50)$$

The discrete total linear momentum at time-level  $n$  and  $n + 1$  is defined by

$$L_n = \int_{\mathcal{B}_0} \mathbf{V}_n \rho_0 \, dV \quad \text{and} \quad L_{n+1} = \int_{\mathcal{B}_0} \mathbf{V}_{n+1} \rho_0 \, dV. \quad (3.51)$$

Therefore, for vanishing external mechanical loads the total discrete linear momentum is a constant of motion of the semi-discrete system.

### 3.2.2.2 Balance of angular momentum

To verify discrete balance of angular momentum we assume that  $\delta \boldsymbol{\varphi} = \zeta \times \boldsymbol{\varphi}_{n+\frac{1}{2}}$  and  $\delta \mathbf{V} = \zeta \times (\boldsymbol{\varphi}_{n+1} - \boldsymbol{\varphi}_n)$  are admissible variations. As before,  $\zeta \in \mathbb{R}^3$  is constant. Then the time-discrete variational formulation (3.33) yields

$$0 = \int_{\mathcal{B}_0} \zeta \times (\boldsymbol{\varphi}_{n+1} - \boldsymbol{\varphi}_n) \cdot \mathbf{V}_{n+\frac{1}{2}} \rho_0 \, dV, \\ \int_{\mathcal{B}_0} \zeta \times \boldsymbol{\varphi}_{n+\frac{1}{2}} \cdot (\mathbf{V}_{n+1} - \mathbf{V}_n) \rho_0 \, dV = - \int_{\mathcal{B}_0} \boldsymbol{\Lambda}^{\mathcal{C}} : \text{DC}[\zeta \times \boldsymbol{\varphi}_{n+\frac{1}{2}}] \Big|_{n+\frac{1}{2}} \, dV - \text{D}\Pi_m^{\text{ext}}[\zeta \times \boldsymbol{\varphi}_{n+\frac{1}{2}}]. \quad (3.52)$$

Similarly to the continuous setting, the first term on the right-hand side of (3.52)<sub>2</sub> yields

$$\int_{\mathcal{B}_0} \boldsymbol{\Lambda}^{\mathcal{C}} : \text{DC}[\zeta \times \boldsymbol{\varphi}_{n+\frac{1}{2}}] \Big|_{n+\frac{1}{2}} \, dV = \int_{\mathcal{B}_0} \boldsymbol{\Lambda}^{\mathcal{C}} : (\mathbf{F}_{n+\frac{1}{2}}^{\text{T}} (\hat{\zeta}^{\text{T}} + \hat{\zeta}) \mathbf{F}_{n+\frac{1}{2}}) \, dV = 0, \quad (3.53)$$

since  $\hat{\zeta}$  is skew-symmetric. For the time-discrete angular momentum at time-nodes  $t_n$  and  $t_{n+1}$  we have

$$J_n = \int_{\mathcal{B}_0} \boldsymbol{\varphi}_n \times \mathbf{V}_n \rho_0 \, dV \quad \text{and} \quad J_{n+1} = \int_{\mathcal{B}_0} \boldsymbol{\varphi}_{n+1} \times \mathbf{V}_{n+1} \rho_0 \, dV. \quad (3.54)$$

The total torque with respect to the  $\zeta$ -axis exerted by external loads on the considered body in the time discrete setting is defined by

$$\zeta \cdot \mathbf{M}^{\text{ext}} \Big|_{n+\frac{1}{2}} = -\text{D}\Pi_m^{\text{ext}}[\zeta \times \boldsymbol{\varphi}_{n+\frac{1}{2}}] = \zeta \cdot \left( \int_{\mathcal{B}_0} \boldsymbol{\varphi}_{n+\frac{1}{2}} \times \bar{\mathbf{B}} \, dV + \int_{\partial \mathcal{B}_0^p} \boldsymbol{\varphi}_{n+\frac{1}{2}} \times \bar{\mathbf{T}} \, dA \right). \quad (3.55)$$

Then subtracting (3.52)<sub>1</sub> from (3.52)<sub>2</sub> along with (3.53), (3.54) and (3.55) we obtain

$$\zeta \cdot \left( \frac{1}{\Delta t} (J_{n+1} - J_n) - \mathbf{M}^{\text{ext}} \Big|_{n+\frac{1}{2}} \right) = 0, \quad (3.56)$$

which corresponds to the balance of angular momentum with respect to the  $\zeta$ -axis.

### 3.2.2.3 Balance of energy

To this end we proceed along the lines of Sec. 3.1.2.3 and choose admissible variations of the following form:  $\delta\boldsymbol{\varphi} = \boldsymbol{\varphi}_{n+1} - \boldsymbol{\varphi}_n \in \mathcal{V}$ ,  $\delta\mathbf{V} = \mathbf{V}_{n+1} - \mathbf{V}_n \in \mathcal{V}$ ,  $\delta\mathbf{C} = \mathbf{C}_{n+1} - \mathbf{C}_n \in \mathbb{V}_{\mathcal{C}}$ ,  $\delta\boldsymbol{\mathcal{G}} = \boldsymbol{\mathcal{G}}_{n+1} - \boldsymbol{\mathcal{G}}_n \in \mathbb{V}_{\boldsymbol{\mathcal{G}}}$ ,  $\delta\mathcal{C} = \mathcal{C}_{n+1} - \mathcal{C}_n \in \mathbb{V}_{\mathcal{C}}$ ,  $\delta\boldsymbol{\Lambda}^{\mathcal{C}} = \boldsymbol{\Lambda}_{n+1}^{\mathcal{C}} \in \mathbb{V}_{\mathcal{C}}$ ,  $\delta\boldsymbol{\Lambda}^{\boldsymbol{\mathcal{G}}} = \boldsymbol{\Lambda}_{n+1}^{\boldsymbol{\mathcal{G}}} \in \mathbb{V}_{\boldsymbol{\mathcal{G}}}$ ,  $\delta\boldsymbol{\Lambda}^{\mathcal{C}} = \boldsymbol{\Lambda}_{n+1}^{\mathcal{C}} \in \mathbb{V}_{\mathcal{C}}$ . Accordingly, (3.33)<sub>1</sub> yields

$$\begin{aligned} \int_{\mathcal{B}_0} (\mathbf{V}_{n+1} - \mathbf{V}_n) \cdot \frac{1}{\Delta t} (\boldsymbol{\varphi}_{n+1} - \boldsymbol{\varphi}_n) \rho_0 \, dV &= \int_{\mathcal{B}_0} (\mathbf{V}_{n+1} - \mathbf{V}_n) \cdot \mathbf{V}_{n+\frac{1}{2}} \rho_0 \, dV \\ &= \frac{1}{2} \int_{\mathcal{B}_0} (\mathbf{V}_{n+1} \cdot \mathbf{V}_{n+1} - \mathbf{V}_n \cdot \mathbf{V}_n) \rho_0 \, dV \quad (3.57) \\ &= T_{n+1} - T_n \\ &= \Delta T, \end{aligned}$$

where expression (3.28) for the kinetic energy has been used. Furthermore, by definition of the partitioned discrete derivative, property (3.38) leads to

$$\begin{aligned} \Pi_{n+1}^{\text{int}} - \Pi_n^{\text{int}} &= \int_{\mathcal{B}_0} (\Psi(\mathbf{C}_{n+1}, \boldsymbol{\mathcal{G}}_{n+1}, \mathcal{C}_{n+1}) - \Psi(\mathbf{C}_n, \boldsymbol{\mathcal{G}}_n, \mathcal{C}_n)) \, dV \\ &= \int_{\mathcal{B}_0} (\text{D}_{\mathcal{C}}\Psi : (\mathbf{C}_{n+1} - \mathbf{C}_n) + \text{D}_{\boldsymbol{\mathcal{G}}}\Psi : (\boldsymbol{\mathcal{G}}_{n+1} - \boldsymbol{\mathcal{G}}_n) + \text{D}_{\mathcal{C}}\Psi (\mathcal{C}_{n+1} - \mathcal{C}_n)) \, dV \\ &= \int_{\mathcal{B}_0} \left( \boldsymbol{\Lambda}_{n+1}^{\mathcal{C}} : (\mathbf{C}_{n+1} - \mathbf{C}_n) - \boldsymbol{\Lambda}_{n+1}^{\boldsymbol{\mathcal{G}}} : (\mathbf{C}_{n+\frac{1}{2}} \star (\mathbf{C}_{n+1} - \mathbf{C}_n) - (\boldsymbol{\mathcal{G}}_{n+1} - \boldsymbol{\mathcal{G}}_n)) \right. \\ &\quad \left. - \boldsymbol{\Lambda}_{n+1}^{\mathcal{C}} \left( \frac{1}{3} \mathbf{C}_{n+\frac{1}{2}} : (\boldsymbol{\mathcal{G}}_{n+1} - \boldsymbol{\mathcal{G}}_n) + \frac{1}{3} \boldsymbol{\mathcal{G}}_{n+\frac{1}{2}} : (\mathbf{C}_{n+1} - \mathbf{C}_n) - (\mathcal{C}_{n+1} - \mathcal{C}_n) \right) \right) \, dV \\ &= \int_{\mathcal{B}_0} \boldsymbol{\Lambda}_{n+1}^{\mathcal{C}} : \text{DC}[\boldsymbol{\varphi}_{n+1} - \boldsymbol{\varphi}_n]_{n+\frac{1}{2}} \, dV \\ &= \Delta \Pi^{\text{int}}. \end{aligned} \quad (3.58)$$

In the above equations use has been made of (3.34) and (3.48). Inserting from (3.57) and (3.58) into (3.33)<sub>2</sub> yields the discrete balance of energy in the form

$$\Delta T + \Delta \Pi^{\text{int}} = W_{n,n+1}^{\text{ext}}, \quad (3.59)$$

where  $W_{n,n+1}^{\text{ext}}$  stands for the work done by the external loads in the time interval. In the case of dead loads,  $W_{n,n+1}^{\text{ext}} = -(\Pi^{\text{ext}}(\boldsymbol{\varphi}_{n+1}) - \Pi^{\text{ext}}(\boldsymbol{\varphi}_n))$ . Thus, for conservative systems the present scheme is capable of preserving the total energy in the sense that  $E_n = E_{n+1}$ , independent of the time-step size.

### 3.3 Discretization in space

The time-discrete variational formulation consisting of (3.33), (3.34) and (3.35) provides the framework for a variety of discretizations in space. We focus on finite elements and present two alternative schemes: (i) the pure displacement formulation based on the interpolation of the deformation field  $\boldsymbol{\varphi}(\mathbf{X}) \in \mathcal{Q}$  and the velocity field  $\mathbf{V}(\mathbf{X}) \in \mathcal{V}$ , and (ii) the fully mixed approach relying on the independent interpolation of the deformation field  $\boldsymbol{\varphi}(\mathbf{X}) \in \mathcal{Q}$ , the velocity field  $\mathbf{V}(\mathbf{X}) \in \mathcal{V}$ , the strain fields  $\{\mathcal{C}(\mathbf{X}), \mathcal{G}(\mathbf{X}), \mathcal{C}(\mathbf{X})\} \in \mathbb{V}_{\mathcal{C}} \times \mathbb{V}_{\mathcal{G}} \times \mathbb{V}_{\mathcal{C}}$  along with the Lagrange multiplier fields  $\{\Lambda^{\mathcal{C}}(\mathbf{X}), \Lambda^{\mathcal{G}}(\mathbf{X}), \Lambda^{\mathcal{C}}(\mathbf{X})\} \in \mathbb{V}_{\mathcal{C}} \times \mathbb{V}_{\mathcal{G}} \times \mathbb{V}_{\mathcal{C}}$ .

#### 3.3.1 Displacement formulation

The displacement formulation makes use of standard isoparametric elements (see, for example, [71]) based on finite-dimensional approximations  $\boldsymbol{\varphi}^h \in \mathcal{Q}^h \subset \mathcal{Q}$  and  $\mathbf{V}^h \in \mathcal{V}^h \subset \mathcal{V}$  of the form

$$\boldsymbol{\varphi}^h(\mathbf{X}) = \sum_{a=1}^{n_{node}} N^a(\mathbf{X}) \boldsymbol{\varphi}_a(t) \quad \text{and} \quad \mathbf{V}^h(\mathbf{X}) = \sum_{a=1}^{n_{node}} N^a(\mathbf{X}) \mathbf{V}_a(t). \quad (3.60)$$

Here  $N^a : \mathcal{B}_0 \rightarrow \mathbb{R}$  denote the nodal shape functions and  $\boldsymbol{\varphi}_a(t), \mathbf{V}_a(t) \in \mathbb{R}^3$  are the respective nodal values at time  $t$ . Moreover,  $n_{node}$  denotes the total number of nodes in the finite element mesh. The standard (Bubnov) Galerkin approach relies on analogous approximations for  $\delta\boldsymbol{\varphi} \in \mathcal{V}$  and  $\delta\mathbf{V} \in \mathcal{V}$  denoted by  $\delta\boldsymbol{\varphi}^h \in \mathcal{V}^h$  and  $\delta\mathbf{V}^h \in \mathcal{V}^h$ . Note that the displacement formulation relies on a pointwise enforcement of the constitutive relations (3.34) and the kinematic constraints (3.35). In particular, (3.35) gives

$$\begin{aligned} \mathcal{C}_{n+1} &= \mathcal{C}_{n+1} = \mathbf{F}_{n+1}^T \mathbf{F}_{n+1}, \\ \mathcal{G}_{n+1} &= \mathcal{G}_{n+1} = \frac{1}{2} \mathcal{C}_{n+1} * \mathcal{C}_{n+1}, \\ \mathcal{C}_{n+1} &= \mathcal{C}_{n+1} = \frac{1}{3} \mathcal{G}_{n+1} : \mathcal{C}_{n+1}. \end{aligned} \quad (3.61)$$

Similarly, a straightforward calculation starting from (3.34) yields

$$\Lambda_{n+1}^{\mathcal{C}} = \mathbf{D}_{\mathcal{C}} \Psi + \mathbf{D}_{\mathcal{G}} \Psi * \mathcal{C}_{\text{alg}} + \mathbf{D}_{\mathcal{C}} \Psi \mathcal{G}_{\text{alg}}, \quad (3.62)$$

where the algorithmic version of  $\mathcal{C}$  is evaluated as

$$\mathcal{C}_{\text{alg}} = \mathcal{C}_{n+\frac{1}{2}} = \frac{1}{2} (\mathcal{C}_n + \mathcal{C}_{n+1}), \quad (3.63)$$

and for the algorithmic version of  $\mathcal{G}$  we use

$$\mathcal{G}_{\text{alg}} = \frac{1}{3}(\mathbf{C}_{n+\frac{1}{2}} * \mathbf{C}_{n+\frac{1}{2}} + \mathcal{G}_{n+\frac{1}{2}}) \quad \text{where} \quad \mathcal{G}_{n+\frac{1}{2}} = \frac{1}{2}(\mathcal{G}_n + \mathcal{G}_{n+1}). \quad (3.64)$$

Now the semi-discrete variational formulation of the displacement formulation emanating from (3.33) can be written in the form

$$\begin{aligned} \int_{\mathcal{B}_0} \delta \mathbf{V} \cdot \frac{1}{\Delta t} (\boldsymbol{\varphi}_{n+1} - \boldsymbol{\varphi}_n) \rho_0 \, dV &= \int_{\mathcal{B}_0} \delta \mathbf{V} \cdot \mathbf{V}_{n+\frac{1}{2}} \rho_0 \, dV, \\ \int_{\mathcal{B}_0} \delta \boldsymbol{\varphi} \cdot \frac{1}{\Delta t} (\mathbf{V}_{n+1} - \mathbf{V}_n) \rho_0 \, dV &= - \int_{\mathcal{B}_0} \mathbf{S}_{\text{alg}} : \text{DC}[\delta \boldsymbol{\varphi}]|_{n+\frac{1}{2}} \, dV - \text{D}\Pi_m^{\text{ext}}[\delta \boldsymbol{\varphi}]|_{n+\frac{1}{2}}, \end{aligned} \quad (3.65)$$

for any  $\delta \boldsymbol{\varphi} \in \mathcal{V}$  and  $\delta \mathbf{V} \in \mathcal{V}$ . In the last equation  $\mathbf{S}_{\text{alg}} = 2 \boldsymbol{\Lambda}_{n+\frac{1}{2}}^{\mathcal{C}}$  denotes the algorithmic stress formula which is a characteristic feature of energy-momentum methods (see [145]). With regard to (3.62), the algorithmic stress formula assumes the specific form

$$\mathbf{S}_{\text{alg}} = 2 \, \text{D}_{\mathcal{C}} \Psi + 2 \, \text{D}_{\mathcal{G}} \Psi * \mathcal{C}_{\text{alg}} + 2 \, \text{D}_{\mathcal{C}} \Psi \, \mathcal{G}_{\text{alg}}. \quad (3.66)$$

Eventually, the fully discrete displacement formulation is obtained in a standard way by inserting the finite element interpolations outlined above into (3.65), see Appendix B.1 for further details.

The newly developed algorithmic stress formula (3.66) can be viewed as time-discrete version of the 2nd Piola-Kirchhoff stress tensor (2.60). It represents a viable alternative to previously developed projection-based formulas (cf. [145]) leading to second order accurate energy-momentum schemes (cf. [51]).

**Remark 3.6.** *Although the displacement-based discretization in space does not necessitate the mixed variational framework developed herein, the algorithmic stress formula (3.66) is a direct result of the discretization in time of the underlying mixed variational formulation. This is to be contrasted with the mid-point type discretization in time of the standard displacement-based variational formulation. The standard mid-point type discretization relies on (3.65) with  $\mathbf{S}_{\text{alg}}$  being replaced by*

$$\begin{aligned} \mathbf{S}_{n+\frac{1}{2}} &= 2\partial_{\mathcal{C}} \Psi(\mathbf{C}_{n+\frac{1}{2}}, \mathbf{G}_{n+\frac{1}{2}}, \mathbf{C}_{n+\frac{1}{2}}) + 2\partial_{\mathcal{G}} \Psi(\mathbf{C}_{n+\frac{1}{2}}, \mathbf{G}_{n+\frac{1}{2}}, \mathbf{C}_{n+\frac{1}{2}}) * \mathbf{C}_{n+\frac{1}{2}} \\ &\quad + 2\partial_{\mathcal{C}} \Psi(\mathbf{C}_{n+\frac{1}{2}}, \mathbf{G}_{n+\frac{1}{2}}, \mathbf{C}_{n+\frac{1}{2}}) \mathbf{G}_{n+\frac{1}{2}}, \end{aligned} \quad (3.67)$$

which coincides with the mid-point evaluation of the 2nd Piola-Kirchhoff stress tensor (2.60). In this connection it is important to realize that in general,  $\mathcal{C}_{\text{alg}} \neq \mathbf{C}_{n+\frac{1}{2}}$ ,  $\mathcal{G}_{\text{alg}} \neq \mathbf{G}_{n+\frac{1}{2}} \neq \mathbf{G}_{n+\frac{1}{2}}$ , and  $\mathbf{C}_{n+\frac{1}{2}} \neq \mathbf{C}_{n+\frac{1}{2}}$ . For example,

$$\mathbf{C}_{n+\frac{1}{2}} = \frac{1}{2}(\mathbf{C}_n + \mathbf{C}_{n+1}) = \frac{1}{2}(\mathbf{F}_n^{\text{T}} \mathbf{F}_n + \mathbf{F}_{n+1}^{\text{T}} \mathbf{F}_{n+1}) = \frac{1}{2}(\mathbf{C}_n + \mathbf{C}_{n+1}), \quad (3.68)$$

whereas

$$\mathbf{C}_{n+\frac{1}{2}} = \mathbf{F}_{n+\frac{1}{2}}^T \mathbf{F}_{n+\frac{1}{2}}. \quad (3.69)$$

We further note that the symmetry of  $\mathbf{S}_{\text{alg}}$  can be easily verified by taking into account relation (2.12)<sub>2</sub>. Moreover, it can be verified by a straightforward calculation that the algorithmic stress formula (3.66) satisfies the directionality property

$$\hat{\Psi}(\mathbf{C}_{n+1}) - \hat{\Psi}(\mathbf{C}_n) = \mathbf{S}_{\text{alg}} : \frac{1}{2} (\mathbf{C}_{n+1} - \mathbf{C}_n). \quad (3.70)$$

**Example (Mooney-Rivlin material cont'd):** To illustrate the application of the newly devised algorithmic stress formula (3.66) we again consider the example of the compressible Mooney-Rivlin material with stored energy function (3.39). Employing the discrete derivatives (3.40) and (3.41), formula (3.66) yields

$$\mathbf{S}_{\text{alg}} = 2a \mathbf{I} + 2b \mathbf{I} * \mathbf{C}_{\text{alg}} + 2 \frac{f(\mathbf{C}_{n+1}) - f(\mathbf{C}_n)}{\mathbf{C}_{n+1} - \mathbf{C}_n} \mathbf{G}_{\text{alg}}. \quad (3.71)$$

This is to be contrasted with the alternative projection based formula (see [52, 145])

$$\mathbf{S}_{\text{SG}} = \mathbf{S}_m + \frac{2\Psi(\mathbf{C}_{n+1}) - 2\Psi(\mathbf{C}_n) - \mathbf{S}_m : (\mathbf{C}_{n+1} - \mathbf{C}_n)}{(\mathbf{C}_{n+1} - \mathbf{C}_n) : (\mathbf{C}_{n+1} - \mathbf{C}_n)} (\mathbf{C}_{n+1} - \mathbf{C}_n), \quad (3.72)$$

where the stored energy function (3.39) is recast in the form

$$\begin{aligned} \hat{\Psi}(\mathbf{C}) &= \Psi(\mathbf{C}, \text{cof}(\mathbf{C}), \det(\mathbf{C})) \\ &= a \text{tr} \mathbf{C} + \frac{b}{2} ((\text{tr} \mathbf{C})^2 - \text{tr}(\mathbf{C}^2)) + f(\det \mathbf{C}), \end{aligned} \quad (3.73)$$

and

$$\begin{aligned} \mathbf{S}_m &= 2 \mathbf{D}\hat{\Psi}(\mathbf{C}_{n+\frac{1}{2}}) \\ &= a \mathbf{I} + b ((\text{tr} \mathbf{C}_{n+\frac{1}{2}}) \mathbf{I} - \mathbf{C}_{n+\frac{1}{2}}) + f'(\det \mathbf{C}_{n+\frac{1}{2}}) \det(\mathbf{C}_{n+\frac{1}{2}}) (\mathbf{C}_{n+\frac{1}{2}})^{-1}. \end{aligned} \quad (3.74)$$

It can be observed that the newly developed formula (3.71) enjoys a particularly simple structure when compared to the alternative formula (3.72). This observation applies particularly to the corresponding tangent moduli needed for the iterative solution process. We refer to Appendix B.1 for further details.

**Example (St. Venant-Kirchhoff material):** It is well known that the stored energy function of a St. Venant-Kirchhoff material is not polyconvex [141]. However, the method developed herein can still be applied. For that purpose we write the stored

energy function of a St. Venant-Kirchhoff material in the form (see, for example, [35])

$$\Psi(\mathbf{C}, \mathbf{G}, \mathcal{C}) = -\frac{3\lambda + 2\mu}{4} \operatorname{tr} \mathbf{C} + \frac{\lambda + 2\mu}{8} \operatorname{tr} \mathbf{C}^2 + \frac{\lambda}{4} \operatorname{tr} \mathbf{G} + \frac{9\lambda + 6\mu}{8}, \quad (3.75)$$

where  $\lambda$  and  $\mu$  are the two Lamé parameters. Associated with (3.75) we introduce the discrete derivatives

$$\begin{aligned} D_{\mathbf{C}} \Psi &= -\frac{3\lambda + 2\mu}{4} \mathbf{I} + \frac{\lambda + 2\mu}{4} \mathbf{C}_{n+\frac{1}{2}}, \\ D_{\mathbf{G}} \Psi &= \frac{\lambda}{4} \mathbf{I}. \end{aligned} \quad (3.76)$$

Now the algorithmic stress formula (3.66) yields

$$\mathbf{S}_{\text{alg}} = -\frac{1}{2} (3\lambda + 2\mu) \mathbf{I} + \frac{1}{2} (\lambda + 2\mu) \mathbf{C}_{\text{alg}} + \frac{\lambda}{2} \mathbf{I} \star \mathbf{C}_{\text{alg}}. \quad (3.77)$$

Taking into account the relationship  $\mathbf{I} \star \mathbf{C} = (\operatorname{tr} \mathbf{C}) \mathbf{I} - \mathbf{C}^T$  we obtain

$$\begin{aligned} \mathbf{S}_{\text{alg}} &= 2\mu \frac{1}{2} (\mathbf{C}_{\text{alg}} - \mathbf{I}) + \lambda \frac{1}{2} (\operatorname{tr} \mathbf{C}_{\text{alg}} - 3) \mathbf{I} \\ &= 2\mu \boldsymbol{\varepsilon}_{n+\frac{1}{2}} + \lambda \operatorname{tr} \boldsymbol{\varepsilon}_{n+\frac{1}{2}} \mathbf{I}. \end{aligned} \quad (3.78)$$

In the last equation the Green-Lagrangean strain tensor  $\boldsymbol{\varepsilon} = \frac{1}{2}(\mathbf{C} - \mathbf{I})$  has been introduced. Using the fourth-order elasticity tensor,  $\mathbf{C}$ , the algorithmic stress tensor can be recast in the form  $\mathbf{S}_{\text{alg}} = \mathbf{C} : \boldsymbol{\varepsilon}_{\text{alg}}$ . This formula has originally been proposed by [153].

### 3.3.2 Mixed formulation

In analogy to the displacement formulation, the continuous finite element interpolation (3.60) for the displacement field and the velocity field are also used in the mixed formulation. In addition to that the semi-discrete variational framework at hand makes possible the independent interpolation of the strain fields  $\{\mathbf{C}, \mathbf{G}, \mathcal{C}\} \in \mathbb{V}_{\mathbf{C}} \times \mathbb{V}_{\mathbf{G}} \times \mathbb{V}_{\mathcal{C}}$  and the Lagrange multiplier fields  $\{\boldsymbol{\Lambda}^{\mathbf{C}}, \boldsymbol{\Lambda}^{\mathbf{G}}, \Lambda^{\mathcal{C}}\} \in \mathbb{V}_{\mathbf{C}} \times \mathbb{V}_{\mathbf{G}} \times \mathbb{V}_{\mathcal{C}}$ . Of course, the choice of approximation formulas is restricted by appropriate stability (or inf-sup) conditions (see, for example, [24]). This issue, however, is beyond the scope of the present work.

From the variety of conceivable interpolations we focus on one specific example. In particular, the mixed formulation is based on polynomial interpolations of second-order tensors  $A$  and scalars  $A$  over a typical element  $\mathcal{B}_0^{(e)} \subset \mathcal{B}_0$ . To this end we

introduce finite-dimensional subspaces  $\mathbb{V}_{\mathcal{C}}^h \subset \mathbb{V}_{\mathcal{C}}$  and  $\mathbb{V}_{\mathcal{G}}^h \subset \mathbb{V}_{\mathcal{G}}$  defined by

$$\mathbb{V}_{\mathbf{A}}^h = \left\{ \mathbf{A} \in \mathbb{V}_{\mathbf{A}} \mid \mathbf{A}^h \Big|_{B_0^{(e)}} = \sum_{b=1}^{n_{\text{en}}} M^b \mathbf{A}_b, \mathbf{A}_b = \mathbf{A}_b^T \right\}, \quad (3.79)$$

where  $\mathbf{A}$  stands for the second-order tensors  $\mathcal{C}$ ,  $\mathcal{G}$ ,  $\Lambda^{\mathcal{C}}$  or  $\Lambda^{\mathcal{G}}$ . Similarly we introduce a finite-dimensional subspace  $\mathbb{V}_{\mathcal{C}}^h \subset \mathbb{V}_{\mathcal{C}}$  defined by

$$\mathbb{V}_A^h = \left\{ A \in \mathbb{V}_A \mid A^h \Big|_{B_0^{(e)}} = \sum_{b=1}^{n_{\text{en}}} M^b A_b, A_b \in \mathbb{R} \right\}, \quad (3.80)$$

where  $A$  stands for the scalars  $\mathcal{C}$  or  $\Lambda^{\mathcal{C}}$ . Accordingly, the present sample application relies on uniform elementwise approximations for the strains and the Lagrange multipliers making use of the shape functions  $M^b$ , with  $b = 1, \dots, n_{\text{en}}$ . Here,  $n_{\text{en}}$  denotes the number of element nodes arising from the use of Lagrangian shape functions (see the next section for more details). The thus defined finite element interpolations can be inserted into the semi-discrete variational equations (3.33), (3.34) and (3.35), leading to a system of nonlinear algebraic equations. Since no inter-element continuity is required for the mixed approximations, the additional unknowns of the mixed formulation can be eliminated on element level by applying the classical static condensation procedure. Accordingly, after finite element assembly, the number of unknowns to be solved for on the global level is the same for both the displacement formulation and the mixed formulation at hand. More details about the implementation of the mixed formulation can be found in Appendix B.2.

## 3.4 Numerical Investigations

In the numerical investigations we employ both the pure displacement formulation (Sec. 3.3.1) and the mixed formulation (Sec. 3.3.2). Concerning the interpolation of the displacements we make use of 20-node serendipity shape functions (cf. the nodal shape functions  $N^a$  in (3.60) and the illustration in Fig. 3.1). In addition to that, the mixed formulation relies on tri-linear Lagrangian shape functions (cf. the shape functions  $M^b$  in (3.79), (3.80), and Fig. 3.1).

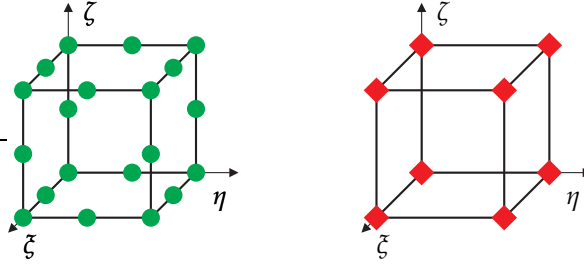


Figure 3.1: Illustration of the nodal points used for the interpolation of the displacements (left) and the additional fields of the mixed formulation (right).

We make use of the compressible Mooney-Rivlin material considered above. Correspondingly, the stored energy function is given by (3.39), where the volumetric contribution is given by

$$f(\mathcal{C}) = -d \ln(\sqrt{\mathcal{C}}) + \frac{c}{2} (\sqrt{\mathcal{C}} - 1)^2. \quad (3.81)$$

The material parameters are given by  $a > 0$ ,  $b > 0$ ,  $c > 0$  and  $d = 2(a + 2b)$ . For an example with the more sophisticated stored energy characterizing transversely isotropic material (3.42), see [23].

### 3.4.1 Patch test

The objective of this example is:

**O1.I** Assess the correctness of the mixed formulation and show the capability of reproducing homogeneous states of stress.

To assess the correctness of the two alternative element formulations at hand and their computer implementation, we first consider the three-dimensional patch test from [106]. Consider a cube  $\Omega \in (0, 1)[\text{m}] \times (0, 1)[\text{m}] \times (0, 1)[\text{m}]$ , depicted in Fig. 3.2, subjected to the following Dirichlet boundary conditions: the face at  $x_1 = 0$  is fixed in  $x_1$ -direction, the face at  $x_2 = 0$  is fixed in  $x_2$ -direction, and the face at  $x_3 = 0$  is fixed in  $x_3$ -direction. Furthermore, the face at  $x_3 = 1$  (see the upper green surface in Fig. 3.2) is displacement-driven to compress the unit-length cube to a hexahedron with halved height. The material parameters, given in Tab. 3.1, corresponds to a Young's modulus of  $E = 10^6$  Pa and a Poisson's ratio of  $\nu = 0.3$  in the case of linear elasticity. Both a regular mesh with 425 Nodes/ 1275 unknowns and an initially distorted mesh with 48 Nodes/ 144 unknowns (Fig. 3.2) are considered. Both element formulations under

consideration pass the patch test and are capable of reproducing the correct value of homogeneous states of stress (see Figs. 3.3 and 3.4).

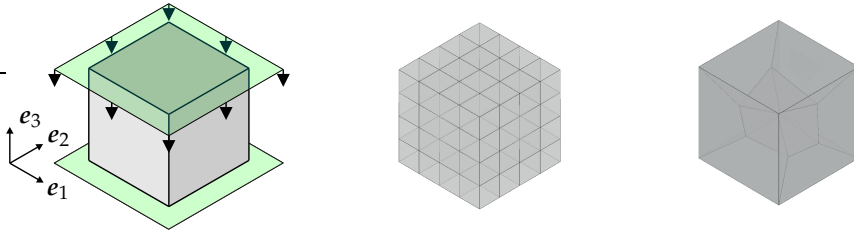
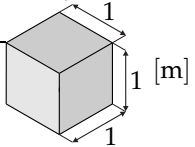


Figure 3.2: Boundary conditions (left), initial regular mesh (center) and initial distorted mesh (right).

Table 3.1: Material and simulation parameters for patch tests.

mechanical parameters	$a$	$15/13 \cdot 10^5$	Pa	geometry of the cube 
	$b$	$10/13 \cdot 10^5$	Pa	
	$c$	$25/3 \cdot 10^5$	Pa	
Newton tolerance	$\varepsilon$	$1 \cdot 10^{-6}$	-	
size of load increment	$\Delta u$	0.02	$m$	

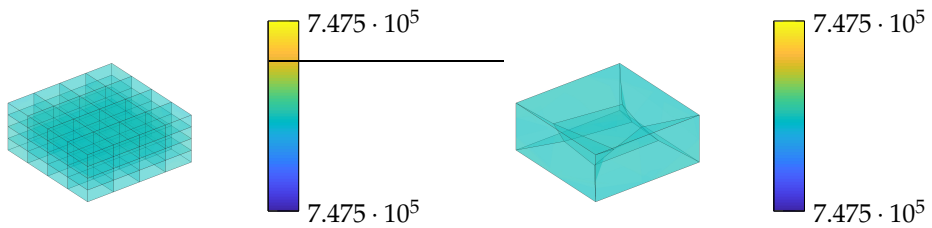


Figure 3.3: Von Mises stress distribution of the regular mesh (left) and distorted mesh (right) of the displacement based formulation.

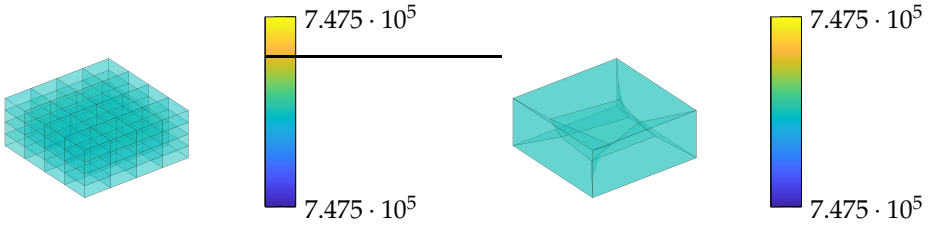


Figure 3.4: Von Mises stress distribution of the regular mesh (left) and distorted mesh (right) of the mixed formulation.

### 3.4.2 Cooks membrane

The objectives of this example are:

- O2.I** Verification of the locking free response of the mixed formulation.
- O2.II** Verification of the improved robustness of the mixed formulation.

Next we consider a three-dimensional version of Cooks membrane (Fig. 3.5) as benchmark problem for large deformation solid mechanics. The membrane is clamped on the left side and loaded by a shear force on the right side. The plane strain condition is enforced by imposing zero displacement boundary conditions in  $e_1$ -direction. The resultant force vector  $\vec{T}$  is oriented in  $e_3$ -direction and has magnitude  $P = 100 \cdot 10^3$  Pa. The parameters of the Mooney-Rivlin material correspond to a Young's modulus of  $E \approx 2850 \cdot 10^3$  Pa and a Poisson's ratio of  $\nu = 0.4954$  in the linear theory. Further data is summarized in Tab. 3.2. The initial mesh and the final von Mises stress distribution of the deformed configuration are depicted in Fig. 3.5. The calculated displacement  $u_3^A$  of the upper right node (point A in Fig. 3.5) is plotted versus the number of elements per side in Fig. 3.6.

It can be observed that the newly developed mixed element performs extremely good when compared to the pure displacement formulation. The improvement in performance of the mixed formulation is also visible in the incremental-iterative solution procedure. In particular, as can be seen from Tab. 3.3, the total number of Newton iterations needed to reach the final result is up to four times greater for the displacement element than for the mixed element. This is partially due to the fact that the mixed element typically needs less Newton iterations to reach the prescribed tolerance than the displacement element. This is exemplarily illustrated with Fig. 3.7

for one representative load step (these results have been obtained with the  $\{4, 4, 4\}$  mesh). In addition to that, the mixed element often allows for larger load increments than the displacement element. The corresponding results of the investigations on the incremental-iterative solution procedure are summarized in Tab. 3.3. The superior robustness of the mixed element normally overcompensates the additional numerical effort on element level due to the static condensation procedure.

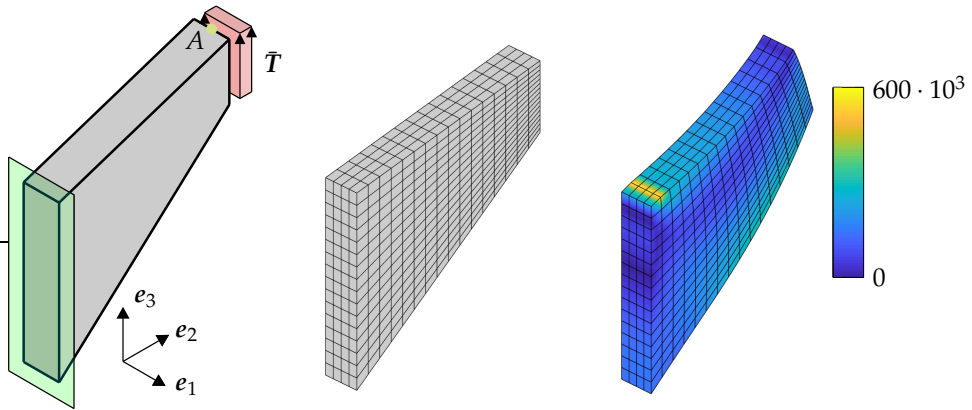


Figure 3.5: Boundary conditions of Cook's membrane (left), initial mesh (center) and von Mises stress distribution of the final configuration (right).

Table 3.2: Material and simulation parameters for Cook's membrane.

mechanical parameters	$a$	$126 \cdot 10^3$	Pa	geometry of membrane 
	$b$	$252 \cdot 10^3$	Pa	
	$c$	$81512 \cdot 10^3$	Pa	
Newton tolerance	$\varepsilon$	$1 \cdot 10^{-6}$	-	

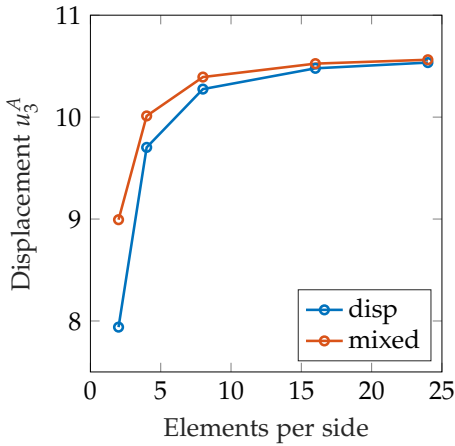


Figure 3.6: Convergence with mesh refinement.

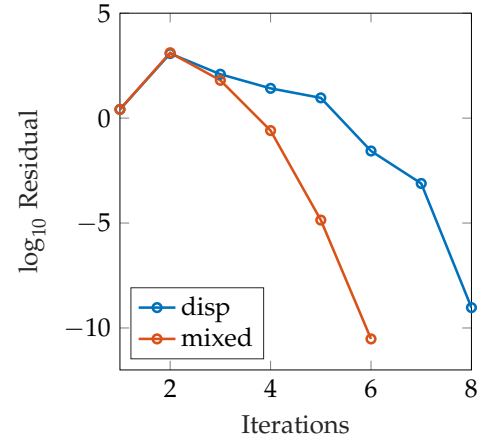


Figure 3.7: Comparison of the Newton iterations in a typical load step.

Table 3.3: Investigation on the robustness of the two element formulations under consideration.

$n_{el}$ in $\{e_1, e_2, e_3\}$ -direction	$\{4, 2, 2\}$	$\{4, 4, 4\}$	$\{4, 8, 8\}$	$\{4, 16, 16\}$	$\{4, 24, 24\}$
Num. of nodes	141	425	1449	5321	11625
Num. of global unknowns	423	1275	4347	15963	34875
Necessary load increments disp/mixed	1/1	1/1	3/1	4/1	4/1
Total Newton iterations disp/mixed	8/6	12/6	11/6	22/6	26/6

### 3.4.3 L-shaped block

The objectives of this example are:

**O3.I** Verification of the algorithmic conservation properties.

**O3.II** Investigation of the numerical stability.

This transient example deals with the classical benchmark problem of a tumbling L-shaped block introduced in [153]. Instead of St. Venant-Kirchhof material employed in [153], we again make use of the Mooney-Rivlin material. The corresponding material parameters are summarized in Tab. 3.5. These parameters correspond to  $E = 12825$  Pa

for Young's modulus and  $\nu = 0.2857$  for Poisson's ratio in the linear theory. Further data used in the simulation can also be found in Tab. 3.5. The initial geometry and the finite element mesh of the L-shaped block are illustrated in Fig. 3.8 and Tab. 3.5.

There are no Dirichlet boundary conditions and after an initial loading phase the block is tumbling through space exhibiting large deformations (Fig. 3.9). The discretized L-shaped block has 768 nodes leading to a total of 2304 global unknowns. Time-dependent pressure loads are acting on the L-shaped block, as illustrated in Fig. 3.8. In this connection, the nodal dead loads are given by

$$P_1(t) = -P_2(t) = f(t) \begin{pmatrix} 256/9 \\ 512/9 \\ 768/9 \end{pmatrix} \frac{\text{N}}{\text{m}^2}, \quad \text{with} \quad f(t) = \begin{cases} t & \text{for } t \leq 2.5\text{s} \\ 5 - t & \text{for } 2.5 \leq t \leq 5\text{s} \\ 0 & \text{for } t > 5\text{s} \end{cases} . \quad (3.82)$$

Note that after the loading phase, the discrete system under consideration can be classified as autonomous Hamiltonian system with symmetry. Correspondingly, for  $t \geq 5\text{s}$ , the total linear momentum, angular momentum and energy are conserved quantities.

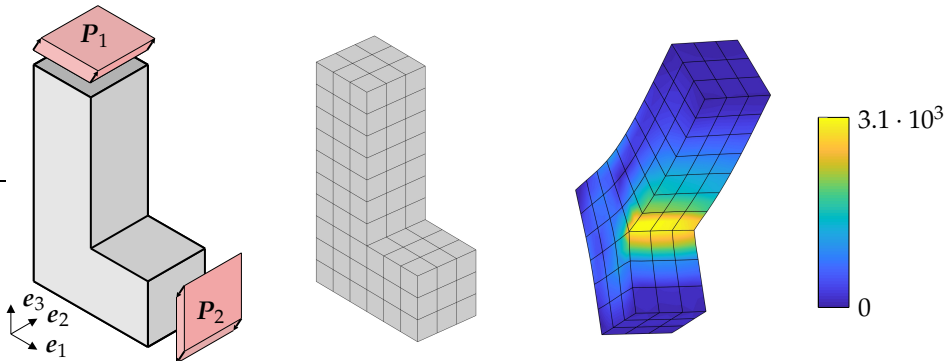


Figure 3.8: Sketch of the L-shaped block in the initial configuration (left), the discretized model (center) and von Mises stress distribution at  $t = 3.6\text{s}$  (right).

As expected both the displacement formulation and the mixed formulation are capable of correctly reproducing the conservation laws of the underlying continuum theory. This is true for arbitrary time steps, including time step changes. Figs. 3.10 and 3.12 corroborate conservation of energy for both formulations under consideration. The incremental change of the total energy is below the Newton tolerance and

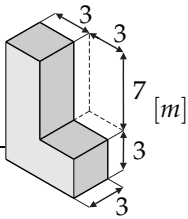
shown for both formulations in Figs. 3.11 and 3.13. It is well-known that standard time-stepping schemes such that the mid-point rule show a tendency to numerical instabilities in nonlinear applications. The numerical instability is typically accompanied by a blow-up of the total energy. The unstable behavior of the mid-point rule can also be observed in this example (see Figs. 3.10 and 3.12). In contrast to that, the present EM schemes are numerically stable. Eventually, conservation of the total angular momentum for both formulations at hand is illustrated in Figs. 3.14 and 3.15.

Similar to the equilibrium problem considered in Section 3.4.2, we investigate the robustness of the two alternative EM schemes at hand. Again the mixed formulation leads to an enhancement of the robustness when compared to the pure displacement formulation. Typically, the mixed formulation (i) needs less Newton iterations per time step, and (ii) allows for greater time steps than the displacement formulation. For example, the displacement formulation allows for a maximum time step size of  $\Delta t = 1.2s$  to attain convergence of the iterative solution procedure. In contrast, the time step size of the mixed formulation can be increased up to  $\Delta t = 2.4s$ , while the average number of Newton iterations per time step is below that of the displacement formulation. Consequently, the total number of iterations required within the time interval of interest is almost three times lower for the mixed formulation than for the displacement formulation (see Tab. 3.4). Moreover, for smaller time steps the mixed formulation saves about one iteration per time step when compared to the displacement formulation (see Tab. 3.4).

Table 3.4: Investigation on the robustness of the two element formulations under consideration when using the respective EM scheme.

Time-step size $\Delta t$	0.8s	1.2s	2.4s
Number of time-steps	126	84	42
Total Newton iterations disp/mixed	737/644	598/500	no convergence/266
Average iterations per time-step disp/mixed	5.85 / 5.11	7.12 / 5.95	no convergence/ 6.33

Table 3.5: Simulation parameters for the L-shaped block.

mechanical parameters	$a$	831.25	Pa	geometry of the L-shaped block
	$b$	1662.5	Pa	
	$c$	0	Pa	
reference density	$\rho_0$	100	$\text{kg m}^{-3}$	
Newton tolerance	$\varepsilon$	$1 \cdot 10^{-5}$	—	
time step size	$\Delta t$	0.8, 1.2	s	
simulation duration	$T$	100.8	s	

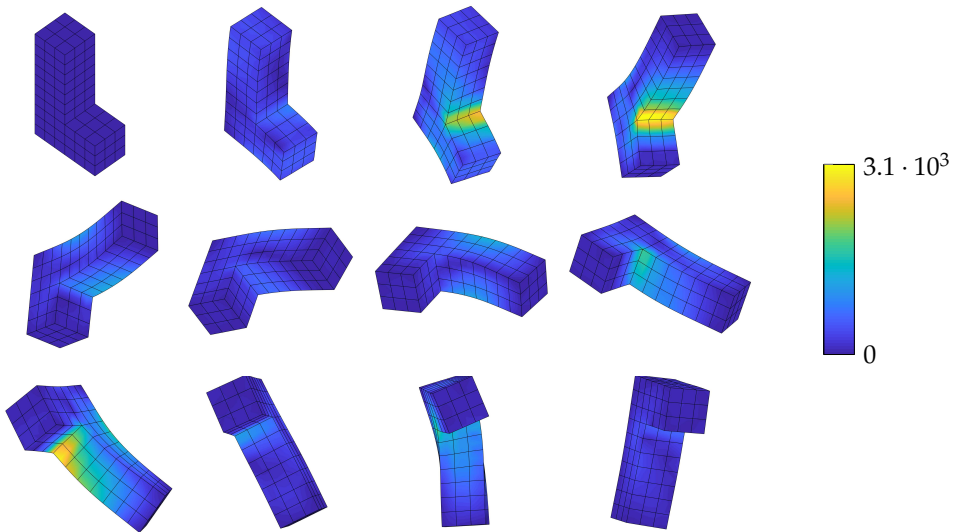


Figure 3.9: Snapshots of configurations at  $t \in \{0, 1.2, 2.4, 3.6, 4.8, 6.0, 7.2, 8.4, 9.6, 10.8, 12.0, 13.2\}$ s. The results have been obtained with the mixed elements, EM Scheme and  $\Delta t = 1.2$  s .

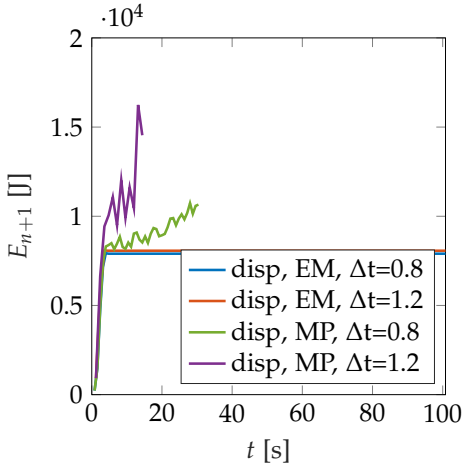


Figure 3.10: Displacement formulation: Total energy versus time.

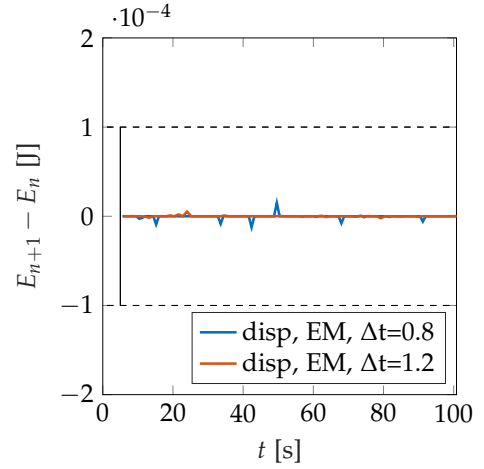


Figure 3.11: Displacement formulation: Incremental change of total energy.

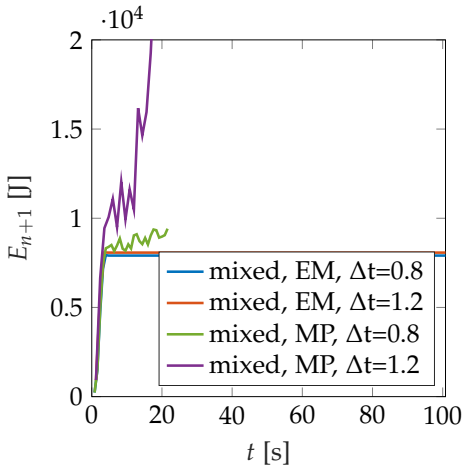


Figure 3.12: Mixed formulation: Total energy versus time.

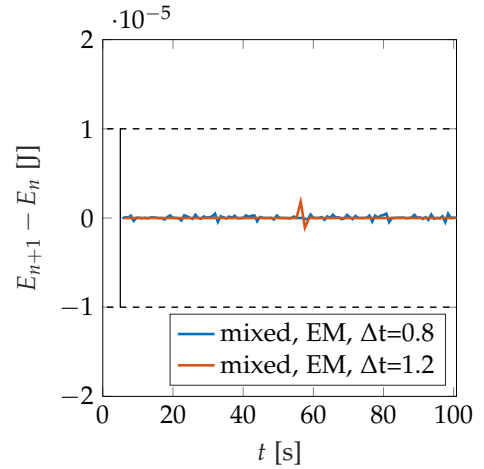


Figure 3.13: Mixed formulation: Incremental change of total energy.

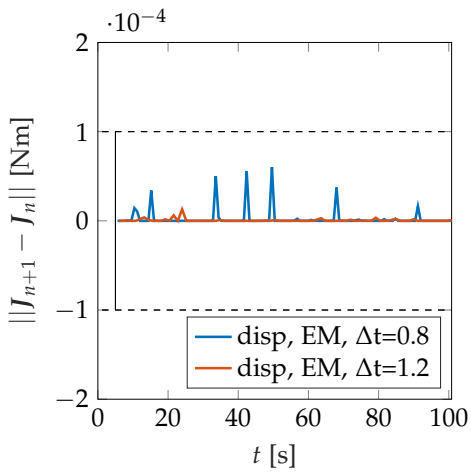


Figure 3.14: Disp. formulation: Incremental change of angular momentum.

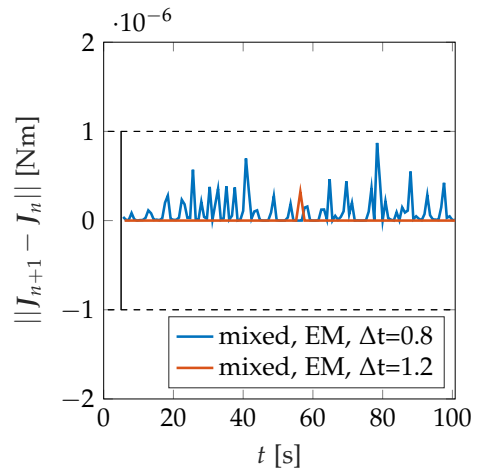


Figure 3.15: Mixed formulation: Incremental change of angular momentum.

# 4 EM schemes for quasi-incompressible elasticity in principal stretches<sup>1</sup>

In this chapter, we introduce a new algorithmic stress formula in its eigenvalue representation to model the transient behavior of hyperelastic bodies of Ogden type materials. Moreover, several numerical examples show the superior performance of the proposed formulation in terms of numerical robustness and stability.

## 4.1 Multiplicative and spectral decomposition

In this section a brief outline of the eigenvalue representation of second order tensors is given. Afterwards, a multiplicative decomposition as well as a spectral decomposition of second order tensors will be presented.

### 4.1.1 Eigenvalue representation

Assuming symmetry of  $A \in \mathbb{R}^{3 \times 3}$ , i.e.  $A = A^T$ , the eigenvalue problem is given by

$$A N_i^A = \lambda_i^A N_i^A, \quad (4.1)$$

---

<sup>1</sup> This chapter is based on [81].

where  $\lambda_i^A$ ,  $i = 1, 2, 3$  denotes the eigenvalues and  $N_i^A$  corresponding orthonormal eigenvectors of  $A$ . Note that in (4.1) no summation is applied. Accordingly, any symmetric tensor may be presented with the use of spectral decomposition, such that

$$A = \sum_{i=1}^3 \lambda_i^A N_i^A \otimes N_i^A. \quad (4.2)$$

The eigenvalues  $\lambda_i^A$  are solutions of the characteristic polynomial

$$\det(A) = (\lambda_i^A)^3 - I_1^A (\lambda_i^A)^2 + I_2^A \lambda_i^A - I_3^A = 0, \quad (4.3)$$

where  $I_1^A$ ,  $I_2^A$  and  $I_3^A$  are the principal invariants of  $A$  defined by

$$\begin{aligned} I_1^A &= I_1(A) = \text{tr}(A) = \lambda_1^A + \lambda_2^A + \lambda_3^A, \\ I_2^A &= I_2(A) = \text{tr}(\text{cof}(A)) = \lambda_1^A \lambda_2^A + \lambda_1^A \lambda_3^A + \lambda_2^A \lambda_3^A, \\ I_3^A &= I_3(A) = \det(A) = \lambda_1^A \lambda_2^A \lambda_3^A. \end{aligned} \quad (4.4)$$

Once the eigenvalues  $\lambda_i^A$  have been calculated, the eigenvectors  $N_i^A$  can be computed via (4.1). In the following distinct eigenvalues ( $\lambda_1^A \neq \lambda_2^A \neq \lambda_3^A \neq \lambda_1^A$ ) are assumed. In the case of two or three equal eigenvalues, a perturbation technique will be applied (see [155, 111, 112] and [119] in case of structure-preserving schemes) to avoid singularities during the numerical analysis. See Appendix C.3 for more information concerning the numerical implementation of the perturbation technique.

**Remark 4.1.** *Alternatively, spectral decomposition (4.2) can be written by using the closed-form expression of the eigenvector basis leading to the explicit expression*

$$A = \sum_{i=1}^3 (\lambda_i^A)^2 \frac{A - (\text{tr}(A) - \lambda_i^A) I + \det(A) (\lambda_i^A)^{-1} A^{-1}}{D_i^A}, \quad (4.5)$$

where

$$D_i^A = 2 (\lambda_i^A)^2 - \text{tr}(A) \lambda_i^A + \det(A) (\lambda_i^A)^{-1}. \quad (4.6)$$

*In contrast to (4.2), the closed form representation (4.5) does not need to compute the eigenvectors. For more background on the spectral decomposition we refer to [121, 164]. The numerical treatment of the closed-form expression (4.5) is discussed in [155, 111, 112]. See [114] for a detailed comparison of alternative approaches based either on (4.2) or the closed-form expression (4.5).*

## 4.1.2 Spectral decomposition

As a consequence of the polar decomposition of the deformation gradient tensor (see e.g. [68]) we obtain

$$\mathbf{F} = \mathbf{R} \mathbf{U}, \quad (4.7)$$

where the rotation tensor  $\mathbf{R} \in \text{SO}(3)$  and the right stretch tensor  $\mathbf{U} : \mathcal{B}_0 \rightarrow \mathbb{R}^{3 \times 3}$  have been introduced. Consequently, the right Cauchy-Green tensor is free of rigid-body rotations, e.g.

$$\mathbf{C} = (\mathbf{R} \mathbf{U})^\top (\mathbf{R} \mathbf{U}) = \mathbf{U}^2. \quad (4.8)$$

Moreover, the eigenvalues of  $\mathbf{U}$  are the principal stretches  $\lambda_i^{\mathbf{U}}$ , whereas the eigenvalues of  $\mathbf{C}$  corresponds to the squares of the principal stretches. That is,  $\lambda_i^{\mathbf{C}} = (\lambda_i^{\mathbf{U}})^2$ . The spectral decomposition of  $\mathbf{C}$  is given by

$$\mathbf{C} = \sum_{i=1}^3 (\lambda_i^{\mathbf{U}})^2 \mathbf{N}_i^{\mathbf{C}} \otimes \mathbf{N}_i^{\mathbf{C}} = \sum_{i=1}^3 \lambda_i^{\mathbf{C}} \mathbf{N}_i^{\mathbf{C}} \otimes \mathbf{N}_i^{\mathbf{C}}, \quad (4.9)$$

where we again assume distinct eigenvalues for  $\mathbf{C}$  (e.g.  $\lambda_1^{\mathbf{C}} \neq \lambda_2^{\mathbf{C}} \neq \lambda_3^{\mathbf{C}}$ ).

## 4.1.3 Multiplicative decomposition

Depending on the material law it might be useful to decouple the deformation into an isochoric and a volumetric part, see [43, 157]. For finite deformation problems, the multiplicative split of the deformation gradient into isochoric part  $\bar{\mathbf{F}}$  and volumetric part  $\hat{\mathbf{F}}$  yields

$$\mathbf{F} = \bar{\mathbf{F}} \hat{\mathbf{F}}. \quad (4.10)$$

Employing (2.20), gives

$$dv = \det(\mathbf{F}) dV = \det(\bar{\mathbf{F}}) \det(\hat{\mathbf{F}}) dV, \quad (4.11)$$

where

$$\det(\bar{\mathbf{F}}) = 1 \quad \text{and} \quad \det(\hat{\mathbf{F}}) = \det(\mathbf{F}), \quad (4.12)$$

respectively. Thus, (2.20), (4.10) and (4.12) leads to

$$\hat{\mathbf{F}} = \det(\mathbf{F})^{1/3} \mathbf{I}, \quad (4.13)$$

for the volumetric part and

$$\bar{\mathbf{F}} = \det(\mathbf{F})^{-1/3} \mathbf{F}, \quad (4.14)$$

for the isochoric part. Similarly, by construction of the right Cauchy-Green strain tensor (2.41), the multiplicative split of  $F$  leads to

$$C = \bar{C} \hat{C}, \quad (4.15)$$

where

$$\hat{C} = \det(C)^{1/3} I \quad \text{and} \quad \bar{C} = \det(C)^{-1/3} C, \quad (4.16)$$

denote the volumetric and isochoric parts, respectively. In accordance to (4.12) we obtain

$$dv^2 = \det(C) dV^2 = \det(\bar{C}) \det(\hat{C}) dV^2, \quad (4.17)$$

with

$$\det(\bar{C}) = 1 \quad \text{and} \quad \det(\hat{C}) = \det(C). \quad (4.18)$$

Furthermore, the principal invariants given in (4.4) can be applied to  $\bar{C}$  leading to

$$\begin{aligned} I_1^{\bar{C}} &= \text{tr}(\bar{C}) = \det(F)^{-2/3} I_1^C, \\ I_2^{\bar{C}} &= \text{tr}(\text{cof}(\bar{C})) = \det(F)^{-4/3} I_2^C, \\ I_3^{\bar{C}} &= \det(\bar{C}) = 1. \end{aligned} \quad (4.19)$$

In view of the multiplicative decomposition (4.10), we obtain for the isochoric stretches

$$\bar{\lambda}_i^U = \det(F)^{-1/3} \lambda_i^U \quad \text{and} \quad \bar{\lambda}_i^C = \det(F)^{-2/3} \lambda_i^C, \quad (4.20)$$

along with the condition of isochoric deformation

$$\bar{\lambda}_1^U \bar{\lambda}_2^U \bar{\lambda}_3^U = \bar{\lambda}_1^C \bar{\lambda}_2^C \bar{\lambda}_3^C = 1. \quad (4.21)$$

The modified eigenvalues  $\bar{\lambda}_i^U$  and  $\bar{\lambda}_i^C$  in (4.20) refer to the corresponding isochoric stretch tensor  $\bar{U} = \det(F)^{-1/3} U$  and the corresponding isochoric strain tensor  $\bar{C}$  as introduced in (4.16). The spectral decomposition of the isochoric part  $\bar{C}$  yields

$$\bar{C} = \sum_{i=1}^3 \bar{\lambda}_i^C N_i^C \otimes N_i^C, \quad (4.22)$$

assuming distinct eigenvalues  $\bar{\lambda}_1^C \neq \bar{\lambda}_2^C \neq \bar{\lambda}_3^C$ .

## 4.2 Constitutive equations for large strain elasticity

In this chapter we focus on hyper-elastic material behavior with a decoupled stored energy density function which fulfills the axiom of frame-indifference and is given

by

$$\tilde{\Psi}(\mathbf{C}) = \Psi(\mathbf{C}, \text{cof}(\mathbf{C}), \det(\mathbf{F})) = \Psi_{\text{iso}}(\bar{\mathbf{C}}, \text{cof}(\bar{\mathbf{C}})) + \Psi_{\text{vol}}(\det(\mathbf{F})), \quad (4.23)$$

In particular, we introduce the stored energy function as

$$\begin{aligned} \Psi(\mathbf{C}, \text{cof}(\mathbf{C}), \det(\mathbf{F})) &= \Psi_{\text{iso}}(\bar{\mathbf{C}}, \bar{\mathbf{G}}) + \Psi_{\text{vol}}(J) \\ &= \Psi_{\text{iso}}^{\mathbf{C}}(\bar{\mathbf{C}}) + \Psi_{\text{iso}}^{\mathbf{G}}(\bar{\mathbf{G}}) + \Psi_{\text{vol}}(J), \end{aligned} \quad (4.24)$$

where  $\bar{\mathbf{G}} : \mathcal{B}_0 \rightarrow \mathbb{R}^{3 \times 3}$  denotes the cofactor of the isochoric part of  $\mathbf{C}$ . That is,

$$\bar{\mathbf{G}} = \text{cof}(\bar{\mathbf{C}}) = \frac{1}{2} \bar{\mathbf{C}} * \bar{\mathbf{C}}. \quad (4.25)$$

Note that the stored energy function given in (4.24) is inspired by the concept of polyconvexity, see [7, 35]. To proof polyconvexity, the stored energy function must be defined in terms of  $\mathbf{F}$ ,  $\text{cof}(\mathbf{F})$  and  $\det(\mathbf{F})$ . Due to the multiplicative split, polyconvexity is only guaranteed under certain circumstances (see [62] for more information). Accordingly, the stored energy function in (4.24) is not polyconvex in general. The specific form (4.24) of the stored energy function turns out to be advantageous for the design of numerical methods, see [27] or Chapter 3.1. Next, the stress response tensor is derived from the decoupled stored energy function (4.24) by employing the tensor cross product operator introduced in Sec. 2.1. The directional derivative of the decoupled stored energy function  $\Psi(\bar{\mathbf{C}}, \bar{\mathbf{G}}, J)$  given in (4.24), yields

$$D\Psi[\delta\boldsymbol{\varphi}] = \partial_{\mathbf{C}}\Psi_{\text{iso}}^{\mathbf{C}} : DC[\delta\boldsymbol{\varphi}] + \partial_{\mathbf{G}}\Psi_{\text{iso}}^{\mathbf{G}} : DG[\delta\boldsymbol{\varphi}] + \partial_J\Psi_{\text{vol}}DJ[\delta\boldsymbol{\varphi}]. \quad (4.26)$$

With the use of the directional derivatives of the kinematic quantities (2.56), (2.57) and the directional derivative of  $J$  given by

$$DJ[\delta\boldsymbol{\varphi}] = \frac{1}{2} J^{-1} \mathbf{G} : DC[\delta\boldsymbol{\varphi}], \quad (4.27)$$

a new stress formula for the decoupled stress tensor is introduced as

$$\mathbf{S} = \mathbf{S}_{\text{iso}} + \mathbf{S}_{\text{vol}}, \quad (4.28)$$

where the purely isochoric contribution  $\mathbf{S}_{\text{iso}}$  is given by

$$\mathbf{S}_{\text{iso}} = 2(\partial_{\mathbf{C}}\Psi_{\text{iso}}^{\mathbf{C}} + \partial_{\mathbf{G}}\Psi_{\text{iso}}^{\mathbf{G}} * \mathbf{C}), \quad (4.29)$$

and for the purely volumetric part we obtain

$$\mathbf{S}_{\text{vol}} = \partial_J\Psi_{\text{vol}}J^{-1}\mathbf{G}. \quad (4.30)$$

In the equations above, use has been made of the relation in (2.59).

## 4.2.1 Hyperelastic model using principal stretches

For the given frame-indifferent stored energy function, we may express  $\Psi$  as a function of the principal stretches of  $\bar{\mathbf{C}}$  and  $\bar{\mathbf{G}}$  in the decoupled form as

$$\Psi(\mathbf{C}) = \Psi(\bar{\mathbf{C}}, \bar{\mathbf{G}}, J) = \Psi_{\text{iso}}(\bar{\lambda}_i^{\mathbf{C}}, \bar{\lambda}_i^{\mathbf{G}}) + \Psi_{\text{vol}}(J) = \Psi_{\text{iso}}^{\mathbf{C}}(\bar{\lambda}_i^{\mathbf{C}}) + \Psi_{\text{iso}}^{\mathbf{G}}(\bar{\lambda}_i^{\mathbf{G}}) + \Psi_{\text{vol}}(J), \quad (4.31)$$

for  $i = 1, 2, 3$  where the following relationships between the eigenvalues and eigenvectors of  $\mathbf{C}$  and  $\mathbf{G}$ , respectively are given by

$$\begin{aligned} \bar{\lambda}_1^{\mathbf{G}} &= \bar{\lambda}_2^{\mathbf{C}} \bar{\lambda}_3^{\mathbf{C}}, & \bar{\lambda}_2^{\mathbf{G}} &= \bar{\lambda}_1^{\mathbf{C}} \bar{\lambda}_3^{\mathbf{C}}, & \bar{\lambda}_3^{\mathbf{G}} &= \bar{\lambda}_1^{\mathbf{C}} \bar{\lambda}_2^{\mathbf{C}}, \\ \mathbf{N}_1^{\mathbf{G}} &= \mathbf{N}_1^{\mathbf{C}}, & \mathbf{N}_2^{\mathbf{G}} &= \mathbf{N}_2^{\mathbf{C}}, & \mathbf{N}_3^{\mathbf{G}} &= \mathbf{N}_3^{\mathbf{C}}, \end{aligned} \quad (4.32)$$

see Appendix C.1 for details.

Next, we express the second Piola-Kirchhoff stress tensor given in (4.28) in terms of the eigenvalues of the kinematic quantities. For the sake of clearness, we further split the isochoric part  $\mathbf{S}_{\text{iso}}$  into the part connected to  $\mathbf{C}$  and  $\mathbf{G}$ , respectively, as

$$\mathbf{S}_{\text{iso}}^{\mathbf{C}} = 2 \partial_{\mathbf{C}} \Psi_{\text{iso}}^{\mathbf{C}}(\bar{\lambda}_i^{\mathbf{C}}) \quad \text{and} \quad \mathbf{S}_{\text{iso}}^{\mathbf{G}} = 2 \partial_{\mathbf{G}} \Psi_{\text{iso}}^{\mathbf{G}}(\bar{\lambda}_i^{\mathbf{G}}) \ast \mathbf{C}. \quad (4.33)$$

In the following we need some important relationships to derive the stress tensor. The derivative of the eigenvalues  $\lambda_i^{\mathbf{C}}$  or  $\lambda_i^{\mathbf{G}}$  with respect to  $\mathbf{C}$  or  $\mathbf{G}$  yields

$$\frac{\partial \lambda_i^{\mathbf{C}}}{\partial \mathbf{C}} = \mathbf{N}_i^{\mathbf{C}} \otimes \mathbf{N}_i^{\mathbf{C}} \quad \text{or} \quad \frac{\partial \lambda_i^{\mathbf{G}}}{\partial \mathbf{G}} = \mathbf{N}_i^{\mathbf{G}} \otimes \mathbf{N}_i^{\mathbf{G}}, \quad (4.34)$$

see [155] or Appendix C.2.

Using the principal stretches for the isochoric stress response of  $\mathbf{S}_{\text{iso}}^{\mathbf{C}}$  we obtain

$$\mathbf{S}_{\text{iso}}^{\mathbf{C}} = 2 \sum_{i=1}^3 \frac{\partial \Psi_{\text{iso}}^{\mathbf{C}}(\bar{\lambda}_i^{\mathbf{C}})}{\partial \bar{\lambda}_i^{\mathbf{C}}} \frac{\partial \bar{\lambda}_i^{\mathbf{C}}}{\partial \lambda_j^{\mathbf{C}}} \frac{\partial \lambda_j^{\mathbf{C}}}{\partial \mathbf{C}} = \sum_{i=1}^3 (\mathbf{S}_{\text{iso}}^{\mathbf{C}})_i \mathbf{N}_i^{\mathbf{C}} \otimes \mathbf{N}_i^{\mathbf{C}}, \quad (4.35)$$

with the following relation

$$\frac{\partial \bar{\lambda}_i^{\mathbf{C}}}{\partial \lambda_j^{\mathbf{C}}} = \frac{\partial (\det(\mathbf{C})^{-1/3} \lambda_i^{\mathbf{C}})}{\partial \lambda_j^{\mathbf{C}}} = \det(\mathbf{C})^{-1/3} \left( \delta_{ij} - \frac{1}{3} \bar{\lambda}_i^{\mathbf{C}} (\bar{\lambda}_j^{\mathbf{C}})^{-1} \right). \quad (4.36)$$

Thus, the principal stresses of  $\mathbf{S}_{\text{iso}}^{\mathbf{C}}$  yield

$$(\mathbf{S}_{\text{iso}}^{\mathbf{C}})_i = 2 \frac{\partial \Psi_{\text{iso}}^{\mathbf{C}}}{\partial \bar{\lambda}_i^{\mathbf{C}}} \frac{\partial \bar{\lambda}_i^{\mathbf{C}}}{\partial \lambda_i^{\mathbf{C}}} = 2 \det(\mathbf{C})^{-1/3} \left( \frac{\partial \Psi_{\text{iso}}^{\mathbf{C}}}{\partial \bar{\lambda}_i^{\mathbf{C}}} - \frac{1}{3} \frac{\partial \Psi_{\text{iso}}^{\mathbf{C}}}{\partial \bar{\lambda}_i^{\mathbf{C}}} (\bar{\lambda}_i^{\mathbf{C}})^{-1} \bar{\lambda}_i^{\mathbf{C}} \right). \quad (4.37)$$

In the last equation summation over  $j$  applies. For the evaluation of the second isochoric stress response  $\mathbf{S}_{\text{iso}}^G$  the relation corresponding to (4.36) is provided as

$$\frac{\partial \bar{\lambda}_i^G}{\partial \lambda_j^G} = \frac{\partial (\det(\mathbf{G})^{-1/3} \lambda_i^G)}{\partial \lambda_j^G} = \det(\mathbf{G})^{-1/3} \left( \delta_{ij} - \frac{1}{3} \bar{\lambda}_i^G (\bar{\lambda}_j^G)^{-1} \right). \quad (4.38)$$

Then we obtain

$$\mathbf{S}_{\text{iso}}^G = 2 \sum_{i=1}^3 \frac{\partial \Psi_{\text{iso}}^G(\bar{\lambda}_i^G)}{\partial \bar{\lambda}_i^G} \frac{\partial \bar{\lambda}_i^G}{\partial \lambda_j^G} \frac{\partial \lambda_j^G}{\partial \mathbf{G}} * \mathbf{C} = \sum_{i=1}^3 (S_{\text{iso}}^G)_i (\mathbf{N}_i^G \otimes \mathbf{N}_i^G) * \mathbf{C}, \quad (4.39)$$

where the principal stresses are given by

$$(S_{\text{iso}}^G)_i = 2 \frac{\partial \Psi_{\text{iso}}^G}{\partial \bar{\lambda}_i^G} \frac{\partial \bar{\lambda}_i^G}{\partial \lambda_i^G} = 2 \det(\mathbf{G})^{-1/3} \left( \frac{\partial \Psi_{\text{iso}}^G}{\partial \bar{\lambda}_i^G} - \frac{1}{3} \frac{\partial \Psi_{\text{iso}}^G}{\partial \bar{\lambda}_i^G} (\bar{\lambda}_i^G)^{-1} \bar{\lambda}_i^G \right). \quad (4.40)$$

To summarize, the second Piola-Kirchhoff stress tensor can be written in the form

$$\mathbf{S} = \sum_{i=1}^3 (S_{\text{iso}}^C)_i \mathbf{N}_i^C \otimes \mathbf{N}_i^C + (S_{\text{iso}}^G)_i (\mathbf{N}_i^G \otimes \mathbf{N}_i^G) * \mathbf{C} + \mathbf{S}_{\text{vol}}. \quad (4.41)$$

## 4.2.2 Ogden-type material model

We are now in the position to deal with Ogden-type material models (see, for example, [107, 126, 35]) whose stored energy function assumes the specific form

$$\Psi(\bar{\lambda}_i^C, \bar{\lambda}_i^G, J) = \Psi_{\text{iso}}^C(\bar{\lambda}_i^C) + \Psi_{\text{iso}}^G(\bar{\lambda}_i^G) + \Psi_{\text{vol}}(J), \quad (4.42)$$

where

$$\Psi_{\text{iso}}^C(\bar{\lambda}_i^C) = \sum_{m=1}^M a_m \left( (\bar{\lambda}_1^C)^{\gamma_m/2} + (\bar{\lambda}_2^C)^{\gamma_m/2} + (\bar{\lambda}_3^C)^{\gamma_m/2} - 3 \right), \quad (4.43)$$

and

$$\Psi_{\text{iso}}^G(\bar{\lambda}_i^G) = \sum_{n=1}^N b_n \left( (\bar{\lambda}_1^G)^{\delta_n/2} + (\bar{\lambda}_2^G)^{\delta_n/2} + (\bar{\lambda}_3^G)^{\delta_n/2} - 3 \right). \quad (4.44)$$

A possible choice for the convex volumetric term  $\Psi_{\text{vol}}(J)$  is given by

$$\Psi_{\text{vol}}(J) = c d^{-2} (d \ln(J) + J^{-d} - 1), \quad (4.45)$$

see, for example [125]. In (4.45),  $c$  represents the bulk modulus and  $d$  an additional material coefficient. Moreover, the stored energy functions yields a stress- and energy-free response for  $\bar{\lambda}_i^C, \bar{\lambda}_i^G = 1$  for  $i = 1, 2, 3$  and  $J = 1$ . Various alternative volumetric strain energy functions and their investigations in terms of convexity and physical behavior are given in [62].

**Example (Mooney-Rivlin material):** For the particular case of  $N = 1$ ,  $M = 1$  and  $\gamma_1 = 2$ ,  $\delta_1 = 2$  the stored energy function (4.42) leads to the Mooney-Rivlin material whose stored energy can be written as

$$\Psi^{MR}(\bar{\lambda}_i^C, \bar{\lambda}_i^G, J) = \Psi_{\text{iso}}^C(\bar{\lambda}_i^C) + \Psi_{\text{iso}}^G(\bar{\lambda}_i^G) + \Psi_{\text{vol}}(J), \quad (4.46)$$

where

$$\Psi_{\text{iso}}^C(\bar{\lambda}_i^C) = a_1 ((\bar{\lambda}_1^C) + (\bar{\lambda}_2^C) + (\bar{\lambda}_3^C)) = a_1 I_1^{\bar{C}}, \quad (4.47)$$

and

$$\Psi_{\text{iso}}^G(\bar{\lambda}_i^G) = b_1 ((\bar{\lambda}_1^G) + (\bar{\lambda}_2^G) + (\bar{\lambda}_3^G)) = b_1 ((\bar{\lambda}_2^C \bar{\lambda}_3^C) + (\bar{\lambda}_1^C \bar{\lambda}_3^C) + (\bar{\lambda}_1^C \bar{\lambda}_2^C)) = b_1 I_2^{\bar{C}}. \quad (4.48)$$

Note that in the above equation use has been made of (4.32).

## 4.3 Variational formulation

In this section we present two possible variational frameworks suitable for large strain elasticity. While the first one is a displacement based formulation, we also introduce a Hu-Washizu type mixed formulation. Afterwards we extend both formulations to the dynamic regime. Eventually, we outline the balance laws for angular momentum and energy pertaining to the hyperelastic body under consideration.

### 4.3.1 Displacement based variational formulation

We start our developments from the total potential energy of the elastic body under consideration. In this chapter the decoupled representation of the internal potential energy yields

$$\hat{\Pi}^{\text{int}}(\varphi) = \int_{\bar{B}_0} \Psi(\bar{\lambda}_i^C, \bar{\lambda}_i^G, J) dV = \int_{\bar{B}_0} \Psi_{\text{iso}}(\bar{\lambda}_i^C, \bar{\lambda}_i^G) + \Psi_{\text{vol}}(J) dV. \quad (4.49)$$

Variation of the total potential energy with respect to the deformation along with the principle of stationary potential energy (see, e.g. [170]) and the directional derivatives

of the kinematic relations provided in (2.56), (2.57) and (4.27), yields the variational equation

$$\begin{aligned}
 D\hat{\Pi}[\delta\boldsymbol{\varphi}] &= \int_{\mathcal{B}_0} D\Psi[\delta\boldsymbol{\varphi}] \, dV + D\Pi_m^{\text{ext}}[\delta\boldsymbol{\varphi}] \\
 &= \int_{\mathcal{B}_0} \partial_{\mathbf{C}}\Psi_{\text{iso}}^{\mathbf{C}} : DC[\delta\boldsymbol{\varphi}] + \partial_{\mathbf{G}}\Psi_{\text{iso}}^{\mathbf{G}} : DG[\delta\boldsymbol{\varphi}] + \partial_J\Psi_{\text{vol}} DJ[\delta\boldsymbol{\varphi}] \, dV + D\Pi_m^{\text{ext}}[\delta\boldsymbol{\varphi}] \\
 &= \int_{\mathcal{B}_0} (\mathbf{S}_{\text{iso}}^{\mathbf{C}} + \mathbf{S}_{\text{iso}}^{\mathbf{G}} + \mathbf{S}_{\text{vol}}) : \frac{1}{2}DC[\delta\boldsymbol{\varphi}] \, dV + D\Pi_m^{\text{ext}}[\delta\boldsymbol{\varphi}] = 0,
 \end{aligned} \tag{4.50}$$

where the external potential is given in (2.25). The equations above have to hold for admissible variations  $\delta\boldsymbol{\varphi} \in \mathcal{V}$ .

### 4.3.2 Mixed formulation for quasi-incompressibility

Next, we introduce a Hu-Washizu type three field functional in the spirit of [157, 155]. Thus we define the functional

$$\Pi(\boldsymbol{\varphi}, p, \tau) = \int_{\mathcal{B}_0} \Psi_{\text{iso}}(\bar{\lambda}_i^{\mathbf{C}}, \bar{\lambda}_i^{\mathbf{G}}) + \Psi_{\text{vol}}(\tau) + p(J - \tau) \, dV + \Pi_m^{\text{ext}}(\boldsymbol{\varphi}), \tag{4.51}$$

where the additional unknowns are the hydrostatic pressure  $p \in \mathbb{V}_p$  and the volumetric dilatation  $\tau \in \mathbb{V}_\tau$ . In this connection, we introduce the sets

$$\begin{aligned}
 \mathbb{V}_\tau &= \{ \tau : \mathcal{B}_0 \rightarrow \mathbb{R} \mid \text{for } \tau \in \mathbb{L}_2(\mathcal{B}_0) \}, \\
 \mathbb{V}_p &= \{ p : \mathcal{B}_0 \rightarrow \mathbb{R} \mid \text{for } p \in \mathbb{L}_2(\mathcal{B}_0) \}.
 \end{aligned} \tag{4.52}$$

Note that  $p$  plays the role of a Lagrange multiplier to enforce the additional constraint  $\tau = J$ . The external potential energy is the same as in the pure displacement formulation and has already been introduced in (2.25). We now impose the stationary conditions on the functional with respect to all field variables, to obtain the Euler-Lagrange equations as

$$\begin{aligned}
 D_{\boldsymbol{\varphi}}\Pi[\delta\boldsymbol{\varphi}] &= \int_{\mathcal{B}_0} \left( \partial_{\mathbf{C}}\Psi_{\text{iso}}^{\mathbf{C}} + \partial_{\mathbf{G}}\Psi_{\text{iso}}^{\mathbf{G}} \star \mathbf{C} + \frac{1}{2}pJ^{-1}\mathbf{G} \right) : DC[\delta\boldsymbol{\varphi}] \, dV + D\Pi_m^{\text{ext}}[\delta\boldsymbol{\varphi}] = 0, \\
 D_p\Pi[\delta p] &= \int_{\mathcal{B}_0} \delta p (J - \tau) \, dV = 0, \\
 D_\tau\Pi[\delta\tau] &= \int_{\mathcal{B}_0} \delta\tau (\partial_\tau\Psi_{\text{vol}} - p) \, dV = 0.
 \end{aligned} \tag{4.53}$$

The above equations have to hold for arbitrary  $\delta\boldsymbol{\varphi} \in \mathcal{V}$ ,  $\delta\boldsymbol{\tau} \in \mathbb{W}_\tau$  and  $\delta p \in \mathbb{W}_p$ . Note that (4.53)<sub>1</sub> contains the two stress-type second-order tensors defined previously in (4.33). Moreover, (4.53)<sub>2</sub> recovers the constraint  $J - \tau = 0$  related to the volumetric dilatation and (4.53)<sub>3</sub> yields a constitutive compatibility condition.

### 4.3.3 Extension to elastodynamics

Next we extend the proposed formulation to the elasto-dynamic regime. The extension of variational formulation (4.53) to the dynamic regime follows the lines of Sec. 3.1.1 and is given by

$$\begin{aligned}
 \int_{\tilde{B}_0} \delta \mathbf{V} \cdot (\dot{\boldsymbol{\varphi}} - \mathbf{V}) \rho_0 \, dV &= 0, \\
 \int_{\tilde{B}_0} \left( \delta \boldsymbol{\varphi} \cdot \rho_0 \dot{\mathbf{V}} + \left( \partial_{\mathbf{C}} \Psi_{\text{iso}} + \partial_{\mathbf{G}} \Psi_{\text{iso}} \star \mathbf{C} + \frac{1}{2} p J^{-1} \mathbf{G} \right) : \text{DC}[\delta \boldsymbol{\varphi}] \right) dV + \text{D}\Pi_m^{\text{ext}}[\delta \boldsymbol{\varphi}] &= 0, \\
 \int_{\tilde{B}_0} \delta p (J - \tau) \, dV &= 0, \\
 \int_{\tilde{B}_0} \delta \boldsymbol{\tau} (\partial_\tau \Psi_{\text{vol}} - p) \, dV &= 0.
 \end{aligned} \tag{4.54}$$

Note that the variational equations (4.54)<sub>3</sub>-(4.54)<sub>4</sub> retain their form. The above equations have to hold for arbitrary  $\{\delta \mathbf{V}, \delta \boldsymbol{\varphi}, \delta p, \delta \boldsymbol{\tau}\} \in \mathcal{V} \times \mathcal{V} \times \mathbb{W}_p \times \mathbb{W}_\tau$  and are supplemented by prescribed initial values  $\boldsymbol{\varphi}_0 \in \mathcal{V}$  and  $\mathbf{V}_0 \in \mathcal{V}$  at time  $t = 0$ . Consistent initial values for the mixed fields,  $\{p_0, \tau_0\}$  can be calculated with the use of (4.54)<sub>3</sub> and (4.54)<sub>4</sub>.

**Remark 4.2.** *Time differentiation of J yields*

$$j = \frac{1}{2} J^{-1} \mathbf{G} : \dot{\mathbf{C}}, \tag{4.55}$$

where the properties of the tensor cross product have been taken into account. Time differentiation of  $\mathbf{C}$ ,  $\mathbf{G}$  have been introduced in (3.15)<sub>1</sub> and (3.15)<sub>2</sub>.

### 4.3.4 Balance laws

In this section we consider the balance laws for linear momentum, angular momentum and energy. We start from the variational equations of the mixed formulation.

#### 4.3.4.1 Balance of linear momentum

For verification of the balance of total linear momentum the admissible variations in (4.54) are  $\delta \mathbf{V} = \mathbf{0}$  and  $\delta \boldsymbol{\varphi} = \boldsymbol{\zeta}$  where  $\boldsymbol{\zeta} \in \mathbb{R}^3$  is arbitrary but constant. This yields

$$\boldsymbol{\zeta} \cdot \left( \frac{d}{dt} \mathbf{L} - \mathbf{F}^{\text{ext}} \right) = 0, \quad (4.56)$$

where the total linear momentum and the total external mechanical loads have been introduced in (3.19) and (3.20), respectively. Therefore for vanishing external mechanical loads the total linear momentum is a constant of motion of the continuous system.

#### 4.3.4.2 Balance of angular momentum

Following the procedure of Sec. 3.1.2.2, we choose admissible variations  $\delta \boldsymbol{\varphi} = \boldsymbol{\zeta} \times \boldsymbol{\varphi}$  and  $\delta \mathbf{V} = \boldsymbol{\zeta} \times \dot{\boldsymbol{\varphi}}$  with constant and arbitrary  $\boldsymbol{\zeta} \in \mathbb{R}^3$  and  $DF[\delta \boldsymbol{\varphi}] = \hat{\boldsymbol{\zeta}} \mathbf{F}$ . From (4.54)<sub>1</sub> and (4.54)<sub>2</sub> we get

$$\begin{aligned} \int_{\mathcal{B}_0} (\boldsymbol{\zeta} \times \dot{\boldsymbol{\varphi}}) \cdot \mathbf{V} \rho_0 \, dV &= 0, \\ \int_{\mathcal{B}_0} \left( \boldsymbol{\zeta} \times \boldsymbol{\varphi} \cdot \rho_0 \dot{\mathbf{V}} + \left( \partial_{\mathbf{C}} \Psi_{\text{iso}}^{\mathbf{C}} + \partial_{\mathbf{G}} \Psi_{\text{iso}}^{\mathbf{G}} \star \mathbf{C} + \frac{1}{2} p J^{-1} \mathbf{G} \right) : \text{DC}[\boldsymbol{\zeta} \times \boldsymbol{\varphi}] \right) dV & \\ + \text{DI}\Pi_m^{\text{ext}}[\boldsymbol{\zeta} \times \boldsymbol{\varphi}] &= 0. \end{aligned} \quad (4.57)$$

Since the inner bracket term in (4.57)<sub>2</sub> is symmetric, we obtain

$$\boldsymbol{\zeta} \cdot \left( \frac{d}{dt} \mathbf{J} - \mathbf{M}^{\text{ext}} \right) = 0, \quad (4.58)$$

compare (3.21)-(3.26). Therefore, the components of the angular momentum,  $J^\zeta = \boldsymbol{\zeta} \cdot \mathbf{J}$  are conserved along solutions of equations of motions when the external torque about the corresponding axes,  $\boldsymbol{\zeta} \cdot \mathbf{M}^{\text{ext}}$ , vanishes.

#### 4.3.4.3 Balance of energy

Next we focus on the balance law for total energy. Again, we start from the variational equations (4.54) and choose admissible variations  $\delta \boldsymbol{\varphi} = \dot{\boldsymbol{\varphi}} \in \mathcal{V}$ ,  $\delta \mathbf{V} = \dot{\mathbf{V}} \in \mathcal{V}$  along

with  $\delta p = \dot{p} \in \mathbb{V}_p$  and  $\delta \tau = \dot{\tau} \in \mathbb{V}_\tau$ . With the definition of the kinetic energy of the continuum body (3.28) we get from (4.54)<sub>1</sub>

$$\int_{\mathcal{B}_0} \dot{\boldsymbol{\varphi}} \cdot \dot{\mathbf{V}} \rho_0 \, dV = \int_{\mathcal{B}_0} \mathbf{V} \cdot \dot{\mathbf{V}} \rho_0 \, dV = \frac{d}{dt} \left( \frac{1}{2} \int_{\mathcal{B}_0} \mathbf{V} \cdot \mathbf{V} \rho_0 \, dV \right) = \dot{T}. \quad (4.59)$$

With (4.54)<sub>2</sub>, (4.55) and the admissible variations, (4.54)<sub>3</sub> and (4.54)<sub>4</sub>, we obtain

$$\begin{aligned} & \int_{\mathcal{B}_0} \dot{\boldsymbol{\varphi}} \cdot \dot{\mathbf{V}} \rho_0 \, dV + \int_{\mathcal{B}_0} \left( \partial_{\mathbf{C}} \Psi_{\text{iso}}^{\mathbf{C}} + \partial_{\mathbf{G}} \Psi_{\text{iso}}^{\mathbf{G}} \star \mathbf{C} + \frac{1}{2} p J^{-1} \mathbf{G} \right) : \dot{\mathbf{C}} \, dV + \dot{\Pi}_m^{\text{ext}}(\boldsymbol{\varphi}) \\ &= \int_{\mathcal{B}_0} \dot{\boldsymbol{\varphi}} \cdot \dot{\mathbf{V}} \rho_0 \, dV + \int_{\mathcal{B}_0} \partial_{\mathbf{C}} \Psi_{\text{iso}}^{\mathbf{C}} : \dot{\mathbf{C}} + \partial_{\mathbf{G}} \Psi_{\text{iso}}^{\mathbf{G}} \star \mathbf{C} : \dot{\mathbf{C}} + \frac{1}{2} p J^{-1} \mathbf{G} : \dot{\mathbf{C}} \, dV + \dot{\Pi}_m^{\text{ext}}(\boldsymbol{\varphi}) \\ &= \int_{\mathcal{B}_0} \dot{\boldsymbol{\varphi}} \cdot \dot{\mathbf{V}} \rho_0 \, dV + \int_{\mathcal{B}_0} \partial_{\mathbf{C}} \Psi_{\text{iso}}^{\mathbf{C}} : \dot{\mathbf{C}} + \partial_{\mathbf{G}} \Psi_{\text{iso}}^{\mathbf{G}} : \dot{\mathbf{G}} + \partial_J \Psi_{\text{vol}} : \dot{J} \, dV + \dot{\Pi}_m^{\text{ext}}(\boldsymbol{\varphi}). \end{aligned} \quad (4.60)$$

By definition of kinetic energy (3.28), internal energy (4.49), total potential energy (2.26) and external power (3.31) we get the desired result as

$$\frac{d}{dt} E = \frac{d}{dt} (T + \Pi^{\text{int}}) = \dot{T} + \dot{\Pi}^{\text{int}} = P^{\text{ext}}. \quad (4.61)$$

Since dead loads have been assumed from the outset, balance law (4.61) corresponds to the conservation of the total energy along solutions of equations of motions defined by

$$E = T + \Pi. \quad (4.62)$$

## 4.4 Discretization in time

In this section we focus on the design of a structure-preserving time-stepping scheme for the underlying formulations. In particular, we introduce the algorithm for the mixed formulation. The time discretization of the displacement formulation follows from that of the mixed formulation in a straightforward way.

The aim of this section is to define an implicit one-step time integrator that determines  $\{\mathbf{V}_{n+1}, \boldsymbol{\varphi}_{n+1}, p_{n+1}, \tau_{n+1}\} \in \mathcal{V} \times \mathcal{Q} \times \mathbb{V}_p \times \mathbb{V}_\tau$  on time node  $t_{n+1}$  from the given approximations  $\{\mathbf{V}_n, \boldsymbol{\varphi}_n, p_n, \tau_n\} \in \mathcal{V} \times \mathcal{Q} \times \mathbb{V}_p \times \mathbb{V}_\tau$  on time node  $t_n$ . This implies, that the constraint in (4.54)<sub>3</sub> is fulfilled at time-node  $t_n$ . The time-discrete version of

the variational equations (4.54) is proposed as

$$\begin{aligned}
\int_{\tilde{B}_0} \delta \mathbf{V} \cdot \frac{1}{\Delta t} (\boldsymbol{\varphi}_{n+1} - \boldsymbol{\varphi}_n) \rho_0 \, dV &= \int_{\tilde{B}_0} \delta \mathbf{V} \cdot \mathbf{V}_{n+\frac{1}{2}} \rho_0 \, dV, \\
\int_{\tilde{B}_0} \delta \boldsymbol{\varphi} \cdot \frac{1}{\Delta t} (\mathbf{V}_{n+1} - \mathbf{V}_n) \rho_0 \, dV &= \\
- \int_{\tilde{B}_0} \left( \mathbf{D}_C \Psi_{\text{iso}}^C + \mathbf{D}_G \Psi_{\text{iso}}^G * \mathbf{C}_{\text{alg}} + \frac{1}{2} p_{n+1} J_{\text{alg}}^{-1} \mathbf{G}_{\text{alg}} \right) : \mathbf{DC}[\delta \boldsymbol{\varphi}]|_{n+\frac{1}{2}} \, dV &- \text{D}\Pi_m^{\text{ext}}[\delta \boldsymbol{\varphi}]|_{n+\frac{1}{2}}, \\
\int_{\tilde{B}_0} \delta p (J_{n+1} - \tau_{n+1}) \, dV &= 0, \\
\int_{\tilde{B}_0} \delta \tau (\mathbf{D}_\tau \Psi_{\text{vol}} - p_{n+1}) \, dV &= 0,
\end{aligned} \tag{4.63}$$

for arbitrary  $\{\delta \mathbf{V}, \delta \boldsymbol{\varphi}\} \in \{\mathcal{V}, \mathcal{V}\}$  and arbitrary  $\delta p \in \mathbb{V}_p$ ,  $\delta \tau \in \mathbb{V}_\tau$ . The constraints in (4.63)<sub>3</sub> and (4.63)<sub>4</sub> are evaluated in their endpoint configurations, see [15] or Sec. 3.1. In the mid-point type (MP) integration scheme, the time discrete versions of the kinematic quantities can be replaced by  $\mathbf{C}_{\text{alg}} = \mathbf{C}(\boldsymbol{\varphi}_{n+\frac{1}{2}})$ ,  $\mathbf{G}_{\text{alg}} = \mathbf{G}(\boldsymbol{\varphi}_{n+\frac{1}{2}})$  and  $J_{\text{alg}} = J(\boldsymbol{\varphi}_{n+\frac{1}{2}})$ . Then the time discrete versions of the partial derivatives assume the form

$$\begin{aligned}
\mathbf{D}_C \Psi_{\text{iso}}^C &= \partial_C \Psi_{\text{iso}}^C(\bar{\lambda}_i^C(\mathbf{C}(\boldsymbol{\varphi}_{n+\frac{1}{2}}))), \\
\mathbf{D}_G \Psi_{\text{iso}}^G &= \partial_G \Psi_{\text{iso}}^G(\bar{\lambda}_i^G(\mathbf{G}(\boldsymbol{\varphi}_{n+\frac{1}{2}}))), \\
\mathbf{D}_\tau \Psi_{\text{vol}} &= \partial_\tau \Psi_{\text{vol}}(\tau_{n+\frac{1}{2}}),
\end{aligned} \tag{4.64}$$

where details about the numerical implementation of the time-discrete eigenvalues are provided in Appendix C.3.

### 4.4.1 Structure-preserving integration scheme

Next, a structure-preserving integration scheme is introduced, which satisfies the balance laws outlined in Sec. 4.3.4. Herein we use the semi-discrete variational equations (4.63) as a basis. The algorithmic expressions of  $\mathbf{C}$  and  $\mathbf{G}$  for a structure preserving integration scheme have already been introduced in 3.3.1. The algorithmic version of  $J$  is defined as

$$J_{\text{alg}} = \frac{1}{2} (J_n + J_{n+1}). \tag{4.65}$$

Note that in general the MP type approximations  $\mathbf{C}(\boldsymbol{\varphi}_{n+\frac{1}{2}})$ ,  $\mathbf{G}(\boldsymbol{\varphi}_{n+\frac{1}{2}})$  and  $J(\boldsymbol{\varphi}_{n+\frac{1}{2}})$  do not coincide with the algorithmic expressions in (3.63), (3.64) and (4.65), see e.g. (3.68) and (3.69). Next we focus on the approximation of the stress-type quantities in (4.63)<sub>2</sub>. In particular, the partial derivatives  $\{\partial_{\mathbf{C}}\Psi_{\text{iso}}^{\mathbf{C}}, \partial_{\mathbf{G}}\Psi_{\text{iso}}^{\mathbf{G}}, \partial_{\tau}\Psi_{\text{vol}}\}$  in (4.53) are replaced by time-discrete derivatives in the sense of [52] denoted by  $\{\mathbf{D}_{\mathbf{C}}\Psi_{\text{iso}}^{\mathbf{C}}, \mathbf{D}_{\mathbf{G}}\Psi_{\text{iso}}^{\mathbf{G}}, \mathbf{D}_{\tau}\Psi_{\text{vol}}\}$ . In the present case the discrete derivatives in question are given by

$$\begin{aligned} \mathbf{D}_{\mathbf{C}}\Psi_{\text{iso}}^{\mathbf{C}} &= \partial_{\mathbf{C}}\Psi_{\text{iso}}^{\mathbf{C}}(\bar{\lambda}_i^{\mathbf{C}}(\mathbf{C}_{n+\frac{1}{2}})) + \frac{(\Psi_{\text{iso}}^{\mathbf{C}}((\bar{\lambda}_i^{\mathbf{C}})_{n+1}) - \Psi_{\text{iso}}^{\mathbf{C}}((\bar{\lambda}_i^{\mathbf{C}})_n)) \Delta \mathbf{C}}{\Delta \mathbf{C} : \Delta \mathbf{C}} \\ &\quad - \frac{\partial_{\mathbf{C}}\Psi_{\text{iso}}^{\mathbf{C}}(\bar{\lambda}_i^{\mathbf{C}}(\mathbf{C}_{n+\frac{1}{2}})) : \Delta \mathbf{C}}{\Delta \mathbf{C} : \Delta \mathbf{C}} \Delta \mathbf{C}, \\ \mathbf{D}_{\mathbf{G}}\Psi_{\text{iso}}^{\mathbf{G}} &= \partial_{\mathbf{G}}\Psi_{\text{iso}}^{\mathbf{G}}(\bar{\lambda}_i^{\mathbf{G}}(\mathbf{G}_{n+\frac{1}{2}})) + \frac{(\Psi_{\text{iso}}^{\mathbf{G}}((\bar{\lambda}_i^{\mathbf{G}})_{n+1}) - \Psi_{\text{iso}}^{\mathbf{G}}((\bar{\lambda}_i^{\mathbf{G}})_n)) \Delta \mathbf{G}}{\Delta \mathbf{G} : \Delta \mathbf{G}} \\ &\quad - \frac{\partial_{\mathbf{G}}\Psi_{\text{iso}}^{\mathbf{G}}(\bar{\lambda}_i^{\mathbf{G}}(\mathbf{G}_{n+\frac{1}{2}})) : \Delta \mathbf{G}}{\Delta \mathbf{G} : \Delta \mathbf{G}} \Delta \mathbf{G}, \\ \mathbf{D}_{\tau}\Psi_{\text{vol}} &= \frac{\Psi_{\text{vol}}(\tau_{n+1}) - \Psi_{\text{vol}}(\tau_n)}{\tau_{n+1} - \tau_n}. \end{aligned} \tag{4.66}$$

where  $\Delta \mathbf{C} = \mathbf{C}_{n+1} - \mathbf{C}_n$ ,  $\Delta \mathbf{G} = \mathbf{G}_{n+1} - \mathbf{G}_n$  and  $\Delta \tau = \tau_{n+1} - \tau_n$ , respectively. Similarly to the kinematic quantities, we obtain  $(\bar{\lambda}_i^{\mathbf{A}})_n = \bar{\lambda}_i^{\mathbf{A}}(\mathbf{A}(\boldsymbol{\varphi}_n))$  and  $(\bar{\lambda}_i^{\mathbf{A}})_{n+1} = \bar{\lambda}_i^{\mathbf{A}}(\mathbf{A}(\boldsymbol{\varphi}_{n+1}))$  where  $\mathbf{A}$  stands for  $\mathbf{C}$  and  $\mathbf{G}$ , respectively. Details concerning the numerical implementation of the time-discrete eigenvalues are provided in Appendix C.3. Note that due to the scalar field variable  $\tau$ , (4.66)<sub>3</sub> collapses to the Greenspan formula introduced in (3.41), see [55]. In case of the limits  $\|\mathbf{C}_{n+1} - \mathbf{C}_n\| \rightarrow 0$ ,  $\|\mathbf{G}_{n+1} - \mathbf{G}_n\| \rightarrow 0$  and  $|\tau_{n+1} - \tau_n| \rightarrow 0$  the discrete gradients in (4.66) have to be replaced by the MP type approximation as given in (4.64). Using the discrete derivatives in (4.66), it can be easily verified that the directionality property

$$\begin{aligned} \mathbf{D}_{\mathbf{C}}\Psi_{\text{iso}}^{\mathbf{C}} : (\mathbf{C}_{n+1} - \mathbf{C}_n) + \mathbf{D}_{\mathbf{G}}\Psi_{\text{iso}}^{\mathbf{G}} : (\mathbf{G}_{n+1} - \mathbf{G}_n) + \mathbf{D}_{\tau}\Psi_{\text{vol}}(\tau_{n+1} - \tau_n) \\ = \Psi_{\text{iso}}^{\mathbf{C}}((\bar{\lambda}_i^{\mathbf{C}})_{n+1}) + \Psi_{\text{iso}}^{\mathbf{G}}((\bar{\lambda}_i^{\mathbf{G}})_{n+1}) - (\Psi_{\text{iso}}^{\mathbf{C}}((\bar{\lambda}_i^{\mathbf{C}})_n) + \Psi_{\text{iso}}^{\mathbf{G}}((\bar{\lambda}_i^{\mathbf{G}})_n)) \\ \quad + \Psi_{\text{vol}}(\tau_{n+1}) - \Psi_{\text{vol}}(\tau_n) \\ = \Psi((\bar{\lambda}_i^{\mathbf{C}})_{n+1}, (\bar{\lambda}_i^{\mathbf{G}})_{n+1}, \tau_{n+1}) - \Psi((\bar{\lambda}_i^{\mathbf{C}})_n, (\bar{\lambda}_i^{\mathbf{G}})_n, \tau_n), \end{aligned} \tag{4.67}$$

holds. The first term of the integrand on the right hand side of (4.63)<sub>2</sub> coincides with the second Piola-Kirchhoff stress in the time-discrete setting, c.f. (4.28). In this chapter, the algorithmic stress tensor, denoted as  $\mathbf{S}_{\text{alg}}$  can be expressed by the use of (3.63) and (3.64) as

$$\mathbf{S}_{\text{alg}} = 2 \left( \mathbf{D}_{\mathbf{C}}\Psi_{\text{iso}}^{\mathbf{C}} + \mathbf{D}_{\mathbf{G}}\Psi_{\text{iso}}^{\mathbf{G}} \star \mathbf{C}_{\text{alg}} + p_{n+1} J_{\text{alg}}^{-1} \frac{1}{2} \mathbf{G}_{\text{alg}} \right), \tag{4.68}$$

and shares the same time-discrete version of the kinematic quantities as the second Piola-Kirchhoff stress resulting from the mixed formulation (3.66).

## 4.4.2 Semi-discrete balance laws

In this section, we show that the semi-discrete mixed formulation inherits the balance laws of the continuous formulation (see Sec. 4.3.4) independent of the time-step size.

### 4.4.2.1 Discrete balance of linear momentum

Following the procedure in Sec. 4.3.4.1 for the verification of the balance of total linear momentum we assume that  $\delta\boldsymbol{\varphi} = \boldsymbol{\zeta}$  and  $\delta\mathbf{V} = \mathbf{0}$  are admissible variations, where  $\boldsymbol{\zeta} \in \mathbb{R}^3$  is arbitrary but constant. Then (4.63)<sub>2</sub> yields

$$\boldsymbol{\zeta} \cdot \left( \frac{1}{\Delta t} (\mathbf{L}_{n+1} - \mathbf{L}_n) - \mathbf{F}^{\text{ext}} \right) = 0. \quad (4.69)$$

Therefore for vanishing external mechanical loads the total discrete linear momentum is a constant of motion of the semi-discrete system.

### 4.4.2.2 Discrete balance of angular momentum

With regard to the developments from Sec. 4.3.4.2, we choose as admissible variations  $\delta\boldsymbol{\varphi} = \boldsymbol{\zeta} \times \boldsymbol{\varphi}_{n+\frac{1}{2}}$  and  $\delta\mathbf{V} = \boldsymbol{\zeta} \times (\boldsymbol{\varphi}_{n+1} - \boldsymbol{\varphi}_n)$ , where  $\boldsymbol{\zeta}$  again is a constant vector. Then the time-discrete variational formulation (4.63) yields

$$\begin{aligned} \int_{\mathcal{B}_0} \boldsymbol{\zeta} \times (\boldsymbol{\varphi}_{n+1} - \boldsymbol{\varphi}_n) \cdot \mathbf{V}_{n+\frac{1}{2}} \rho_0 \, dV &= 0, \\ \int_{\mathcal{B}_0} \boldsymbol{\zeta} \times \boldsymbol{\varphi}_{n+\frac{1}{2}} \cdot (\mathbf{V}_{n+1} - \mathbf{V}_n) \rho_0 \, dV &= - \int_{\mathcal{B}_0} \mathbf{S}_{alg} : \frac{1}{2} \text{DC}[\boldsymbol{\zeta} \times \boldsymbol{\varphi}_{n+\frac{1}{2}}] \Big|_{n+\frac{1}{2}} \, dV \\ &\quad - \text{D}\Pi_m^{\text{ext}}[\boldsymbol{\zeta} \times \boldsymbol{\varphi}_{n+\frac{1}{2}}]. \end{aligned} \quad (4.70)$$

Similarly to  $\boldsymbol{\Lambda}^{\mathcal{C}}$  in (3.52), the algorithmic stress tensor  $\mathbf{S}_{alg}$  in (4.70)<sub>2</sub> is symmetric and therefore, we obtain

$$\boldsymbol{\zeta} \cdot \left( \frac{1}{\Delta t} (\mathbf{J}_{n+1} - \mathbf{J}_n) - \mathbf{M}^{\text{ext}} \Big|_{n+\frac{1}{2}} \right) = 0, \quad (4.71)$$

see (3.53)-(3.56). The equation above corresponds to the balance of angular momentum with respect to the  $\boldsymbol{\zeta}$ -axis.

### 4.4.2.3 Discrete balance of energy

To proof the balance of energy, we follow the procedure from Sec. 4.3.4.3 by choosing admissible variations of the form:  $\delta V = V_{n+1} - V_n \in \mathcal{V}$  and  $\delta \boldsymbol{\varphi} = \boldsymbol{\varphi}_{n+1} - \boldsymbol{\varphi}_n \in \mathcal{V}$ . As shown in (3.57), we obtain for (4.63)<sub>1</sub> the following result:

$$\int_{\mathcal{B}_0} (\mathbf{V}_{n+1} - \mathbf{V}_n) \cdot \frac{1}{\Delta t} (\boldsymbol{\varphi}_{n+1} - \boldsymbol{\varphi}_n) \rho_0 \, dV = T_{n+1} - T_n. \quad (4.72)$$

Accordingly, taking into account the relationships

$$\begin{aligned} \text{DC}[\boldsymbol{\varphi}_{n+1} - \boldsymbol{\varphi}_n] \Big|_{n+\frac{1}{2}} &= \mathbf{C}_{n+1} - \mathbf{C}_n, \\ \mathbf{C}_{alg} \star \text{DC}[\boldsymbol{\varphi}_{n+1} - \boldsymbol{\varphi}_n] \Big|_{n+\frac{1}{2}} &= \mathbf{G}_{n+1} - \mathbf{G}_n, \\ \mathbf{G}_{alg} : \text{DC}[\boldsymbol{\varphi}_{n+1} - \boldsymbol{\varphi}_n] \Big|_{n+\frac{1}{2}} &= J_{n+1}^2 - J_n^2, \end{aligned} \quad (4.73)$$

(4.63)<sub>2</sub> yields

$$\begin{aligned} T_{n+1} - T_n = - \int_{\mathcal{B}_0} & \left( \text{DC} \Psi_{\text{iso}}^{\mathbf{C}} : (\mathbf{C}_{n+1} - \mathbf{C}_n) + \text{D}_{\mathbf{G}} \Psi_{\text{iso}}^{\mathbf{G}} : (\mathbf{G}_{n+1} - \mathbf{G}_n) \right. \\ & \left. + p_{n+1} (J_{n+1} - J_n) \right) \, dV - \text{D}\Pi_m^{\text{ext}}[\boldsymbol{\varphi}_{n+1} - \boldsymbol{\varphi}_n]. \end{aligned} \quad (4.74)$$

Furthermore, choosing  $\delta p = p_{n+1} \in \mathbb{V}_p$  in (4.63)<sub>3</sub> leads to

$$\int_{\mathcal{B}_0} p_{n+1} (J_{n+1} - \tau_{n+1}) \, dV = 0, \quad (4.75)$$

and, analogously,

$$\int_{\mathcal{B}_0} p_n (J_n - \tau_n) \, dV = 0. \quad (4.76)$$

The last two equations give rise to

$$\int_{\mathcal{B}_0} p_{n+1} (J_{n+1} - J_n) \, dV = \int_{\mathcal{B}_0} p_{n+1} (\tau_{n+1} - \tau_n) \, dV = \int_{\mathcal{B}_0} \text{D}_{\tau} \Psi_{\text{vol}} (\tau_{n+1} - \tau_n) \, dV. \quad (4.77)$$

Note that the last equation results from the choice  $\delta \tau = \tau_{n+1} - \tau_n$  in (4.63)<sub>4</sub>. Now (4.74) can be written as

$$\begin{aligned} T_{n+1} - T_n = - \int_{\mathcal{B}_0} & \left( \text{DC} \Psi_{\text{iso}}^{\mathbf{C}} : (\mathbf{C}_{n+1} - \mathbf{C}_n) + \text{D}_{\mathbf{G}} \Psi_{\text{iso}}^{\mathbf{G}} : (\mathbf{G}_{n+1} - \mathbf{G}_n) \right. \\ & \left. + \text{D}_{\tau} \Psi_{\text{vol}} (\tau_{n+1} - \tau_n) \right) \, dV - (\Pi_m^{\text{ext}}(\boldsymbol{\varphi}_{n+1}) - \Pi_m^{\text{ext}}(\boldsymbol{\varphi}_n)). \end{aligned} \quad (4.78)$$

Directionality property (4.67) implies

$$T_{n+1} - T_n = -(\Pi^{\text{int}}(\boldsymbol{\varphi}_{n+1}, \tau_{n+1}) - \Pi^{\text{int}}(\boldsymbol{\varphi}_n, \tau_n)) - (\Pi_m^{\text{ext}}(\boldsymbol{\varphi}_{n+1}) - \Pi_m^{\text{ext}}(\boldsymbol{\varphi}_n)). \quad (4.79)$$

In analogy to (4.49) and (2.26) we define, respectively,

$$\Pi^{\text{int}}(\boldsymbol{\varphi}, \tau) = \int_{\mathcal{B}_0} \Psi(\bar{\lambda}_i^C, \bar{\lambda}_i^G, \tau) dV = \int_{\mathcal{B}_0} (\Psi_{\text{iso}}(\bar{\lambda}_i^C, \bar{\lambda}_i^G) + \Psi_{\text{vol}}(\tau)) dV, \quad (4.80)$$

and

$$\Pi(\boldsymbol{\varphi}, \tau) = \Pi^{\text{int}}(\boldsymbol{\varphi}, \tau) + \Pi_m^{\text{ext}}(\boldsymbol{\varphi}). \quad (4.81)$$

Accordingly, (4.79) can be recast in the form

$$T_{n+1} + \Pi_{n+1} = T_n + \Pi_n, \quad (4.82)$$

such that the present integrator is capable to preserve the total energy of a conservative system, independent of the time-step size.

## 4.5 Discretization in space

For the discretization in space we apply, similar to Sec. 3.3, the standard isoparametric finite element approach based on finite-dimensional approximations  $\{\boldsymbol{\varphi}^h, V^h\} \in \{\mathcal{Q}^h \times \mathcal{V}^h\} \subset \mathcal{Q} \times \mathcal{V}$ . Moreover, the additional field variables  $\tau^h$  and  $p^h$  are based on approximations  $\mathbb{V}_\tau, \mathbb{V}_p$  of the form

$$\mathbb{V}_A^h = \left\{ A \in \mathbb{V}_A \mid A^h \Big|_{\mathcal{B}_0^{(e)}} = \sum_{b=1}^{n_{\text{en}}} M_b^A A^b \right\}, \quad (4.83)$$

where  $A$  stands for  $\tau$  or  $p$ . Here,  $n_{\text{en}}$  denotes the number of element nodes arising from the interpolation of the additional fields. The present sample application relies on uniform element-wise approximations for the volumetric dilatation  $\tau$  and the hydrostatic pressure field  $p$  making use of the shape functions  $M_b^A : \mathcal{B}_0 \rightarrow \mathbb{R}$ , with  $b = 1, \dots, n_{\text{en}}$ . The standard (Bubnov-) Galerkin approach relies on analogous approximations for the corresponding variations. Since no inter-element continuity is required for the mixed approximations (related to the shape functions  $M_b^A$ ), the additional unknowns can be eliminated on element level, see [27, 23]. Note that the proposed discretization in space does not affect the structure-preserving scheme and inherits the fundamental balance laws.

## 4.6 Numerical Investigations

In this section we verify the improved numerical performance due to both the mixed finite element formulation and the structure-preserving integration scheme. In the following, displacement based finite elements are denoted as Q1 with linear continuous interpolation space for the displacement field and the mixed finite elements are denoted as Q1P0 with linear continuous interpolation space for the displacement field and a constant discontinuous interpolation space for the mixed fields, see Fig. 4.1.

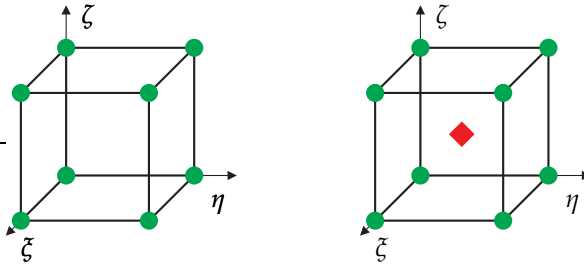


Figure 4.1: Illustration of the nodal points for the Q1 finite element (left) and the Q1P0 finite element (right). The bullets represent the nodal points of the continuous displacement field and the square represents the nodal points of the discontinuous mixed fields.

Moreover, the mid-point scheme outlined in Sec. 4.4 is denoted as MP, whereas the energy-momentum consistent time-stepping scheme, outlined in Sec. 4.4.1, is denoted as EM. Finally, we would like to emphasize that the patch-test, investigated in Sec. 3.4.1, is fulfilled for the elements presented in this chapter, see [81].

### 4.6.1 Static convergence analysis

The objectives of this example are:

- 01.I** Verification of the order of accuracy with respect to mesh refinement.
- 01.II** Verification of quadratic convergence of Newton-Rhapson solution process.

This example is constructed following [129, 140] where we assume a prescribed deformation field  $\varphi^{\text{pre}}$  given as

$$\varphi^{\text{pre}} = \mathbf{X} + U_1 \sin(X) \mathbf{e}_1 + U_2 \sin(Y) \mathbf{e}_2 + U_3(\sin(Z) + \cos(Z)) \mathbf{e}_3. \quad (4.84)$$

Therein  $U_i = \{0.1 \ 0.2 \ 0.3\}$  and  $e_i$  are the basis vectors in the spatial configuration. Accordingly, the prescribed deformation gradient  $F^{\text{pre}}$  can analytically be computed by employing (2.14), such that

$$\begin{aligned} F^{\text{pre}} = & (1 + U_1 \cos(X)) e_1 \otimes E_1 + (1 - U_2 \sin(Y)) e_2 \otimes E_2 \\ & + (1 + U_3 (\cos(Z) - \sin(Z))) e_3 \otimes E_3, \end{aligned} \quad (4.85)$$

where  $E_i$  are the basis vectors in the material configuration. Afterwards, the prescribed right Cauchy-Green strain tensor,  $C^{\text{pre}}$ , its co-factor  $G^{\text{pre}}$  and the determinant of the prescribed deformation gradient  $J^{\text{pre}}$  can be calculated as

$$C^{\text{pre}} = (F^{\text{pre}})^T F^{\text{pre}}, \quad G^{\text{pre}} = \frac{1}{2} C^{\text{pre}} \star C^{\text{pre}}, \quad J^{\text{pre}} = \det(F^{\text{pre}}). \quad (4.86)$$

The prescribed pressure  $p^{\text{pre}}$  and volumetric dilatation  $\tau^{\text{pre}}$  are given by

$$\tau^{\text{pre}} = J^{\text{pre}} \quad \text{and} \quad p^{\text{pre}} = \partial_\tau \Psi_{\text{vol}}(\tau^{\text{pre}}), \quad (4.87)$$

which result in a prescribed second Piola-Kirchhoff stress tensor given as

$$S^{\text{pre}} = 2 \partial_C \Psi_{\text{iso}}^C(\bar{\lambda}_i^C(C^{\text{pre}})) + 2 \partial_G \Psi_{\text{iso}}^G(\bar{\lambda}_i^G(G^{\text{pre}})) \star C^{\text{pre}} + p^{\text{pre}} (J^{\text{pre}})^{-1} G^{\text{pre}}. \quad (4.88)$$

Eventually, the first Piola-Kirchhoff stress tensor and the respective prescribed volume load are given by

$$P^{\text{pre}} = F^{\text{pre}} S^{\text{pre}} \quad \text{and} \quad \bar{B}^{\text{pre}} = -\text{Div}(P^{\text{pre}}). \quad (4.89)$$

Now we investigate the approximated solution of the displacements and their analytical counterparts for the given volume load  $\bar{B}^{\text{pre}}$  and determine the rate of convergence. As a domain of interest, we consider a cube with  $\Omega \in (0, 1)[\text{m}] \times (0, 1)[\text{m}] \times (0, 1)[\text{m}]$  as depicted in Fig. 4.2. Dirichlet boundaries which coincide with the prescribed deformation given in (4.84) are applied on all surfaces ( $x_i = 0 \wedge x_i = 1$ ,  $i = 1, 2, 3$ ) of the cube. In this example we make use of an Ogden type material model as introduced in Sec. 4.2.2. The geometry and the material as well as the simulation parameters are given in Tab. 4.1. These material parameters correspond to the Lamé parameters  $\lambda_0 = 1.05 \cdot 10^6$  Pa and  $\mu_0 = 1.18 \cdot 10^3$  Pa in the linear theory. See Fig. 4.2 for the von Mises stress distribution of the given deformation field. In Fig. 4.3, the  $L_2$  norm of the error is displayed over different mesh sizes.

As expected, the convergence observed is (nearly)  $n_p + 1$ , where  $n_p$  is the order of the finite element approximation space. Since we focus on low-order finite elements and the rate of convergence seems to be optimal, we focus on this type of approximation in

the following. Finally, in Fig. 4.4, the quadratic convergence of the Newton-Rhapson type of solution process can be observed (in here, we plot the iterations for the first load-step of the finest mesh). Accordingly, the consistent linearization of the non-linear problem is verified.

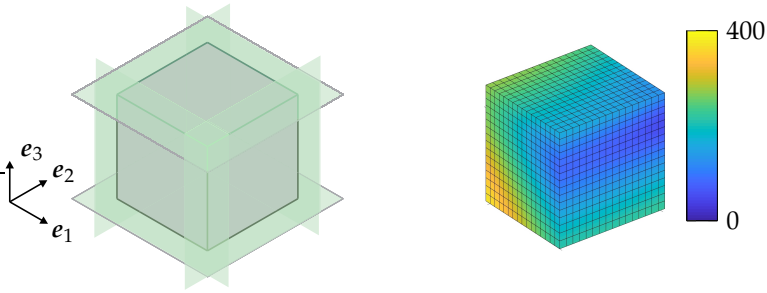


Figure 4.2: Boundary conditions (left) and von Mises stress distribution of the final configuration (right).

Table 4.1: Material and simulation parameters for static convergence test.

mechanical parameters	$a_m$	$\{6.3, 0.012, -0.1\} \cdot 10^2$	Pa	geometry of the cube 
	$b_m$	$\{6.3, 0.012, -0.1\} \cdot 10^2$	Pa	
	$\gamma_m$	$\{1.3, 5, -2\}$	-	
	$\delta_m$	$\{1.3, 5, -2\}$	-	
	$c$	$2 \cdot 10^5$	Pa	
	$d$	$-2$	-	
Newton tolerance	$\varepsilon$	$1 \cdot 10^{-7}$	-	
size of increment	$\Delta U$	0.1	$m$	

## 4.6.2 Compressed block

The objectives of this example are:

**O2.I** Verification of the algorithmic energy approximation.

**O2.II** Verification of numerical stability and validity.

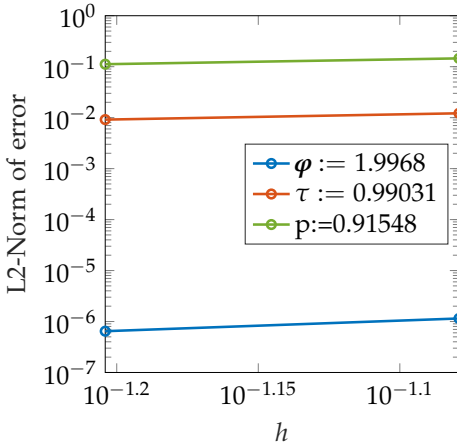


Figure 4.3: Convergence with mesh refinement.

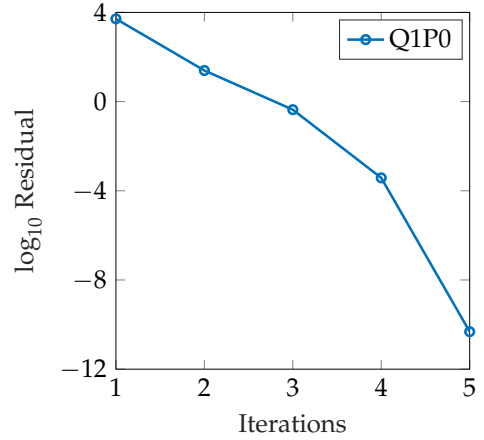


Figure 4.4: Newton iterations in a load-step.

The first transient example deals with a nearly incompressible block as shown in Fig. 4.5. The block is fully clamped on its bottom face (at  $x_3 = 0$ ) and symmetry conditions are taken into account on the surface at  $x_1 = 1$  (zero displacements in  $e_1$ -direction) and  $x_2 = 0$  (zero displacements in  $e_2$ -direction). A time-dependent surface load with magnitude  $P$  is acting on a quarter of the top of the block in negative  $e_3$ -direction as illustrated in Fig. 4.5. In this connection, the nodal dead load is given by

$$P(t) = f(t) \hat{p}, \quad \text{with} \quad f(t) = \begin{cases} \sin\left(\frac{\pi}{2t_{ml}} t\right) & t \leq t_{ml} \\ \cos\left(\frac{\pi}{2(t_{el}-t_{ml})} (t - t_{ml})\right) & t_{ml} \geq t > t_{ml} \\ 0 & t > t_{el} \end{cases}, \quad (4.90)$$

where at  $t_{ml} = 1\text{s}$  the load reaches its maximum and at  $t_{el} = 2\text{s}$  the load interval ends. In the compressible case we set  $\hat{p} = (-1 \cdot 10^3)$  Pa, whereas for the incompressible case we set  $\hat{p} = (-3 \cdot 10^3)$  Pa. The Ogden's type material model is given in Sec. 4.2.2 and the corresponding material and simulation parameters are provided in Tab. 4.2. In the linear theory, these material parameters correspond to the Lamé parameters  $\mu_0 = 1.18 \cdot 10^3$  Pa and  $\lambda_0 = 1.05 \cdot 10^6$  Pa for the incompressible case and  $\lambda_0 = 1.13 \cdot 10^3$  Pa in the compressible case, respectively.

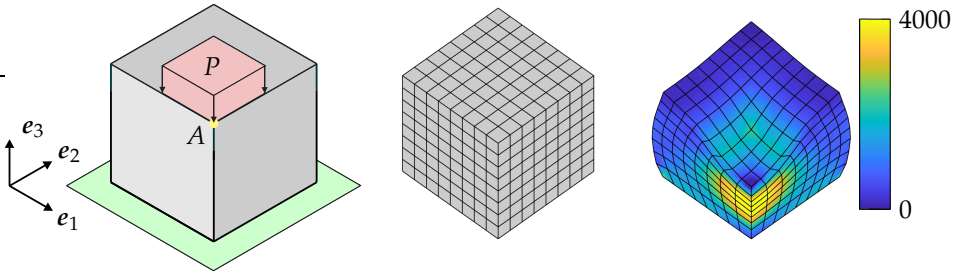
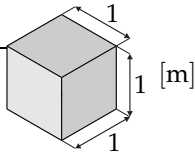


Figure 4.5: Boundary conditions of the compressed block (left), initial mesh (center) and von Mises stress distribution of the incompressible block at 0.5s (right).

First, we verify the validity of the proposed formulation. In Figs. 4.6 and 4.7 the position in  $e_3$  direction of node  $A$  is plotted over time. Herein we use the EM scheme along with a time-step size of  $\Delta t = 0.05s$  and a coarse discretization (crs) with  $4 \times 4 \times 4$  finite elements, a medium discretization (mdm) with  $6 \times 6 \times 6$  finite elements and a fine discretization (fn) with  $8 \times 8 \times 8$  finite elements. As it can be observed in Fig. 4.6, for the compressible case both formulations are in a good agreement. In contrast, the incompressible case is investigated in Fig. 4.7, where the locking phenomena of the Q1 formulation can be observed in this transient example. While the Q1P0 formulation shows a good spatial convergence behavior, the Q1 formulation shows strong locking effects, which lead to invalid simulation results. Interestingly, due to locking, the period length of the Q1 formulation is much smaller which can cause serious problems e.g. in fatigue studies. Next we verify the algorithmic conservation of the total energy for the presented EM scheme. In here, we use the Q1P0 formulation along with the nearly incompressible material behavior. In Fig. 4.8 we observe that the standard MP time-stepping scheme overestimates the total energy and after that, numerical instabilities lead to a termination of the simulation. In contrast, the presented EM scheme is numerically stable for the whole simulation time, see Fig. 4.8. Moreover, the EM scheme is capable to reproduce the balance of energy in the time-discrete setting independent of the time-step size, where the difference of the total energy of a time-step is under the user defined Newton tolerance, see Fig. 4.9. Note that we obtain the same improved stability and robustness of the EM scheme for the compressible case, too. Fig. 4.10 shows the deformation for some time points of the compressed block with its von Mises stress distribution.

Table 4.2: Material and simulation parameters for the compressed block.

mech. parameters	$a_m$	$\{9.45, 0.012, -0.1\} \cdot 10^2$	Pa	geometry of the block 
	$b_m$	$\{9.45, 0.012, -0.1\} \cdot 10^2$	Pa	
	$\gamma_m$	$\{1.3, 5, -2\}$	-	
	$\delta_m$	$\{1.3, 5, -2\}$	-	
	$c$	$2 \cdot 10^2 / 2 \cdot 10^5$	Pa	
	$d$	-2	-	
	reference density	$\rho$	1000	
Newton tolerance	$\varepsilon$	$1 \cdot 10^{-5}$	-	
time-step size	$\Delta t$	0.2/0.1/0.025	s	
simulation time	$T$	20	s	

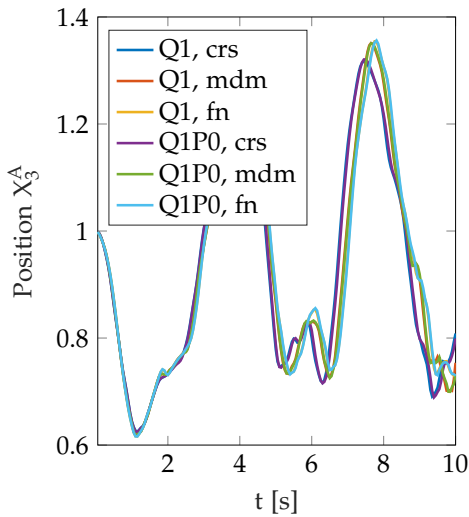


Figure 4.6: Convergence with mesh refinement for the compressible case. Calculated with EM scheme and time-step size  $\Delta t = 0.025\text{s}$ .

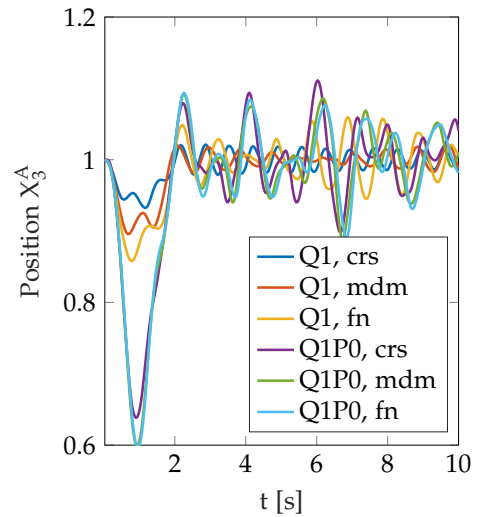


Figure 4.7: Convergence with mesh refinement for the nearly incompressible case. Calculated with EM scheme and time-step size  $\Delta t = 0.025\text{s}$ .

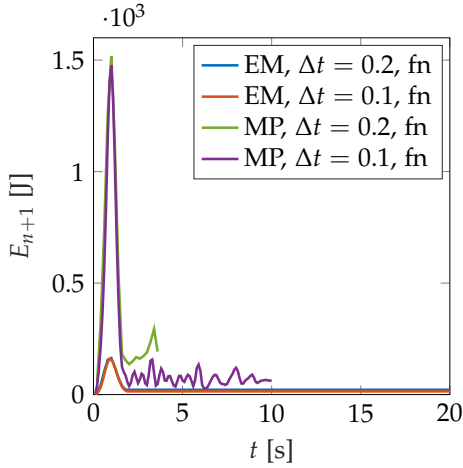


Figure 4.8: Total energy evolution of the Q1P0 formulation for the nearly incompressible case.

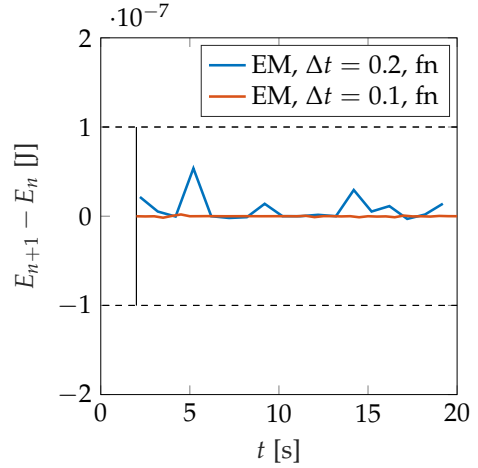


Figure 4.9: Incremental change of total energy of the Q1P0 formulation for the nearly incompressible case.

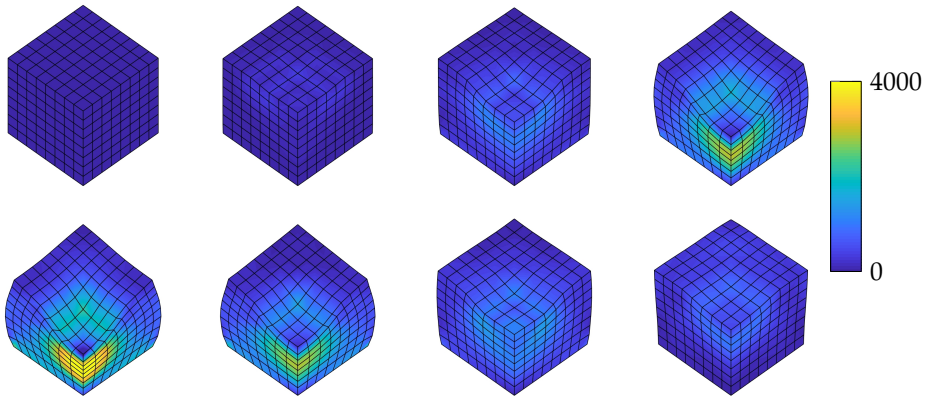


Figure 4.10: Snapshots of configurations with von Mises stress distribution at  $t = \{ 0, 0.125, 0.25, 0.375, 0.5, 0.625, 0.75, 0.875 \}$ s. The results for nearly incompressibility are obtained with the EM scheme and  $\Delta t = 0.025$ s.

### 4.6.3 Twisting column

The objectives of this example are:

**O3.I** Verification of the algorithmic conservation properties.

**O3.II** Verification of numerical stability and validity.

**O3.III** Verification of order of accuracy.

The last example deals with a twisting column depicted in Fig. 4.11, which is a modification of the example presented in [25, 61].

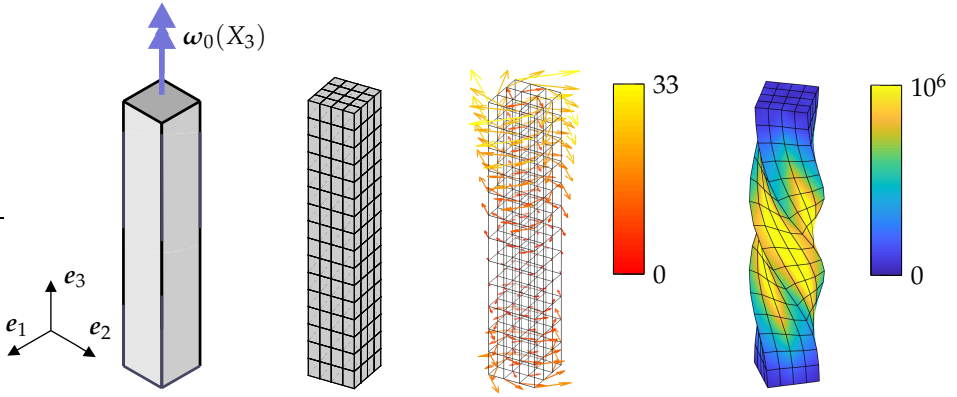


Figure 4.11: Boundary conditions of the column (left), initial mesh (center-left), initial nodal velocity distribution (center-right) and von Mises stress distribution at 0.12s (right).

In here, we would like to show that the EM scheme correctly approximates the energy as well as the angular momentum of the mechanical system at hand even for very complex deformations and extremely large strains. Again, we make use of quasi incompressible Ogden material as presented in Sec. 4.2.2, where the material and simulation parameters are summarized in Tab. 4.3. In the linear theory, these material parameters correspond to the Lamé parameters  $\lambda_0 = 2.63 \cdot 10^8$  Pa and  $\mu_0 = 1.18 \cdot 10^6$  Pa. As indicated in Fig. 4.11, the initial velocity field is prescribed by

$$\mathbf{V}_0 = \boldsymbol{\omega}_0 \times \mathbf{X}, \quad \text{with} \quad \boldsymbol{\omega}_0 = [0, 0, \Omega_1 \sin(\frac{\pi(X_3 - 0.5l)}{2l}) + \Omega_2], \quad (4.91)$$

with  $\Omega_1 = 50s^{-1}$  and  $\Omega_2 = 10s^{-1}$ . Note that the initial angular velocity  $\boldsymbol{\omega}_0$  depends on the  $X_3$  coordinate, see Fig. 4.11 for an illustration of the nodal velocity vectors and their magnitudes in  $\frac{m}{s}$ . In addition, neither Dirichlet nor Neumann boundary

conditions are employed in this example and therefore, the system can be classified as autonomous Hamiltonian system with symmetry implying conservation of total linear momentum, angular momentum and energy. The objective of this example is to show that these quantities are indeed conserved by the present EM scheme.

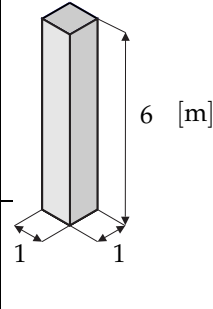
Fig. 4.12 shows that the EM scheme is numerically stable for the whole simulation time and capable to reproduce the conservation of energy correctly, independent of the time-step size, see Fig. 4.13 . Moreover, we can observe that standard schemes like the mid-point rule typically exhibit numerical instabilities in non-linear applications, which leads to a termination of the simulation after about  $\{0.07, 0.09, 1.525\}$ s for  $\Delta t = \{0.01, 0.0075, 0.005\}$ s. Eventually, the total angular momentum is correctly conserved independent of the time-step size for the presented EM scheme, which can be observed from Figs. 4.14 and 4.15. Furthermore, we investigate the numerical accuracy of the present EM time integrator, which should be of second order likewise the mid-point integrator. To investigate this, we define the  $L_2$  norm of the error in the positions as

$$\|e\|_{L_2} = \frac{\|\boldsymbol{\varphi} - \boldsymbol{\varphi}_r\|_{L_2}}{\|\boldsymbol{\varphi}_r\|_{L_2}}, \quad (4.92)$$

where

$$\|\boldsymbol{\varphi}\|_{L_2} = \left[ \int_{\mathcal{B}_0} (\boldsymbol{\varphi} \cdot \boldsymbol{\varphi}) \, dV \right]^{1/2}. \quad (4.93)$$

Table 4.3: Material and simulation parameters for the column.

mech. parameters	$a_m$	$\{6.3, 0.012, -0.1\} \cdot 10^5$	Pa	geometry of the column 
	$b_m$	$\{6.3, 0.012, -0.1\} \cdot 10^5$	Pa	
	$\gamma_m$	$\{1.3, 5, -2\}$	-	
	$\delta_m$	$\{1.3, 5, -2\}$	-	
	$c$	$5 \cdot 10^7$	Pa	
	$d$	$-2$	-	
reference density	$\rho$	1000	$\text{kg m}^{-3}$	
Newton tolerance	$\varepsilon$	$1 \cdot 10^{-5}$	-	
time-step size	$\Delta t$	0.01/0.0075/0.005	s	
simulation time	$T$	10	s	

In (4.92),  $\boldsymbol{\varphi}_r$  defines the reference solution of the positions, calculated with the smallest time-step size ( $\Delta t = 0.00001$ s). We investigate the time interval  $0 \leq t \leq 0.01$  s along

with a spatial discretization of  $\{1 \times 1 \times 4\}$  finite elements. As expected, all integrators show second order of accuracy in the positions, see Fig. 4.16. Fig. 4.17 contains a series of snapshots illustrating the twist of the column during the simulation.

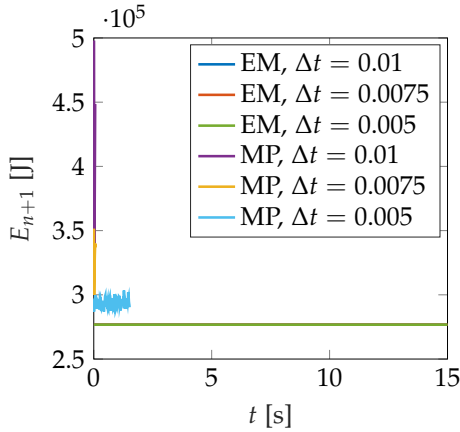


Figure 4.12: Total energy evolution of the Q1P0 formulation for the nearly incompressible case.

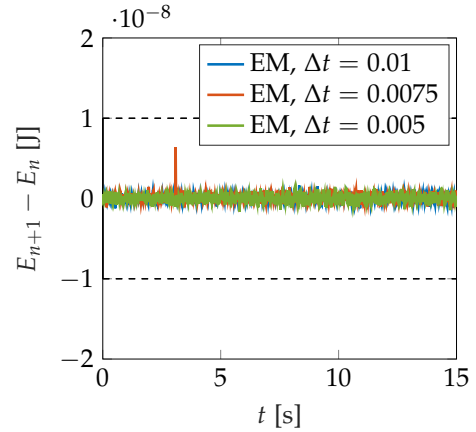


Figure 4.13: Incremental change of total energy of the Q1P0 formulation for the nearly incompressible case.

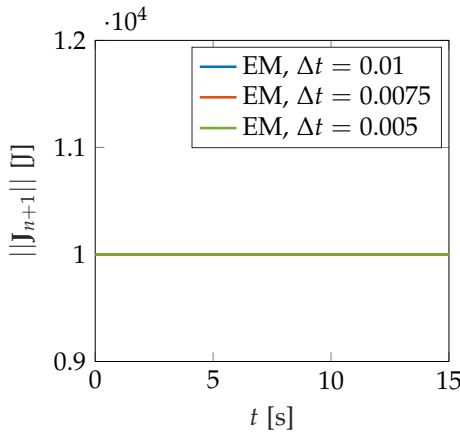


Figure 4.14: Total  $J$  evolution of the Q1P0 formulation for the nearly incompressible case.

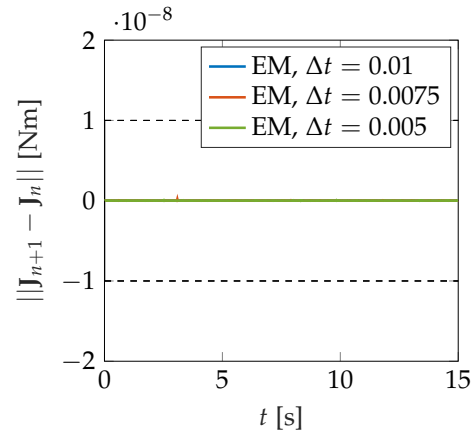


Figure 4.15: Incremental change of  $J$  of the Q1P0 formulation for the nearly incompressible case.

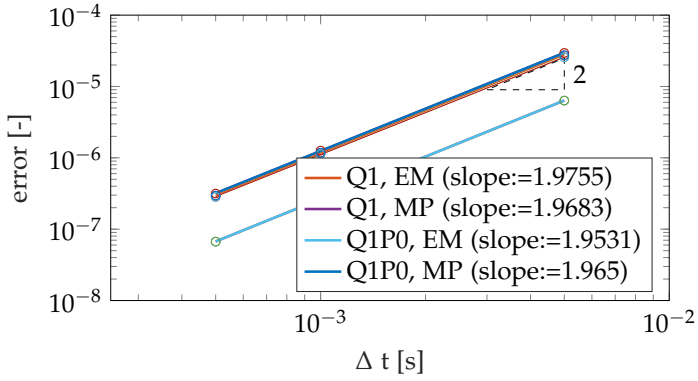


Figure 4.16: Column: Error in the displacements.

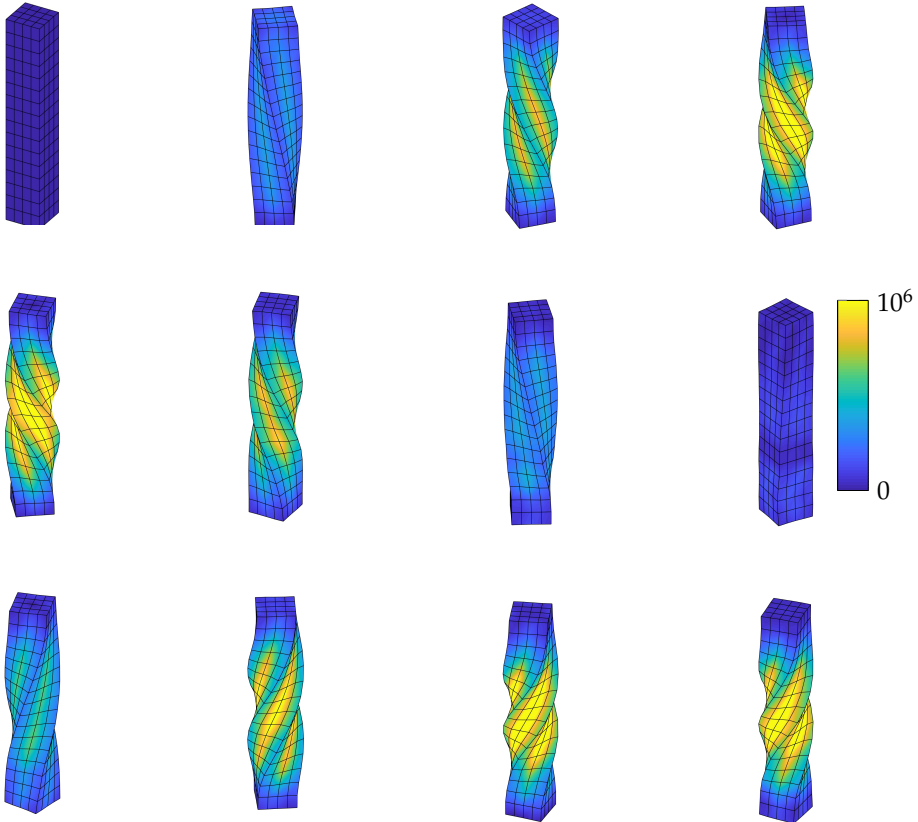


Figure 4.17: Snapshots of configurations with von Mises stress distribution at  $t = \{ 0, 0.03, 0.06, 0.09, 0.12, 0.15, 0.18, 0.21, 0.24, 0.27, 0.3, 0.33 \}$ s. The results have been obtained for a nearly incompressible material model with EM scheme and  $\Delta t = 0.0075$ s.

# 5 EM scheme for nonlinear thermo-elastodynamics<sup>1</sup>

In this chapter we provide a new approach to the design of EM consistent integration schemes in the field of non-linear thermo-elastodynamics. A temperature based weak form is employed which facilitates the design of a structure-preserving time-stepping scheme for coupled thermo-elastic problems. This approach is motivated by the general equation for non-equilibrium reversible-irreversible coupling (GENERIC) framework for open systems. In contrast to complex projection based discrete derivatives, a new form of an algorithmic stress formula is proposed. The spatial discretization relies on finite element interpolations for the displacements and the temperature. The superior performance of the proposed formulation is shown by means of representative numerical examples.

## 5.1 Finite strain thermo-elastodynamics

The body  $\mathcal{B}_0$ , introduced in Sec. 2.2, is now considered as a thermoelastic body with the absolute temperature  $\theta : \mathcal{B}_0 \times \mathcal{I} \rightarrow \mathbb{R}^+$  which is assumed to be a smooth function

$$\theta = \theta(\mathbf{X}, t). \quad (5.1)$$

The material gradient of the temperature field  $\gamma : \mathcal{B}_0 \times \mathcal{I} \rightarrow \mathbb{R}^3$  is given by

$$\gamma = \partial_{\mathbf{X}}\theta. \quad (5.2)$$

---

<sup>1</sup> This chapter is based on [44].

Next to the pure mechanical boundaries, the thermal Neumann boundaries and Dirichlet boundaries are  $\partial\mathcal{B}_0^Q \subset \partial\mathcal{B}_0$  and  $\partial\mathcal{B}_0^\theta \subset \partial\mathcal{B}_0$ , respectively. Moreover, the respective boundaries may not overlap each other, i.e.  $\partial\mathcal{B}_0^Q \cup \partial\mathcal{B}_0^\theta = \partial\mathcal{B}_0$ ,  $\partial\mathcal{B}_0^Q \cap \partial\mathcal{B}_0^\theta = \emptyset$ . Furthermore  $\mathbf{p} : \mathcal{B}_0 \times \mathcal{I} \rightarrow \mathbb{R}^3$  denotes the material density of linear momentum given by

$$\mathbf{p} := \rho_0 \mathbf{V}. \quad (5.3)$$

Introducing the state vector  $\mathbf{z} = \{\boldsymbol{\varphi}, \mathbf{p}, \theta\}$  of the thermodynamical system, the solution space is now defined by the infinite dimensional set

$$\mathcal{S} = \{\mathbf{z} : \mathcal{B}_0 \times \mathcal{I} \rightarrow \mathbb{R}^3 \times \mathbb{R}^3 \times \mathbb{R}^+ \mid \det(\mathbf{F}) > 0, \boldsymbol{\varphi} = \bar{\boldsymbol{\varphi}} \forall \mathbf{X} \in \partial\mathcal{B}_0^Q \text{ and } \theta = \bar{\theta} \forall \mathbf{X} \in \partial\mathcal{B}_0^\theta\}. \quad (5.4)$$

In order to describe finite strain thermo-elastodynamics a Helmholtz free energy density function  $\hat{\Psi} : \mathbb{R}^{3 \times 3} \times \mathbb{R}^+ \rightarrow \mathbb{R}$  is introduced

$$\hat{\Psi}(\mathbf{F}, \theta) = \hat{\Psi}(\mathbf{C}, \theta), \quad (5.5)$$

which is assumed to be twice continuously differentiable with respect to its arguments. Furthermore in (5.5) a frame-indifferent material formulation  $\hat{\Psi} : \mathbb{R}^{3 \times 3} \times \mathbb{R}^+ \rightarrow \mathbb{R}$  is introduced which is invariant under superposed rigid motions, see Sec. 2.2.2.

Based on the Helmholtz free energy, the second Piola-Kirchhoff stress tensor

$$\mathbf{S} = 2 \partial_{\mathbf{C}} \hat{\Psi}(\mathbf{C}, \theta), \quad (5.6)$$

and the entropy density

$$\eta = -\partial_{\theta} \hat{\Psi}(\mathbf{C}, \theta), \quad (5.7)$$

are introduced. The heat transfer is governed by Duhamel's law of heat conduction

$$\mathbf{Q} = -\mathbf{K}(\mathbf{C}, \theta) \boldsymbol{\gamma}, \quad (5.8)$$

where  $\mathbf{K} : \mathbb{R}^{3 \times 3} \times \mathbb{R}^+ \rightarrow \mathbb{R}^{3 \times 3}$  denotes the material thermal conductivity tensor which is assumed to be semi-positive definite and  $\mathbf{Q} : \mathcal{B}_0 \times \mathcal{I} \rightarrow \mathbb{R}^3$  is the Piola heat flux vector. Note that the constitutive equations (5.6)-(5.8) are thermodynamically consistent in the sense that they satisfy the Clausius-Duhem inequality. The global balance of linear momentum is given by

$$\int_{\mathcal{B}_0} \dot{\mathbf{p}} \, dV = \int_{\mathcal{B}_0} \dot{\mathbf{B}} \, dV + \int_{\partial\mathcal{B}_0^P} \mathbf{P} \mathbf{N} \, dA, \quad (5.9)$$

where the volume force density  $\bar{\mathbf{B}}$ , the first Piola-Kirchhoff stress tensor  $\mathbf{P}$  and the unit outward normal  $\mathbf{N}$  have been introduced in Sec. 2.2. The global energy balance is given by

$$\int_{\mathcal{B}_0} \theta \dot{\eta} \, dV = \int_{\mathcal{B}_0} R \, dV - \int_{\partial \mathcal{B}_0^Q} \mathbf{Q} \cdot \mathbf{N} \, dA. \quad (5.10)$$

Therein  $R : \mathcal{B}_0 \times \mathcal{I} \rightarrow \mathbb{R}$  denotes the heat source density. For a detailed derivation of (5.9) and (5.10) the reader is referred to e.g. [53, 68]. Using standard arguments from continuum mechanics, the strong form governing the evolution of the coupled system at hand can be stated as

$$\begin{aligned} \dot{\boldsymbol{\varphi}} &= \rho_0^{-1} \mathbf{p}, \\ \dot{\mathbf{p}} &= \text{Div}(\mathbf{F} \mathbf{S}) + \bar{\mathbf{B}}, \\ \theta \dot{\eta} &= -\text{Div}(\mathbf{Q}) + \bar{R}, \end{aligned} \quad (5.11)$$

in  $\mathcal{B}_0 \forall t \in \mathcal{I}$ , where the energy balance (5.11)<sub>3</sub> is formulated in entropy form. The formulation (5.11) is referred to as the standard formulation in the sequel. In the above, (5.11)<sub>2</sub> corresponds to the local balance of linear momentum and (5.11)<sub>3</sub> denotes the local energy balance. For the coupled thermo-elastodynamic problem comprised of the partial-differential equations (PDE) in (5.11) suitable initial and boundary conditions are necessary. In particular prescribed deformations  $\bar{\boldsymbol{\varphi}} : \partial \mathcal{B}_0^\varphi \times \mathcal{I} \rightarrow \mathbb{R}^3$ , temperatures  $\bar{\theta} : \partial \mathcal{B}_0^\theta \times \mathcal{I} \rightarrow \mathbb{R}^+$ , Piola tractions  $\bar{\mathbf{T}} : \partial \mathcal{B}_0^P \times \mathcal{I} \rightarrow \mathbb{R}^3$  and Piola heat fluxes  $\bar{\mathbf{Q}} : \partial \mathcal{B}_0^Q \times \mathcal{I} \rightarrow \mathbb{R}$  need to be provided, such that

$$\begin{aligned} \boldsymbol{\varphi} &= \bar{\boldsymbol{\varphi}} && \text{on } \partial \mathcal{B}_0^\varphi, \\ \mathbf{P} \mathbf{N} &= \bar{\mathbf{T}} && \text{on } \partial \mathcal{B}_0^P, \\ \theta &= \bar{\theta} && \text{on } \partial \mathcal{B}_0^\theta, \\ \mathbf{Q} \cdot \mathbf{N} &= -\bar{\mathbf{Q}} && \text{on } \partial \mathcal{B}_0^Q, \end{aligned} \quad (5.12)$$

for all  $t \in \mathcal{I}$ . Furthermore prescribed volume force  $\bar{\mathbf{B}}$  and heat source densities  $\bar{R}$  need to be provided. Likewise, suitable initial conditions for configuration, velocity and temperature fields need to be provided with

$$\begin{aligned} \boldsymbol{\varphi}(\mathbf{X}, 0) &= \boldsymbol{\varphi}_0, \\ \mathbf{V}(\mathbf{X}, 0) &= \mathbf{V}_0, \\ \theta(\mathbf{X}, 0) &= \theta_0, \end{aligned} \quad (5.13)$$

in  $\mathcal{B}_0$ . Eventually, the initial boundary value problem (IBVP) is comprised of PDEs (5.11), boundary conditions (5.12) and initial conditions (5.13). For the ensuing application of the finite element method a time independent tangent space is introduced

as

$$\mathcal{W} = \{w_z = (w_\varphi, w_p, w_e) : \mathcal{B}_0 \rightarrow \mathbb{R}^3 \times \mathbb{R}^3 \times \mathbb{R}\}. \quad (5.14)$$

The spaces of virtual or admissible test functions for the deformation and linear momentum  $\mathcal{W}_\bullet \subset \mathcal{W}$ , where  $\bullet \in \{\varphi, p\}$ , as well as the temperature  $\mathcal{W}_e \subset \mathcal{W}$  are given by

$$\begin{aligned} \mathcal{W}_\bullet &= \{w_\bullet : w_\bullet(\mathbf{X}) \in H^1(\mathcal{B}_0) \mid w_\bullet(\mathbf{X}) = \mathbf{0} \text{ on } \partial\mathcal{B}_0^\varphi\}, \\ \mathcal{W}_e &= \{w_e : w_e(\mathbf{X}) \in H^1(\mathcal{B}_0) \mid w_e(\mathbf{X}) = 0 \text{ on } \partial\mathcal{B}_0^\theta\}, \end{aligned} \quad (5.15)$$

where  $H^1$  denotes the Sobolev functional space of square integrable functions and derivatives. Next, the strong forms in (5.11) are multiplied by test functions  $w_z \in \mathcal{W}$  and integrated afterwards over the domain  $\mathcal{B}_0$ . Finally, the weak forms of the balance of linear momentum and of the energy are obtained by using standard techniques like partial integration, the divergence theorem of Gauss, etc. leading to

$$\begin{aligned} \int_{\mathcal{B}_0} w_\varphi \cdot \dot{\boldsymbol{\varphi}} \, dV &= \int_{\mathcal{B}_0} w_\varphi \cdot \rho_0^{-1} \mathbf{p} \, dV, \\ \int_{\mathcal{B}_0} w_p \cdot \dot{\mathbf{p}} \, dV &= - \int_{\mathcal{B}_0} (\mathbf{F} \mathbf{S}) : \partial_{\mathbf{X}} w_p \, dV + \int_{\mathcal{B}_0} w_p \cdot \bar{\mathbf{B}} \, dV + \int_{\partial\mathcal{B}_0^p} w_p \cdot \bar{\mathbf{T}} \, dA, \\ \int_{\mathcal{B}_0} w_e \theta \, \dot{\eta} \, dV &= \int_{\mathcal{B}_0} \mathbf{Q} \cdot \partial_{\mathbf{X}} w_e \, dV + \int_{\mathcal{B}_0} w_e \bar{R} \, dV + \int_{\partial\mathcal{B}_0^Q} w_e \bar{Q} \, dA, \end{aligned} \quad (5.16)$$

which have to hold for arbitrary  $w_z \in \mathcal{W}$ . Further details about this formulation can be found in [69].

## 5.2 Constitutive equations for large strain thermo-elasticity

A thermal hyperelastic material model with a polyconvexity-based Helmholtz free energy density function can be formulated as

$$\hat{\Psi}(\mathbf{F}, \theta) = \tilde{\Psi}(\mathbf{F}, \mathbf{H}, J, \theta), \quad (5.17)$$

where  $\tilde{\Psi} : \mathbb{R}^{3 \times 3} \times \mathbb{R}^{3 \times 3} \times \mathbb{R}^+ \times \mathbb{R}^+ \rightarrow \mathbb{R}$  is polyconvex in  $\mathbf{F}$ ,  $\mathbf{H}$  and  $J$  and concave in  $\theta$ . In contrast to the Helmholtz free energy density function given in (5.5), the kinematic fields  $\mathbf{H}$  and  $J$  are explicit arguments of the function. Again, we focus on a

frame-indifferent Helmholtz free energy density function resulting from (5.17) given as

$$\hat{\Psi}(\mathbf{F}, \theta) = \hat{\Psi}(\mathbf{C}, \theta) = \Psi(\mathbf{C}, \mathbf{G}, \mathbf{C}, \theta). \quad (5.18)$$

The second Piola-Kirchhoff stress tensor described in the tensor cross product notion has already been introduced in (2.60) and is given by

$$\mathbf{S} = 2 (\partial_{\mathbf{C}} \Psi + \partial_{\mathbf{G}} \Psi \ast \mathbf{C} + \partial_{\mathbf{C}} \Psi \mathbf{G}). \quad (5.19)$$

For the entropy density resulting from (5.18) we obtain

$$\eta(\mathbf{C}, \theta) = -\partial_{\theta} \Psi(\mathbf{C}, \mathbf{G}, \mathbf{C}, \theta). \quad (5.20)$$

We make the common assumption that the entropy is a function of both, the temperature  $\theta$  and the volumetric part of the deformation  $\mathbf{C}$ . To describe the behavior of the thermo-elastic material we specify the Piola-Kirchhoff heat flux tensor, given in (5.8). The thermal conductivity tensor  $\mathbf{K}$  is defined as

$$\mathbf{K}(\mathbf{G}, \mathbf{C}, \theta) = k_0 C^{-1} \mathbf{G}, \quad (5.21)$$

for a thermally isotropic behavior where  $k_0 = C^{1/2} k \geq 0$  is the coefficient of thermal conductivity in the reference configuration. In contrast to the classical formulation (5.8), the Piola-Kirchhoff heat flux tensor is now given by

$$\mathbf{Q}(\mathbf{G}, \mathbf{C}, \theta) = -k_0 C^{-1} \mathbf{G} \gamma. \quad (5.22)$$

Note that in (5.21) and (5.22) use has been made of (2.3), the second equality in (2.12), of (2.42) and of (2.43).

**Example (Mooney-Rivlin material):** The polyconvexity-based Helmholtz free energy density of a compressible Mooney-Rivlin thermo-elastic material model defined in a frame-indifferent formulation is given by

$$\Psi(\mathbf{C}, \mathbf{G}, \mathbf{C}, \theta) = \Psi^{\text{mech},1}(\mathbf{C}, \mathbf{G}) + \Psi^{\text{mech},2}(\mathbf{C}) + \Psi^{\text{temp}}(\theta) + \Psi^{\text{couple}}(\mathbf{C}, \theta). \quad (5.23)$$

Here, the purely mechanical parts  $\Psi^{\text{mech},1}(\mathbf{C}, \mathbf{G})$  and  $\Psi^{\text{mech},2}(\mathbf{C})$  have been introduced in (2.52) and (2.53), respectively. The convex function  $\Gamma^1$  now reads  $\Gamma^1(\delta) = \frac{c_1}{2} (\delta - 1)^2 - d_1 \log(\delta)$ , with the material constants  $c_1, d_1 \geq 0$ . The thermal response of the material due the thermal part of  $\Psi$  is given by

$$\Psi^{\text{temp}}(\theta) = \kappa \left( \theta - \theta_0 - \theta \log \left( \frac{\theta}{\theta_0} \right) \right), \quad (5.24)$$

where the parameter  $\kappa \geq 0$  is the specific heat capacity and  $\theta_0 : \mathcal{B}_0 \rightarrow \mathbb{R}^+$  the reference temperature. The coupled term of the Helmholtz free energy density is described by the scalar-valued function

$$\Psi^{\text{couple}}(C, \theta) = -3\beta(\theta - \theta_0)\Gamma^2(C), \quad (5.25)$$

with a suitable convex function  $\Gamma^2 : \mathbb{R}^+ \rightarrow \mathbb{R}$ . For example,  $\Gamma^2(\delta) = c_2(\delta - 1) - \frac{d_2}{\delta}$ , where  $c_2, d_2 \geq 0$ . Note that the parameter  $\beta \geq 0$  characterizes the strength of the thermo-mechanical coupling. See Sec. 5.6 for a specific choice of the Helmholtz free energy density function.

## 5.3 Temperature-based governing equations

In this section we derive an alternative formulation of the thermo-elastodynamical problem by rephrasing the strong form of the energy balance in entropy form (5.11)<sub>3</sub> into temperature form. In addition we make use of the polyconvexity-based form of the constitutive equations (5.19), (5.20) and (5.21). We then show that the temperature-based formulation satisfies the fundamental balance laws and therefore provides a new basis for the construction of EM integrators.

### 5.3.1 Temperature-based strong form

To gain the strong form of the thermo-elastodynamical problem in temperature form we express the rate of the entropy density (5.20) using the chain rule

$$\dot{\eta} = \partial_C \eta \dot{C} + \partial_\theta \eta \dot{\theta} = \partial_C \eta \mathbf{G} : \dot{C} + \partial_\theta \eta \dot{\theta}, \quad (5.26)$$

being only a function of the temperature and the volumetric part of the deformation. This corresponds to the assumption that only volumetric deformation drives changes in the absolute temperature. Substituting (5.26) into (5.11)<sub>3</sub> and further using the classical definition of the absolute temperature (see [117])

$$\theta = \partial_\theta u (\partial_\theta \eta)^{-1}, \quad (5.27)$$

where  $u$  denotes the specific inner energy, the above leads to the energy balance expressed in temperature-form

$$\dot{\theta} = -(\partial_\theta \eta)^{-1} \partial_C \eta \mathbf{G} : \dot{C} - (\partial_\theta u)^{-1} \text{Div}(\mathbf{Q}) + (\partial_\theta u)^{-1} \bar{R}. \quad (5.28)$$

Note that in (5.26) and (5.28) use have been made of the relationships provided by Remark 3.3.

Further expressing the second Piola-Kirchhoff stress tensor (5.19) in terms of the inner energy and the entropy density using  $\Psi(\mathbf{C}, \mathbf{G}, C, \theta) = \tilde{u}(\mathbf{C}, \mathbf{G}, C, \eta(\mathbf{C}, \theta)) - \theta \eta(\mathbf{C}, \theta)$  and  $u(\mathbf{C}, \mathbf{G}, C, \theta) = \tilde{u}(\mathbf{C}, \mathbf{G}, C, \eta(\mathbf{C}, \theta))$  yields

$$\mathbf{S} = 2(\partial_{\mathbf{C}}\Psi + \partial_{\mathbf{G}}\Psi * \mathbf{C} + \partial_C\Psi \mathbf{G}) = 2(\partial_{\mathbf{C}}u + \partial_{\mathbf{G}}u * \mathbf{C} + (\partial_{\mathbf{C}}u - \theta \partial_{\mathbf{C}}\eta) \mathbf{G}). \quad (5.29)$$

Using (5.27) and (5.28) makes possible to recast the governing equations (5.11) in the temperature form

$$\begin{aligned} \dot{\boldsymbol{\varphi}} &= \rho_0^{-1} \mathbf{p}, \\ \dot{\mathbf{p}} &= -\text{Div}(\mathbf{F} \mathbf{S}) + \bar{\mathbf{B}}, \\ \dot{\theta} &= -(\partial_{\theta}\eta)^{-1} \partial_{\mathbf{C}}\eta \mathbf{G} : \dot{\mathbf{C}} - (\partial_{\theta}u)^{-1} \text{Div}(\mathbf{Q}) + (\partial_{\theta}u)^{-1} \bar{R}, \end{aligned} \quad (5.30)$$

in  $\mathcal{B}_0$  for all  $t \in \mathcal{I}$  with suitable initial conditions (5.13).

**Remark 5.1.** Comparing (5.30) to (5.11) the formulation distinguishes three different key elements

- 1) the definition of the absolute temperature is used (see (5.27)),
- 2) the second Piola-Kirchhoff stress tensor is based on the internal energy and entropy density rather than the Helmholtz free energy (see (5.29)),
- 3) the balance of energy is rewritten in temperature-form (compare (5.30)<sub>3</sub> with the standard form (5.11)<sub>3</sub>),

which enable the design of structure preserving numerical methods as will be introduced, subsequently.

### 5.3.2 Temperature-based weak form

Introducing a time independent tangent space

$$\mathcal{W} = \{\mathbf{w}_z = (w_{\varphi}, w_{\mathbf{p}}, w_{\theta}) : \mathcal{B}_0 \rightarrow \mathbb{R}^3 \times \mathbb{R}^3 \times \mathbb{R}\}, \quad (5.31)$$

and the spaces of virtual or admissible test functions for the deformation and linear momentum  $\mathcal{W}_{\bullet} \subset \mathcal{W}$ , where  $\bullet \in \{\varphi, \mathbf{p}\}$ , as well as for the temperature  $\mathcal{W}_{\theta} \subset \mathcal{W}$  are given by

$$\begin{aligned} \mathcal{W}_{\bullet} &= \{\mathbf{w}_{\bullet} : \mathbf{w}_{\bullet}(\mathbf{X}) \in H^1(\mathcal{B}_0) \mid \mathbf{w}_{\bullet}(\mathbf{X}) = \mathbf{0} \text{ on } \partial\mathcal{B}_0^{\varphi}\}, \\ \mathcal{W}_{\theta} &= \{w_{\theta} : w_{\theta}(\mathbf{X}) \in H^1(\mathcal{B}_0) \mid w_{\theta}(\mathbf{X}) = 0 \text{ on } \partial\mathcal{B}_0^{\theta}\}, \end{aligned} \quad (5.32)$$

we obtain the temperature-based weak form by considering standard techniques like partial integration, the divergence theorem of Gauss etc.

$$\begin{aligned}
\int_{\mathcal{B}_0} \mathbf{w}_\varphi \cdot \dot{\boldsymbol{\varphi}} \, dV &= \int_{\mathcal{B}_0} \mathbf{w}_\varphi \cdot \rho_0^{-1} \mathbf{p} \, dV, \\
\int_{\mathcal{B}_0} \mathbf{w}_p \cdot \dot{\mathbf{p}} \, dV &= - \int_{\mathcal{B}_0} \mathbf{S} : (\partial_{\mathbf{X}} \mathbf{w}_p^T \mathbf{F}) \, dV + \int_{\mathcal{B}_0} \mathbf{w}_p \cdot \bar{\mathbf{B}} \, dV + \int_{\partial \mathcal{B}_0^p} \mathbf{w}_p \cdot \bar{\mathbf{T}} \, dA, \\
\int_{\mathcal{B}_0} \mathbf{w}_\theta \dot{\theta} \, dV &= - \int_{\mathcal{B}_0} \mathbf{w}_\theta (\partial_{\theta} \eta)^{-1} \partial_{\mathbf{C}} \eta \mathbf{G} : \dot{\mathbf{C}} + \partial_{\mathbf{X}} (\mathbf{w}_\theta (\partial_{\theta} u)^{-1}) \cdot \mathbf{Q} \, dV \\
&\quad + \int_{\mathcal{B}_0} \mathbf{w}_\theta (\partial_{\theta} u)^{-1} \bar{\mathbf{R}} \, dV + \int_{\partial \mathcal{B}_0^Q} \mathbf{w}_\theta (\partial_{\theta} u)^{-1} \bar{\mathbf{Q}} \, dA,
\end{aligned} \tag{5.33}$$

which have to hold for arbitrary  $\mathbf{w}_z \in \mathcal{W}$ . Further the weak form in (5.33) is supplemented with suitable initial conditions

$$\begin{aligned}
\int_{\mathcal{B}_0} \mathbf{w}_\varphi \cdot \boldsymbol{\varphi} \, dV &= \int_{\mathcal{B}_0} \mathbf{w}_\varphi \cdot \boldsymbol{\varphi}_0 \, dV, \\
\int_{\mathcal{B}_0} \mathbf{w}_p \cdot \mathbf{p} \, dV &= \int_{\mathcal{B}_0} \mathbf{w}_p \cdot \mathbf{p}_0 \, dV, \\
\int_{\mathcal{B}_0} \mathbf{w}_\theta \theta \, dV &= \int_{\mathcal{B}_0} \mathbf{w}_\theta \theta_0 \, dV.
\end{aligned} \tag{5.34}$$

### 5.3.3 Balance laws

Next we will show that the temperature-based formulation derived in the last section is just a reformulation of the classical formulation. The temperature-based formulation expresses the same physics in a slightly different way which provides a more elegant structure for the construction of EM consistent integrators. For a detailed investigation of the conservation properties a homogeneous Neumann problem is considered. In particular no Dirichlet boundaries are employed such that  $\partial \mathcal{B}_0^p = \partial \mathcal{B}_0^\theta = \emptyset$ . We verify the classical balance laws pertaining to the coupled problem at hand. The main goal of the present work is the design of numerical methods which preserve these balance laws under discretization.

### 5.3.3.1 Balance of linear momentum

For verification of the balance of total linear momentum the test functions in (5.33) are replaced by  $w_\varphi = \mathbf{0} \in \mathcal{W}_\varphi$ ,  $w_p = \zeta \in \mathcal{W}_p$  where  $\zeta \in \mathbb{R}^3$  is arbitrary but constant and  $w_\theta = 0 \in \mathcal{W}_\theta$ . This yields

$$\zeta \cdot \left( \frac{d}{dt} L - F^{\text{ext}} \right) = 0, \quad (5.35)$$

where the total linear momentum and the total external mechanical loads have been introduced in (3.19) and (3.20), respectively. Therefore, for vanishing external mechanical loads the total linear momentum is a constant of motion of the continuous system.

### 5.3.3.2 Balance of angular momentum

To verify the balance of angular momentum we choose the following admissible test functions  $w_\varphi = \zeta \times \dot{\varphi} \rho_0 \in \mathcal{W}_\varphi$ ,  $w_p = \zeta \times \varphi \in \mathcal{W}_p$  and  $w_\theta = 0 \in \mathcal{W}_e$  in (5.33), where  $\zeta \in \mathbb{R}^3$  is arbitrary, but constant. This choice of  $w_p$  leads to the relation  $\partial_\chi w_p = \hat{\zeta} F$  where  $\hat{\zeta}$  is a skew-symmetric tensor such that  $\hat{\zeta} a = \zeta \times a$  for any  $a \in \mathbb{R}^3$ . Following the lines of Sec. 3.1.2.2 we end up at the desired result

$$\zeta \cdot \left( \frac{d}{dt} J - M^{\text{ext}} \right) = 0, \quad (5.36)$$

where the total angular momentum and the total torque about a corresponding axis have been introduced in (3.24) and (3.25), respectively. Accordingly, for vanishing external mechanical loads the total angular momentum is a constant of motion of the continuous system.

### 5.3.3.3 Balance of energy

Total energy  $E = T + U$  is comprised of kinetic energy  $T = \int_{B_0} \frac{1}{2} \rho_0^{-1} \mathbf{p} \cdot \mathbf{p} dV$  and inner energy  $U = \int_{B_0} u dV$ . Furthermore  $Q^{\text{ext}}$  denotes the external thermal power containing bulk and boundary contributions given by

$$Q^{\text{ext}} = \int_{B_0} \bar{R} dV + \int_{\partial B_0^Q} \bar{Q} dA. \quad (5.37)$$

We choose the following admissible test functions  $w_\varphi = \dot{\mathbf{p}} \in \mathcal{W}_\varphi$ ,  $w_p = \dot{\boldsymbol{\varphi}} \in \mathcal{W}_p$  and  $w_\theta = \partial_\theta u \in \mathcal{W}_e$  in (5.33) for the verification of the balance of total energy to obtain

$$\begin{aligned}
\int_{\mathcal{B}_0} \dot{\mathbf{p}} \cdot \dot{\boldsymbol{\varphi}} \, dV &= \int_{\mathcal{B}_0} \dot{\mathbf{p}} \cdot \rho_0^{-1} \mathbf{p} \, dV, \\
\int_{\mathcal{B}_0} \dot{\boldsymbol{\varphi}} \cdot \dot{\mathbf{p}} \, dV &= - \int_{\mathcal{B}_0} 2 (\partial_{\mathbf{C}} u + \partial_{\mathbf{G}} u \star \mathbf{C} + (\partial_{\mathbf{C}} u - \theta \partial_{\mathbf{C}} \eta) \mathbf{G}) : (\dot{\mathbf{F}}^T \mathbf{F}) \, dV \\
&\quad + \int_{\mathcal{B}_0} \dot{\boldsymbol{\varphi}} \cdot \bar{\mathbf{B}} \, dV + \int_{\partial \mathcal{B}_0^p} \dot{\boldsymbol{\varphi}} \cdot \bar{\mathbf{T}} \, dA, \\
\int_{\mathcal{B}_0} \partial_{\theta u} \dot{\theta} \, dV &= - \int_{\mathcal{B}_0} \partial_{\theta u} (\partial_\theta \eta)^{-1} \partial_{\mathbf{C}} \eta \mathbf{G} : \dot{\mathbf{C}} \, dV + \partial_{\mathbf{x}} (\partial_{\theta u} (\partial_{\theta u})^{-1}) \cdot \mathbf{Q} \, dV \\
&\quad + \int_{\mathcal{B}_0} \partial_{\theta u} (\partial_{\theta u})^{-1} \bar{\mathbf{R}} \, dV + \int_{\partial \mathcal{B}_0^Q} \partial_{\theta u} (\partial_{\theta u})^{-1} \bar{\mathbf{Q}} \, dA.
\end{aligned} \tag{5.38}$$

Inserting (5.38)<sub>1</sub> into (5.38)<sub>2</sub>, using the time derivative of the total kinetic energy

$$\dot{T} = \frac{d}{dt} \int_{\mathcal{B}_0} \frac{1}{2} \rho_0^{-1} \mathbf{p} \cdot \mathbf{p} \, dV = \int_{\mathcal{B}_0} \rho_0^{-1} \dot{\mathbf{p}} \cdot \mathbf{p} \, dV, \tag{5.39}$$

adding (5.38)<sub>3</sub> and further using symmetry conditions we obtain the balance of total energy

$$\dot{E} = \dot{T} + \dot{U} = P^{\text{ext}} + Q^{\text{ext}}, \tag{5.40}$$

where we can identify the time derivative of the total internal energy

$$\dot{U} = \int_{\mathcal{B}_0} \partial_{\mathbf{C}} u : \dot{\mathbf{C}} + \partial_{\mathbf{G}} u : \dot{\mathbf{G}} + \partial_{\mathbf{C}} u \dot{\mathbf{C}} + \partial_{\theta u} \dot{\theta} \, dV, \tag{5.41}$$

using the identities  $\partial_{\mathbf{G}} u \star \mathbf{C} : \dot{\mathbf{C}} = \partial_{\mathbf{G}} u : \dot{\mathbf{G}}$ ,  $\mathbf{G} : \dot{\mathbf{C}} = \dot{\mathbf{C}}$ . For vanishing external mechanical and thermal loads the total energy is a constant of motion of the continuous system.

## 5.4 Discretization in time

Next we seek a sequence of states  $\{\boldsymbol{\varphi}_n, \mathbf{p}_n, \theta_n\}_{n=0}^N$  in  $\mathcal{S}$  approximating  $\{\boldsymbol{\varphi}_n, \mathbf{p}_n, \theta_n\} \approx \{\boldsymbol{\varphi}(t_n), \mathbf{p}(t_n), \theta(t_n)\}$ . To this end we aim at an one-step scheme which determines  $\{\boldsymbol{\varphi}_{n+1}, \mathbf{p}_{n+1}, \theta_{n+1}\}$  at time-level  $n+1$  from given approximations  $\{\boldsymbol{\varphi}_n, \mathbf{p}_n, \theta_n\}$  at time-level  $n$ .

### 5.4.1 Structure-preserving integration scheme

We propose the following semi-discrete version of the variational formulation (5.33). In this connection we make use of the notion of a discrete gradient derivative in the sense of [50]. Accordingly, consider the time-discrete version of (5.33) given by

$$\begin{aligned} \int_{\mathcal{B}_0} \mathbf{w}_\varphi \cdot \frac{1}{\Delta t} (\boldsymbol{\varphi}_{n+1} - \boldsymbol{\varphi}_n) \, dV &= \int_{\mathcal{B}_0} \mathbf{w}_\varphi \cdot \rho_0^{-1} \mathbf{p}_{n+\frac{1}{2}} \, dV, \\ \int_{\mathcal{B}_0} \mathbf{w}_\mathbf{p} \cdot \frac{1}{\Delta t} (\mathbf{p}_{n+1} - \mathbf{p}_n) \, dV &= - \int_{\mathcal{B}_0} \mathbf{S}_{\text{alg}} : (\partial_{\mathbf{X}} \mathbf{w}_\mathbf{p}^\top \mathbf{F}_{n+\frac{1}{2}}) \, dV \\ &\quad + \int_{\mathcal{B}_0} \mathbf{w}_\mathbf{p} \cdot \bar{\mathbf{B}}_{n+\frac{1}{2}} \, dV + \int_{\partial \mathcal{B}_0^p} \mathbf{w}_\mathbf{p} \cdot \bar{\mathbf{T}}_{n+\frac{1}{2}} \, dA, \end{aligned} \quad (5.42)$$

$$\begin{aligned} \int_{\mathcal{B}_0} \mathbf{w}_\theta \frac{1}{\Delta t} (\theta_{n+1} - \theta_n) \, dV &= - \int_{\mathcal{B}_0} \mathbf{w}_\theta (\mathbf{D}_\theta \eta)^{-1} \partial_{\mathbf{C}} \eta(\mathbf{z}_{n+\frac{1}{2}}) \mathbf{G}(\mathbf{z}_{n+\frac{1}{2}}) : \frac{1}{\Delta t} (\mathbf{C}_{n+1} - \mathbf{C}_n) \, dV \\ &\quad + \int_{\mathcal{B}_0} \partial_{\mathbf{X}} (\mathbf{w}_\theta (\mathbf{D}_\theta u)^{-1}) \cdot \mathbf{Q}(\mathbf{z}_{n+\frac{1}{2}}) \, dV \\ &\quad + \int_{\mathcal{B}_0} \mathbf{w}_\theta (\mathbf{D}_\theta u)^{-1} \bar{\mathbf{R}}_{n+\frac{1}{2}} \, dV + \int_{\partial \mathcal{B}_0^Q} \mathbf{w}_\theta (\mathbf{D}_\theta u)^{-1} \bar{\mathbf{Q}}_{n+\frac{1}{2}} \, dA, \end{aligned} \quad (5.43)$$

where

$$\theta_{\text{alg}} = \mathbf{D}_\theta u (\mathbf{D}_\theta \eta)^{-1}, \quad (5.44)$$

is the algorithmic temperature,  $\mathbf{G}_{\text{alg}}$  is the algorithmic cofactor of  $\mathbf{C}$  as introduced in (3.64), and

$$\mathbf{S}_{\text{alg}} = 2 (\mathbf{D}_{\mathbf{C}} u + \mathbf{D}_{\mathbf{G}} u * \mathbf{C}_{\text{alg}} + \mathbf{D}_{\mathbf{C}} u \mathbf{G}_{\text{alg}} - \theta_{\text{alg}} \partial_{\mathbf{C}} \eta(\mathbf{z}_{n+\frac{1}{2}}) \mathbf{G}(\mathbf{z}_{n+\frac{1}{2}})), \quad (5.45)$$

is the algorithmic second Piola-Kirchhoff stress tensor. In (5.43) the time-discrete version  $\mathbf{G}(\mathbf{z}_{n+\frac{1}{2}})$  yields

$$\mathbf{G}(\mathbf{z}_{n+\frac{1}{2}}) = \frac{1}{2} \mathbf{C}(\boldsymbol{\varphi}_{n+\frac{1}{2}}) * \mathbf{C}(\boldsymbol{\varphi}_{n+\frac{1}{2}}). \quad (5.46)$$

We collect the arguments of the density functions in the following quadruple

$$\boldsymbol{\pi} = \{\mathbf{C}, \mathbf{G}, \mathbf{C}, \theta\} = \{\pi^1, \pi^2, \pi^3, \pi^4\}. \quad (5.47)$$

Using the notation  $u(\boldsymbol{\pi}) = u(\mathbf{C}, \mathbf{G}, C, \theta)$  we introduce partitioned discrete gradients  $\bar{D}_{\pi^1}u = D_{\mathbf{C}}u$ ,  $\bar{D}_{\pi^2}u = D_{\mathbf{G}}u$ ,  $\bar{D}_{\pi^3}u = D_Cu$  and  $\bar{D}_{\pi^4}u = D_\theta u$  in the sense of [50] by

$$\begin{aligned}\bar{D}_{\pi^i}u &= \frac{1}{2}(\bar{D}_{\pi^i}u_{n+1,n} + \bar{D}_{\pi^i}u_{n,n+1}), \quad i \in Y = \{1, 2, 3, 4\}, \\ \bar{D}_{\pi_{n+1,n}^i}u &= \bar{D}_{\pi^i}u(\pi_{n+1}^i, \pi_n^i)|_{\pi_{n+1}^j, \pi_n^k}, \quad \forall j \in Y : j < i, k \in Y : k > i, \\ \bar{D}_{\pi_{n,n+1}^i}u &= \bar{D}_{\pi^i}u(\pi_n^i, \pi_{n+1}^i)|_{\pi_n^j, \pi_{n+1}^k}, \quad \forall j \in Y : j < i, k \in Y : k > i,\end{aligned}\quad (5.48)$$

where the discrete operators  $\bar{D}_{\pi^i}u(\pi_{n+1}^i, \pi_n^i)|_{\pi_{n+1}^j, \pi_n^k}$  and  $\bar{D}_{\pi^i}u(\pi_n^i, \pi_{n+1}^i)|_{\pi_n^j, \pi_{n+1}^k}$  are defined as

$$\begin{aligned}\bar{D}_{\pi^i}u|_{\pi_{n+1}^j, \pi_n^k} &= \partial_{\pi^i}u(\pi_{n+\frac{1}{2}}^i)|_{\pi_{n+1}^j, \pi_n^k} \\ &\quad + \frac{u(\pi_{n+1}^i)|_{\pi_{n+1}^j, \pi_n^k} - u(\pi_n^i)|_{\pi_{n+1}^j, \pi_n^k} - \langle \partial_{\pi^i}u(\pi_{n+\frac{1}{2}}^i)|_{\pi_{n+1}^j, \pi_n^k}, \Delta\pi^i \rangle}{\|\Delta\pi^i\|^2} \Delta\pi^i, \\ \bar{D}_{\pi^i}u|_{\pi_n^j, \pi_{n+1}^k} &= \partial_{\pi^i}u(\pi_{n+\frac{1}{2}}^i)|_{\pi_n^j, \pi_{n+1}^k} \\ &\quad + \frac{u(\pi_{n+1}^i)|_{\pi_n^j, \pi_{n+1}^k} - u(\pi_n^i)|_{\pi_n^j, \pi_{n+1}^k} - \langle \partial_{\pi^i}u(\pi_{n+\frac{1}{2}}^i)|_{\pi_n^j, \pi_{n+1}^k}, \Delta\pi^i \rangle}{\|\Delta\pi^i\|^2} \Delta\pi^i.\end{aligned}\quad (5.49)$$

Hereby  $\langle \cdot, \cdot \rangle$  denotes the inner product and  $\bar{D}_{\pi^i}u$  the discrete gradient of  $u$  with respect to  $\pi^i$ . From the directionality property of a discrete gradient [50] follows the relationship

$$\begin{aligned}\bar{D}_{\pi^1}u : (\pi_{n+1}^1 - \pi_n^1) &+ \bar{D}_{\pi^2}u : (\pi_{n+1}^2 - \pi_n^2) + \bar{D}_{\pi^3}u(\pi_{n+1}^3 - \pi_n^3) + \bar{D}_{\pi^4}u(\pi_{n+1}^4 - \pi_n^4) \\ &= D_{\mathbf{C}}u : (\mathbf{C}_{n+1} - \mathbf{C}_n) + D_{\mathbf{G}}u : (\mathbf{G}_{n+1} - \mathbf{G}_n) + D_Cu(C_{n+1} - C_n) + D_\theta u(\theta_{n+1} - \theta_n) \\ &= u(\mathbf{C}_{n+1}, \mathbf{G}_{n+1}, C_{n+1}, \theta_{n+1}) - u(\mathbf{C}_n, \mathbf{G}_n, C_n, \theta_n) = u_{n+1} - u_n.\end{aligned}\quad (5.50)$$

Further the quantity  $\rho_0^{-1}\mathbf{p}_{n+\frac{1}{2}}$  is a discrete gradient of the kinetic energy density since

$$\bar{D}_{\mathbf{p}}k \cdot (\mathbf{p}_{n+1} - \mathbf{p}_n) = \frac{1}{2}\rho_0^{-1}\mathbf{p}_{n+1} \cdot \mathbf{p}_{n+1} - \frac{1}{2}\rho_0^{-1}\mathbf{p}_n \cdot \mathbf{p}_n = k_{n+1} - k_n. \quad (5.51)$$

**Example (Mooney-Rivlin material cont'd):** Applying the Mooney-Rivlin material model introduced in Sec. 5.2 leads to the constant expressions of the discrete gradients

$$\begin{aligned}D_{\mathbf{C}}u &= a \mathbf{I}, \\ D_{\mathbf{G}}u &= b \mathbf{I}, \\ D_\theta u &= \kappa.\end{aligned}\quad (5.52)$$

Furthermore the discrete gradient  $D_C u$  reduces to a partitioned form of the well-known Greenspan formula [55], such that

$$D_C u = \frac{1}{2} \frac{u(C_{n+1}, \theta_n) - u(C_n, \theta_n)}{C_{n+1} - C_n} + \frac{1}{2} \frac{u(C_{n+1}, \theta_{n+1}) - u(C_n, \theta_{n+1})}{C_{n+1} - C_n}. \quad (5.53)$$

It is important to remark that the classical description of the density functions via only  $C$  and  $\theta$  would need tensor- and scalar-structured discrete gradient operators which greatly complicates the description.

## 5.4.2 Semi-discrete balance laws

Next we show that the semi-discrete formulation proposed in Sec. 5.4.1 satisfies specific balance laws in analogy to the continuous setting. As before in Sec. 5.3.3, we focus on the homogeneous Neumann problem.

### 5.4.2.1 Balance of linear momentum

Following the procedure in Sec. 5.3.3.1 for the verification of the balance of total linear momentum, the variations in (5.42) and (5.43) are replaced by  $w_\varphi = \mathbf{0} \in \mathcal{W}_\varphi$  and  $w_p = \zeta \in \mathcal{W}_p$  where  $\zeta \in \mathbb{R}^3$  is arbitrary but constant and  $w_\theta = 0 \in \mathcal{W}_e$  which yields

$$\zeta \cdot \left( \frac{1}{\Delta t} (L_{n+1} - L_n) - \mathbf{F}^{\text{ext}} \right) = 0. \quad (5.54)$$

Therefore, for vanishing external mechanical loads the total discrete linear momentum is a constant of motion of the semi-discrete system.

### 5.4.2.2 Balance of angular momentum

Following the procedure in Sec. 5.3.3.2 we choose the following admissible test functions  $w_\varphi = \zeta \times \frac{1}{\Delta t} (\varphi_{n+1} - \varphi_n) \rho_0 \in \mathcal{W}_\varphi$ ,  $w_p = \zeta \times \varphi_{n+\frac{1}{2}} \in \mathcal{W}_p$  and  $w_\theta = 0 \in \mathcal{W}_\theta$ , where  $\zeta \in \mathbb{R}^3$  is constant, in (5.42) and (5.43) to verify the balance of angular momentum. In the same way as in Sec. 3.1.2.2 we obtain the desired result

$$\zeta \cdot \left( \frac{1}{\Delta t} (J_{n+1} - J_n) - \mathbf{M}_{n,n+1}^{\text{ext}} \right) = 0, \quad (5.55)$$

where

$$\begin{aligned}
& \int_{\mathcal{B}_0} \zeta \times \frac{1}{\Delta t} (\boldsymbol{\varphi}_{n+1} - \boldsymbol{\varphi}_n) \cdot \boldsymbol{p}_{n+\frac{1}{2}} \, dV + \int_{\mathcal{B}_0} (\zeta \times \boldsymbol{\varphi}_{n+\frac{1}{2}}) \cdot \frac{1}{\Delta t} (\boldsymbol{p}_{n+1} - \boldsymbol{p}_n) \, dV \\
&= \zeta \cdot \int_{\mathcal{B}_0} \frac{1}{\Delta t} (\boldsymbol{\varphi}_{n+1} - \boldsymbol{\varphi}_n) \times \boldsymbol{p}_{n+\frac{1}{2}} + \boldsymbol{\varphi}_{n+\frac{1}{2}} \times \frac{1}{\Delta t} (\boldsymbol{p}_{n+1} - \boldsymbol{p}_n) \, dV \quad (5.56) \\
&= \zeta \cdot \int_{\mathcal{B}_0} \frac{1}{\Delta t} (\boldsymbol{\varphi}_{n+1} \times \boldsymbol{p}_{n+1} - \boldsymbol{\varphi}_n \times \boldsymbol{p}_n) \, dV = \zeta \cdot \int_{\mathcal{B}_0} \frac{1}{\Delta t} (\boldsymbol{J}_{n+1} - \boldsymbol{J}_n) \, dV,
\end{aligned}$$

has been used. For vanishing external mechanical loads the total discrete angular momentum is a constant of motion of the semi-discrete system.

### 5.4.2.3 Balance of energy

Following the procedure in Sec. 5.3.3.3 we choose the following admissible test functions  $\boldsymbol{w}_\varphi = \frac{1}{\Delta t} (\boldsymbol{p}_{n+1} - \boldsymbol{p}_n) \in \mathcal{W}_\varphi$ ,  $\boldsymbol{w}_p = \frac{1}{\Delta t} (\boldsymbol{\varphi}_{n+1} - \boldsymbol{\varphi}_n) \in \mathcal{W}_p$  and  $\boldsymbol{w}_\theta = D_\theta u \in \mathcal{W}_\theta$  in (5.42) and (5.43). We obtain

$$\begin{aligned}
0 &= \int_{\mathcal{B}_0} \frac{1}{\Delta t} (\boldsymbol{p}_{n+1} - \boldsymbol{p}_n) \cdot \frac{1}{\Delta t} (\boldsymbol{\varphi}_{n+1} - \boldsymbol{\varphi}_n) \, dV - \int_{\mathcal{B}_0} \frac{1}{\Delta t} (\boldsymbol{p}_{n+1} - \boldsymbol{p}_n) \cdot \rho_0^{-1} \boldsymbol{p}_{n+\frac{1}{2}} \, dV, \\
0 &= \int_{\mathcal{B}_0} \frac{1}{\Delta t} (\boldsymbol{\varphi}_{n+1} - \boldsymbol{\varphi}_n) \cdot \frac{1}{\Delta t} (\boldsymbol{p}_{n+1} - \boldsymbol{p}_n) \, dV + \int_{\mathcal{B}_0} \mathcal{S}_{\text{alg}} : \frac{1}{\Delta t} (\partial_x (\boldsymbol{\varphi}_{n+1} - \boldsymbol{\varphi}_n))^T \boldsymbol{F}_{n+\frac{1}{2}} \, dV \\
&\quad - \int_{\mathcal{B}_0} \frac{1}{\Delta t} (\boldsymbol{\varphi}_{n+1} - \boldsymbol{\varphi}_n) \cdot \bar{\boldsymbol{B}}_{n+\frac{1}{2}} \, dV - \int_{\partial \mathcal{B}_0^p} \frac{1}{\Delta t} (\boldsymbol{\varphi}_{n+1} - \boldsymbol{\varphi}_n) \cdot \bar{\boldsymbol{T}}_{n+\frac{1}{2}} \, dA, \\
0 &= \int_{\mathcal{B}_0} D_\theta u \frac{1}{\Delta t} (\theta_{n+1} - \theta_n) \, dV + \int_{\mathcal{B}_0} \theta_{\text{alg}} \partial_C \eta(z_{n+\frac{1}{2}}) \boldsymbol{G}(z_{n+\frac{1}{2}}) : \frac{1}{\Delta t} (\boldsymbol{C}_{n+1} - \boldsymbol{C}_n) \, dV \\
&\quad - \int_{\mathcal{B}_0} \bar{\boldsymbol{R}}_{n+\frac{1}{2}} \, dV - \int_{\partial \mathcal{B}_0^Q} \bar{\boldsymbol{Q}}_{n+\frac{1}{2}} \, dA. \quad (5.57)
\end{aligned}$$

Subtracting (5.57)<sub>1</sub> from (5.57)<sub>2</sub>, adding the last equation yields the discrete balance of total energy

$$\frac{1}{\Delta t} (E_{n+1} - E_n) - P_{n,n+1}^{\text{ext}} - Q_{n,n+1} = 0. \quad (5.58)$$

In this connection use has been made of the identity  $\text{sym}(2\partial_{\mathbf{x}}(\boldsymbol{\varphi}_{n+1} - \boldsymbol{\varphi}_n)^T \mathbf{F}_{n+\frac{1}{2}}) = \mathbf{C}_{n+1} - \mathbf{C}_n$  to obtain

$$\begin{aligned} & \int_{\mathcal{B}_0} \mathbf{D}_{\mathbf{C}} u : (\mathbf{C}_{n+1} - \mathbf{C}_n) + \mathbf{D}_{\mathbf{G}} u : (\mathbf{G}_{n+1} + \mathbf{G}_n) + \mathbf{D}_{\mathbf{C}} u (\mathbf{C}_{n+1} - \mathbf{C}_n) + \mathbf{D}_{\theta} u (\theta_{n+1} - \theta_n) \, dV \\ &= \int_{\mathcal{B}_0} u_{n+1} - u_n \, dV = U_{n+1} - U_n. \end{aligned} \quad (5.59)$$

Furthermore, we find

$$\int_{\mathcal{B}_0} (\mathbf{p}_{n+1} - \mathbf{p}_n) \cdot \rho_0^{-1} \mathbf{p}_{n+\frac{1}{2}} \, dV = \int_{\mathcal{B}_0} \frac{1}{2} \rho_0^{-1} \mathbf{p}_{n+1} \cdot \mathbf{p}_{n+1} - \frac{1}{2} \rho_0^{-1} \mathbf{p}_n \cdot \mathbf{p}_n \, dV = T_{n+1} - T_n. \quad (5.60)$$

In balance equation (5.58), the discrete versions of the total mechanical power (3.31) and the total thermal power  $Q_{n,n+1}$  are given by

$$\begin{aligned} P_{n,n+1}^{\text{ext}} &= \int_{\mathcal{B}_0} \frac{1}{\Delta t} (\boldsymbol{\varphi}_{n+1} - \boldsymbol{\varphi}_n) \cdot \bar{\mathbf{B}} \, dV + \int_{\partial \mathcal{B}_0^p} \frac{1}{\Delta t} (\boldsymbol{\varphi}_{n+1} - \boldsymbol{\varphi}_n) \cdot \bar{\mathbf{T}} \, dA, \\ Q_{n,n+1} &= \int_{\mathcal{B}_0} \bar{R}_{n+\frac{1}{2}} \, dV + \int_{\partial \mathcal{B}_0^Q} \bar{Q}_{n+\frac{1}{2}} \, dA, \end{aligned} \quad (5.61)$$

with bulk and boundary contributions have been used. Therefore for vanishing external mechanical and thermal power the total energy is conserved in the discrete setting.

## 5.5 Discretization in space

For the discretization in space we apply standard isoparametric finite elements (see, for example, Hughes [71]) based on finite-dimensional approximations

$\mathbf{z}^h = \{\boldsymbol{\varphi}^h, \mathbf{p}^h, \theta^h\} \in \mathcal{S}^h \subset \mathcal{S}$  of the form

$$\begin{aligned} \boldsymbol{\varphi}^h(\mathbf{X}) &= \sum_{a=1}^{n_{\text{node}}} N_a(\mathbf{X}) \boldsymbol{\varphi}_a(t), \quad \mathbf{p}^h(\mathbf{X}) = \sum_{a=1}^{n_{\text{node}}} N_a(\mathbf{X}) \mathbf{p}_a(t) \quad \text{and} \\ \theta^h(\mathbf{X}) &= \sum_{a=1}^{n_{\text{node}}} N_a(\mathbf{X}) \theta_a(t). \end{aligned} \quad (5.62)$$

Here  $N_a : \mathcal{B}_0 \rightarrow \mathbb{R}$  denote the nodal shape functions with associated nodal quantities  $\boldsymbol{\varphi}_a(t), \mathbf{p}_a(t) \in \mathbb{R}^3$  and  $\theta_a(t) \in \mathbb{R}^+$  the respective nodal values at time  $t$ . Moreover,  $n_{\text{node}}$

denotes the total number of nodes in the finite element mesh. The standard (Bubnov) Galerkin approach relies on analogous approximations for  $w_\varphi \in \mathcal{W}_\varphi$ ,  $w_p \in \mathcal{W}_p$  and  $w_\theta \in \mathcal{W}_\theta$  denoted by  $w_\varphi^h \in \mathcal{W}_\varphi^h$ ,  $w_p^h \in \mathcal{W}_p^h$  and  $w_\theta^h \in \mathcal{W}_\theta^h$ . It can easily be proven that the spatial discretization process does not affect the balance laws in Sec. 5.4.2.1, 5.4.2.2 and 5.4.2.3. Accordingly, the proposed discretization in space and time leads to a scheme that inherits the fundamental balance laws from the continuous formulation. It is important to mention that the energy balance consistency for the fully discretized system is restricted to constant (temperature-independent) values of the specific heat capacity  $\kappa$  as considered in the material model in Sec. 5.2. If a non-constant function for the specific heat capacity is considered a  $L_2$ -projection similar to the procedure proposed in [90, 144] is necessary for energy consistency.

## 5.6 Numerical Investigations

In this section, we show the improved behavior of the energy-momentum consistent algorithm by some classical thermo-elastodynamic benchmark problems. For subsequent examples a compressible Mooney-Rivlin material model is employed given by

$$\Psi(C, G, C, \theta) = \Psi^{\text{mech},1}(C, G) + \Psi^{\text{mech},2}(C) + \Psi^{\text{temp}}(\theta) + \Psi^{\text{couple}}(C, \theta), \quad (5.63)$$

where the mechanical, the thermal and the coupling contribution of  $\Psi$  are chosen as

$$\begin{aligned} \Psi^{\text{mech},1}(C, G) &= a (\text{tr}(C) - 3) + b (\text{tr}(G) - 3), \\ \Psi^{\text{mech},2}(C) &= \frac{c_1}{2} (C^{1/2} - 1)^2 - d_1 \log(C^{1/2}), \\ \Psi^{\text{temp}}(\theta) &= \kappa \left( \theta - \theta_0 - \theta \log \left( \frac{\theta}{\theta_0} \right) \right), \\ \Psi^{\text{couple}}(C, \theta) &= 3\beta (\theta - \theta_0) (c_2 (C^{1/2} - 1) - d_2 C^{-1/2}). \end{aligned} \quad (5.64)$$

The parameters  $a, b, c_1, d_1, \kappa, c_2, d_2, \beta \geq 0$  are specified in the sequel and can be linked to linear theory (for more information see Appendix D.3). It is important to remark that  $d_1 = 2(a + 2b)$  is a dependend parameter.

For a comparison of the proposed EM consistent formulation, we use a classical thermo-mechanical finite element along with the mid-point (MP) rule as a standard time-stepping scheme, see Appendix D.2 for details. Concerning the iterative solution by Newton's method, we apply an energy-based termination criterion described in Appendix D.1.

**Remark 5.2.** As shown in [44, Sec. 7.1.1], the formulation presented in this chapter is capable to reproduce homogeneous states of stress and temperature. Moreover we show in [44, Sec. 7.1.2] that the newly proposed EM consistent scheme and the standard mid-point-type scheme yield practically identical numerical results for quasi-static problems at hand.

## 5.6.1 L-shaped block

The objectives of this example are:

- O1.I** Verification of the algorithmic conservation properties.
- O1.II** Verification of numerical stability.
- O1.III** Verification of order of accuracy.

As a first example we consider a L-shaped block depicted in Fig. 5.1 as a thermo-elastodynamical extension of the example presented in Sec. 3.4.3. The block can freely move in space. Time-dependent pressure loads are acting on the L-shaped block as illustrated in Fig. 5.1. In this connection, the nodal dead loads are given by

$$\mathbf{P}_1(t) = -\mathbf{P}_2(t) = f(t) \begin{pmatrix} 256/9 \\ 512/9 \\ 768/9 \end{pmatrix} \frac{\text{N}}{\text{m}^2}, \quad \text{with} \quad f(t) = \begin{cases} t & \text{for } t \leq 2.5\text{s} \\ 5 - t & \text{for } 2.5 \leq t \leq 5\text{s} \\ 0 & \text{for } t > 5\text{s} \end{cases} . \quad (5.65)$$

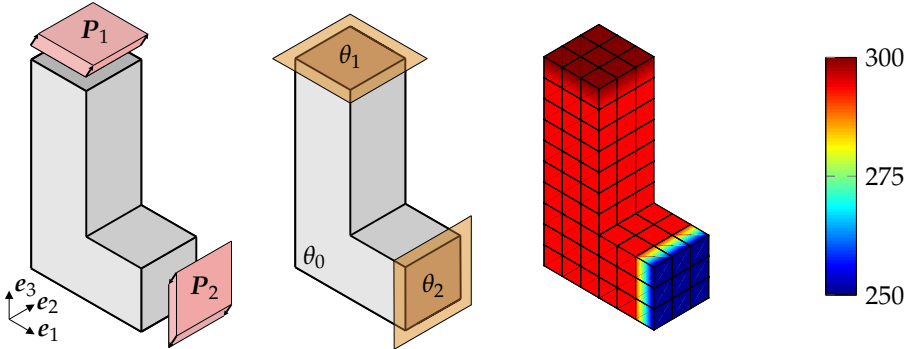
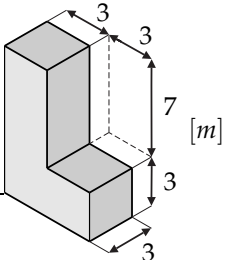


Figure 5.1: L-shaped block: Mechanical boundary conditions (left), initial temperature conditions (center), discretized model (right).

Moreover, two faces of the block are subjected to initial temperature conditions (see Fig. 5.1). The temperature of these faces deviates from the initially homogeneous

temperature distribution of the solid. For the discretization of the L-shaped block 117 tri-linear finite elements with 224 nodes have been used (see Fig. 5.1). The thermo-hyperelastic behavior of the L-shaped block is governed by the material model given in (5.63). The data for this example is summarized in Tab. 5.1. Due the chosen material parameters and boundary conditions, the L-shaped block undergoes large deformations coupled with large rotations and translations. Note that after the loading phase, there are no external loads acting on the system and the discrete system under consideration can be classified as an isolated system with symmetry. Correspondingly, after  $t > 5s$ , the total linear momentum, the total angular momentum as well as the total energy are conserved quantities. All simulations have been performed with the newly introduced EM consistent integrator and the standard midpoint (MP) scheme (see Appendix D.2).

Table 5.1: Thermoelastic compressible Mooney-Rivlin material data, simulation parameters and geometry.

mechanical parameters	$a$	831.2500	Pa	geometry of the L-Shape 
	$b$	166.2500	Pa	
	$c_1 = c_2$	0	Pa	
	$d_2 = d_1$	$2(a+2b)$	Pa	
specific heat capacity	$\kappa$	100	$\text{JK}^{-1}\text{m}^{-3}$	
coupling coefficient	$\beta$	$2.233 \cdot 10^{-4}$	$\text{K}^{-1}$	
thermal conductivity	$k_0$	10	$\text{WK}^{-1}\text{m}^{-1}$	
reference temperature	$\theta_0$	293.15	K	
density	$\rho_0$	100	$\text{kgm}^{-3}$	
initial temperature	$\theta_1$	300	K	
	$\theta_2$	250	K	
Newton tolerance	$\varepsilon$	$10^{-6}$	-	
simulation time	$T$	100	s	
timestep size	$\Delta t$	0.8	s	

It can be observed in Fig. 5.2, that the EM consistent integrator correctly reproduces conservation of energy and is numerically stable during the simulation. In contrast, the midpoint integrator leads to numerical instabilities accompanied by an energy blow-up. Fig. 5.3 shows that after loading phase the change of energy from time step to time step is bounded by the Newton tolerance. Eventually, conservation of the total

angular momentum and the incremental change thereof is illustrated in Fig. 5.4 and Fig. 5.5.

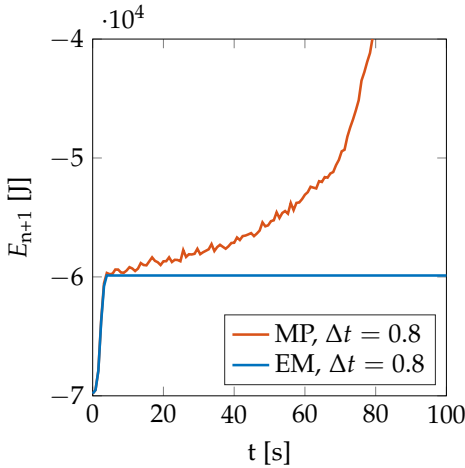


Figure 5.2: Total energy evolution.

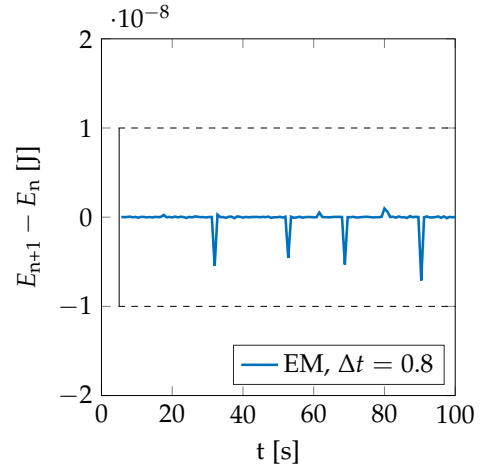


Figure 5.3: Discrete energy difference.

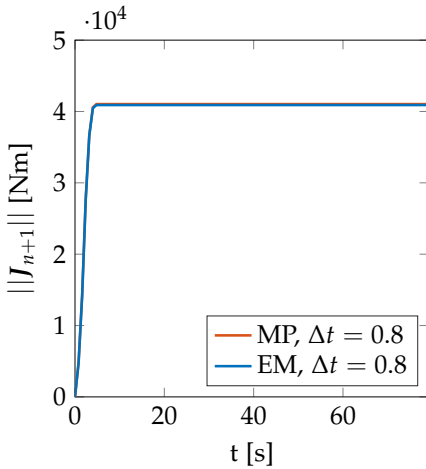


Figure 5.4: Total angular momentum evolution.

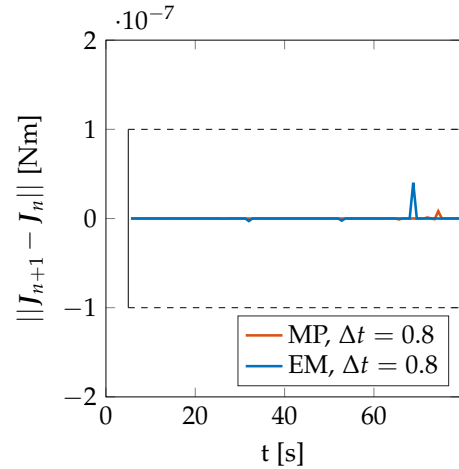


Figure 5.5: Discrete angular momentum difference.

Moreover, we investigate the order of accuracy of the present method. Similar to the midpoint rule we expect second-order accuracy. To verify this, we define the  $L_2$  norm of the error in the positions as given by (4.92). We investigate the free-flying motion of the L-shaped block and consider the time-interval  $5s \leq t \leq 6s$ . As it can be observed

in Fig. 5.6, the proposed formula has a second order of accuracy in the positions.

The motion of the L-shaped block with its corresponding temperature distribution is depicted in Fig. 5.7.

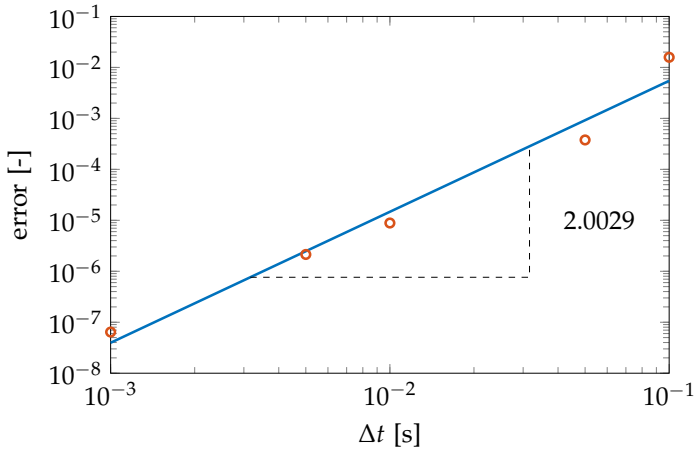


Figure 5.6: Study of convergence of the error in displacements.

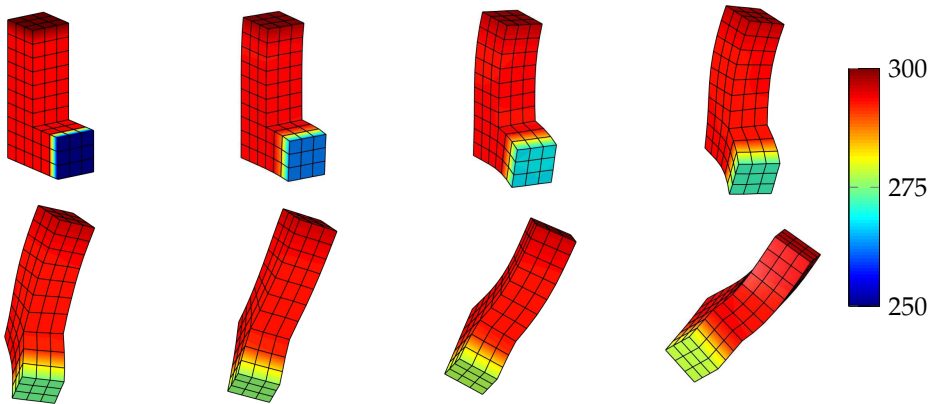


Figure 5.7: Snapshots with temperature distribution of the flying L-shape at  $t = \{0, 1.5, 3.0, 4.5, 6.0, 7.5, 9.0, 10.5\}$  s.

## 5.6.2 Rotating disc

The objectives of this example are:

**O2.I** Verification of the algorithmic energy approximation.

**O2.II** Verification of numerical stability.

The next numerical example deals with the simulation of a free flying disc as introduced in [57]. The thermo-hyperelastic solid, shown in Fig. 5.8, is not subject to any mechanical loads. The motion of the disc is initialized by the given vector field

$$\mathbf{V}_0(\mathbf{X}) = \mathbf{V}_0^{\text{tr}} + \boldsymbol{\omega}_0 \times \mathbf{X}, \quad (5.66)$$

where  $\mathbf{V}_0^{\text{tr}} = \mathbf{0} \frac{\text{m}}{\text{s}}$  and  $\boldsymbol{\omega}_0 = (e_1 + e_2 + e_3) \frac{1}{5}$ . Moreover, the disc has a homogeneous distribution of the initial temperature  $\theta_0$ . A thermal Neumann boundary condition on a quarter of the lateral surface  $A_0$  (see Fig. 5.8) is considered, where the sinusoidal heat flow  $Q$  into the system is given by

$$Q = \frac{2000W}{A_0} f(t), \quad \text{with} \quad f(t) = \begin{cases} \sin\left(2\frac{\pi}{4}t\right) & \text{for } t \leq 4\text{s} \\ 0 & \text{for } t > 4\text{s} \end{cases}, \quad (5.67)$$

Note that the prescribed heat flow vanishes at  $t = 4\text{s}$ . The initial configuration of the discretized system is depicted in Fig. 5.8 where 200 tri-linear finite elements with 360 nodes have been used.

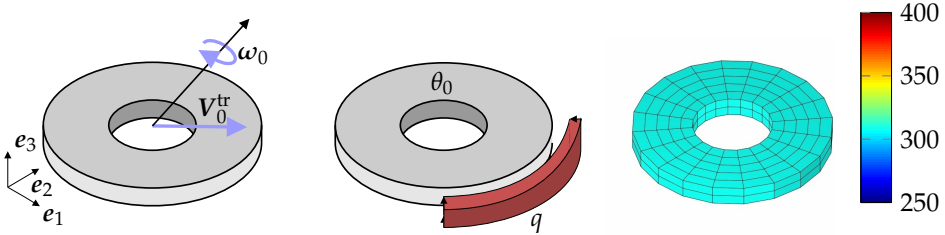


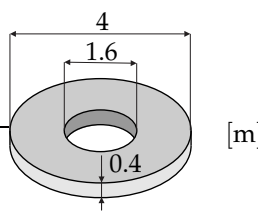
Figure 5.8: Initial configuration of the moving disc. Initialized motion (left), thermal boundary conditions (center), discretized model (right).

Again the constitutive model is given in (5.63). The material data, the simulation parameters and the geometry of the disc are summarized in Tab. 5.2.

Depending on the heat flow across the boundary, we expect an increase followed by a decrease of the total energy within the initial phase. Note that for  $t \geq 4\text{s}$ ,

the total energy is a conserved quantity. These properties are reproduced by the proposed EM consistent time integrator as it can be observed in Fig. 5.9. Moreover, after loading phase the incremental change of the total energy (see Appendix D.1), which is bounded by the Newton tolerance, is shown in Fig. 5.10. In contrast to that, the MP integrator fails to preserve the energy and exhibits an energy blow-up at about  $t = 9$ s.

Table 5.2: Thermoelastic compressible Mooney-Rivlin material data, simulation parameters and geometry.

mechanical parameters	$a$	831.2500	Pa	geometry of the disc 
	$b$	166.2500	Pa	
specific heat capacity	$\kappa$	100	$\text{JK}^{-1}\text{m}^{-3}$	
coupling coefficient	$\beta$	$2.223 \cdot 10^{-4}$	$\text{K}^{-1}$	
thermal conductivity	$k_0$	10	$\text{WK}^{-1}\text{m}^{-1}$	
reference temperature	$\theta_0$	308.15	K	
density	$\rho_0$	10	$\text{kgm}^{-3}$	
Newton tolerance	$\varepsilon$	$1 \cdot 10^{-6}$	-	
timestep size	$\Delta t$	0.2	s	
simulation time	$T$	20	s	

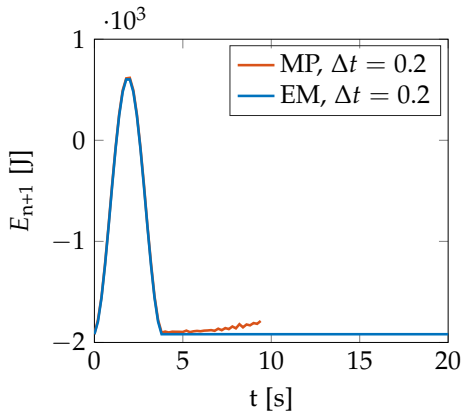


Figure 5.9: Total energy evolution.

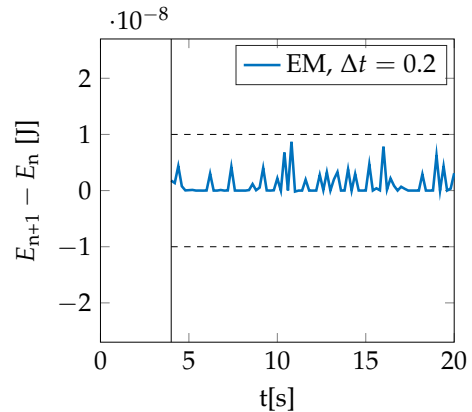


Figure 5.10: Discrete energy difference.

Eventually, the motion of the rotating disc is illustrated in Fig. 5.11 with a sequence of subsequent snapshots.

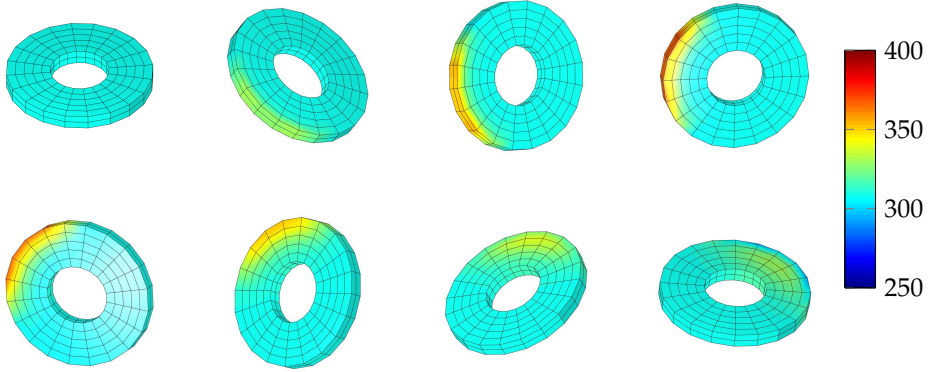


Figure 5.11: Snapshots and temperature plots of the rotating disc at  $t = \{0, 0.4, 0.8, 1.2, 1.6, 2.0, 2.4, 2.8\}$ s.

### 5.6.3 Moving disc

The objectives of this example are:

**O3.I** Verification of the algorithmic energy approximation.

**O3.II** Verification of numerical stability and validity.

The last example of this chapter deals with a moving disc subjected to both, mechanical and thermal Dirichlet boundary conditions. The thermo-hyperelastic free flying disc can be viewed as a three dimensional version of the problem introduced in [57], where the disc thickness is equal 1m. As illustrated in Fig. 5.12, the mechanical Dirichlet boundary conditions constrained the height of the disc, so that plane strain condition is enforced.

In addition, the translation and rotation of the disc is initialized by

$$\mathbf{V}_0(\mathbf{X}) = \mathbf{V}_0^{\text{tr}} + \boldsymbol{\omega}_0 \times \mathbf{X}, \quad (5.68)$$

where the initial translation velocity is given by  $\mathbf{V}_0^{\text{tr}} = 20 \mathbf{e}_1 \frac{\text{m}}{\text{s}}$  and the initial angular velocity about the  $\mathbf{e}_3$ -axis is given by  $\boldsymbol{\omega}_0 = -7 \mathbf{e}_3 \frac{1}{\text{s}}$ .

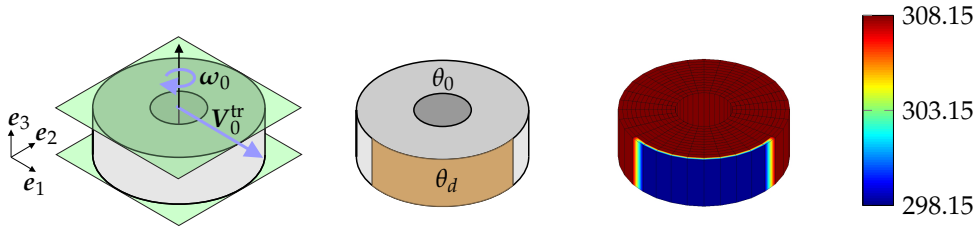
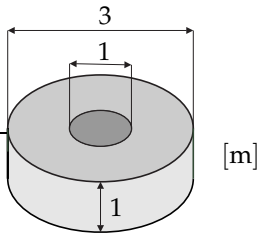


Figure 5.12: Initial configuration of the moving disc. Initialized motion (left), thermal boundary conditions (center), discretized model (right).

The thermal Dirichlet boundary condition constrains one quarter of the lateral surface of the disc to  $\theta_d = \theta_0 - 10\text{K}$  where  $\theta_0$  is the reference temperature homogeneously distributed over the rest of the body. Furthermore, Fig. 5.12 shows the discretized disc where 416 tri-linear finite elements with 896 nodes have been used. The thermo-hyperelastic material data, the simulation parameters as well as the geometry of the disc are summarized in Tab. 5.3.

Table 5.3: Thermoelastic compressible Mooney-Rivlin material data, simulation parameters and geometry.

mechanical parameters	$a$	831.2500	Pa	geometry of the disc 
	$b$	166.2500	Pa	
specific heat capacity	$\kappa$	300	$\text{JK}^{-1}\text{m}^{-3}$	
coupling coefficient	$\beta$	$2.223 \cdot 10^{-4}$	$\text{K}^{-1}$	
thermal conductivity	$k_0$	300	$\text{WK}^{-1}\text{m}^{-1}$	
reference temperature	$\theta_0$	308.15	K	
density	$\rho_0$	10	$\text{kgm}^{-3}$	
Newton tolerance	$\varepsilon$	$1 \cdot 10^{-6}$	-	
timestep size	$\Delta t$	0.035	s	
simulation time	$T$	20.3	s	

Due to the thermal Neumann boundary condition and the associated temperature gradient, heat is withdrawn from the body till temperature is distributed almost equally across the body. The loss of energy during the simulated cooling is correctly reproduced by the EM consistent integrator as observed from Fig. 5.13. In contrast, the midpoint integrator leads to numerical instabilities for the chosen time-step size.

Before the energy-blow up at about  $t = 7\text{s}$ , the MP scheme yields a non-physical temperature distribution, whereas the EM consistent integrator shows a smooth behavior of the temperature gradient which can be observed in Fig. 5.14. Finally, to illustrate the motion and temperature distribution of the body at hand several snapshots are plotted in Fig. 5.15 where the EM consistent integrator has been used.

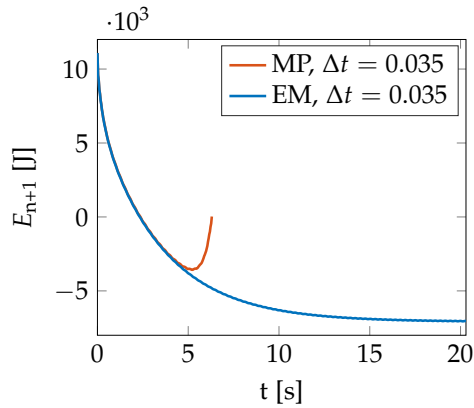


Figure 5.13: Total energy evolution.

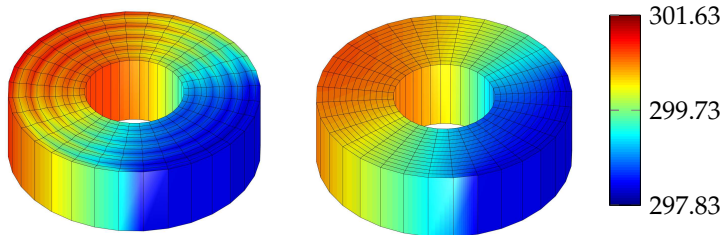


Figure 5.14: Temperature distribution at  $t = 5.39\text{s}$  using the midpoint integrator (left) and the EM consistent integrator (right).

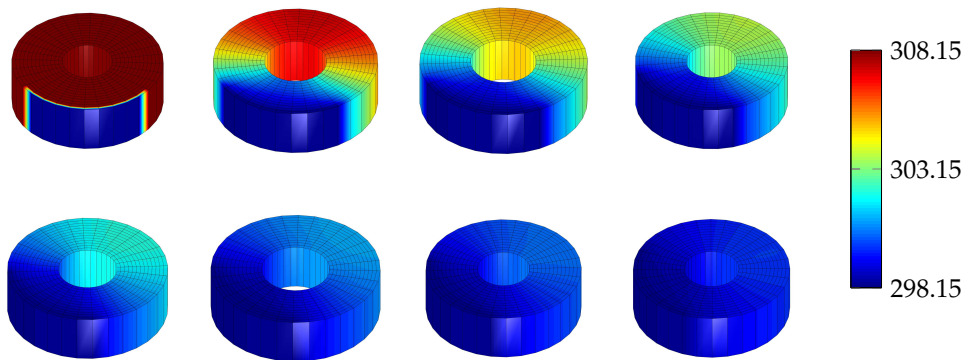


Figure 5.15: Snapshots and temperature plots of the moving disc at  $t = \{0, 1.015, 2.03, 3.045, 4.06, 5.075, 6.09, 7.105\}$ s.

## 6 EM scheme for nonlinear electro-elastodynamics<sup>1</sup>

In this chapter we provide a new approach of a one-step second order accurate EM time integrator scheme in the context of nonlinear electro-elastodynamics. Moreover, we consider well-posed *ab initio* convex multi-variable constitutive models. The new time integrator relies on the definition of four discrete derivatives of the internal energies representing the algorithmic counterparts of the work conjugates of the right Cauchy-Green deformation tensor, its co-factor, its determinant and the Lagrangian electric displacement field. Finally, a series of numerical examples are included in order to demonstrate the robustness and conservation properties of the proposed scheme, specifically in the case of long-term simulations.

### 6.1 Finite strain electrostatic-elastodynamics

Let us now consider the body  $\mathcal{B}_0$ , introduced in Sec. 2.2, as an EAP. The local form of conservation of linear momentum [53] can be written as

$$\begin{aligned} \rho_0 \dot{V} - \text{Div} (F S) - \bar{B} &= \mathbf{0}, & \text{in } \mathcal{B}_0, \\ (F S) N &= \bar{T}, & \text{on } \partial \mathcal{B}_0^P, \\ \varphi &= \bar{\varphi}, & \text{on } \partial \mathcal{B}_0^\varphi, \end{aligned} \quad (6.1)$$

where (6.1) can be recast from (5.11) along with (5.12) if we consider thermal isolated systems.

---

<sup>1</sup> This chapter is based on [133].

The governing equations in non-linear electromechanics are the Gauss's and Faraday's laws which can be recast from the well-known Maxwell equations in the absence of magnetic and time dependent effects. The local form of the Gauss's law [161, 116, 110] can be written in a Lagrangian setting as

$$\begin{aligned} \operatorname{Div} \mathbf{D} - \rho_0^e &= 0, & \text{in } \mathcal{B}_0, \\ \mathbf{D} \cdot \mathbf{N} &= -\omega_0^e, & \text{on } \partial \mathcal{B}_0^\omega, \end{aligned} \quad (6.2)$$

where  $\mathbf{D} : \mathcal{B}_0 \rightarrow \mathbb{R}^3$  is the Lagrangian electric displacement vector,  $\rho_0^e : \mathcal{B}_0 \rightarrow \mathbb{R}$  represents an electric volume charge per unit of undeformed volume  $\mathcal{B}_0$  and  $\omega_0^e : \partial \mathcal{B}_0^\omega \rightarrow \mathbb{R}$ , an electric surface charge per unit of undeformed area  $\partial \mathcal{B}_0^\omega \subset \partial \mathcal{B}_0$ . Furthermore, in the absence of magnetic fields, the local form of the static Faraday's law can be written in a Lagrangian setting as

$$\begin{aligned} \mathbf{E} &= -\bar{\partial} \chi \phi, & \text{in } \mathcal{B}_0, \\ \phi &= \bar{\phi}, & \text{on } \partial \mathcal{B}_0^\phi, \end{aligned} \quad (6.3)$$

where  $\mathbf{E} : \mathcal{B}_0 \rightarrow \mathbb{R}^3$  is the Lagrangian electric field vector and  $\phi : \mathcal{B}_0 \rightarrow \mathbb{R}$ , the scalar electric potential. In (6.3),  $\partial \mathcal{B}_0^\phi$  represents the part of the boundary  $\partial \mathcal{B}_0$  where essential electric potential boundary conditions are applied such that  $\partial \mathcal{B}_0^\omega \cup \partial \mathcal{B}_0^\phi = \partial \mathcal{B}_0$  and  $\partial \mathcal{B}_0^\omega \cap \partial \mathcal{B}_0^\phi = \emptyset$ .

## 6.2 Constitutive equations for large strain electro-elasticity

The governing equations presented in Section 6.1 are coupled by means of a suitable constitutive law. The objective of the following section is to introduce some notions on constitutive laws in nonlinear electro-elasticity.

In the case of reversible electro-elasticity, the internal energy density  $u$  per unit of undeformed volume can be defined in terms of the deformation and the electric displacement field, namely  $\hat{u} = \hat{u}(\mathbf{F}, \mathbf{D})$ , see [116]. Motivated solely by considerations of material stability, Gil and Ortigosa [47, 129, 128, 131] extended the concept of polyconvexity [7, 8] to the context of electromechanics and defined new convexity restrictions on the internal energy, postulating a convex multi-variable definition as

$$\hat{u}(\mathbf{F}, \mathbf{D}) = \tilde{u}(\mathbf{F}, \mathbf{H}, \mathbf{J}, \mathbf{D}, \mathbf{d}), \quad \mathbf{d} = \mathbf{F} \mathbf{D}, \quad (6.4)$$

where  $\tilde{u}$  must be a convex function with respect to the extended set  $\{F, H, J, D, d\}$ . It is crucial that the above convex multi-variable representation in (6.4) satisfies the concept of ellipticity for the entire range of deformations and electric displacement fields. In addition, for the requirement of objectivity, the convex multi-variable energy  $\tilde{u}$  (6.4) can be re-expressed in terms of a set of objective arguments (see Sec. 2.2.2) as

$$\hat{u}(F, D) = \hat{u}(C, D) = u_{\text{obj}}(C, G, C, D, CD) = u(C, G, C, D), \quad (6.5)$$

where  $\hat{u}$  represents the internal energy in terms of the right Cauchy-Green strain tensor  $C$  and  $D$  and  $u$  denotes the internal energy expressed in terms of the extended symmetric mechanical kinematic set  $\{C, G, C\}$  as introduced in (2.41)-(2.43) and  $D$ . Notice in equation (6.5) the argument  $CD$  has been removed as it is redundant (it can be expressed in terms of  $C$  and  $D$ ). It is worth noting that  $u$  is not convex with respect to the individual components of the set  $\{C, G, C, D\}$ , but rather an objective (frame invariant) re-expression of the convex multi-variable functional  $\tilde{u}$ . In this case<sup>2</sup>,

$$D\hat{u}(C, D)[\delta\varphi] = S : \frac{1}{2} DC[\delta\varphi], \quad D\hat{u}(C, D)[\delta D] = E \cdot \delta D, \quad (6.6)$$

where the second Piola-Kirchhoff stress tensor  $S$  and the material electric field  $E$  are defined in terms of the derivatives of the internal energy  $\hat{u}(C, D)$ , namely

$$S = 2\partial_C \hat{u}(C, D), \quad E = \partial_D \hat{u}(C, D). \quad (6.7)$$

An alternative but equivalent definition of the directional derivatives of the internal energy  $\hat{u}(C, D)$  to those in (6.6) can be obtained by considering its equivalent extended representation  $u$ ,

$$Du[\delta\varphi] = \partial_C u : DC[\delta\varphi] + \partial_G u : DG[\delta\varphi] + \partial_C u DC[\delta\varphi], \quad (6.8)$$

and

$$Du[\delta D] = \partial_D u \cdot \delta D. \quad (6.9)$$

Finally, inserting (2.56), (2.57) and (2.58) into (6.8) and comparison with (6.6)<sub>1</sub> enables to obtain an equivalent expression for  $S$  and  $E$  to those in equations (6.7)<sub>1</sub> and (6.7)<sub>2</sub>, respectively, as

$$S = 2\partial_C u + 2\partial_G u * C + 2\partial_C u G, \quad E = \partial_D u. \quad (6.10)$$

<sup>2</sup> Use of the first law of thermodynamics and consideration of reversibility has been made of.

**Example (Mooney-Rivlin material):** It is customary to propose an additive decomposition of the internal energy  $\hat{u}(C, D)$  into a purely mechanical contribution and a coupled electromechanical contribution [31, 168, 75] as

$$\hat{u}(C, D) = \hat{u}_m(C) + \hat{u}_{em}(C, D). \quad (6.11)$$

The purely mechanical contribution of a Mooney-Rivlin model is defined via the following polyconvex energy functional

$$\hat{u}_m^{MR}(C) = u_m^{MR}(C, G, C) = u^{\text{mech},1}(C, G) + u^{\text{mech},2}(C), \quad (6.12)$$

where the purely mechanical parts  $u^{\text{mech},1}(C, G)$  and  $u^{\text{mech},2}(C)$  have been introduced in (2.52) and (2.53), respectively. The convex function  $\Gamma^1$  now reads  $\Gamma^1(\delta) = \frac{c_1}{2}(\delta - 1)^2 - d_1 \log(\delta)$ , where  $a$ ,  $b$  and  $c_1$  are material parameters with units of stress related to the shear modulus  $\mu$  and the bulk modulus  $\lambda$  in the origin as  $\mu = 2a + 2b$  and  $\lambda = c_1 + 4b$ .

The simplest expression for the electromechanical contribution corresponds to that of an ideal dielectric elastomer, defined as

$$\hat{u}_{em}(C, D) = u_{em}(C, C, D) = \frac{1}{2 \varepsilon_r \varepsilon C^{1/2}} D \cdot C D, \quad (6.13)$$

where  $\varepsilon$  represents the permittivity of vacuum, with  $\varepsilon = 8.8541 \times 10^{-12} \text{NC}^{-2}\text{m}^{-2}$  and  $\varepsilon_r$  represents the relative permittivity of the material.

## 6.3 Variational formulation

The objective of this section is to present the variational formulation that will be used in order to develop an EM time integration scheme in Sec. 6.4.

### 6.3.1 Three-field mixed formulation for electro-mechanics

A three-field mixed variational principle in the context of static electro-mechanics (where inertial effects are not considered) can be defined as

$$\Pi(\varphi, \phi, D) = \int_{\mathcal{B}_0} u(C, G, C, D) \, dV - \int_{\mathcal{B}_0} D \cdot E \, dV + \Pi_m^{\text{ext}}(\varphi) - \Pi_e^{\text{ext}}(\phi). \quad (6.14)$$

The reader is referred to Reference [47] for the derivation of above variational principle. In (6.14), the mechanical contribution of the external potential energy  $\Pi_m^{\text{ext}}(\boldsymbol{\varphi})$  has been introduced in (2.25) and the electro contribution  $\Pi_e^{\text{ext}}(\phi)$  is defined as

$$\Pi_e^{\text{ext}}(\phi) = - \int_{\mathcal{B}_0} \rho_0^e \phi \, dV - \int_{\partial \mathcal{B}_0^e} \omega_0^e \phi \, dA. \quad (6.15)$$

In equation (6.14),  $\boldsymbol{\varphi} \in \mathcal{Q}$ ,  $\phi \in \mathcal{Q}_\phi$  and  $\mathbf{D} \in \mathbb{V}_D$  where

$$\begin{aligned} \mathcal{Q}_\phi &= \{ \phi : \mathcal{B}_0 \rightarrow \mathbb{R} \mid \phi = \bar{\phi} \, \forall \, \mathbf{X} \in \partial \mathcal{B}_0^\phi \}, \\ \mathbb{V}_D &= \{ \mathbf{D} : \mathcal{B}_0 \rightarrow \mathbb{R}^3 \mid \text{for } D_i \in \mathbb{L}_2(\mathcal{B}_0) \}. \end{aligned} \quad (6.16)$$

Similarly, let us consider admissible variations  $\delta \boldsymbol{\varphi} \in \mathcal{V}$ ,  $\delta \phi \in \mathcal{V}_\phi$  and  $\delta \mathbf{D} \in \mathbb{V}_D$  with

$$\mathcal{V}_\phi = \{ \delta \phi : \mathcal{B}_0 \rightarrow \mathbb{R} \mid \delta \phi = 0 \text{ for } \mathbf{X} \in \partial \mathcal{B}_0^\phi \}. \quad (6.17)$$

The stationary conditions of the mixed variational principle  $\Pi$  in (6.14) yield

$$\begin{aligned} \mathbf{D}_\boldsymbol{\varphi} \Pi[\delta \boldsymbol{\varphi}] &= \int_{\mathcal{B}_0} \mathbf{S} : \frac{1}{2} \mathbf{DC}[\delta \boldsymbol{\varphi}] \, dV - \int_{\mathcal{B}_0} \bar{\mathbf{B}} \cdot \delta \boldsymbol{\varphi} \, dV - \int_{\partial \mathcal{B}_0^p} \bar{\mathbf{T}} \cdot \delta \boldsymbol{\varphi} \, dA = 0, \\ \mathbf{D}_\phi \Pi[\delta \phi] &= \int_{\mathcal{B}_0} -\mathbf{D} \cdot \mathbf{DE}[\delta \phi] \, dV + \int_{\mathcal{B}_0} \rho_0^e \delta \phi \, dV + \int_{\partial \mathcal{B}_0^e} \omega_0^e \delta \phi \, dA = 0, \\ \mathbf{D}_D \Pi[\delta \mathbf{D}] &= \int_{\mathcal{B}_0} \delta \mathbf{D} \cdot (\partial_D u - \mathbf{E}) \, dV = 0, \end{aligned} \quad (6.18)$$

with  $\mathbf{S}$  defined in (6.10)<sub>1</sub>. Above equation (6.18)<sub>1</sub> represents the weak form of the local balance of linear momentum in (6.1) for the case where no inertia effects are considered. In addition, equation (6.18)<sub>2</sub> corresponds to the weak form of the Gauss law in (6.2). Finally, equation (6.18)<sub>3</sub> represents the weak form of the Faraday law in (6.3).

**Remark 6.1.** *The convex multi-variable nature of the internal energy  $\hat{u}(\mathbf{F}, \mathbf{D})$  ensures convexity of  $\hat{u}(\mathbf{C}, \mathbf{D})$  and  $u(\mathbf{C}, \mathbf{G}, \mathbf{C}, \mathbf{D})$  with respect to  $\mathbf{D}$ . Consequently, a one-to-one and invertible relationship between variables  $\mathbf{D}$  and  $\mathbf{E}$  can always be established. Therefore, it is possible to make use of a partial Legendre transform of the internal energy which leads to the definition of the Helmholtz free energy functional  $\Psi(\mathbf{C}, \mathbf{G}, \mathbf{C}, \mathbf{E})$  as*

$$\Psi(\mathbf{C}, \mathbf{G}, \mathbf{C}, \mathbf{E}) = -\mathbf{E} \cdot \mathbf{D} + u(\mathbf{C}, \mathbf{G}, \mathbf{C}, \mathbf{D}), \quad (6.19)$$

where use of (6.10)<sub>2</sub> has been made of.

Furthermore, starting from the total potential  $\Pi$  in (6.14), use of the Legendre transformation in (6.19) leads to a two-field formulation with unknowns  $\{\boldsymbol{\varphi}, \phi\}$  in terms of the Helmholtz functional as

$$\Pi_{\Psi}(\boldsymbol{\varphi}, \phi) = \int_{\mathcal{B}_0} \Psi(\mathbf{C}, \mathbf{G}, \mathbf{C}, \mathbf{E}) dV + \Pi_m^{\text{ext}}(\boldsymbol{\varphi}) - \Pi_e^{\text{ext}}(\phi). \quad (6.20)$$

The stationary conditions of the functional yields

$$\begin{aligned} D_{\boldsymbol{\varphi}} \Pi_{\Psi}[\delta\boldsymbol{\varphi}] &= \int_{\mathcal{B}_0} \mathbf{S} : \frac{1}{2} \text{DC}[\delta\boldsymbol{\varphi}] dV - \int_{\mathcal{B}_0} \bar{\mathbf{B}} \cdot \delta\boldsymbol{\varphi} dV - \int_{\partial\mathcal{B}_0^p} \bar{\mathbf{T}} \cdot \delta\boldsymbol{\varphi} dA = 0, \\ D_{\phi} \Pi_{\Psi}[\delta\phi] &= \int_{\mathcal{B}_0} \partial_E \Psi \cdot \text{DE}[\delta\phi] dV + \int_{\mathcal{B}_0} \rho_0^e \delta\phi dV + \int_{\partial\mathcal{B}_0^q} \omega_0^e \delta\phi dA = 0, \end{aligned} \quad (6.21)$$

with

$$\mathbf{S} = 2 \partial_{\mathbf{C}} \Psi + 2 \partial_{\mathbf{G}} \Psi * \mathbf{C} + 2 \partial_{\mathbf{C}} \Psi \mathbf{G}. \quad (6.22)$$

The variational principle in (6.20) is typically preferred in finite element implementations. However, the a priori definition of a materially stable Helmholtz functional is not in general possible due to its saddle point nature. Therefore, we advocate in this work for the definition of materially stable convex multi-variable internal energy functionals  $u(\mathbf{C}, \mathbf{G}, \mathbf{C}, \mathbf{D})$  (featuring in the three-field principle) which through (6.19), yield materially stable Helmholtz energy functionals [47]. More information concerning the Helmholtz free energy function can be found in [133].

### 6.3.2 Extension to electro-elastodynamics

The objective of this section is to extend the proposed formulation of electro-elastostatics to the electro-elastodynamic regime. The extension of the variational formulation (6.18) to elasto-dynamics follows the lines of Sec. 3.1.1 and is given by

$$\begin{aligned} \int_{\mathcal{B}_0} (\mathbf{V} - \dot{\boldsymbol{\varphi}}) \cdot \rho_0 \delta\mathbf{V} dV &= 0, \\ \int_{\mathcal{B}_0} \rho_0 \dot{\mathbf{V}} \cdot \delta\boldsymbol{\varphi} dV + \int_{\mathcal{B}_0} \mathbf{S} : \frac{1}{2} \text{DC}[\delta\boldsymbol{\varphi}] dV - \int_{\mathcal{B}_0} \bar{\mathbf{B}} \cdot \delta\boldsymbol{\varphi} dV - \int_{\partial\mathcal{B}_0^p} \bar{\mathbf{T}} \cdot \delta\boldsymbol{\varphi} dA &= 0, \\ \int_{\mathcal{B}_0} -\mathbf{D} \cdot \text{DE}[\delta\phi] dV + \int_{\mathcal{B}_0} \rho_0^e \delta\phi dV + \int_{\partial\mathcal{B}_0^q} \omega_0^e \delta\phi dA &= 0, \\ \int_{\mathcal{B}_0} \delta\mathbf{D} \cdot (\partial_D u - \mathbf{E}) dV &= 0. \end{aligned} \quad (6.23)$$

The above equations have to hold for arbitrary  $\{\delta \mathbf{V}, \delta \boldsymbol{\varphi}\} \in \mathcal{V}$ ,  $\delta \boldsymbol{\varphi} \in \mathcal{V}_\varphi$  and  $\delta \mathbf{D} \in \mathbb{V}_D$ . Note that an integration by parts with respect to time has been used on the first term on the right hand-side of (6.23)<sub>2</sub>. Equation (6.23)<sub>1</sub> represents the weak form for the relationship between the velocity field  $\mathbf{V}$  and the time derivative of the mapping  $\boldsymbol{\varphi}$  and equation (6.23)<sub>2</sub>, the extension of the weak form of the balance of linear momentum in (6.18)<sub>1</sub> to electro-elastodynamics (hence the equation is supplemented with the inertia term). Finally, notice that both weak forms for the Gauss and Faraday law in (6.23)<sub>3</sub> and (6.23)<sub>4</sub> are identical to those in the static case in (6.18)<sub>2</sub> and (6.18)<sub>3</sub>, respectively.

**Remark 6.2.** *Similarly to Remark 3.5, the Euler-Lagrange equations that correspond to the variational equations (6.23) can be derived by the conditions of stationarity on the following action functional:*

$$S(\mathbf{V}, \boldsymbol{\varphi}, \phi, \mathbf{D}) = \int_{t_0}^t \left( \int_{B_0} \left( \dot{\boldsymbol{\varphi}} - \frac{1}{2} \mathbf{V} \right) \cdot \mathbf{V} \rho_0 \, dV - \int_{B_0} u(\mathbf{C}, \mathbf{G}, \mathbf{C}, \mathbf{D}) \, dV \right. \\ \left. + \int_{B_0} \mathbf{D} \cdot \mathbf{E} \, dV - \Pi_m^{\text{ext}}(\boldsymbol{\varphi}) + \Pi_e^{\text{ext}}(\phi) \right) dt, \quad (6.24)$$

where  $t_0$  and  $t$  represent any two instances of time with  $t > t_0$ .

### 6.3.3 Balance laws

Starting with the stationary conditions (6.23) the following sections derive the global balance laws for linear momentum, angular momentum, the Gauss's law and energy of the EAP.

#### 6.3.3.1 Balance of linear momentum

For an admissible variation of the displacement field we choose  $\delta \boldsymbol{\varphi} = \boldsymbol{\zeta}$ , with  $\boldsymbol{\zeta} \in \mathbb{R}^3$ , where  $\boldsymbol{\zeta}$  is constant. Then the stationary condition in (6.23)<sub>2</sub> leads to the global form of the conservation of linear momentum, namely

$$\boldsymbol{\zeta} \cdot \left( \frac{d}{dt} \mathbf{L} - \mathbf{F}^{\text{ext}} \right) = 0, \quad (6.25)$$

where the total linear momentum  $\mathbf{L}$  and the total external force  $\mathbf{F}^{\text{ext}}$  have been introduced in (3.19) and (3.20), respectively. From (6.25) it is possible to conclude that  $\mathbf{L}$  is a constant of motion for the case of vanishing external forces  $\mathbf{F}^{\text{ext}}$ .

### 6.3.3.2 Balance of angular momentum

For an admissible variation of  $\delta\boldsymbol{\varphi}$  we choose a rotational field  $\delta\boldsymbol{\varphi} = \boldsymbol{\zeta} \times \boldsymbol{\varphi}$  and  $\delta\mathbf{V} = \boldsymbol{\zeta} \times \dot{\boldsymbol{\varphi}}$ , with  $\boldsymbol{\zeta} \in \mathbb{R}^3$ . Following the lines of 3.1.2.2, the stationary condition in (6.23)<sub>2</sub> leads to the global form of the conservation of angular momentum, namely

$$\boldsymbol{\zeta} \cdot \left( \frac{d}{dt} \mathbf{J} - \mathbf{M}^{\text{ext}} \right) = 0, \quad (6.26)$$

where  $\mathbf{J}$  represents the total angular momentum and  $\mathbf{M}^{\text{ext}}$ , the total external torque, see (3.24) and (3.25), respectively. From (6.26), it is clear that  $\mathbf{J}$  is a constant of motion for vanishing external torques  $\mathbf{M}^{\text{ext}}$ .

### 6.3.3.3 Balance of Gauss's law

Taking  $\delta\boldsymbol{\varphi} = \boldsymbol{\zeta}$ , where  $\boldsymbol{\zeta} \in \mathbb{R}$  is arbitrary but constant, the stationary condition (6.23)<sub>3</sub> leads to the global form of the Gauss' law

$$\int_{\mathcal{B}_0} \rho_0^e dV + \int_{\partial\mathcal{B}_0^e} \omega_0^e dA = 0. \quad (6.27)$$

Then, for time independent volumetric and surface electrical charges  $\rho_0^e$  and  $\omega_0^e$ , equation (6.27) dictates that the total electric charge of the system is conserved and equal to zero.

### 6.3.3.4 Balance of energy

We now focus on the balance law for total energy. Choose admissible variations of the form  $\delta\mathbf{V} = \dot{\mathbf{V}} \in \mathcal{V}$ ,  $\delta\boldsymbol{\varphi} = \dot{\boldsymbol{\varphi}} \in \mathcal{V}$ ,  $\delta\boldsymbol{\phi} = \dot{\boldsymbol{\phi}} \in \mathcal{V}_\phi$  and  $\delta\mathbf{D} = \dot{\mathbf{D}} \in \mathbb{V}_D$  in (6.23). This yields

$$\begin{aligned} \int_{\mathcal{B}_0} (\mathbf{V} - \dot{\boldsymbol{\varphi}}) \cdot \rho_0 \dot{\mathbf{V}} dV &= 0, \\ \int_{\mathcal{B}_0} \rho_0 \dot{\mathbf{V}} \cdot \dot{\boldsymbol{\varphi}} dV + \int_{\mathcal{B}_0} \mathbf{S} : \frac{1}{2} \dot{\mathbf{C}} dV - \int_{\mathcal{B}_0} \bar{\mathbf{B}} \cdot \dot{\boldsymbol{\varphi}} dV - \int_{\partial\mathcal{B}_0^p} \bar{\mathbf{T}} \cdot \dot{\boldsymbol{\varphi}} dA &= 0, \\ \int_{\mathcal{B}_0} -\mathbf{D} \cdot \dot{\mathbf{E}} dV + \int_{\mathcal{B}_0} \rho_0^e \dot{\boldsymbol{\phi}} dV + \int_{\partial_\omega\mathcal{B}_0} \omega_0^e \dot{\boldsymbol{\phi}} dA &= 0, \\ \int_{\mathcal{B}_0} \dot{\mathbf{D}} \cdot (\partial_D u - \mathbf{E}) dV &= 0. \end{aligned} \quad (6.28)$$

Addition of the four equations in (6.28) leads, in the case of time independent forces  $\bar{\mathbf{B}}$  and  $\bar{\mathbf{T}}$  and charges  $\rho_0^e$  and  $\omega_0^e$  to

$$\begin{aligned} \dot{T} + \int_{\mathcal{B}_0} \left( \mathbf{S} : \frac{1}{2} \dot{\mathbf{C}} + \partial_D u \cdot \dot{\mathbf{D}} \right) dV - \int_{\mathcal{B}_0} (\mathbf{D} \cdot \dot{\mathbf{E}} + \dot{\mathbf{D}} \cdot \mathbf{E}) dV \\ + \dot{\Pi}_m^{\text{ext}}(\boldsymbol{\varphi}) - \dot{\Pi}_e^{\text{ext}}(\boldsymbol{\phi}) = 0, \end{aligned} \quad (6.29)$$

where the kinetic power  $\dot{T}$  has been introduced in (3.27). Finally, equation (6.29) can be re-written as

$$\dot{T} + \int_{\mathcal{B}_0} \dot{u}(\mathbf{C}, \mathbf{G}, \mathbf{C}, \mathbf{D}) dV - \int_{\mathcal{B}_0} \frac{d}{dt} (\mathbf{D} \cdot \mathbf{E}) dV + \dot{\Pi}_m^{\text{ext}}(\boldsymbol{\varphi}) - \dot{\Pi}_e^{\text{ext}}(\boldsymbol{\phi}) = 0. \quad (6.30)$$

It is therefore clear that in the case of time independent forces and electric charges, the following condition holds

$$\dot{H} = 0, \quad H = T + \int_{\mathcal{B}_0} u(\mathbf{C}, \mathbf{G}, \mathbf{C}, \mathbf{D}) dV - \int_{\mathcal{B}_0} \mathbf{D} \cdot \mathbf{E} dV + \Pi_m^{\text{ext}}(\boldsymbol{\varphi}) - \Pi_e^{\text{ext}}(\boldsymbol{\phi}), \quad (6.31)$$

and therefore the scalar field  $H$  is preserved throughout the motion of the EAP.

## 6.4 Discretization in time

Now we deal with the structure-preserving discretization in time of the underlying variational formulation of the electro-elastodynamic system. The discretization of the time interval of interest follows the lines of Sec. 3.2. The aim of this section is to define an implicit one-step time integrator that determines  $\{\mathbf{V}_{n+1}, \boldsymbol{\varphi}_{n+1}, \phi_{n+1}, \mathbf{D}_{n+1}\} \in \mathcal{V} \times \mathcal{Q} \times \mathcal{Q}_\phi \times \mathbb{V}_D$  on time node  $t_{n+1}$  from the given approximations  $\{\mathbf{V}_n, \boldsymbol{\varphi}_n, \phi_n, \mathbf{D}_n\} \in \mathcal{V} \times \mathcal{Q} \times \mathcal{Q}_\phi \times \mathbb{V}_D$  on time node  $t_n$ .

### 6.4.1 Structure-preserving integration scheme

Following the ideas of Sec. 3.2, Sec. 4.4 and Sec. 5.4, the objective of this section is to propose a structure-preserving time discretization scheme for the set of weak forms

in (6.23). From the stationary conditions in (6.23), the following implicit one-step time integrator is proposed

$$\begin{aligned}
\int_{\mathcal{B}_0} \delta \mathbf{V} \cdot \frac{1}{\Delta t} (\boldsymbol{\varphi}_{n+1} - \boldsymbol{\varphi}_n) \rho_0 \, dV &= \int_{\mathcal{B}_0} \delta \mathbf{V} \cdot \mathbf{V}_{n+\frac{1}{2}} \rho_0 \, dV, \\
\int_{\mathcal{B}_0} \delta \boldsymbol{\varphi} \cdot \frac{1}{\Delta t} (\mathbf{V}_{n+1} - \mathbf{V}_n) \rho_0 \, dV &= - \int_{\mathcal{B}_0} \mathbf{S}_{\text{alg}} : \frac{1}{2} \text{DC}[\delta \boldsymbol{\varphi}]|_{n+\frac{1}{2}} \, dV - \text{D}\Pi_m^{\text{ext}}[\delta \boldsymbol{\varphi}]|_{n+\frac{1}{2}} \\
\int_{\mathcal{B}_0} -\mathbf{D}_{n+\frac{1}{2}} \cdot \text{DE}[\delta \phi] \, dV - \text{D}\Pi_e^{\text{ext}}[\delta \phi]|_{n+\frac{1}{2}} &= 0, \\
\int_{\mathcal{B}_0} \delta \mathbf{D} \cdot (\mathbf{D}_{\mathbf{D}} u - \mathbf{E}_{n+\frac{1}{2}}) \, dV &= 0,
\end{aligned} \tag{6.32}$$

for arbitrary  $\{\delta \mathbf{V}, \delta \boldsymbol{\varphi}\} \in \mathcal{V}$ ,  $\delta \phi \in \mathcal{V}_\phi$  and  $\delta \mathbf{D} \in \mathbb{V}_{\mathbf{D}}$ . In the first term on the right-hand side of (6.32)<sub>2</sub> the algorithmic stress tensor  $\mathbf{S}_{\text{alg}}$  is given by

$$\mathbf{S}_{\text{alg}} = 2 (\text{D}_{\mathbf{C}} u + \text{D}_{\mathbf{G}} u \star \mathbf{C}_{\text{alg}} + \text{D}_{\mathbf{C}} u \mathbf{G}_{\text{alg}}), \tag{6.33}$$

where the algorithmic expressions  $\mathbf{C}_{\text{alg}}$  and  $\mathbf{G}_{\text{alg}}$  have been introduced in (3.63) and (3.64), respectively. In (6.32) and (6.33),  $\{\text{D}_{\mathbf{C}} u, \text{D}_{\mathbf{G}} u, \text{D}_{\mathbf{C}} u, \text{D}_{\mathbf{D}} u\}$  represent the discrete derivatives [52] of the internal energy  $u$ , which are the algorithmic or time discrete counterparts of  $\{\partial_{\mathbf{C}} u, \partial_{\mathbf{G}} u, \partial_{\mathbf{C}} u, \partial_{\mathbf{D}} u\}$ , respectively.

In this work, we use a definition of the (multiple) discrete derivative expressions  $\{\text{D}_{\mathbf{C}} u, \text{D}_{\mathbf{G}} u, \text{D}_{\mathbf{C}} u, \text{D}_{\mathbf{D}} u\}$  of the internal energy based on the derivation presented in Sec. 5.4.1 for energies depending upon several arguments.

Similarly to (5.47), we now introduce the quadruple where we collect the arguments of the internal energy density function as

$$\boldsymbol{\pi} = \{\mathbf{C}, \mathbf{G}, \mathbf{C}, \mathbf{D}\} = \{\pi^1, \pi^2, \pi^3, \pi^4\}. \tag{6.34}$$

Next, the partitioned discrete gradients  $\bar{\text{D}}_{\pi^1} u = \text{D}_{\mathbf{C}} u$ ,  $\bar{\text{D}}_{\pi^2} u = \text{D}_{\mathbf{G}} u$ ,  $\bar{\text{D}}_{\pi^3} u = \text{D}_{\mathbf{C}} u$  and  $\bar{\text{D}}_{\pi^4} u = \text{D}_{\mathbf{D}} u$  can be constructed by (5.48) and (5.49).

It can be verified, by using the discrete derivatives the important directionality property

$$\begin{aligned}
\bar{\text{D}}_{\pi^1} u : (\pi_{n+1}^1 - \pi_n^1) + \bar{\text{D}}_{\pi^2} u : (\pi_{n+1}^2 - \pi_n^2) + \bar{\text{D}}_{\pi^3} u (\pi_{n+1}^3 - \pi_n^3) + \bar{\text{D}}_{\pi^4} u (\pi_{n+1}^4 - \pi_n^4) \\
= \text{D}_{\mathbf{C}} u : (\mathbf{C}_{n+1} - \mathbf{C}_n) + \text{D}_{\mathbf{G}} u : (\mathbf{G}_{n+1} - \mathbf{G}_n) + \text{D}_{\mathbf{C}} u (\mathbf{C}_{n+1} - \mathbf{C}_n) + \text{D}_{\mathbf{D}} u \cdot (\mathbf{D}_{n+1} - \mathbf{D}_n) \\
= u(\mathbf{C}_{n+1}, \mathbf{G}_{n+1}, \mathbf{C}_{n+1}, \mathbf{D}_{n+1}) - u(\mathbf{C}_n, \mathbf{G}_n, \mathbf{C}_n, \mathbf{D}_n) = u_{n+1} - u_n,
\end{aligned} \tag{6.35}$$

holds (see Appendix E.1) and the algorithm preserves energy under zero or time invariant external forces and electric charges. Moreover, the discrete gradients are well defined in the limit as  $\|C_{n+1} - C_n\| \rightarrow 0$ ,  $\|G_{n+1} - G_n\| \rightarrow 0$ ,  $|C_{n+1} - C_n| \rightarrow 0$  and  $\|D_{n+1} - D_n\| \rightarrow 0$  which ensures that for sufficiently regular solutions

$$S_{\text{alg}} = S(\pi_{n+\frac{1}{2}}) + O(\Delta t^2) \quad \text{and} \quad D_D u = \partial_D u(\pi_{n+\frac{1}{2}}) + O(\Delta t^2), \quad (6.36)$$

and therefore, the proposed EM time integrator is second order accurate, see Appendix E.2 for details.

**Example (Mooney-Rivlin material cont'd):** Again, we focus on a Mooney-Rivlin material model as introduced in (6.12). Next, we derive the generic expression for the discrete derivatives.

The discrete gradients  $D_C u$  is given as

$$\begin{aligned} D_C u &= \frac{1}{2} (\partial_C u(C_{n+\frac{1}{2}}, G_{n+1}, C_{n+1}, D_{n+1}) + \partial_C u(C_{n+\frac{1}{2}}, G_n, C_n, D_n)) \\ &\quad + \frac{1}{2} \frac{u(C_{n+1}, G_{n+1}, C_{n+1}, D_{n+1}) - u(C_n, G_{n+1}, C_{n+1}, D_{n+1})}{\|C_{n+1} - C_n\|^2} (C_{n+1} - C_n) \\ &\quad + \frac{1}{2} \frac{u(C_{n+1}, G_n, C_n, D_n) - u(C_n, G_n, C_n, D_n)}{\|C_{n+1} - C_n\|^2} (C_{n+1} - C_n) \\ &\quad - \frac{1}{2} \frac{\partial_C u(C_{n+\frac{1}{2}}, G_{n+1}, C_{n+1}, D_{n+1}) : (C_{n+1} - C_n)}{\|C_{n+1} - C_n\|^2} (C_{n+1} - C_n) \\ &\quad - \frac{1}{2} \frac{\partial_C u(C_{n+\frac{1}{2}}, G_n, C_n, D_n) : (C_{n+1} - C_n)}{\|C_{n+1} - C_n\|^2} (C_{n+1} - C_n), \end{aligned} \quad (6.37)$$

with

$$\partial_C u = a \mathbf{I} + \frac{1}{2 \varepsilon_0 \varepsilon_r} C^{-1/2} \mathbf{D} \otimes \mathbf{D}, \quad (6.38)$$

where  $C, C$  and  $D$  are evaluated at the corresponding time nodes. Similarly to (3.40)<sub>2</sub>, the discrete gradients  $D_G u$  can be computed as

$$D_G u = b \mathbf{I}. \quad (6.39)$$

Furthermore, the discrete gradients  $D_C u$  reduces to the well-known Greenspan formula [55] such that

$$\begin{aligned} D_C u &= \frac{1}{2} \frac{u(C_n, G_n, C_{n+1}, D_{n+1}) - u(C_n, G_n, C_n, D_{n+1})}{\|C_{n+1} - C_n\|} \\ &\quad + \frac{1}{2} \frac{u(C_{n+1}, G_{n+1}, C_{n+1}, D_n) - u(C_{n+1}, G_{n+1}, C_n, D_n)}{\|C_{n+1} - C_n\|}. \end{aligned} \quad (6.40)$$

Finally, the discrete gradients  $D_D u$  can be computed as

$$\begin{aligned}
D_D u &= \frac{1}{2} (\partial_D u(C_n, G_n, C_n, D_{n+\frac{1}{2}}) + \partial_D u(C_{n+1}, G_{n+1}, C_{n+1}, D_{n+\frac{1}{2}})) \\
&\quad + \frac{1}{2} \frac{u(C_n, G_n, C_n, D_{n+1}) - u(C_n, G_n, C_n, D_n)}{\|D_{n+1} - D_n\|^2} (D_{n+1} - D_n) \\
&\quad + \frac{1}{2} \frac{u(C_{n+1}, G_{n+1}, C_{n+1}, D_{n+1}) - u(C_{n+1}, G_{n+1}, C_{n+1}, D_n)}{\|D_{n+1} - D_n\|^2} (D_{n+1} - D_n) \\
&\quad - \frac{1}{2} \frac{\partial_D u(C_n, G_n, C_n, D_{n+\frac{1}{2}}) \cdot (D_{n+1} - D_n)}{\|D_{n+1} - D_n\|^2} (D_{n+1} - D_n) \\
&\quad - \frac{1}{2} \frac{\partial_D u(C_{n+1}, G_{n+1}, C_{n+1}, D_{n+\frac{1}{2}}) \cdot (D_{n+1} - D_n)}{\|D_{n+1} - D_n\|^2} (D_{n+1} - D_n),
\end{aligned} \tag{6.41}$$

with

$$\partial_D u = \frac{1}{\varepsilon_o \varepsilon_r} C^{-1/2} C D, \tag{6.42}$$

where  $C, C$  and  $D$  are evaluated at the corresponding time nodes. Note that in the limits  $\|C_{n+1} - C_n\| \rightarrow 0$ ,  $\|G_{n+1} - G_n\| \rightarrow 0$ ,  $|C_{n+1} - C_n| \rightarrow 0$  and  $\|D_{n+1} - D_n\| \rightarrow 0$  the formulas (6.37)-(6.41) should be replaced with  $\bar{D}_{\pi^i} u = \partial_{\pi^i} u(\pi_{n+\frac{1}{2}})$ .

**Remark 6.3.** *The consideration of convex multi-variable internal energy functionals ensures the satisfaction of ellipticity at the continuum level. This condition cannot be verified at the (time) discrete level, where the derivatives of the energy are replaced by their discrete counterparts. Ellipticity can only be mathematically proven in the limit, i.e.  $\Delta t \rightarrow 0$ , when both the discrete and continuum levels coincide, see (6.36).*

## 6.4.2 Semi-discrete balance laws

A similar procedure to that in Section 6.3.3 will be followed in order to verify that the proposed time integration scheme (6.32) possesses the conservation properties as presented in Sections 6.3.3.1 to 6.3.3.4.

### 6.4.2.1 Balance of linear momentum

Following the procedure in Sec. 6.3.3.1, we choose admissible variations  $\delta V = \mathbf{0}$  and  $\delta \varphi = \zeta$  where  $\zeta \in \mathbb{R}^3$  is arbitrary but constant. Then (6.32)<sub>2</sub> yields

$$\zeta \cdot \left( \frac{1}{\Delta t} (L_{n+1} - L_n) - F^{\text{ext}} \right) = 0. \tag{6.43}$$

Therefore for vanishing external mechanical loads the total discrete linear momentum is a constant of motion of the semi-discrete system.

### 6.4.2.2 Discrete balance of angular momentum

With regard to the developments from Sec. 6.3.3.2, we choose as admissible variations  $\delta\boldsymbol{\varphi} = \boldsymbol{\zeta} \times \boldsymbol{\varphi}_{n+\frac{1}{2}}$  and  $\delta\mathbf{V} = \boldsymbol{\zeta} \times (\boldsymbol{\varphi}_{n+1} - \boldsymbol{\varphi}_n)$ , where  $\boldsymbol{\zeta}$  again is a constant vector. Then the time-discrete variational formulation (6.32) yields in the same way as in Sec. 3.1.2.2 the desired result

$$\boldsymbol{\zeta} \cdot \left( \frac{1}{\Delta t} (J_{n+1} - J_n) - M_{n,n+1}^{\text{ext}} \right) = 0. \quad (6.44)$$

For vanishing external mechanical loads the total discrete angular momentum is a constant of motion of the semi-discrete system.

### 6.4.2.3 Discrete balance of Gauss's law

Following the procedure in 6.3.3.3 we use  $\delta\phi = \zeta$ , with  $\zeta \in \mathbb{R}$  in (6.32)<sub>3</sub>. This leads to

$$\int_{\mathcal{B}_0} \rho_0^e \Big|_{n+\frac{1}{2}} dV + \int_{\partial\mathcal{B}_0^\omega} \omega_0^e \Big|_{n+\frac{1}{2}} dA = 0. \quad (6.45)$$

Therefore, the total electrical charge is zero for time independent volumetric and surface electrical charges  $\rho_0^e$  and  $\omega_0^e$ , (6.45).

### 6.4.2.4 Discrete balance of energy

In this section, a similar analysis to that in Section (6.3.3.4) will be presented for the semi-discrete weak forms in (6.32). For this purpose, we choose admissible variations  $\{\delta\mathbf{V}, \delta\boldsymbol{\varphi}, \delta\phi, \delta\mathbf{D}\} = \{\mathbf{V}_{n+1} - \mathbf{V}_n, \boldsymbol{\varphi}_{n+1} - \boldsymbol{\varphi}_n, \phi_{n+1} - \phi_n, \mathbf{D}_{n+1} - \mathbf{D}_n\} \in \mathcal{V} \times \mathcal{V} \times \mathcal{V}_\phi \times \mathbb{V}^D$

in (6.32). This yields

$$\begin{aligned}
\int_{\mathcal{B}_0} (\mathbf{V}_{n+1} - \mathbf{V}_n) \cdot \frac{1}{\Delta t} (\boldsymbol{\varphi}_{n+1} - \boldsymbol{\varphi}_n) \rho_0 \, dV &= \int_{\mathcal{B}_0} (\mathbf{V}_{n+1} - \mathbf{V}_n) \cdot \mathbf{V}_{n+\frac{1}{2}} \rho_0 \, dV, \\
\int_{\mathcal{B}_0} (\mathbf{V}_{n+1} - \mathbf{V}_n) \cdot \frac{1}{\Delta t} (\boldsymbol{\varphi}_{n+1} - \boldsymbol{\varphi}_n) \rho_0 \, dV &+ \int_{\mathcal{B}_0} \mathbf{S}_{\text{alg}} : \frac{1}{2} \text{DC}[\boldsymbol{\varphi}_{n+1} - \boldsymbol{\varphi}_n] \Big|_{n+\frac{1}{2}} \, dV \\
&+ \text{D}\Pi_m^{\text{ext}}[\boldsymbol{\varphi}_{n+1} - \boldsymbol{\varphi}_n] \Big|_{n+\frac{1}{2}} \, dV = 0, \\
\int_{\mathcal{B}_0} -\mathbf{D}_{n+1/2} \cdot \text{DE}[\boldsymbol{\varphi}_{n+1} - \boldsymbol{\varphi}_n] \, dV &- \text{D}\Pi_e^{\text{ext}}[\boldsymbol{\varphi}_{n+1} - \boldsymbol{\varphi}_n] \Big|_{n+\frac{1}{2}} \, dA = 0, \\
\int_{\mathcal{B}_0} (\mathbf{D}_{n+1} - \mathbf{D}_n) \cdot \left( \text{D}\mathbf{D}u - \mathbf{E}_{n+\frac{1}{2}} \right) \, dV &= 0.
\end{aligned} \tag{6.46}$$

Consideration of time independent forces  $\bar{\mathbf{B}}$  and  $\bar{\mathbf{T}}$  and charges  $\rho_0^e$  and  $\omega_0^e$  and after addition of the four equations in (6.46), it yields

$$\begin{aligned}
T_{n+1} - T_n + \int_{\mathcal{B}_0} \left( \mathbf{S}_{\text{alg}} : \frac{1}{2} \text{DC}[\boldsymbol{\varphi}_{n+1} - \boldsymbol{\varphi}_n] \Big|_{n+\frac{1}{2}} + \text{D}\mathbf{D}u \cdot (\mathbf{D}_{n+1} - \mathbf{D}_n) \right) \, dV \\
- \int_{\mathcal{B}_0} \mathbf{D}_{n+\frac{1}{2}} \cdot \text{DE}[\boldsymbol{\varphi}_{n+1} - \boldsymbol{\varphi}_n] \, dV - \int_{\mathcal{B}_0} (\mathbf{D}_{n+1} - \mathbf{D}_n) \cdot \mathbf{E}_{n+\frac{1}{2}} \, dV \\
+ \text{D}\Pi_m^{\text{ext}}[\boldsymbol{\varphi}_{n+1} - \boldsymbol{\varphi}_n] - \text{D}\Pi_e^{\text{ext}}[\boldsymbol{\varphi}_{n+1} - \boldsymbol{\varphi}_n] = 0,
\end{aligned} \tag{6.47}$$

The terms in the second line of (6.47) can be re-written as

$$\begin{aligned}
\int_{\mathcal{B}_0} \mathbf{D}_{n+\frac{1}{2}} \cdot \text{DE}[\boldsymbol{\varphi}_{n+1} - \boldsymbol{\varphi}_n] \, dV + \int_{\mathcal{B}_0} (\mathbf{D}_{n+1} - \mathbf{D}_n) \cdot \mathbf{E}_{n+\frac{1}{2}} \, dV \\
= \int_{\mathcal{B}_0} (\mathbf{D}_{n+1} \cdot \mathbf{E}_{n+1} - \mathbf{D}_n \cdot \mathbf{E}_n) \, dV.
\end{aligned} \tag{6.48}$$

From the definition of the algorithmic stress  $\mathbf{S}_{\text{alg}}$  in (6.33) and those for  $\mathbf{C}_{\text{alg}}$  and  $\mathbf{G}_{\text{alg}}$  in (3.63) and (3.64), respectively, it is possible to re-write the second term in (6.46)<sub>2</sub> as

$$\begin{aligned}
\mathbf{S}_{\text{alg}} : \frac{1}{2} \text{DC}[\boldsymbol{\varphi}_{n+1} - \boldsymbol{\varphi}_n] \Big|_{n+\frac{1}{2}} \\
= (\text{D}\mathbf{C}u + \text{D}\mathbf{G}u \star \mathbf{C}_{\text{alg}} + \text{D}\mathbf{C}u \mathbf{G}_{\text{alg}}) : \text{DC}[\boldsymbol{\varphi}_{n+1} - \boldsymbol{\varphi}_n] \Big|_{n+\frac{1}{2}} \\
= \text{D}\mathbf{C}u : (\mathbf{C}_{n+1} - \mathbf{C}_n) + \text{D}\mathbf{G}u : (\mathbf{G}_n - \mathbf{G}_n) + \text{D}\mathbf{C}u (\mathbf{C}_{n+1} - \mathbf{C}_n).
\end{aligned} \tag{6.49}$$

Substitution of (6.48) and (6.49) into (6.47) yields

$$\begin{aligned}
T_{n+1} - T_n + \int_{\mathcal{B}_0} \left( \mathbf{D}_{\mathbf{C}u} : (\mathbf{C}_{n+1} - \mathbf{C}_n) + \mathbf{D}_{\mathbf{G}u} : (\mathbf{G}_{n+1} - \mathbf{G}_n) + \mathbf{D}_{\mathbf{C}u} (\mathbf{C}_{n+1} - \mathbf{C}_n) \right. \\
\left. + \mathbf{D}_{\mathbf{D}u} \cdot (\mathbf{D}_{n+1} - \mathbf{D}_n) \right) dV + \int_{\mathcal{B}_0} (\mathbf{D}_{n+1} \cdot \mathbf{E}_{n+1} - \mathbf{D}_n \cdot \mathbf{E}_n) dV \\
+ \Pi_m^{\text{ext}}(\boldsymbol{\varphi}_{n+1}) - \Pi_m^{\text{ext}}(\boldsymbol{\varphi}_n) - \Pi_e^{\text{ext}}(\phi_{n+1}) - \Pi_e^{\text{ext}}(\phi_n) = H_{n+1} - H_n.
\end{aligned} \tag{6.50}$$

Comparison of (6.50) and the definition of the total Hamiltonian  $H$  in (6.31) enables to conclude that conservation of energy for the implicit one-step time integrator in equation (6.32) requires the directionality property in equation (6.35) to be satisfied. Three points have been crucial to arrive at this conclusion. First, the consideration of the algorithmic fields  $\mathbf{C}_{\text{alg}}$  and  $\mathbf{G}_{\text{alg}}$  in (3.63) and (3.64) has enabled to obtain the identity in equation (6.49). Second, the consideration of  $\mathbf{D}_{n+1/2}$  in (6.32)<sub>3</sub> and of  $\mathbf{E}_{n+1/2}$  in (6.32)<sub>4</sub> has been essential in order to re-write the third and fourth terms in (6.47) as in (6.48). Third, the use of the discrete gradients in the sense of [52].

## 6.5 Discretization in space

The underlying formulation makes use of standard isoparametric elements (see, for example, [71]) based on finite-dimensional approximations for  $\boldsymbol{\varphi}^h \in \mathcal{Q}^h \subset \mathcal{Q}$ ,  $\mathbf{V}^h \in \mathcal{V}^h \subset \mathcal{V}$  and  $\phi^h \in \mathcal{Q}_\phi^h \subset \mathcal{Q}_\phi$  of the form

$$\begin{aligned}
\boldsymbol{\varphi}^h(\mathbf{X}) &= \sum_{a=1}^{n_{\text{node}}} N_a(\mathbf{X}) \boldsymbol{\varphi}_a(t), \quad \mathbf{V}^h(\mathbf{X}) = \sum_{a=1}^{n_{\text{node}}} N_a(\mathbf{X}) \mathbf{V}_a(t) \quad \text{and} \\
\phi^h(\mathbf{X}) &= \sum_{a=1}^{n_{\text{node}}} N_a(\mathbf{X}) \phi_a(t).
\end{aligned} \tag{6.51}$$

Here  $N^a : \mathcal{B}_0 \rightarrow \mathbb{R}$  denote the nodal shape functions and  $\boldsymbol{\varphi}_a(t), \mathbf{V}_a(t) \in \mathbb{R}^3$  and  $\phi_a(t) \in \mathbb{R}$  are the respective nodal values at time  $t$ . Moreover,  $n_{\text{node}}$  denotes the total number of nodes in the finite element mesh. In addition, we introduce finite-dimensional subspaces  $\mathbb{V}_D^h \subset \mathbb{V}_D$  defined by

$$\mathbb{V}_D^h = \left\{ \mathbf{D} \in \mathbb{V}_D \mid \mathbf{D}^h \Big|_{\mathcal{B}_0(e)} = \sum_{b=1}^{n_{\text{en}}} M^b \mathbf{D}_b(t) \right\}, \tag{6.52}$$

which relies on uniform elementwise approximations for the electrical displacements field  $\mathbf{D}$  at time  $t$ . The shape functions are  $M^b$ , with  $b = 1, \dots, n_{\text{en}}$ , where  $n_{\text{en}}$  denotes

the number of element nodes arising from the use of Lagrangian shape functions. The standard (Bubnov) Galerkin approach relies on analogous approximations for  $\delta\boldsymbol{\varphi} \in \mathcal{V}$ ,  $\delta\mathbf{V} \in \mathcal{V}$ ,  $\delta\phi \in \mathcal{V}_\phi$  and  $\delta\mathbf{D} \in \mathbb{V}_D$  denoted by  $\delta\boldsymbol{\varphi}^h \in \mathcal{V}^h \subset \mathcal{V}$ ,  $\delta\mathbf{V}^h \in \mathcal{V}^h$ ,  $\delta\phi^h \in \mathcal{V}_\phi^h \subset \mathcal{V}_\phi$  and  $\delta\mathbf{D}^h \in \mathbb{V}_D^h \subset \mathbb{V}_D$ . Since no inter-element continuity is required for the approximation of  $\mathbf{D}$ , a static condensation procedure [128, 26] can be applied to eliminate the additional unknowns on element level. Finally, the thus defined finite element interpolations can be inserted into the semi-discrete variational equations (6.32), leading to a system of nonlinear algebraic equations.

## 6.6 Numerical Investigations

The objective of this section is to study the performance of the newly proposed EM time integration scheme presented in equation (6.32) in a variety of examples. Different discretization spaces for hexahedral-based and tetrahedral-based finite elements are used, see Fig. 6.1.

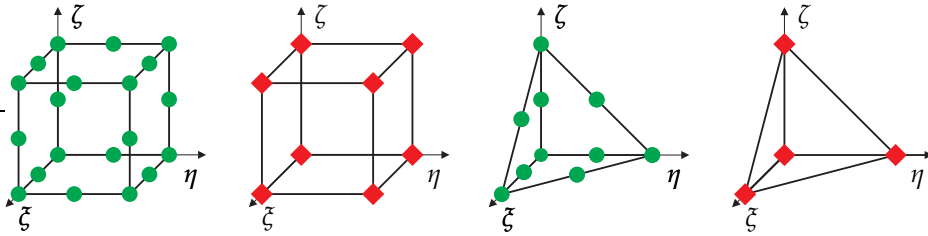


Figure 6.1: Illustration of the nodal points for the hex-based serendipity finite element  $Q2$  (left), a hex-based linear finite element  $Q1$  (center-left), a tet-based quadratic finite element  $P2$  (center-right) and a tet-based linear finite element  $P1$  (right). The bullets represent the nodes of the continuous fields  $\{V^h, \boldsymbol{\varphi}^h, \phi^h\}$  and the squares represent the nodes of the discontinuous field  $D^h$ .

### 6.6.1 Rotating actuator

The objective of this example is:

- O1.I** Study of the accuracy of the proposed EM time integration scheme given in equation (6.32). Specifically, the objective is to verify the mathematical conclusion obtained in Appendix E, according to which the proposed EM scheme must converge at the same (second order) rate as the midpoint (MP) scheme.

The geometry and the boundary conditions for the actuator considered in this example are depicted in Figure 6.2 and Table 6.1. The actuator is free in space. An initial velocity  $V_0$  is given by

$$V_0 = \boldsymbol{\omega} \times \mathbf{X}, \quad \boldsymbol{\omega} = [0, 0, 10]^T \text{ s}^{-1}, \quad \mathbf{X} = [X_1, X_2, X_3]^T, \quad (6.53)$$

with  $\{X_1, X_2, X_3\}$  aligned with the orthonormal basis  $\{e_1, e_2, e_3\}$ , respectively (see Figure 6.2). Electrical Dirichlet boundary conditions are applied on top and bottom of the plate. Specifically, a value of the potential  $\phi_t = 0 \text{ V}$  is applied on the top (blue) electrode and of  $\phi_b = 100 \text{ kV}$  on the bottom (blue) electrode (refer to Figure 6.2).

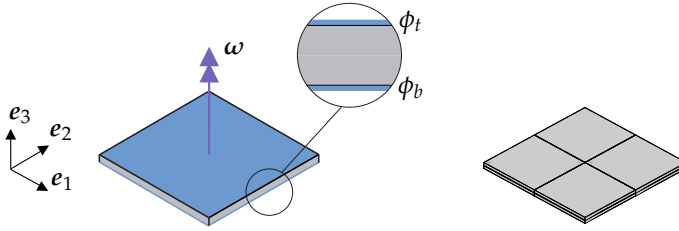
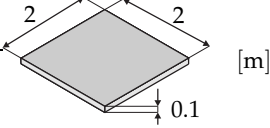


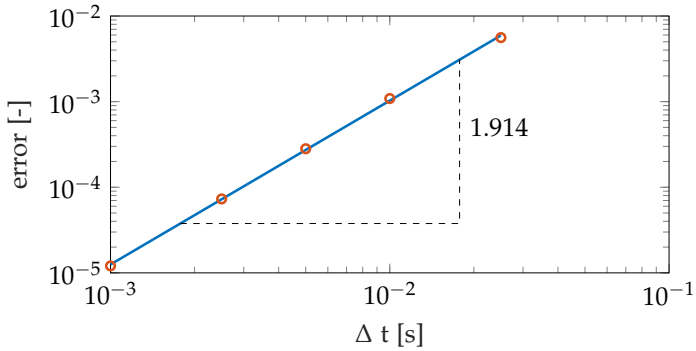
Figure 6.2: Rotating actuator: Configuration and boundary conditions (left), discretization (right).

The purely mechanical contribution of the constitutive model considered corresponds to that of a Mooney-Rivlin model (refer to equation (6.12)). The electromechanical component corresponds to that of an ideal dielectric elastomer (see equation (6.13)). The material parameters of the constitutive model can be found in Table 6.1. The discretization shown in Figure 6.2 has been used in this example, comprised of 8 hexahedral elements with  $\{243, 81, 192\}$  degrees of freedom for  $\{\boldsymbol{\varphi}, \phi, \mathbf{D}\}$ . A continuous serendipity-type Q2 interpolation has been used for the fields  $\{\boldsymbol{\varphi}, \phi\}$  and a discontinuous trilinear Q1 interpolation has been used for  $\mathbf{D}$ .

In relation to objective **O1.I**, a study of the accuracy of the proposed EM scheme in (6.32) has been carried out. This is shown in Figure 6.3, which depicts the convergence with respect to time of the solution when using the hexahedral finite element described above. Specifically, for the mesh depicted in Figure 6.2, the  $L_2$  norm of the error in the displacements (see (4.92)) between the solution obtained with five different time steps  $\{\Delta t_1, \dots, \Delta t_5\}$  such that  $\Delta t_1 = 2.5e-2s$ ,  $\Delta t_2 = 1e-2s$ ,  $\Delta t_3 = 5e-3s$ ,  $\Delta t_4 = 2.5e-3s$ ,  $\Delta t_5 = 1e-3s$  and that obtained with a reference time step  $\Delta t_{\text{ref}}$  such that  $\Delta t_{\text{ref}} \ll \Delta t_5$  has been computed. A time-interval of 0.1s has been considered in order to carry out the described convergence study. Crucially, Figure 6.3 proves that the proposed EM scheme is second order accurate in time (slope of 1.914).

Table 6.1: Numerical example 1. Material parameters, simulation parameters and geometry.

mech. parameters	$a$	$2.5 \times 10^4$	Pa	geometry of the actuator 
	$b$	$5 \times 10^4$	Pa	
	$\lambda$	$4 \times 10^4$	Pa	
el. parameters	$\varepsilon_0$	$8.854 \times 10^{-12}$	$F \text{ kg}^{-1}$	
	$\varepsilon_r$	5	—	
ref. pot.	$\phi_0$	0	V	
el. pot. at $X_3 = 0.1$	$\phi_t$	$10^5$	V	
el. pot. at $X_3 = 0$	$\phi_b$	0	V	
density	$\rho_0$	900	$\text{kg m}^{-3}$	
simulation time	$T$	0.1	s	
ref time-step size	$\Delta t_{ref}$	$10^{-4}$	s	
Newton tolerance	$\varepsilon$	$10^{-6}$	J	

Figure 6.3: Rotating actuator: Second order (1.914) accuracy of the proposed EM scheme in (6.32) with respect to time for the field  $\varphi$ . Results obtained for hexahedral  $Q2^C$ - $Q2^C$ - $Q1^D$  element.

## 6.6.2 Bending actuator

The objective of this example is two-fold:

**O2.I** Comparison of the performance of two families of finite elements. Specifically, a tetrahedral-based and a hexahedral-based finite element will be considered. The interpolation spaces for the fields  $\{\varphi, \phi, D\}$  will be carried out in accordance to Table 6.2.

**O2.II** Assessment of the thermodynamical consistency of the time integration scheme presented in (6.32) for both families of finite elements. In particular, the conservation properties of the proposed EM scheme will be analysed.

Table 6.2: Bending actuator: Discretization spaces for tetrahedral-based and hexahedral-based finite elements considered. The superscripts *C* and *D* stand for continuous and discontinuous interpolations of fields  $\{\varphi, \phi, D\}$ .

Discretization in space		
Fields	Tet-based	Hex-based
$\varphi$	$P2^C$	$Q2^C$
$\phi$	$P2^C$	$Q2^C$
$D$	$P1^D$	$Q1^D$

The geometry and boundary conditions for the actuator considered in this example are described in Figure 6.4 and Table 6.3. The actuator is clamped on one side (zero Dirichlet displacement boundary conditions). A surface electrical charge  $\omega_0^e$  is applied on the top (purple) electrode (refer to Figure 6.4) whereas a prescribed value of the electric potential of  $\phi = 0$  V is applied on the electrode (blue) in the middle of the actuator. The time dependent function  $\omega_0^e$  is given by

$$\omega_0^e = 10^{-3} \times \begin{cases} \sin\left(\frac{0.5\pi}{0.4s}t\right) & \text{for } t \leq 0.4 \text{ s} \\ 1 & \text{for } 0.4 \text{ s} < t \leq 1.0 \text{ s} \\ \cos\left(\frac{0.5\pi}{1.4s-1.0s}(t-1\text{ s})\right) & \text{for } 1.0 \text{ s} < t \leq 1.4 \text{ s} \\ 0 & \text{for } t > 1.4 \text{ s} \end{cases} \quad [\text{Q}/\text{m}^2]. \quad (6.54)$$

The purely mechanical contribution of the constitutive model considered corresponds to that of a Mooney-Rivlin model (refer to equation (6.12)). The electromechanical

component corresponds to that of an ideal dielectric elastomer (see equation (6.13)). The material parameters of the constitutive model can be found in Table 6.3.

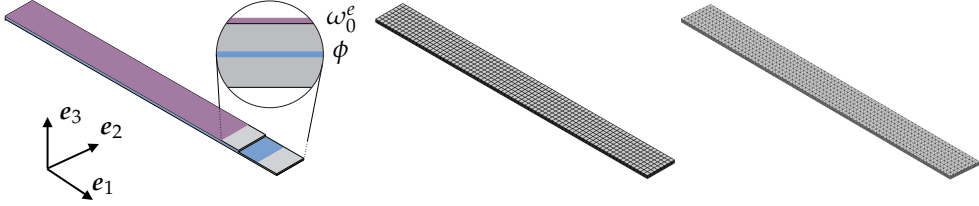


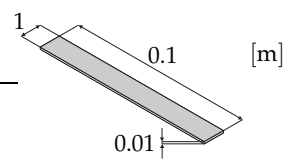
Figure 6.4: Bending actuator: Configuration and boundary conditions (left). Discretizations considered: hexahedral mesh (center), tetrahedral mesh (right).

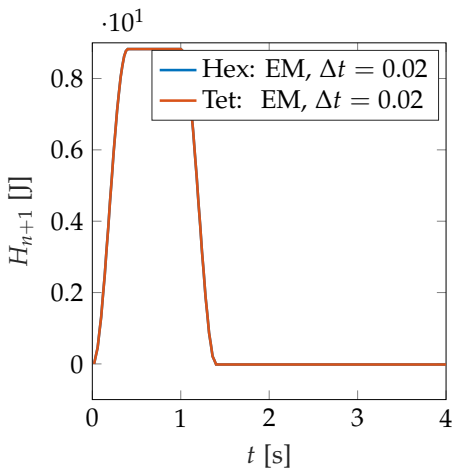
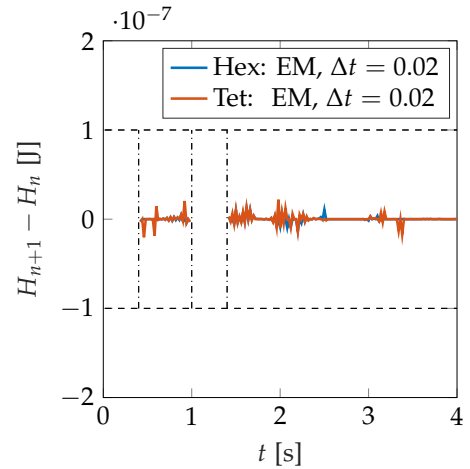
With regards to **O2.I**, two discretizations are considered, one for each of the two families of finite elements described in Table 6.2. Both hexahedral-based and tetrahedral-based meshes are represented in Figure 6.4. The mesh associated with the hexahedral-based discretization has 2,560 elements, 13,401 nodes for both fields  $\{\varphi, \phi\}$  (40203, 13401} degrees of freedom associated to each field) and 20,480 nodes for  $D$  (61,440 degrees of freedom). The mesh associated with the tetrahedral-based discretization has 10,882 elements, 18633 nodes for both fields  $\{\varphi, \phi\}$  (55899, 18633} degrees of freedom associated to each field) and 43,528 nodes for  $D$  (130,584 degrees of freedom). In both cases,  $D$  is interpolated using a discontinuous interpolation across elements, which allows to condense out this field.

Figure 6.5 shows the contour plot distribution of the von Mises stress for both, the hexahedral-based and the tetrahedral-based discretization, respectively, for different time steps. A good agreement is observed between both discretizations in terms of the final configuration (displacements) as well as the stress distribution.

Regarding objective **O2.II**, Figure 6.6 shows the evolution of the Hamiltonian  $H$  (6.31) using both hexahedral and tetrahedral discretizations for a given time step size of  $\Delta t = 0.02$  s. The evolution of  $H$  is exactly identical for both discretizations. Crucially,  $H$  remains constant for the time interval  $[0.4, 1] \text{ s} \cup [1.4, 4] \text{ s}$ , namely, when the surface charge  $\omega_0^e$  in equation (6.54) remains constant, proving that the Hamiltonian is conserved in that range. This can be more clearly appreciated in Figure 6.7, where the variation  $\Delta H = H_{n+1} - H_n$  is depicted for the aforementioned time interval. Crucially, the maximum value of  $|\Delta H|$  is always bounded below the user-defined Newton tolerance  $\varepsilon$ , which for this case was selected as  $\varepsilon = 10^{-5}$  (refer to Table 6.3).

Table 6.3: Bending actuator: Material parameters, simulation parameters and geometry.

mech. parameters	$a$	$2.5 \times 10^4$	Pa	geometry of the actuator 
	$b$	$5 \times 10^4$	Pa	
	$\lambda$	$1 \times 10^5$	Pa	
el. parameters	$\varepsilon_0$	$8.854 \times 10^{-12}$	$F \text{ kg}^{-1}$	
	$\varepsilon_r$	3	—	
ref. potential	$\varphi_0$	0	V	
max. surface charge	$\omega_0$	$1 \times 10^{-3}$	$\text{Q}/\text{m}^2$	
density	$\rho_0$	1000	$\text{kg m}^{-3}$	
timestep size	$\Delta t$	0.02	s	
simulation time	$T$	4	s	
Newton tolerance	$\varepsilon$	$10^{-5}$	J	

Figure 6.6: Bending actuator: Time evolution of  $H$  for both hexahedral and tetrahedral discretizations using the proposed EM scheme.Figure 6.7: Bending actuator: Time evolution of  $\Delta H$  for time interval  $[0.4, 1] \text{ s} \cup [1.4, 4] \text{ s}$  for hexahedral and tetrahedral elements with proposed EM scheme.

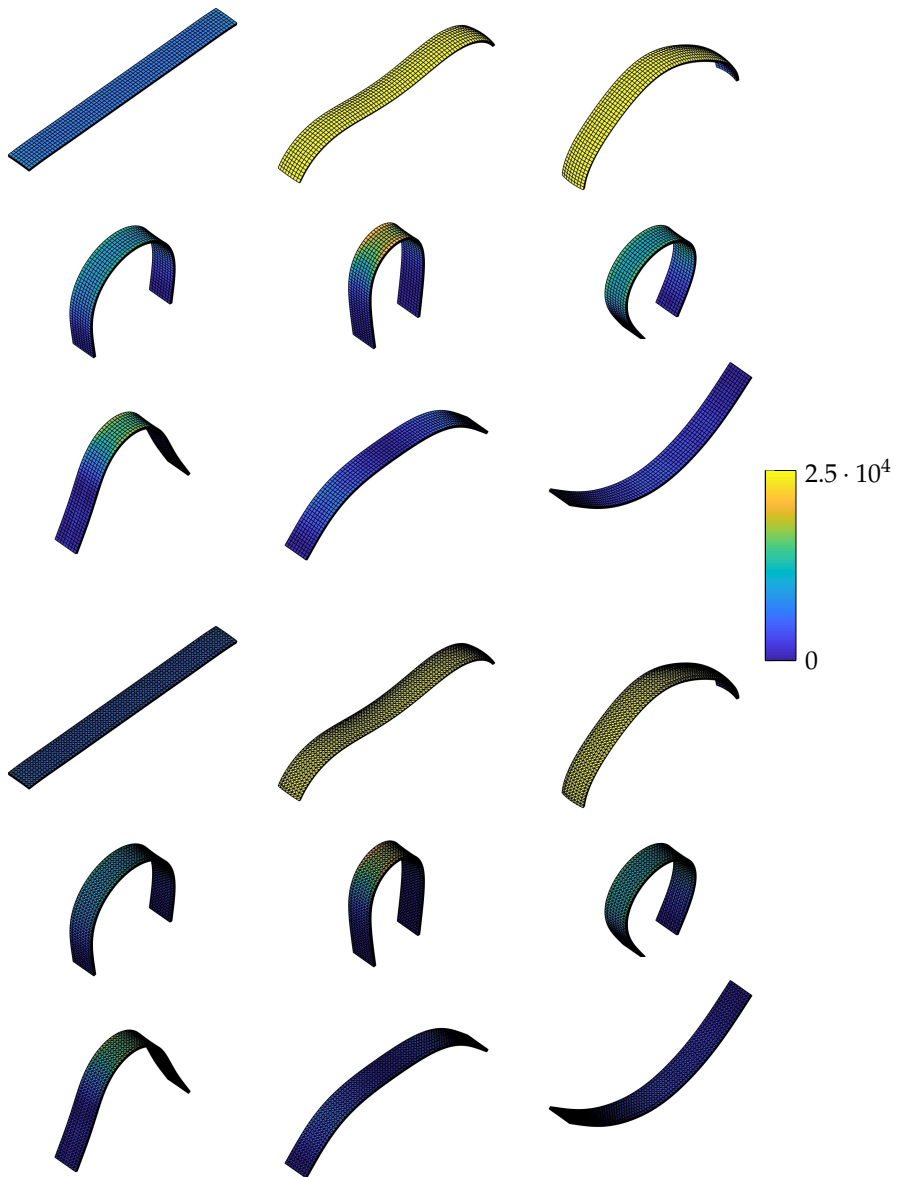


Figure 6.5: Bending actuator: Contour plot of von Mises stress for the hexahedral-based and the tetrahedral-based discretization for different configurations corresponding to (left to right-top to bottom):  $t = \{0, 0.5, 1, 1.5, 2, 2.5, 3, 3.5, 4\}$ s.

### 6.6.3 Rotating cross

The objective of this example is three-fold:

- O3.I** Comparison of the stability and robustness of the proposed EM scheme against the MP scheme.
- O3.II** Comparison of the thermodynamical consistency of the proposed time integrator to that of the MP integrator.
- O3.III** Verification of consistent angular momentum approximation.

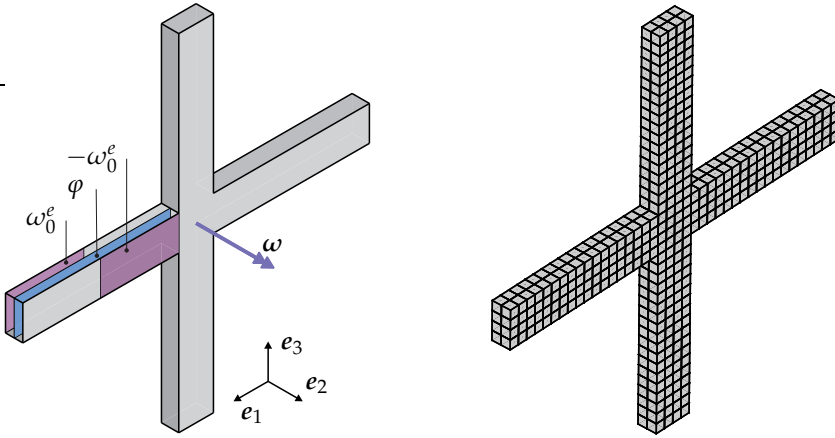


Figure 6.8: Rotating cross: Configuration and boundary conditions (left), discretization (right).

The geometry and boundary conditions for the actuator considered in this example are described in Figure 6.8 and Table 6.4. The actuator is completely free (no Dirichlet boundary conditions are considered for the field  $\varphi$ ). An initial velocity  $V_0$  is prescribed and given by

$$V_0 = \omega \times X, \quad \omega = [0, 0, 4]^T \text{ s}^{-1}, \quad X = [X_1, X_2, X_3]^T, \quad (6.55)$$

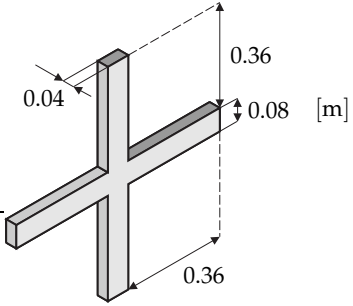
with  $\{X_1, X_2, X_3\}$  aligned with the orthonormal basis  $\{e_1, e_2, e_3\}$ , respectively (see Figure 6.8). A constant value for the electric potential of  $\phi = 0\text{V}$  is applied on the blue electrode. A surface electric charge  $\omega_0^e$  is applied on the purple electrode (see

detailed view in Figure 6.8). The time dependent function  $\omega_0^e$  is given by

$$\omega_0^e = \left(5 \times 10^{-3}\right) \times \begin{cases} \sin\left(\frac{0.5\pi}{0.4\text{s}} t\right) & \text{for } t \leq 0.4\text{ s} \\ 1 & \text{for } 0.4\text{ s} < t \leq 3.0\text{ s} \\ \cos\left(\frac{0.5\pi}{3.4\text{s}-3.0\text{s}} (t-3\text{ s})\right) & \text{for } 3.0\text{ s} < t \leq 3.4\text{ s} \\ 0 & \text{for } t > 3.4\text{ s} \end{cases} \quad [\text{Q}/\text{m}^2]. \quad (6.56)$$

The constitutive model is the same as that used in the two preceding examples with the material parameters defined in Table 6.4. The discretization shown in Figure 6.8 has been used in this example. Specifically, a total of 672 hexahedral  $Q2^C$ - $Q2^C$ - $Q1^D$  finite elements have been considered, yielding a total number of degrees of freedom of  $\{13215, 4405, 16128\}$  for the fields  $\{\varphi, \phi, \mathbf{D}\}$ .

Table 6.4: Rotating cross: Material parameters, simulation parameters and geometry.

mech. parameters	$a$	$2.5 \times 10^4$	Pa	<p>geometry of the cross</p> 
	$b$	$5 \times 10^4$	Pa	
	$\lambda$	$5 \times 10^5$	Pa	
el. parameters	$\varepsilon_0$	$8.854 \times 10^{-12}$	$\text{F kg}^{-1}$	
	$\varepsilon_r$	4	$\text{N}/\text{V}^2$	
ref. potential	$\varphi_0$	0	V	
max. surface charge	$\omega_0$	$5 \times 10^{-3}$	$\text{Q}/\text{m}^2$	
density	$\rho_0$	1000	$\text{kg m}^{-3}$	
timestep size	$\Delta t$	0.01	s	
simulation time	$T$	10	s	
Newton tolerance	$\varepsilon$	$10^{-5}$	J	

Regarding objective **O3.I**, Figure 6.9 shows that the MP time integrator exhibits an energy blow-up and becomes unstable approximately in the interval  $1\text{ s} < t < 2\text{ s}$ . However, the newly proposed EM scheme remains stable for the whole simulation for the same fixed time step size of  $\Delta t = 0.01\text{ s}$ . This proves that the proposed scheme is more robust and stable than the classical MP scheme.

In relation to objective **O3.II**, Figure 6.9 shows the evolution of  $H$  for both the proposed EM scheme and the MP scheme. Crucially,  $H$  remains constant when using

the proposed EM scheme for the time interval  $[0.4, 3] \text{ s} \cup [3.4, 10] \text{ s}$ , namely, when the surface charge  $\omega_0^e$  in equation (6.56) remains constant, proving that the Hamiltonian is conserved in that range. This can be more clearly appreciated in Figure 6.10, where the variation  $\Delta H = H_{n+1} - H_n$  is depicted for the aforementioned time interval. Crucially, the maximum value of  $|\Delta H|$  is always bounded below the user-defined Newton tolerance  $\varepsilon$ , which for this case was selected as  $\varepsilon = 10^{-5}$  (refer to Table 6.4).

Additionally, in relation to objective **O3.III** Figure 6.12 shows the evolution of the norm of the total angular momentum  $J$  of the system for both the proposed EM scheme and the MP scheme (before the latter becomes unstable). Crucially,  $\|J\|$  remains constant when using the proposed EM scheme for the whole simulation, proving that the total angular momentum is conserved. This can be more clearly appreciated in Figure 6.13, where the variation  $\|\Delta J\| = \|J_{n+1} - J_n\|$  is depicted for the whole simulation. Crucially, the maximum value of  $\|\Delta J\|$  is also always bounded below the user-defined Newton tolerance  $\varepsilon$  (here  $\varepsilon = 10^{-5}$ , refer to Table 6.4). A clearer evolution of the energy blow-up for the MP scheme can be appreciated in Figure 6.11. For the interval  $1 \text{ s} < t < 2 \text{ s}$ , a diverging pattern is observed in the evolution of the Hamiltonian for the MP scheme which ends in an energy blow-up.

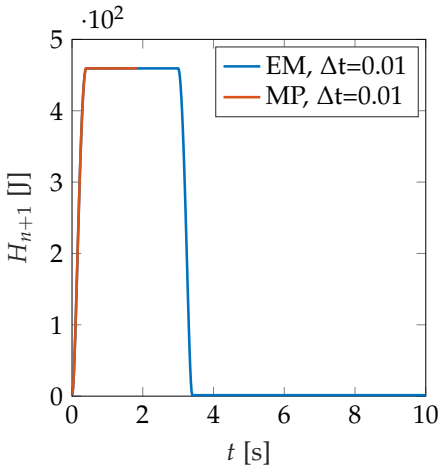


Figure 6.9: Rotating cross: Time evolution of  $H$  with the proposed EM and MP scheme. Energy blow-up for MP scheme within time interval  $1 \text{ s} < t < 2 \text{ s}$ .

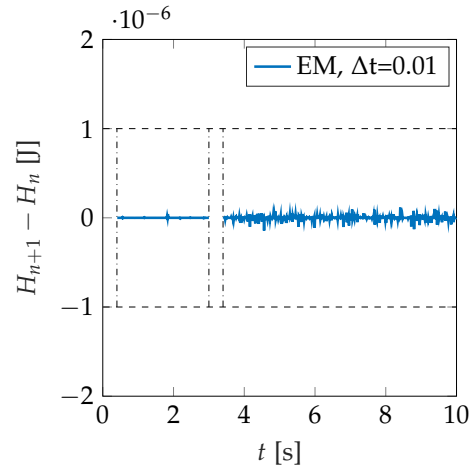


Figure 6.10: Rotating cross: Time evolution of  $\Delta H$  in the time interval  $[0.4, 3] \text{ s} \cup [3.4, 10] \text{ s}$  for hexahedral element with the proposed EM consistent scheme.

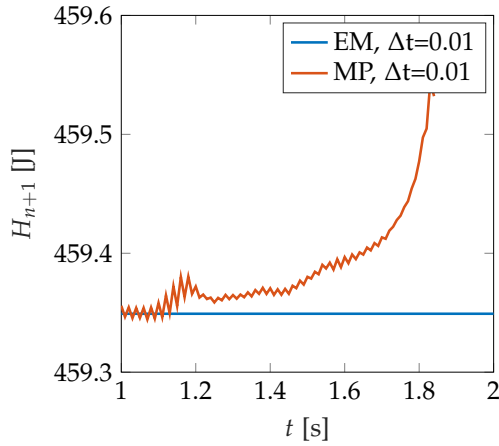


Figure 6.11: Rotating cross: Time evolution of  $\Delta H$  in the time interval  $1s < t < 2s$  for hexahedral element. Energy blow-up of the MP scheme. Conservation of the Hamiltonian for proposed scheme.

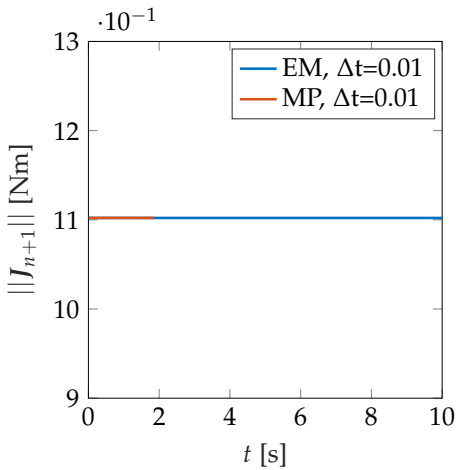


Figure 6.12: Rotating cross: Time evolution of  $\|J\|$  with proposed EM scheme and MP scheme.

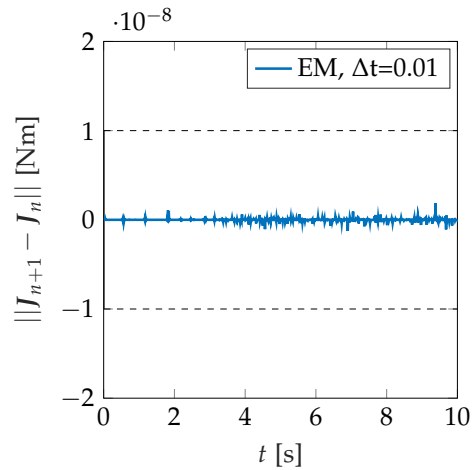


Figure 6.13: Rotating cross: Time evolution of  $\|\Delta J\|$  for hexahedral element with proposed EM scheme.

Finally, the contour plot distribution for the electric potential  $\phi$  and the evolution of the combined rotation and electrically induced deformation in the actuator is depicted in Figure 6.14 for difference instances of time.

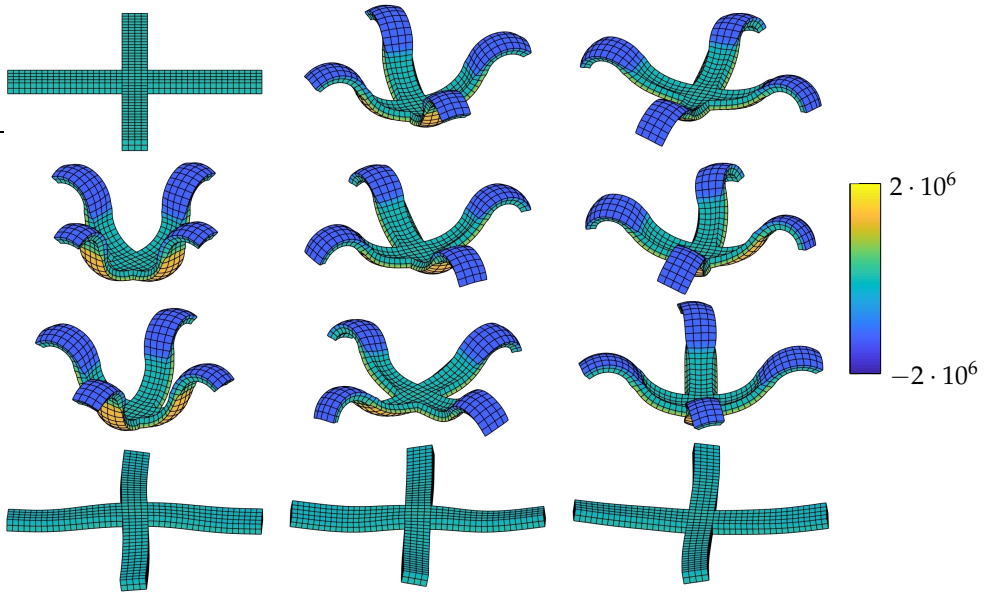


Figure 6.14: Rotating cross: Contour plot of electric potential  $\phi$  for hexahedral element for different configurations corresponding to (left to right-top to bottom):

$$t = \{ 0, 0.4, 0.8, 1.2, 1.6, 2, 2.4, 2.8, 3.2, 3.6, 4, 4.4 \} \text{s.}$$

## 6.6.4 Twisting actuator

The objective of this example is:

**O4.I** The consideration of more sophisticated constitutive models allowing for the consideration of anisotropic effects. A comparison of the stability and robustness between the proposed EM scheme and the MP scheme will also be carried out in this example.

The geometry and boundary conditions for the actuator considered in this example are described in Figure 6.15 and Table 6.5. The actuator is clamped on one side (zero Dirichlet displacement boundary conditions). A surface electrical charge  $\omega_0^e$  is applied on the purple electrode (refer to detailed view in Figure 6.15) whereas a prescribed value of the electric potential of  $\phi = 0 \text{ V}$  is applied on the blue electrode (see detailed

view in Figure 6.15). The time dependent function  $\omega_0^e$  is given by

$$\omega_0^e = \left(2 \times 10^{-3}\right) \times \begin{cases} \sin\left(\frac{0.5\pi}{0.5\text{s}} t\right) & \text{for } t \leq 0.5\text{ s} \\ 1 & \text{for } 0.5\text{ s} < t \leq 1\text{ s} \\ \cos\left(\frac{0.5\pi}{1.5\text{s}-1\text{s}}(t-1\text{ s})\right) & \text{for } 1\text{ s} < t \leq 1.5\text{ s} \\ 0 & \text{for } t > 1.5\text{ s} \end{cases} \quad [\text{Q}/\text{m}^2]. \quad (6.57)$$

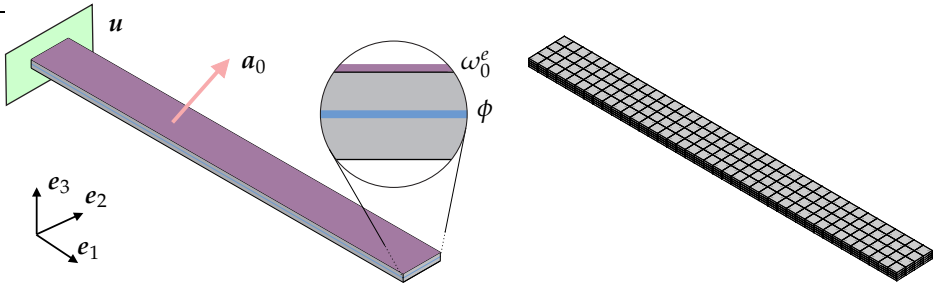


Figure 6.15: Twisting actuator: Configuration and boundary conditions (left), discretization (right).

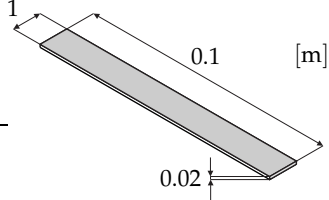
Regarding the constitutive model, its electromechanical component corresponds to that of an ideal dielectric elastomer (see equation (6.13)). The purely mechanical contribution is more complex than that considered in the preceding examples. This can be additively decomposed into purely isotropic and transversely anisotropic parts, see (3.42). In this example, the isotropic contribution  $u_m^{\text{iso}}(C, G, C)$  will be taken exactly as that a Mooney-Rivlin model (refer to equation (6.12)). The anisotropic contribution is defined in (3.44), where the material parameters  $g_0 > 0$ ,  $g_C > 0$ ,  $g_G > 0$  and  $g_C \geq 1$  for this model can be found in Table 6.5. Moreover, in Fig. 6.15,  $a_0$  represents the preferred direction of anisotropy in the material configuration. In this example,  $a_0$  is defined as  $a_0 = [0.320 \ -0.9712 \ 0.320]^T$ . The discretization shown in Figure 6.15 has been used in this example. Specifically, a total of 640 hexahedral  $Q2^C$ - $Q2^C$ - $Q1^D$  finite elements have been considered, yielding a total number of degrees of freedom of  $\{10995, 3665, 15360\}$  for the fields  $\{\varphi, \phi, D\}$ .

Regarding objective **O4.I**, Figure 6.16 shows that the MP scheme exhibits an energy blow-up and becomes unstable approximately in the interval  $4 < t < 5$ . However, the proposed EM scheme remains stable for the whole simulation for the same fixed time step size of  $\Delta t = 0.0025\text{ s}$ . Like in the preceding example, where a simpler constitutive law was used, this proves that the proposed EM scheme is more robust

and stable than the classical MP scheme. In addition, 6.16 shows the evolution of  $H$  for both the proposed EM scheme and the MP scheme (before the latter becomes unstable). Crucially,  $H$  remains constant when using the proposed EM scheme for the time interval  $[0.5, 1] \text{ s} \cup [1.5, 7.5] \text{ s}$ , namely, when the surface charge  $\omega_0^e$  in equation (6.57) remains constant, proving that the Hamiltonian is conserved in that range. This can be more clearly appreciated in Figure 6.17, where the variation  $\Delta H = H_{n+1} - H_n$  is depicted for the aforementioned time interval. The maximum value of  $|\Delta H|$  is always bounded below the user-defined Newton tolerance  $\varepsilon$  (refer to Table 6.5).

Finally, the contour plot distribution for the von Mises stress and the evolution of the electrically induced deformation in the actuator is depicted in Figure 6.18 for different instances of time.

Table 6.5: Twisting actuator: Material parameters, simulation parameters and geometry.

mech. parameters	$a$	$2.5 \times 10^4$	Pa	<p>geometry of the actuator</p> 
	$b$	$5 \times 10^4$	Pa	
	$\lambda$	$1 \times 10^6$	Pa	
	$g_0$	$3 \times 10^5$	Pa	
	$g_C$	4	-	
	$g_G$	8	-	
el. parameters	$g_C$	1	-	
	$\varepsilon_0$	$8.854 \times 10^{-12}$	$F \text{ kg}^{-1}$	
	$\varepsilon_r$	4	-	
ref. potential	$\varphi_0$	0	V	
max. surface charge	$\omega_0$	$2 \times 10^{-3}$	$\text{Q}/\text{m}^2$	
Density	$\rho_0$	1000	$\text{kg m}^{-3}$	
timestep size	$\Delta t$	0.0025	s	
simulation time	$T$	7.5	s	
Newton tolerance	$\varepsilon$	$10^{-5}$	J	

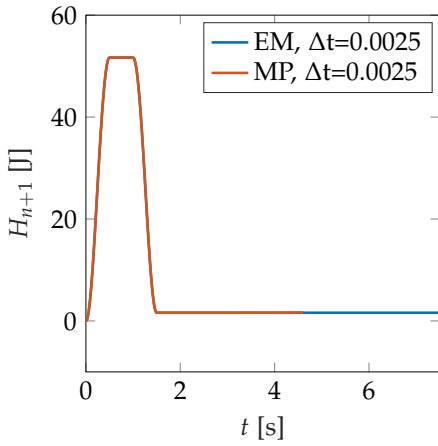


Figure 6.16: Twisting actuator: Time evolution of  $H$  with the proposed EM scheme and the MP scheme. Energy blow-up for MP scheme.

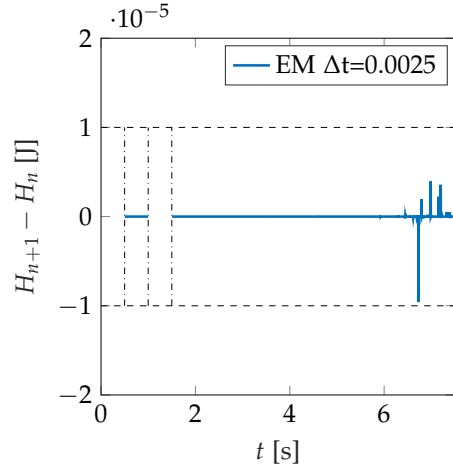


Figure 6.17: Twisting actuator: Time evolution of  $\Delta H$  in the time interval  $[0.5, 1.5] \text{ s} \cup [1.5, 7.5] \text{ s}$  for hexahedral element with the proposed scheme.

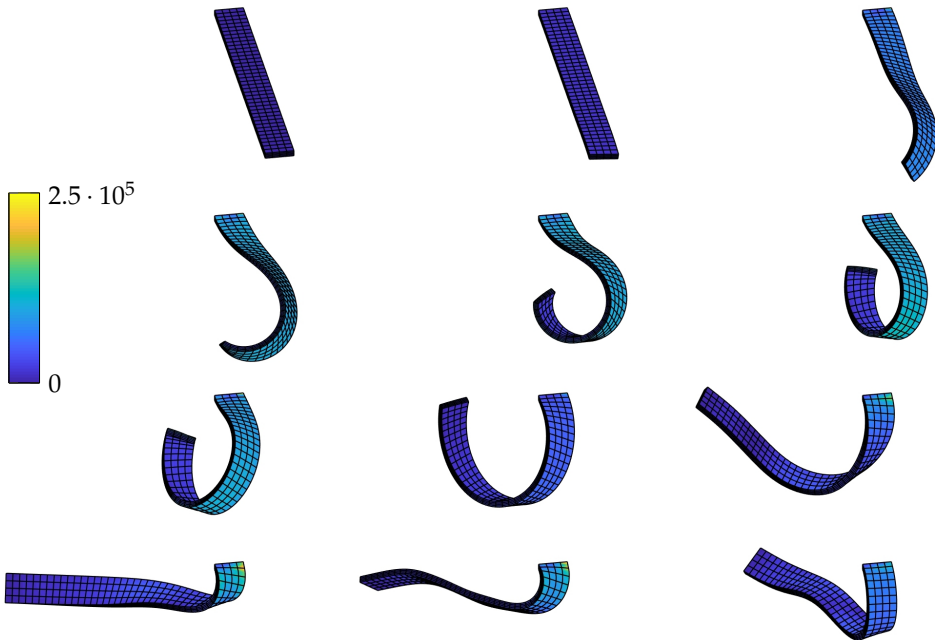


Figure 6.18: Twisting actuator: Contour plot of the von Mises stress for hexahedral element for different configurations corresponding to (left to right-top to bottom):  $t = \{ 0, 0.2, 0.4, 0.6, 0.8, 1, 1.2, 1.4, 1.6, 1.8, 2, 2.2 \} \text{ s}$ .

## 6.6.5 Clamped membrane

The objective of this example is:

**O5.I** Comparison of the robustness between the proposed EM scheme and the MP scheme in scenarios with more sophisticated electrically induced configurations which can represent a real challenge from the robustness standpoint of the algorithm.

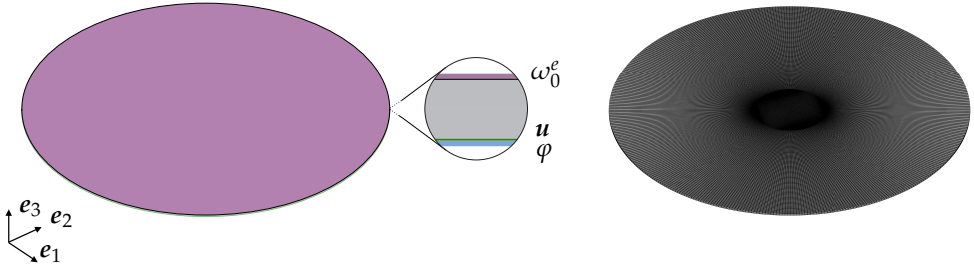


Figure 6.19: Clamped membrane: Configuration and boundary conditions (left), discretization (right).

The geometry and boundary conditions for the actuator considered in this example are very similar to those considered in Reference [140] and are described in Figure 6.19 and Table 6.6. The actuator is fully clamped on the perimeter of the blue electrode (see detailed view in Figure 6.19). A surface electrical charge  $\omega_0^e$  is applied on the purple electrode (refer to detailed view in Figure 6.19) whereas a prescribed value of the electric potential of  $\varphi = 0$  V is applied on the blue electrode. The time dependent function  $\omega_0^e$  is given by

$$\omega_0^e = \left(2 \times 10^{-3}\right) \times \begin{cases} \sin\left(\frac{0.5\pi}{1\text{s}} t\right) & \text{for } t \leq 1\text{ s} \\ 1 & \text{for } t > 1\text{ s} \end{cases} \quad [Q/m^2]. \quad (6.58)$$

The purely mechanical contribution of the constitutive model considered corresponds to that of a Mooney-Rivlin model (refer to equation (6.12)). The electromechanical component corresponds to that of an ideal dielectric elastomer (see equation (6.13)). The material parameters of the constitutive model can be found in Table 6.6.

The discretization shown in Figure 6.19 has been used in this example. Specifically, a total of 25200 hexahedral  $Q2^C$ - $Q2^C$ - $Q1^D$  finite elements for one quarter of the disc have been considered, yielding a total number of degrees of freedom (for one quarter) of  $\{420639, 140213, 604800\}$  for the fields  $\{\varphi, \phi, \mathbf{D}\}$ .

Table 6.6: Clamped membrane: Material parameters, simulation parameters and geometry.

mech. parameters	$\mu_1$	$1 \times 10^5$	Pa	<p>geometry of the disc</p>
	$\mu_2$	$2 \times 10^5$	Pa	
	$\lambda$	$1 \times 10^5$	Pa	
el. parameters	$\varepsilon_0$	$8.854 \times 10^{-12}$	$F kg^{-1}$	
	$\varepsilon_r$	4	$N/V^2$	
ref. potential	$\varphi_0$	0	V	
max. surface charge	$\omega_0$	$2 \times 10^{-3}$	$Q/m^2$	
Density	$\rho_0$	1000	$kg m^{-3}$	
timestep size	$\Delta t$	0.01	s	
simulation time	$T$	20	s	
Newton tolerance	$\varepsilon$	$10^{-4}$	J	

Regarding objective **O5.I**, Figure 6.20 shows that the MP scheme exhibits an energy blow-up and becomes unstable approximately at the beginning of the time interval for which  $\omega_0^e$  becomes constant. However, the proposed EM scheme remains stable for the whole simulation for the same fixed time step size of  $\Delta t = 0.01$  s. This example is particularly challenging, specially when using the MP scheme, as it can be observed from the early energy blow-up just described. In addition, Figure 6.20 shows the evolution of  $H$  for both the proposed EM scheme and the MP scheme (before the latter becomes unstable). Crucially,  $H$  remains constant when using the proposed EM scheme for the time interval  $t > 1$  s, namely, when the surface charge  $\omega_0^e$  in equation (6.58) remains constant, proving that the Hamiltonian is conserved in that range. This can be more clearly appreciated in Figure 6.21, where the variation  $\Delta H = H_{n+1} - H_n$  is depicted for the aforementioned time interval. The maximum value of  $|\Delta H|$  is always bounded below the user-defined Newton tolerance  $\varepsilon$  (refer to Table 6.6).

Finally, the contour plot distribution for the von Mises stress and the evolution of the electrically induced deformation in the actuator is depicted in Figure 6.22 for difference instances of time.

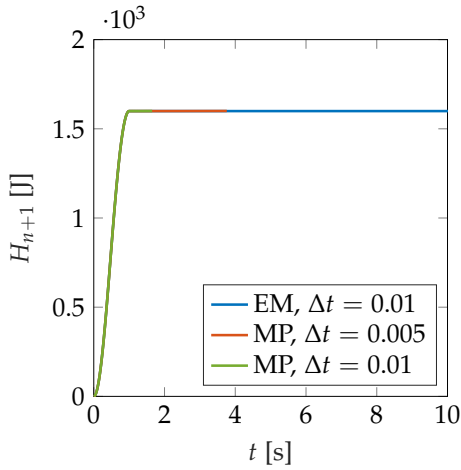


Figure 6.20: Clamped membrane: Time evolution of  $H$  with the proposed EM scheme and the MP scheme.

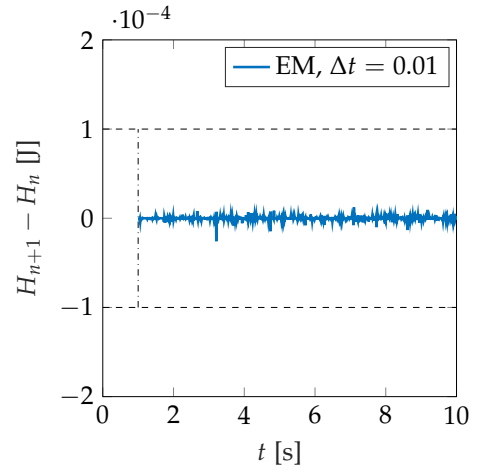


Figure 6.21: Clamped membrane: Time evolution of  $\Delta H$  in the time interval  $t > 1$  s for hexahedral element.

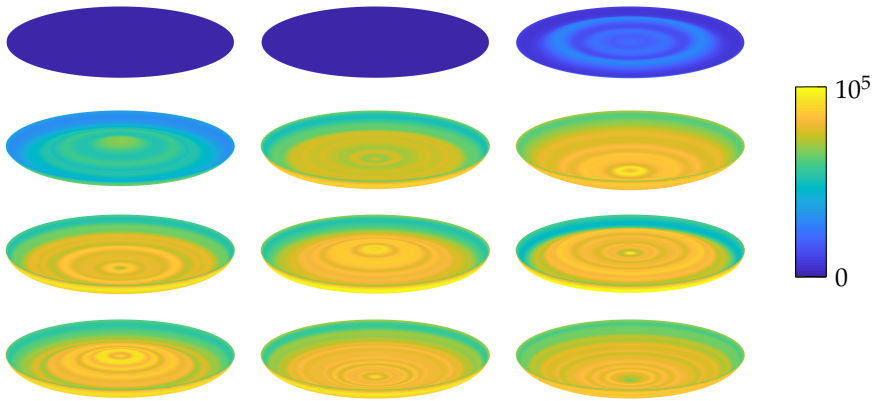


Figure 6.22: Clamped membrane: Contour plot of the von Mises stress for hexahedral element for different configurations corresponding to (left to right-top to bottom)  $t = \{ 0, 0.05, 0.3, 0.55, 0.8, 1.05, 1.3, 1.55, 1.8, 2.05, 2.3, 2.55 \}$ s.



# 7 Summary and outlook

## 7.1 Summary<sup>1</sup>

This thesis deals with the formulation of a mixed framework for the design of EM consistent schemes inspired by the structure of polyconvex stored energy functions. This framework has been extended to more involved problems, such as modeling quasi-incompressible material behavior or the simulation of multi-field problems.

In the beginning we proposed a new mixed variational framework that opens up a new avenue to the design of EM schemes. The mixed variational framework has been motivated by the structure of polyconvex stored energy functions. Consequently, the structure of the underlying frame-indifferent stored energy function gives rise to three strain-type fields that play the role of independent variables in the Hu-Washizu type variational formulation. In particular, the strain-type variables are introduced through a cascade of kinematic relationships, which ultimately makes possible the design of the present EM method. The mixed framework at hand yields variational equations that have been discretized first in time. The resulting mixed semi-discrete EM method facilitates the design of a whole family of EM schemes, dependent on the specific choice of the spatial discretization. This has been illustrated in the present work with (i) the pure displacement formulation, and (ii) the fully mixed element formulation relying on the independent approximation of the displacements, the three strain-type variables, and the corresponding three stress-type Lagrange multipliers. Concerning the fully mixed approach, we have restricted ourselves to one particular implementation, relying on 20-node serendipity shape functions for the displacements (yielding a globally  $C^0$  approximation of the displacement field), along with tri-linear Lagrangian shape functions for the remaining six independent fields. Since the mixed

---

<sup>1</sup> This section is based on the conclusions given in [23, 81, 44, 133].

fields do not require inter-element continuity, the classical static condensation procedure has been applied. Thus, the mixed formulation does not lead to an increase in the number of unknowns to be solved for at the global level. Interestingly, the mixed approach has led to a new form of the algorithmic stress formula, which is a typical feature of EM schemes for displacement elements. It has been shown that the new stress formula leads to significant simplifications for the numerical implementation when compared to previously developed projection-based formulas. Apart from the advantages for the structure-preserving discretization in time, the newly proposed mixed variational formulation also offers new options for the design of mixed finite elements. It has been shown that the specific mixed element formulation singled out in the present work shows superior numerical robustness and accuracy, when compared to the corresponding displacement element.

Based on this formulation, we extended the recently developed framework of mixed finite elements to the class of Ogden-type material models. Typically, this class of material models shows a good correlation between simulations and experiments of rubber-like materials and contains Mooney-Rivlin and Neo-Hookean material models as special cases. Since rubber-like materials are known to be nearly incompressible, we used a multiplicative split of the deformation gradient. This ensures a decoupled expression of the underlying stored energy function in an isochoric part and a volume-changing part. Afterwards, we proposed a mixed variational framework based on a three-field Hu-Washizu-type variational formulation, where the displacements, the determinant of the deformation gradient, and the hydrostatic pressure enter the functional. Employing stationarity conditions yield the variational equations which have been discretized in time and space. For the discretization in time, we introduced a newly developed algorithmic stress formula, tailor-made for EM consistent time approximation of Ogden-type material models, within the mixed formulation. The newly proposed EM time discretization of the underlying mixed variational formulation allows for alternative spatial approximations of the mixed fields. The numerical examples show that the newly proposed EM time-discretization, along with the mixed space-discretization (e.g., Q1P0), performs extremely well in terms of numerical stability and accuracy.

The key follow-up point in this thesis is the extension of the newly developed stress formula to multi-field problems. We presented a new approach to the design of EM consistent time integration schemes in the field of nonlinear thermo-elastodynamics. The key element for this development is the tensor cross product, which allows us to find a polyconvexity-based, frame-indifferent Helmholtz free energy functional

and greatly simplifies the algebra. Based on this, a new temperature-based variational formulation has been devised, which made possible the design of an EM consistent scheme. The polyconvexity-based framework has been discretized first in time. In particular, a new algorithmic stress formula has been developed with a remarkably simple structure for the numerical implementation that avoids the use of previously developed projection-based formulas. The EM consistent time integrator consistently reproduces the physical behavior of the coupled thermo-elastodynamic model. In addition, the algorithm presented herein is numerically stable for different types of initial and boundary conditions. The newly proposed integration scheme was investigated with respect to the numerical behavior in different transient examples. It turned out that the advocated approach exhibited superior numerical stability properties, which is due to the consistent reproduction of the fundamental thermo-mechanical balance laws in the discrete setting. It became evident that the proposed polyconvexity-based formulation, in terms of the temperature, yields a particularly robust scheme. This leads to remarkably reliable results, even for coarse time-steps, which is in contrast to standard second-order implicit integrators.

Finally, a new, consistent energy-momentum one-step time stepping scheme was presented in the context of nonlinear electro-elastodynamics. The new time integrator relies on the definition of four discrete derivative expressions of the internal energy, where each one represents the algorithmic counterpart of the work conjugates of the right Cauchy-Green deformation tensor, its co-factor, its determinant, and the Lagrangian electric displacement field. Proof of thermodynamical consistency and of second-order accuracy with respect to time of the resulting algorithm, are presented. A series of numerical examples have been included in order to prove the superior robustness and conservation properties of the (internal energy-based) EM time-stepping scheme proposed.

## 7.2 Outlook

Based on the present contribution, some research projects are currently in progress or seem to be worth investigating. In particular, we focus on the intersections of the three circles, as illustrated in Fig. 1.1.

- In [45], the time integrator for finite strain electromechanics, as proposed in Chapter 6, has been developed from a new mixed variational framework to

make possible several discretizations in space. According to a suitable choice of the interpolation spaces for the mixed fields, the new formulation exhibits superior numerical performance compared to the formulation proposed in Chapter 6.

- In a similar way, it would be worth investigating a mixed formulation for finite strain thermo-elastodynamics. With regards to Chapter 3, the mixed formulation at hand should show superior numerical robustness and accuracy compared to the formulation proposed in Chapter 5. Moreover, the algorithm proposed in Chapter 5 only approximates the first law of thermodynamics in the full discrete setting consistently. The consistent formulation of the second law of thermodynamics could be addressed as well.
- Another field of interest would be a combination of the EM consistent time-stepping schemes proposed in Chapter 5 and 6. The new time integrator for finite strain electro-thermo-elastodynamics should show the well-known advantages of structure-preserving time-stepping schemes and would be useful for many applications of interest. Additionally, a mixed formulation could be addressed in the context of the electro-thermo-elastodynamic problem at hand.

As mentioned in the beginning of this thesis, variational integrators represent an interesting class of structure-preserving numerical methods. In the context of the mixed variational framework, it would be of interest to focus on variational integrators originating from Hu-Washizu-type or Hellinger-Reissner-type variational principles.

# A Appendix to Chapter 2<sup>1</sup>

## A.1 Relations for the tensor cross product

The relationships for the tensor cross product summarized in (2.12) can be easily verified by resorting to index notation. Accordingly, using definition (2.8) of the tensor cross product, commutative property (2.12)<sub>1</sub> can be verified by considering

$$\begin{aligned}(\mathbf{A} \star \mathbf{B})_{ij} &= \varepsilon_{i\alpha\beta} \varepsilon_{jab} A_{\alpha a} B_{\beta b} \\ &= \varepsilon_{i\beta\alpha} \varepsilon_{jba} B_{\beta b} A_{\alpha a} \\ &= (\mathbf{B} \star \mathbf{A})_{ij}.\end{aligned}\tag{A.1}$$

Here, the fact that the permutation symbol  $\varepsilon_{i\alpha\beta}$  changes sign under transposition, i.e.  $\varepsilon_{i\alpha\beta} = -\varepsilon_{i\beta\alpha}$ , has been used twice. To verify relation (2.12)<sub>2</sub>, consider

$$\begin{aligned}(\mathbf{A} \star \mathbf{B})_{ij}^T &= (\mathbf{A} \star \mathbf{B})_{ji} \\ &= \varepsilon_{j\alpha\beta} \varepsilon_{iab} A_{\alpha a} B_{\beta b} \\ &= \varepsilon_{iab} \varepsilon_{j\alpha\beta} (\mathbf{A}^T)_{a\alpha} (\mathbf{B}^T)_{b\beta} \\ &= \mathbf{A}^T \star \mathbf{B}^T.\end{aligned}\tag{A.2}$$

Permutation property (2.12)<sub>3</sub> follows directly from the fact that the permutation symbol is invariant under cyclic permutation of indices. That is,  $\varepsilon_{i\alpha\beta} = \varepsilon_{\alpha\beta i} = \varepsilon_{\beta i\alpha}$ . Thus, we obtain, for example,

$$\begin{aligned}(\mathbf{A} \star \mathbf{B}) : \mathbf{C} &= (\mathbf{A} \star \mathbf{B})_{ij} (\mathbf{C})_{ij} \\ &= \varepsilon_{i\alpha\beta} \varepsilon_{jab} A_{\alpha a} B_{\beta b} C_{ij} \\ &= \varepsilon_{\alpha\beta i} \varepsilon_{abj} B_{\beta b} C_{ij} A_{\alpha a} \\ &= (\mathbf{B} \star \mathbf{C})_{aa} (\mathbf{A})_{aa} \\ &= (\mathbf{B} \star \mathbf{C}) : \mathbf{A}.\end{aligned}\tag{A.3}$$

---

<sup>1</sup> This chapter is based on the appendix given in [23].

To verify relation (2.12)<sub>4</sub>, we make use of the epsilon-delta identity (see, for example, [53]),

$$\varepsilon_{jab}\varepsilon_{j\gamma\delta} = \delta_{a\gamma}\delta_{b\delta} - \delta_{a\delta}\delta_{b\gamma}, \quad (\text{A.4})$$

to obtain

$$\begin{aligned} ((\mathbf{A}*\mathbf{B})(\mathbf{C}* \mathbf{D}))_{ik} &= (\mathbf{A}*\mathbf{B})_{ij}(\mathbf{C}* \mathbf{D})_{jk} \\ &= \varepsilon_{i\alpha\beta}\varepsilon_{jab}A_{\alpha a}B_{\beta b}\varepsilon_{j\gamma\delta}\varepsilon_{kcd}C_{\gamma c}D_{\delta d} \\ &= \varepsilon_{i\alpha\beta}\varepsilon_{kcd}(\delta_{a\gamma}\delta_{b\delta} - \delta_{a\delta}\delta_{b\gamma})A_{\alpha a}B_{\beta b}C_{\gamma c}D_{\delta d} \\ &= \varepsilon_{i\alpha\beta}\varepsilon_{kcd}(A_{\alpha\gamma}C_{\gamma c}B_{\beta\delta}D_{\delta d} - A_{\alpha\delta}D_{\delta d}B_{\beta\gamma}C_{\gamma c}) \\ &= \varepsilon_{i\alpha\beta}\varepsilon_{kcd}(\mathbf{AC})_{\alpha c}(\mathbf{BD})_{\beta d} + \varepsilon_{i\alpha\beta}\varepsilon_{kdc}(\mathbf{BC})_{\beta c}(\mathbf{AD})_{\alpha d} \\ &= (\mathbf{AC})*(\mathbf{BD}) + (\mathbf{BC})*(\mathbf{AD}). \end{aligned} \quad (\text{A.5})$$

Eventually, distributive property (2.12)<sub>5</sub> is obviously satisfied.

# B Appendix to Chapter 3<sup>1</sup>

## B.1 Implementation details of the displacement formulation

Inserting the approximations from (6.51) into the semi-discrete variational formulation (3.65) yields the nodal residual vectors  $\mathbf{R}_V^a \in \mathbb{R}^3$  and  $\mathbf{R}_\varphi^a \in \mathbb{R}^3$  given by

$$\begin{aligned} \mathbf{R}_V^a &= \mathbf{M}^{ab} (\varphi_{b_{n+1}} - \varphi_{b_n} - \Delta t \mathbf{V}_{b_{n+\frac{1}{2}}}), \\ \mathbf{R}_\varphi^a &= \int_{\mathcal{B}_0} \mathbf{B}_{n+\frac{1}{2}}^{aT} \mathbf{S}_A^V dV + \int_{\mathcal{B}_0} \rho_0 \bar{\mathbf{B}} N^a dV + \mathbf{M}^{ab} \frac{1}{\Delta t} (\mathbf{V}_{b_{n+1}} - \mathbf{V}_{b_n}), \end{aligned} \quad (\text{B.1})$$

with mass matrix  $\mathbf{M}^{ab} \in \mathbb{R}^{3 \times 3}$  of the form

$$\mathbf{M}^{ab} = \int_{\mathcal{B}_0} \rho_0 N^a N^b dV \mathbf{I}, \quad (\text{B.2})$$

and the standard operator-matrix  $\mathbf{B}^a \in \mathbb{R}^{6 \times 3}$  which links the nodal displacements to the strains (see, for example, [175]). For the sake of clearness, we neglect superscript  $h$  throughout this appendix. Taking into account the symmetry of  $\mathbf{S}_A \in \mathbb{R}^{3 \times 3}$ , the independent components of  $\mathbf{S}_A$  are arranged in a column vector  $\mathbf{S}_A^V \in \mathbb{R}^6$ . Specifically,  $\mathbf{A}^V \in \mathbb{R}^6$  refers to the so-called Voigt's vector notation of a symmetric stress-type quantity  $\mathbf{A} \in \mathbb{R}^{3 \times 3}$  given by

$$\mathbf{A} = \begin{bmatrix} A_{11} & A_{12} & A_{13} \\ A_{21} & A_{22} & A_{23} \\ A_{31} & A_{32} & A_{33} \end{bmatrix} \rightarrow \mathbf{A}^V = [A_{11} \quad A_{22} \quad A_{33} \quad A_{12} \quad A_{23} \quad A_{13}]^T. \quad (\text{B.3})$$

---

<sup>1</sup> This chapter is based on the appendix given in [23].

Similarly,  $\bar{A}^V \in \mathbb{R}^6$  collects the independent components of a symmetric strain-type quantity  $\bar{A} \in \mathbb{R}^{3 \times 3}$  leading to

$$\bar{A} = \begin{bmatrix} \bar{A}_{11} & \bar{A}_{12} & \bar{A}_{13} \\ \bar{A}_{21} & \bar{A}_{22} & \bar{A}_{23} \\ \bar{A}_{31} & \bar{A}_{32} & \bar{A}_{33} \end{bmatrix} \rightarrow \bar{A}^V = [\bar{A}_{11} \quad \bar{A}_{22} \quad \bar{A}_{33} \quad 2\bar{A}_{12} \quad 2\bar{A}_{23} \quad 2\bar{A}_{13}]^T. \quad (\text{B.4})$$

In this way work-conjugate pairings of stress-type and strain-type quantities can be written as

$$A : \bar{A} = \bar{A}^{V^T} A^V. \quad (\text{B.5})$$

For an efficient implementation, the nodal velocities are expressed in terms of the displacements. Accordingly,  $(B.1)_1$  yields

$$\mathbf{V}_{bn+1} = -\mathbf{V}_{bn} + \frac{2}{\Delta t} (\boldsymbol{\varphi}_{bn+1} - \boldsymbol{\varphi}_{bn}). \quad (\text{B.6})$$

Inserting (B.6) into  $(B.1)_2$  leads to a size-reduced global residual vector  $\tilde{\mathbf{R}}_\varphi \in \mathbb{R}^{3n_{node}}$ , with nodal contributions  $\tilde{\mathbf{R}}_\varphi^a \in \mathbb{R}^3$  given by

$$\tilde{\mathbf{R}}_\varphi^a = \int_{\mathcal{B}_0} \mathbf{B}_{n+\frac{1}{2}}^{a^T} \mathbf{S}_A^V dV + \int_{\mathcal{B}_0} \rho_0 \bar{\mathbf{B}} N^a dV - \frac{2}{\Delta t} \mathbf{M}^{ab} \mathbf{V}_{bn} + \frac{2}{\Delta t^2} \mathbf{M}^{ab} (\boldsymbol{\varphi}_{bn+1} - \boldsymbol{\varphi}_{bn}), \quad (\text{B.7})$$

( $a = 1, \dots, n_{node}$ ). For the iterative solution process, the corresponding tangent moduli are needed. The linearization of the fully discrete system results in

$$D\tilde{\mathbf{R}}_\varphi^a \cdot \Delta \mathbf{d}_{n+1} = \mathbf{K}^{ab} \Delta \boldsymbol{\varphi}_{bn+1}, \quad (\text{B.8})$$

where  $\mathbf{d} \in \mathbb{R}^{3n_{node}}$  contains the nodal position vectors  $\boldsymbol{\varphi}_b \in \mathbb{R}^3$ . The contribution of node  $a$  and node  $b$  to the effective element tangent matrix,  $\mathbf{K}^{ab} \in \mathbb{R}^{3 \times 3}$ , can be written as

$$\mathbf{K}^{ab} = \mathbf{K}_{\text{dyn}}^{ab} + \mathbf{K}_{\text{geo}}^{ab} + \mathbf{K}_{\text{mat}}^{ab}. \quad (\text{B.9})$$

Note that we assume dead loads acting on the body ( $\mathbf{K}_{\text{ext}}^{ab} = \mathbf{0}$ ). The dynamical part of the tangent matrix is given by

$$\mathbf{K}_{\text{dyn}}^{ab} = \frac{2}{\Delta t^2} \mathbf{M}^{ab}. \quad (\text{B.10})$$

For the geometrical part we obtain

$$\mathbf{K}_{\text{geo}}^{ab} = \frac{1}{2} \int_{\mathcal{B}_0} N_{,I}^a N_{,J}^b (\mathbf{S}_A)_{IJ} \mathbf{I} dV, \quad (\text{B.11})$$

while the material part is given by

$$\mathbf{K}_{\text{mat}}^{ab} = \frac{1}{2} \int_{\mathcal{B}_0} \mathbf{B}_{n+\frac{1}{2}}^{a\top} \tilde{\mathbf{D}} \mathbf{B}_{n+\frac{1}{2}}^b \, dV. \quad (\text{B.12})$$

Here,  $\tilde{\mathbf{D}} \in \mathbb{R}^{6 \times 6}$  contains the algorithmic material tangent moduli arising from the linearization of the algorithmic stress tensor (3.66). For example, in case of the Mooney-Rivlin material we obtain

$$\begin{aligned} \tilde{\mathbf{D}} = & \mathcal{D}(\text{D}_{\mathcal{G}}\Psi + \text{D}_{\mathcal{C}}\Psi \mathcal{D}\left(\frac{2}{3}(\mathbf{c}_{n+\frac{1}{2}} + \frac{1}{2}\mathbf{c}_{n+1})\right) \\ & + \partial_{\mathbf{c}_{n+1}}\left(\text{D}_{\mathcal{C}}\Psi \frac{1}{3}\left(\mathcal{G}_{\varphi_{n+\frac{1}{2}}}^V + \overline{(\mathbf{c}_{n+\frac{1}{2}} * \mathbf{c}_{n+\frac{1}{2}})}^V\right)\right) \otimes \mathcal{G}_{\varphi_{n+1}}^V), \end{aligned} \quad (\text{B.13})$$

where  $\text{D}_{\mathcal{G}}\Psi$  and  $\text{D}_{\mathcal{C}}\Psi$  stand for the discrete derivatives given by (3.40)<sub>2</sub> and (3.41), respectively. Moreover, in (B.13), the operator matrix  $\mathcal{D}(\mathbf{A})$  embodies the operation  $\mathbf{A} : (\mathbf{V} * \mathbf{W})$ , where  $\mathbf{V}$  and  $\mathbf{W}$  are symmetric, leading to  $\mathbf{V}^{\text{VT}} \mathcal{D}(\mathbf{A}) \mathbf{W}^V$ , where

$$\mathcal{D}(\mathbf{A}) = \begin{bmatrix} 0 & 2A_{33} & 2A_{22} & 0 & -2A_{23} & 0 \\ 2A_{33} & 0 & 2A_{11} & 0 & 0 & -2A_{13} \\ 2A_{22} & 2A_{11} & 0 & -2A_{12} & 0 & 0 \\ 0 & 0 & -2A_{21} & -A_{33} & A_{13} & A_{23} \\ -2A_{23} & 0 & 0 & A_{13} & -A_{11} & A_{12} \\ 0 & -2A_{13} & 0 & A_{23} & A_{12} & -A_{22} \end{bmatrix}. \quad (\text{B.14})$$

The assembly procedure of the element contributions to the global tangent matrix and the global residual vector is standard and can be found in textbooks such as [175].

## B.2 Implementation details of the mixed formulation

In an analogous way to the implementation of the displacement formulation (see Appendix B.1) we provide the residual vector and tangent moduli for the mixed element formulation. As mentioned in Section 3.3.2, it is possible to use different interpolation formulas for the mixed fields. In the following we allow for different interpolations of the individual mixed fields on element level. The corresponding shape functions are distinguished by a subscript. For example, we write

$$\mathbf{A}^h \Big|_{\mathcal{B}_0^{(e)}} = \sum_{b=1}^{n_{\text{en}}^{\mathbf{A}}} M_{\mathbf{A}}^b \mathbf{A}_b, \quad \mathbf{A}^h \Big|_{\mathcal{B}_0^{(e)}} = \sum_{b=1}^{n_{\text{en}}^{\mathbf{A}}} M_{\mathbf{A}}^b \mathbf{A}_b, \quad (\text{B.15})$$

where  $A \in \mathbb{R}^{3 \times 3}$  stands for  $\mathcal{C}$ ,  $\mathcal{G}$ ,  $\Lambda^{\mathcal{C}}$  or  $\Lambda^{\mathcal{G}}$  and  $A \in \mathbb{R}$  stands for  $\mathcal{C}$  or  $\Lambda^{\mathcal{C}}$ . Moreover,  $n_{\text{en}}^{\Lambda}$  or  $n_{\text{en}}^{\Lambda}$  stands for the nodes per element of the corresponding quantity. For the sake of clearness we neglect the superscript  $h$  in the sequel. Inserting the interpolation formulas into the semi-discrete variational equations (3.33), (3.34) and (3.35) we get

$$\begin{aligned} \mathbf{R}_{\mathbf{V}}^a &= \mathbf{M}^{ab} (\boldsymbol{\varphi}_{b_{n+1}} - \boldsymbol{\varphi}_{b_n} - \Delta t \mathbf{V}_{b_{n+\frac{1}{2}}}), \\ \mathbf{R}_{\boldsymbol{\varphi}}^a &= \int_{\mathcal{B}_0} \mathbf{B}_{n+\frac{1}{2}}^{aT} (\Lambda_{n+1}^{\mathcal{C}})^V dV + \int_{\mathcal{B}_0} \rho_0 \bar{\mathbf{B}} N^a dV + \mathbf{M}^{ab} \frac{1}{\Delta t} (\mathbf{V}_{b_{n+1}} - \mathbf{V}_{b_n}), \end{aligned} \quad (\text{B.16})$$

$$\begin{aligned} \mathbf{R}_{\mathcal{C}}^a &= \int_{\mathcal{B}_0} \left( \text{D}_{\mathcal{C}} \Psi - \Lambda_{n+1}^{\mathcal{C}} + \Lambda_{n+1}^{\mathcal{G}} * \mathcal{C}_{n+\frac{1}{2}} + \frac{1}{3} \Lambda_{n+1}^{\mathcal{C}} \mathcal{G}_{n+\frac{1}{2}} \right) M_{\mathcal{C}}^a dV, \\ \mathbf{R}_{\mathcal{G}}^a &= \int_{\mathcal{B}_0} \left( \text{D}_{\mathcal{G}} \Psi - \Lambda_{n+1}^{\mathcal{G}} + \frac{1}{3} \Lambda_{n+1}^{\mathcal{C}} \mathcal{C}_{n+\frac{1}{2}} \right) M_{\mathcal{G}}^a dV, \end{aligned} \quad (\text{B.17})$$

$$\begin{aligned} \mathbf{R}_{\mathcal{C}}^a &= \int_{\mathcal{B}_0} (\text{D}_{\mathcal{C}} \Psi - \Lambda_{n+1}^{\mathcal{C}}) M_{\mathcal{C}}^a dV, \\ \mathbf{R}_{\Lambda^{\mathcal{C}}}^a &= \int_{\mathcal{B}_0} (\mathcal{C}_{n+1} - \mathcal{C}_{n+1}) M_{\Lambda^{\mathcal{C}}}^a dV, \\ \mathbf{R}_{\Lambda^{\mathcal{G}}}^a &= \int_{\mathcal{B}_0} \left( \frac{1}{2} \mathcal{C}_{n+1} * \mathcal{C}_{n+1} - \mathcal{G}_{n+1} \right) M_{\Lambda^{\mathcal{G}}}^a dV, \\ \mathbf{R}_{\Lambda^{\mathcal{C}}}^a &= \int_{\mathcal{B}_0} \left( \frac{1}{3} \mathcal{G}_{n+1} : \mathcal{C}_{n+1} - \mathcal{C}_{n+1} \right) M_{\Lambda^{\mathcal{C}}}^a dV, \end{aligned} \quad (\text{B.18})$$

with the mass matrix  $\mathbf{M}^{ab}$  as introduced in (B.2), the standard nodal operator matrix  $\mathbf{B}^a \in \mathbb{R}^{6 \times 3}$ , and the vector notation introduced in Appendix B.1. Similar to the displacement-based formulation, the nodal velocities  $\mathbf{V}_{b_{n+1}}$  are eliminated by using (B.6) to obtain the size-reduced nodal residual vector given by

$$\tilde{\mathbf{R}}_{\boldsymbol{\varphi}}^a = \int_{\mathcal{B}_0} \mathbf{B}_{n+\frac{1}{2}}^{aT} (\Lambda_{n+1}^{\mathcal{C}})^V dV + \int_{\mathcal{B}_0} \rho_0 \bar{\mathbf{B}} N^a dV - \frac{2}{\Delta t} \mathbf{M}^{ab} \mathbf{V}_{b_n} + \frac{2}{\Delta t^2} \mathbf{M}^{ab} (\boldsymbol{\varphi}_{b_{n+1}} - \boldsymbol{\varphi}_{b_n}). \quad (\text{B.19})$$

Next, we arrange the nodal residual vectors in element residual vectors of the form

$$\begin{aligned} \tilde{\mathbf{R}}_{\boldsymbol{\varphi}} &= \left[ \tilde{\mathbf{R}}_{\boldsymbol{\varphi}}^1; \dots; \tilde{\mathbf{R}}_{\boldsymbol{\varphi}}^{n_{\text{en}}^{\boldsymbol{\varphi}}} \right], \\ \mathbf{R}_{\Xi} &= \left[ (\mathbf{R}_{\mathcal{C}}^1)^V; \dots; (\mathbf{R}_{\mathcal{C}^{\text{en}}}^{\mathcal{C}})^V; (\mathbf{R}_{\mathcal{G}}^1)^V; \dots; (\mathbf{R}_{\mathcal{G}^{\text{en}}}^{\mathcal{G}})^V; (\mathbf{R}_{\mathcal{C}}^1)^V; \dots; (\mathbf{R}_{\mathcal{C}^{\text{en}}}^{\mathcal{C}})^V \right], \\ \mathbf{R}_{\Lambda} &= \left[ (\mathbf{R}_{\Lambda^{\mathcal{C}}}^1)^V; \dots; (\mathbf{R}_{\Lambda^{\mathcal{C}}^{\text{en}}}^{\Lambda^{\mathcal{C}}})^V; (\mathbf{R}_{\Lambda^{\mathcal{G}}}^1)^V; \dots; (\mathbf{R}_{\Lambda^{\mathcal{G}}^{\text{en}}}^{\Lambda^{\mathcal{G}}})^V; (\mathbf{R}_{\Lambda^{\mathcal{C}}}^1)^V; \dots; (\mathbf{R}_{\Lambda^{\mathcal{C}}^{\text{en}}}^{\Lambda^{\mathcal{C}}})^V \right], \end{aligned} \quad (\text{B.20})$$

where

$$\tilde{\mathbf{R}}_{\boldsymbol{\varphi}} \in \mathbb{R}^{3n_{\text{en}}^{\boldsymbol{\varphi}}}, \quad \mathbf{R}_{\Xi} \in \mathbb{R}^{6(n_{\text{en}}^{\mathcal{C}} + n_{\text{en}}^{\mathcal{G}}) + n_{\text{en}}^{\mathcal{C}}}, \quad \mathbf{R}_{\Lambda} \in \mathbb{R}^{6(n_{\text{en}}^{\Lambda^{\mathcal{C}}} + n_{\text{en}}^{\Lambda^{\mathcal{G}}}) + n_{\text{en}}^{\Lambda^{\mathcal{C}}}}. \quad (\text{B.21})$$

## Tangent operator

Next, we consider the tangent moduli pertaining to one individual element. As before we assume that dead loads are acting on the body. In analogy to Appendix B.1 we assume that the discrete derivatives  $D_{\mathcal{C}}\Psi$ ,  $D_{\mathcal{G}}\Psi$  and  $D_{\mathcal{C}}\Psi$  refer to those of the Mooney-Rivlin material, given by (3.40)<sub>2</sub> and (3.41). We start with the linearization of (B.19) to obtain

$$\begin{aligned} D_{\varphi_b} \tilde{\mathbf{R}}_{\varphi}^a : \Delta \varphi_{b_{n+1}} &= \mathbf{K}_{\varphi\varphi}^{ab} \Delta \varphi_{b_{n+1}}, & \mathbf{K}_{\varphi\varphi}^{ab} &= \int_{\mathcal{B}_0} N_{,I}^a N_{,J}^b (2 \Lambda_{n+1}^{\mathcal{C}})_{IJ} \mathbf{I} \, dV + M^{ab} \frac{1}{\Delta t^2}, \\ D_{\Lambda_b^{\mathcal{C}}} \tilde{\mathbf{R}}_{\varphi}^a : \Delta \Lambda_{b_{n+1}}^{\mathcal{C}} &= \mathbf{K}_{\varphi\Lambda^{\mathcal{C}}}^{ab} (\Delta \Lambda_{n+1}^{\mathcal{C}})_b^V, & \mathbf{K}_{\varphi\Lambda^{\mathcal{C}}}^{ab} &= \int_{\mathcal{B}_0} \mathbf{B}_{n+\frac{1}{2}}^{aT} M_{\Lambda^{\mathcal{C}}}^b \, dV. \end{aligned} \quad (\text{B.22})$$

The linearization of (B.17)<sub>1</sub> yields

$$\begin{aligned} D_{\mathcal{C}_b} \mathbf{R}_{\mathcal{C}}^a : \Delta \mathcal{C}_{b_{n+1}} &= \mathbf{K}_{\mathcal{C}\mathcal{C}}^{ab} \Delta \bar{\mathcal{C}}_{b_{n+1}}^V, & \mathbf{K}_{\mathcal{C}\mathcal{C}}^{ab} &= \frac{1}{2} \int_{\mathcal{B}_0} M_{\mathcal{C}}^a \mathcal{D}(\Lambda_{n+1}^{\mathcal{G}}) M_{\mathcal{C}}^b \, dV, \\ D_{\mathcal{G}_b} \mathbf{R}_{\mathcal{C}}^a : \Delta \mathcal{G}_{b_{n+1}} &= \mathbf{K}_{\mathcal{C}\mathcal{G}}^{ab} \Delta \bar{\mathcal{G}}_{b_{n+1}}^V, & \mathbf{K}_{\mathcal{C}\mathcal{G}}^{ab} &= \frac{1}{6} \int_{\mathcal{B}_0} M_{\mathcal{C}}^a M_{\mathcal{G}}^b \Lambda_{n+1}^{\mathcal{C}} \mathbb{I} \, dV, \\ D_{\Lambda_b^{\mathcal{C}}} \mathbf{R}_{\mathcal{C}}^a : \Delta \Lambda_{b_{n+1}}^{\mathcal{C}} &= \mathbf{K}_{\mathcal{C}\Lambda^{\mathcal{C}}}^{ab} (\Delta \Lambda_{n+1}^{\mathcal{C}})_b^V, & \mathbf{K}_{\mathcal{C}\Lambda^{\mathcal{C}}}^{ab} &= - \int_{\mathcal{B}_0} M_{\mathcal{C}}^a M_{\Lambda^{\mathcal{C}}}^b \mathbb{I} \, dV, \\ D_{\Lambda_b^{\mathcal{G}}} \mathbf{R}_{\mathcal{C}}^a : \Delta \Lambda_{b_{n+1}}^{\mathcal{G}} &= \mathbf{K}_{\mathcal{C}\Lambda^{\mathcal{G}}}^{ab} (\Delta \Lambda_{n+1}^{\mathcal{G}})_b^V, & \mathbf{K}_{\mathcal{C}\Lambda^{\mathcal{G}}}^{ab} &= \int_{\mathcal{B}_0} M_{\mathcal{C}}^a \mathcal{D}(\mathcal{C}_{n+\frac{1}{2}}) M_{\Lambda^{\mathcal{G}}}^b \, dV, \\ D_{\Lambda_b^{\mathcal{C}}} \mathbf{R}_{\mathcal{C}}^a : \Delta \Lambda_{b_{n+1}}^{\mathcal{C}} &= \mathbf{K}_{\mathcal{C}\Lambda^{\mathcal{C}}}^{ab} \Delta \Lambda_{b_{n+1}}^{\mathcal{C}}, & \mathbf{K}_{\mathcal{C}\Lambda^{\mathcal{C}}}^{ab} &= \frac{1}{3} \int_{\mathcal{B}_0} M_{\mathcal{C}}^a \bar{\mathcal{G}}_{n+\frac{1}{2}}^V M_{\Lambda^{\mathcal{C}}}^b \, dV, \end{aligned} \quad (\text{B.23})$$

where  $\mathbb{I} \in \mathbb{R}^{6 \times 6}$  is given by  $\mathbb{I} = \text{diag}(1, 1, 1, 2, 2, 2)$ . Concerning the linearization of (B.17)<sub>2</sub>, we obtain

$$\begin{aligned} D_{\mathcal{C}_b} \mathbf{R}_{\mathcal{G}}^a : \Delta \mathcal{C}_{b_{n+1}} &= \mathbf{K}_{\mathcal{G}\mathcal{C}}^{ab} \Delta \bar{\mathcal{C}}_{b_{n+1}}^V, & \mathbf{K}_{\mathcal{G}\mathcal{C}}^{ab} &= \frac{1}{6} \int_{\mathcal{B}_0} M_{\mathcal{G}}^a M_{\mathcal{C}}^b \Lambda_{n+1}^{\mathcal{C}} \mathbb{I} \, dV, \\ D_{\Lambda_b^{\mathcal{G}}} \mathbf{R}_{\mathcal{G}}^a : \Delta \Lambda_{b_{n+1}}^{\mathcal{G}} &= \mathbf{K}_{\mathcal{G}\Lambda^{\mathcal{G}}}^{ab} (\Delta \Lambda_{n+1}^{\mathcal{G}})_b^V, & \mathbf{K}_{\mathcal{G}\Lambda^{\mathcal{G}}}^{ab} &= - \int_{\mathcal{B}_0} M_{\mathcal{G}}^a M_{\Lambda^{\mathcal{G}}}^b \mathbb{I} \, dV, \\ D_{\Lambda_b^{\mathcal{C}}} \mathbf{R}_{\mathcal{G}}^a : \Delta \Lambda_{b_{n+1}}^{\mathcal{C}} &= \mathbf{K}_{\mathcal{G}\Lambda^{\mathcal{C}}}^{ab} \Delta \Lambda_{b_{n+1}}^{\mathcal{C}}, & \mathbf{K}_{\mathcal{G}\Lambda^{\mathcal{C}}}^{ab} &= \frac{1}{3} \int_{\mathcal{B}_0} M_{\mathcal{G}}^a M_{\Lambda^{\mathcal{C}}}^b \bar{\mathcal{C}}_{n+\frac{1}{2}}^V \, dV. \end{aligned} \quad (\text{B.24})$$

Furthermore (B.17)<sub>3</sub> yields

$$D_{C_b} R_C^a \Delta C_{b_{n+1}} = K_{CC}^{ab} \Delta C_{b_{n+1}} \quad K_{CC}^{ab} = \int_{B_0} \partial_{C_{n+1}} D_C \Psi M_C^a M_C^b dV, \quad (\text{B.25})$$

where  $\partial_{C_{n+1}} D_C \Psi$  is the derivative of the Greenspan formula (3.41). Note that this formula should be replaced with  $\frac{1}{2} f''(C_{n+\frac{1}{2}})$  in the limit  $C_{n+1} \rightarrow C_n$ . At last, we obtain

$$\begin{aligned} D_{\varphi_b} R_{\Lambda C}^a \cdot \Delta \varphi_{b_{n+1}} &= K_{\Lambda C \varphi}^{ab} \Delta \varphi_{b_{n+1}}, & K_{\Lambda C \varphi}^{ab} &= \int_{B_0} M_{\Lambda C}^a B_{n+1}^b dV, \\ D_{C_b} R_{\Lambda C}^a : \Delta C_{b_{n+1}} &= K_{\Lambda C C}^{ab} \Delta \bar{C}_{b_{n+1}}^V, & K_{\Lambda C C}^{ab} &= - \int_{B_0} M_{\Lambda C}^a M_C^b \mathbb{I} dV, \\ D_{C_b} R_{\Lambda \mathcal{G}}^a : \Delta C_{b_{n+1}} &= K_{\Lambda \mathcal{G} C}^{ab} \Delta \bar{C}_{b_{n+1}}^V, & K_{\Lambda \mathcal{G} C}^{ab} &= \int_{B_0} M_{\Lambda \mathcal{G}}^a \mathcal{D}(C_{n+1}) M_C^b dV, \\ D_{\mathcal{G}_b} R_{\Lambda \mathcal{G}}^a : \Delta \mathcal{G}_{b_{n+1}} &= K_{\Lambda \mathcal{G} \mathcal{G}}^{ab} \Delta \bar{\mathcal{G}}_{b_{n+1}}^V, & K_{\Lambda \mathcal{G} \mathcal{G}}^{ab} &= - \int_{B_0} M_{\Lambda \mathcal{G}}^a M_{\mathcal{G}}^b \mathbb{I} dV, \end{aligned} \quad (\text{B.26})$$

$$\begin{aligned} D_{C_b} R_{\Lambda C}^a : \Delta C_{b_{n+1}} &= K_{\Lambda^c C}^{ab} \Delta \bar{C}_{b_{n+1}}^V, & K_{\Lambda^c C}^{ab} &= \frac{1}{3} \int_{B_0} M_{\Lambda^c}^a \bar{\mathcal{G}}_{n+1}^{V^T} M_C^b dV, \\ D_{\mathcal{G}_b} R_{\Lambda^c}^a : \Delta \mathcal{G}_{b_{n+1}} &= K_{\Lambda^c \mathcal{G}}^{ab} \Delta \bar{\mathcal{G}}_{b_{n+1}}^V, & K_{\Lambda^c \mathcal{G}}^{ab} &= \frac{1}{3} \int_{B_0} M_{\Lambda^c}^a \bar{C}_{n+1}^{V^T} M_{\mathcal{G}}^b dV, \\ D_{C_b} R_{\Lambda^c}^a \Delta C_{b_{n+1}} &= K_{\Lambda^c C}^{ab} \Delta C_{b_{n+1}}, & K_{\Lambda^c C}^{ab} &= - \int_{B_0} M_{\Lambda^c}^a M_C^b dV. \end{aligned} \quad (\text{B.27})$$

Next, we obtain the element tangent stiffness matrix as

$$\begin{bmatrix} K_{\varphi\varphi}^{(e)} & \mathbf{0} & \mathbf{0} & \mathbf{0} & K_{\varphi\Lambda^c}^{(e)} & \mathbf{0} & \mathbf{0} \\ \mathbf{0} & K_{CC}^{(e)} & K_{C\mathcal{G}}^{(e)} & K_{CC}^{(e)} & K_{C\Lambda^c}^{(e)} & K_{C\Lambda\mathcal{G}}^{(e)} & K_{C\Lambda^c}^{(e)} \\ \mathbf{0} & K_{\mathcal{G}C}^{(e)} & K_{\mathcal{G}\mathcal{G}}^{(e)} & K_{\mathcal{G}C}^{(e)} & \mathbf{0} & K_{\mathcal{G}\Lambda\mathcal{G}}^{(e)} & K_{\mathcal{G}\Lambda^c}^{(e)} \\ \mathbf{0} & K_{CC}^{(e)} & K_{C\mathcal{G}}^{(e)} & K_{CC}^{(e)} & \mathbf{0} & \mathbf{0} & K_{C\Lambda^c}^{(e)} \\ K_{\Lambda^c\varphi}^{(e)} & K_{\Lambda^c C}^{(e)} & \mathbf{0} & \mathbf{0} & \mathbf{0} & \mathbf{0} & \mathbf{0} \\ \mathbf{0} & K_{\Lambda^c\mathcal{G}}^{(e)} & K_{\Lambda^c\mathcal{G}}^{(e)} & \mathbf{0} & \mathbf{0} & \mathbf{0} & \mathbf{0} \\ \mathbf{0} & K_{\Lambda^c C}^{(e)} & K_{\Lambda^c\mathcal{G}}^{(e)} & K_{\Lambda^c C}^{(e)} & \mathbf{0} & \mathbf{0} & \mathbf{0} \end{bmatrix} = \begin{bmatrix} K_{\varphi\varphi}^{(e)} & \mathbf{0} & K_{\varphi\Lambda}^{(e)} \\ \mathbf{0} & K_{\Xi\Xi}^{(e)} & K_{\Xi\Lambda}^{(e)} \\ K_{\Lambda\varphi}^{(e)} & K_{\Lambda\Xi}^{(e)} & \mathbf{0} \end{bmatrix}. \quad (\text{B.28})$$

Note that the submatrices of the above tangent stiffness matrix have been arranged in the same way as the element residual vector (B.20). The superscript e refers to the finite element under consideration. Note that for the Mooney-Rivlin material the entries in  $K_{\Xi\Xi}^{(e)}$  are zero except for  $K_{CC}^{(e)}$ . Together with (B.20), the linearized discrete

variational equation on element level can be written in the form

$$\begin{bmatrix} \delta\varphi \\ \delta\Xi \\ \delta\Lambda \end{bmatrix}^T \begin{bmatrix} \mathbf{K}_{\varphi\varphi}^{(e)} & \mathbf{0} & \mathbf{K}_{\varphi\Lambda}^{(e)} \\ \mathbf{0} & \mathbf{K}_{\Xi\Xi}^{(e)} & \mathbf{K}_{\Xi\Lambda}^{(e)} \\ \mathbf{K}_{\Lambda\varphi}^{(e)} & \mathbf{K}_{\Lambda\Xi}^{(e)} & \mathbf{0} \end{bmatrix} \begin{bmatrix} \Delta\varphi_{n+1}^{(e)} \\ \Delta\Xi_{n+1}^{(e)} \\ \Delta\Lambda_{n+1}^{(e)} \end{bmatrix} = - \begin{bmatrix} \delta\varphi \\ \delta\Xi \\ \delta\Lambda \end{bmatrix}^T \begin{bmatrix} \mathbf{R}_{\varphi}^{(e)} \\ \mathbf{R}_{\Xi}^{(e)} \\ \mathbf{R}_{\Lambda}^{(e)} \end{bmatrix}. \quad (\text{B.29})$$

## Static condensation process

Since the interpolation of  $\Xi$  and  $\Lambda$  is confined to each element, a static condensation procedure can be applied (see also [26]). On the element level we consider the algebraic system of equations given by

$$\begin{bmatrix} \mathbf{K}_{\varphi\varphi}^{(e)} & \mathbf{0} & \mathbf{K}_{\varphi\Lambda}^{(e)} \\ \mathbf{0} & \mathbf{K}_{\Xi\Xi}^{(e)} & \mathbf{K}_{\Xi\Lambda}^{(e)} \\ \mathbf{K}_{\Lambda\varphi}^{(e)} & \mathbf{K}_{\Lambda\Xi}^{(e)} & \mathbf{0} \end{bmatrix} \begin{bmatrix} \Delta\varphi_{n+1}^{(e)} \\ \Delta\Xi_{n+1}^{(e)} \\ \Delta\Lambda_{n+1}^{(e)} \end{bmatrix} = - \begin{bmatrix} \mathbf{R}_{\varphi}^{(e)} \\ \mathbf{R}_{\Xi}^{(e)} \\ \mathbf{R}_{\Lambda}^{(e)} \end{bmatrix}. \quad (\text{B.30})$$

The third row of (B.30) yields

$$\Delta\Xi_{n+1}^{(e)} = (\mathbf{K}_{\Lambda\Xi}^{(e)})^{-1} (-\mathbf{R}_{\Lambda}^{(e)} - \mathbf{K}_{\Lambda\varphi}^{(e)} \Delta\varphi_{n+1}^{(e)}). \quad (\text{B.31})$$

From the second row of (B.30), we obtain

$$\Delta\Lambda_{n+1}^{(e)} = (\mathbf{K}_{\Xi\Lambda}^{(e)})^{-1} (-\mathbf{R}_{\Xi}^{(e)} - \mathbf{K}_{\Xi\Xi}^{(e)} \Delta\Xi_{n+1}^{(e)}). \quad (\text{B.32})$$

Inserting (B.31) into (B.32) yields

$$\Delta\Lambda_{n+1}^{(e)} = (\mathbf{K}_{\Xi\Lambda}^{(e)})^{-1} (-\mathbf{R}_{\Xi}^{(e)} + \mathbf{K}_{\Xi\Xi}^{(e)} (\mathbf{K}_{\Lambda\Xi}^{(e)})^{-1} (\mathbf{R}_{\Lambda}^{(e)} + \mathbf{K}_{\Lambda\varphi}^{(e)} \Delta\varphi_{n+1}^{(e)})). \quad (\text{B.33})$$

Substituting (B.33) into the first row of (B.30) leads to

$$(\mathbf{K}_{\varphi\varphi}^{(e)} + \mathbf{K}_{\varphi\Lambda}^{(e)} (\mathbf{K}_{\Xi\Lambda}^{(e)})^{-1} \mathbf{K}_{\Xi\Xi}^{(e)} (\mathbf{K}_{\Lambda\Xi}^{(e)})^{-1} \mathbf{K}_{\Lambda\varphi}^{(e)}) \Delta\varphi_{n+1}^{(e)} \quad (\text{B.34})$$

$$+ \mathbf{R}_{\varphi}^{(e)} + \mathbf{K}_{\varphi\Lambda}^{(e)} (\mathbf{K}_{\Xi\Lambda}^{(e)})^{-1} (-\mathbf{R}_{\Xi}^{(e)} + \mathbf{K}_{\Xi\Xi}^{(e)} (\mathbf{K}_{\Lambda\Xi}^{(e)})^{-1} \mathbf{R}_{\Lambda}^{(e)}) = \mathbf{0}. \quad (\text{B.35})$$

Thus, on element level we obtain

$$\tilde{\mathbf{K}}_{\varphi\varphi}^{(e)} \Delta\varphi_{n+1}^{(e)} = -\tilde{\mathbf{R}}_{\varphi}^{(e)}, \quad (\text{B.36})$$

where

$$\begin{aligned} \tilde{\mathbf{K}}_{\varphi\varphi}^{(e)} &= (\mathbf{K}_{\varphi\varphi}^{(e)} + \mathbf{K}_{\varphi\Lambda}^{(e)} (\mathbf{K}_{\Xi\Lambda}^{(e)})^{-1} \mathbf{K}_{\Xi\Xi}^{(e)} (\mathbf{K}_{\Lambda\Xi}^{(e)})^{-1} \mathbf{K}_{\Lambda\varphi}^{(e)}), \\ \tilde{\mathbf{R}}_{\varphi}^{(e)} &= \mathbf{R}_{\varphi}^{(e)} + \mathbf{K}_{\varphi\Lambda}^{(e)} (\mathbf{K}_{\Xi\Lambda}^{(e)})^{-1} (-\mathbf{R}_{\Xi}^{(e)} + \mathbf{K}_{\Xi\Xi}^{(e)} (\mathbf{K}_{\Lambda\Xi}^{(e)})^{-1} \mathbf{R}_{\Lambda}^{(e)}). \end{aligned} \quad (\text{B.37})$$

The element tangent matrix  $\tilde{\mathbf{K}}_{\varphi\varphi}^{(e)}$  and the element residual vector  $\tilde{\mathbf{R}}_{\varphi}^{(e)}$  can now be assembled in the standard way as in the case of the displacement formulation dealt with in Appendix B.1.



## C Appendix to Chapter 4<sup>1</sup>

### C.1 Spectral decomposition of a symmetric tensor and its cofactor

We introduce the cofactor  $B = \text{cof}(A)$  of a second order tensor  $A$  as

$$B = \text{cof } A = \frac{1}{2} A \star A. \quad (\text{C.1})$$

The spectral decomposition of  $A$  yields

$$A = \lambda_1^A N_1^A \otimes N_1^A + \lambda_2^A N_2^A \otimes N_2^A + \lambda_3^A N_3^A \otimes N_3^A. \quad (\text{C.2})$$

Now (C.1) gives rise to

$$\begin{aligned} B &= \frac{1}{2} (\lambda_1^A N_1^A \otimes N_1^A + \lambda_2^A N_2^A \otimes N_2^A + \lambda_3^A N_3^A \otimes N_3^A) \\ &\quad \star (\lambda_1^A N_1^A \otimes N_1^A + \lambda_2^A N_2^A \otimes N_2^A + \lambda_3^A N_3^A \otimes N_3^A) \\ &= \lambda_2^A \lambda_3^A (N_2^A \otimes N_2^A) \star (N_3^A \otimes N_3^A) + \lambda_1^A \lambda_3^A (N_1^A \otimes N_1^A) \star (N_3^A \otimes N_3^A) \\ &\quad + \lambda_1^A \lambda_2^A (N_1^A \otimes N_1^A) \star (N_2^A \otimes N_2^A) \\ &= \lambda_2^A \lambda_3^A (N_2^A \times N_3^A) \otimes (N_2^A \times N_3^A) + \lambda_1^A \lambda_3^A (N_1^A \times N_3^A) \otimes (N_1^A \times N_3^A) \\ &\quad + \lambda_1^A \lambda_2^A (N_1^A \times N_2^A) \otimes (N_1^A \times N_2^A). \end{aligned} \quad (\text{C.3})$$

In the above use has been made of the relationship  $(\mathbf{a} \otimes \mathbf{b}) \star (\mathbf{c} \otimes \mathbf{d}) = (\mathbf{a} \times \mathbf{c}) \otimes (\mathbf{b} \times \mathbf{d})$  along with the orthonormality of the eigenvectors  $N_i^A$ . Accordingly, the spectral decomposition of  $B$  is given by

$$B = \lambda_1^B N_1^B \otimes N_1^B + \lambda_2^B N_2^B \otimes N_2^B + \lambda_3^B N_3^B \otimes N_3^B, \quad (\text{C.4})$$

---

<sup>1</sup> This chapter is based on the appendix given in [81].

where

$$\lambda_1^B = \lambda_2^A \lambda_3^A, \quad \lambda_2^B = \lambda_1^A \lambda_3^A, \quad \lambda_3^B = \lambda_1^A \lambda_2^A, \quad (\text{C.5})$$

and

$$N_1^B = N_1^A, \quad N_2^B = N_2^A, \quad N_3^B = N_3^A. \quad (\text{C.6})$$

## C.2 Relationship between the eigenvalue of a tensor and its derivative

The spectral decomposition, introduced in (4.2), is given by

$$A = \sum_{i=1}^3 \lambda_i^A N_i^A \otimes N_i^A. \quad (\text{C.7})$$

For the differentiation of (C.7) we get

$$dA = \sum_{i=1}^3 d\lambda_i^A N_i^A \otimes N_i^A + \lambda_i^A (dN_i^A \otimes N_i^A + N_i^A \otimes dN_i^A). \quad (\text{C.8})$$

Scalar multiplication of (C.8) by  $N_k^A \otimes N_k^A$  yields

$$\begin{aligned} \sum_{i=1}^3 N_i^A \cdot dA N_i^A &= \sum_{i=1}^3 d\lambda_i^A N_i^A \cdot (N_i^A \otimes N_i^A) N_i^A \\ &\quad + \lambda_i^A (N_i^A \cdot (dN_i^A \otimes N_i^A) N_i^A + N_i^A \cdot (N_i^A \otimes dN_i^A) N_i^A) \\ &= \sum_{i=1}^3 d\lambda_i^A, \end{aligned} \quad (\text{C.9})$$

where  $N_i^A \cdot (N_i^A \otimes N_i^A) N_i^A = 1$  and  $N_i^A \cdot (dN_i^A \otimes N_i^A) N_i^A + N_i^A \cdot (N_i^A \otimes dN_i^A) N_i^A = 0$  since  $N_i^A$  form an orthonormal basis. From (C.9), we obtain the following result

$$\sum_{i=1}^3 d\lambda_i^A = \sum_{i=1}^3 dA : (N_i^A \otimes N_i^A). \quad (\text{C.10})$$

Finally, for the derivative of the eigenvalue  $\lambda_i^A$  with respect to  $A$ , we obtain the following result

$$N_i^A \otimes N_i^A = \frac{\partial \lambda_i^A}{\partial A}. \quad (\text{C.11})$$

For more details see [155, 68].

## C.3 Remarks on the numerical implementation

### C.3.1 Time discrete eigenvalues

Similarly to the kinematic quantities, we obtain for the eigenvalues at a specific time-node

$$\begin{aligned} (\bar{\lambda}_i^C)_n &= \bar{\lambda}_i^C(\mathbf{C}(\boldsymbol{\varphi}_n)), & (\bar{\lambda}_i^C)_{n+1} &= \bar{\lambda}_i^C(\mathbf{C}(\boldsymbol{\varphi}_{n+1})), \\ (\bar{\lambda}_i^G)_n &= \bar{\lambda}_i^G(\mathbf{G}(\boldsymbol{\varphi}_n)), & (\bar{\lambda}_i^G)_{n+1} &= \bar{\lambda}_i^G(\mathbf{G}(\boldsymbol{\varphi}_{n+1})). \end{aligned} \quad (\text{C.12})$$

Note that the relationships provided in (4.32), are still valid in the time-discrete setting. For example, in case of the mid-point type discretization as introduced in Section 4.4 we get

$$\begin{aligned} \bar{\lambda}_1^G(\mathbf{G}(\boldsymbol{\varphi}_{n+\frac{1}{2}})) &= \bar{\lambda}_2^C(\mathbf{C}(\boldsymbol{\varphi}_{n+\frac{1}{2}})) \bar{\lambda}_3^C(\mathbf{C}(\boldsymbol{\varphi}_{n+\frac{1}{2}})), \\ \bar{\lambda}_2^G(\mathbf{G}(\boldsymbol{\varphi}_{n+\frac{1}{2}})) &= \bar{\lambda}_1^C(\mathbf{C}(\boldsymbol{\varphi}_{n+\frac{1}{2}})) \bar{\lambda}_3^C(\mathbf{C}(\boldsymbol{\varphi}_{n+\frac{1}{2}})), \\ \bar{\lambda}_3^G(\mathbf{G}(\boldsymbol{\varphi}_{n+\frac{1}{2}})) &= \bar{\lambda}_1^C(\mathbf{C}(\boldsymbol{\varphi}_{n+\frac{1}{2}})) \bar{\lambda}_2^C(\mathbf{C}(\boldsymbol{\varphi}_{n+\frac{1}{2}})). \end{aligned} \quad (\text{C.13})$$

In order to solve a minimum number of eigenvalue problems, the eigenvalues of  $\mathbf{G}$  in Section 4.4.1 are defined as

$$\begin{aligned} \bar{\lambda}_1^G(\mathbf{G}_{n+\frac{1}{2}}) &= \bar{\lambda}_2^C\left(\frac{1}{2}\mathbf{C}_{n+\frac{1}{2}} * \mathbf{C}_{n+\frac{1}{2}}\right) \bar{\lambda}_3^C\left(\frac{1}{2}\mathbf{C}_{n+\frac{1}{2}} * \mathbf{C}_{n+\frac{1}{2}}\right), \\ \bar{\lambda}_2^G(\mathbf{G}_{n+\frac{1}{2}}) &= \bar{\lambda}_1^C\left(\frac{1}{2}\mathbf{C}_{n+\frac{1}{2}} * \mathbf{C}_{n+\frac{1}{2}}\right) \bar{\lambda}_3^C\left(\frac{1}{2}\mathbf{C}_{n+\frac{1}{2}} * \mathbf{C}_{n+\frac{1}{2}}\right), \\ \bar{\lambda}_3^G(\mathbf{G}_{n+\frac{1}{2}}) &= \bar{\lambda}_1^C\left(\frac{1}{2}\mathbf{C}_{n+\frac{1}{2}} * \mathbf{C}_{n+\frac{1}{2}}\right) \bar{\lambda}_2^C\left(\frac{1}{2}\mathbf{C}_{n+\frac{1}{2}} * \mathbf{C}_{n+\frac{1}{2}}\right). \end{aligned} \quad (\text{C.14})$$

Therefore, in case of the mid-point discretization we have to solve one eigenvalue problem for  $\bar{\lambda}_i^C(\mathbf{C}(\boldsymbol{\varphi}_{n+\frac{1}{2}}))$ . In case of the structure preserving integration scheme, we have to solve three eigenvalue problems for  $\bar{\lambda}_i^C(\mathbf{C}_n)$ ,  $\bar{\lambda}_i^C(\mathbf{C}_{n+1})$  and  $\bar{\lambda}_i^C(\mathbf{C}_{n+\frac{1}{2}})$ , respectively. The eigenvalues of  $\mathbf{G}$  can then be calculated by use of (C.13) or (C.14), respectively.

### C.3.2 Perturbation technique

As already mentioned in Section 4.1.1, we focus on a perturbation technique to treat the case of equal eigenvalues and circumvent numerical problems. Depending on the value of the perturbation parameter, this technique can cause numerical

difficulties or spoil the energy-consistency of the algorithm. The perturbation algorithm as given in [111] is as follows: for two numerical equal eigenvalues  $|\bar{\lambda}_i - \bar{\lambda}_j| / (\max(|\bar{\lambda}_i|, |\bar{\lambda}_j|, |\bar{\lambda}_k|)) < \text{tol}$  we set

$$\bar{\lambda}_i = \bar{\lambda}_i (1 + \delta), \quad \bar{\lambda}_j = \bar{\lambda}_j (1 - \delta), \quad \bar{\lambda}_k = \bar{\lambda}_k / ((1 + \delta)(1 - \delta)), \quad (\text{C.15})$$

where the perturbation  $\delta$  is sufficiently small. A careful analysis of the perturbation technique in the context with structure-preserving integration schemes has been done in [118]. To define the desired structure-preserving integration scheme without numerical problems, the discrete derivatives in (4.66) are modified such that

$$\begin{aligned} D_{\mathbf{C}} \Psi_{iso}^{\mathbf{C}} &= \partial_{\mathbf{C}} \Psi_{iso}^{\mathbf{C}}(\bar{\lambda}_i^*(\mathbf{C}_{n+\frac{1}{2}})) + \frac{(\Psi_{iso}^{\mathbf{C}}((\bar{\lambda}_i^{\mathbf{C}})_{n+1}) - \Psi_{iso}^{\mathbf{C}}((\bar{\lambda}_i^{\mathbf{C}})_n)) \Delta \mathbf{C}}{\Delta \mathbf{C} : \Delta \mathbf{C}} \\ &\quad - \frac{\partial_{\mathbf{C}} \Psi_{iso}^{\mathbf{C}}(\bar{\lambda}_i^*(\mathbf{C}_{n+\frac{1}{2}})) : \Delta \mathbf{C}}{\Delta \mathbf{C} : \Delta \mathbf{C}} \Delta \mathbf{C}, \\ D_{\mathbf{G}} \Psi_{iso}^{\mathbf{G}} &= \partial_{\mathbf{G}} \Psi_{iso}^{\mathbf{G}}(\bar{\lambda}_i^*(\mathbf{G}_{n+\frac{1}{2}})) + \frac{(\Psi_{iso}^{\mathbf{G}}((\bar{\lambda}_i^{\mathbf{G}})_{n+1}) - \Psi_{iso}^{\mathbf{G}}((\bar{\lambda}_i^{\mathbf{G}})_n)) \Delta \mathbf{G}}{\Delta \mathbf{G} : \Delta \mathbf{G}} \\ &\quad - \frac{\partial_{\mathbf{G}} \Psi_{iso}^{\mathbf{G}}(\bar{\lambda}_i^*(\mathbf{G}_{n+\frac{1}{2}})) : \Delta \mathbf{G}}{\Delta \mathbf{G} : \Delta \mathbf{G}} \Delta \mathbf{G}. \end{aligned} \quad (\text{C.16})$$

In (C.16) we apply perturbation on  $\bar{\lambda}_i^{*\mathbf{C}}, \bar{\lambda}_i^{*\mathbf{G}}$  and no perturbation on  $\bar{\lambda}_i^{\mathbf{C}}$  and  $\bar{\lambda}_i^{\mathbf{G}}$ .

# D Appendix to Chapter 5<sup>1</sup>

## D.1 Energy termination

Since the EM consistent integrator is able to represent the balance of total energy in a consistent manner we can define an alternative termination criterion for the Newton-Raphson method based on the discrete balance of total energy

$$\left| \frac{1}{\Delta t} (E_{n+1} - E_n) - \mathcal{P}_{n,n+1}^{\text{ext}} - \mathcal{Q}_{n,n+1}^{\text{ext}} \right| \leq \varepsilon, \quad (\text{D.1})$$

where  $\varepsilon$  is the tolerance of the Newton-Raphson method.

## D.2 Classical mid-point discretization

A fully discrete thermo-elastodynamic system, derived from a classical formulation (cf. weak form (5.16)), is given by

$$\begin{aligned} \int_{\tilde{\mathcal{B}}_0} \mathbf{w}_\varphi^h \cdot \frac{1}{\Delta t} (\boldsymbol{\varphi}_{n+1}^h - \boldsymbol{\varphi}_n^h) \, dV &= \int_{\tilde{\mathcal{B}}_0} \mathbf{w}_\varphi^h \cdot \rho_0^{-1} \mathbf{p}_{n+\frac{1}{2}}^h \, dV, \\ \int_{\tilde{\mathcal{B}}_0} \mathbf{w}_p^h \cdot \frac{1}{\Delta t} (\mathbf{p}_{n+1}^h - \mathbf{p}_n^h) \, dV &= - \int_{\tilde{\mathcal{B}}_0} \mathbf{S}_{n+\frac{1}{2}}^h : (\partial_\chi \mathbf{w}_p^h \cdot \mathbf{F}_{n+\frac{1}{2}}^h) \, dV \\ &\quad + \int_{\tilde{\mathcal{B}}_0} \mathbf{w}_p^h \cdot \bar{\mathbf{B}}_{n+\frac{1}{2}} \, dV + \int_{\partial \mathcal{B}_0^p} \mathbf{w}_p^h \cdot \bar{\mathbf{T}}_{n+\frac{1}{2}} \, dA, \\ \int_{\tilde{\mathcal{B}}_0} \mathbf{w}_e^h \theta_{n+\frac{1}{2}}^h \cdot \frac{1}{\Delta t} (\eta_{n+1}^h - \eta_n^h) \, dV &= \int_{\tilde{\mathcal{B}}_0} \partial_\chi \mathbf{w}_e^h \cdot \mathbf{Q}_{n+\frac{1}{2}}^h \, dV \\ &\quad + \int_{\tilde{\mathcal{B}}_0} \mathbf{w}_e^h \bar{\mathbf{R}}_{n+\frac{1}{2}} \, dV + \int_{\partial \mathcal{B}_0^Q} \mathbf{w}_e^h \bar{\mathbf{Q}}_{n+\frac{1}{2}} \, dA, \end{aligned} \quad (\text{D.2})$$

---

<sup>1</sup> This chapter is based on the appendix given in [44].

where a mid-point integration scheme for the temporal discretization has been applied. The second Piola-Kirchhoff stress tensor in (D.2) is defined in its midpoint configuration as

$$\mathbf{S}_{n+\frac{1}{2}}^h = 2 \partial_{\mathbf{C}} \hat{\Psi}(\mathbf{C}(\boldsymbol{\varphi}_{n+\frac{1}{2}}^h), \theta_{n+\frac{1}{2}}^h). \quad (\text{D.3})$$

For the Piola heat flux vector in its midpoint configuration we obtain

$$\mathbf{Q}_{n+\frac{1}{2}}^h = -\mathbf{K}(\mathbf{C}(\boldsymbol{\varphi}_{n+\frac{1}{2}}^h), \theta_{n+\frac{1}{2}}^h) \gamma(\theta_{n+\frac{1}{2}}^h). \quad (\text{D.4})$$

Further details about the spatial discretization can be found e.g. in Miehe [113] and Holzapfel and Simo [69].

### D.3 Linearisation of the material model

We consider the Helmholtz free energy density function given in (5.64). This material model is consistent with the theory of linear thermoelasticity under certain restrictions on the material parameters which will be provided in the following. To proof consistency we perform a push forward operation on the second Piola-Kirchhoff stress tensor described in the polyconvex framework given by (5.19) and after division by the volume-map  $J = \det(\mathbf{F}) = C^{1/2}$  we obtain the Cauchy stress tensor, which can be divided into three parts

$$\boldsymbol{\sigma} = C^{-1/2} \mathbf{F} \mathbf{S} \mathbf{F}^T = \boldsymbol{\sigma}_1 + \boldsymbol{\sigma}_2 + \boldsymbol{\sigma}_3, \quad (\text{D.5})$$

where the specific parts are given by

$$\begin{aligned} \boldsymbol{\sigma}_1 &= 2a C^{-1/2} \mathbf{F} \mathbf{F}^T, \\ \boldsymbol{\sigma}_2 &= 2b C^{-1/2} (\text{tr}(\mathbf{C}) \mathbf{F} \mathbf{F}^T - \mathbf{F} \mathbf{C} \mathbf{F}^T), \\ \boldsymbol{\sigma}_3 &= (c_1 (C^{-1/2} - C^{-1}) - d_1 C^{-3/2} - 3\beta(\theta - \theta_0) (c_2 C^{-1} + d_2 C^{-2})) \mathbf{F} \mathbf{G} \mathbf{F}^T. \end{aligned} \quad (\text{D.6})$$

Expressing the deformation gradient using the displacement field  $\mathbf{u} : \mathcal{B}_0 \times \mathcal{I} \rightarrow \mathbb{R}^3$

$$\mathbf{F} = \mathbf{I} + \partial_{\mathbf{X}} \mathbf{u} \text{ with } \mathbf{u} = \boldsymbol{\varphi} - \mathbf{X}, \quad (\text{D.7})$$

and performing a linearisation in direction of  $\Delta \boldsymbol{\varphi} = \Delta \mathbf{u} = \mathbf{u} - \mathbf{u}_0$  and  $\Delta \theta = \theta - \theta_0$  with respect to operating points  $\mathbf{u}_0 = \mathbf{0}$  and  $\theta_0$

$$\text{Lin} \boldsymbol{\sigma}(\mathbf{u}_0, \theta_0)[\Delta \mathbf{u}, \Delta \theta] = \boldsymbol{\sigma}(\mathbf{u}_0, \theta_0) + \frac{d}{d\varepsilon} \boldsymbol{\sigma}(\mathbf{u}_0 + \varepsilon \Delta \mathbf{u}, \theta_0) \Big|_{\varepsilon=0} + \frac{d}{d\varepsilon} \boldsymbol{\sigma}(\mathbf{u}_0, \theta_0 + \varepsilon \Delta \theta) \Big|_{\varepsilon=0}, \quad (\text{D.8})$$

using the properties of the tensor cross product in (2.12) yields

$$\begin{aligned}
\text{Lin}\sigma_1(\mathbf{u}_0, \theta_0)[\Delta\mathbf{u}, \Delta\theta] &= 2a(\mathbf{I} - \text{tr}(\boldsymbol{\varepsilon})\mathbf{I} + 2\boldsymbol{\varepsilon}), \\
\text{Lin}\sigma_2(\mathbf{u}_0, \theta_0)[\Delta\mathbf{u}, \Delta\theta] &= 2b(2\mathbf{I} + 2\boldsymbol{\varepsilon}), \\
\text{Lin}\sigma_3(\mathbf{u}_0, \theta_0)[\Delta\mathbf{u}, \Delta\theta] &= c_1 \text{tr}(\boldsymbol{\varepsilon})\mathbf{I} + d_1(-\mathbf{I} + \text{tr}(\boldsymbol{\varepsilon})\mathbf{I}) - 3\beta(\theta - \theta_0)(c_2 + d_2)\mathbf{I},
\end{aligned} \tag{D.9}$$

where  $\boldsymbol{\varepsilon} = \frac{1}{2}(\partial_{\mathbf{x}}\mathbf{u} + \partial_{\mathbf{x}}\mathbf{u}^T)$  denotes the infinitesimal strain tensor. Accordingly the linearized Cauchy stress tensor is provided by

$$\begin{aligned}
\text{Lin}\sigma(\mathbf{u}_0, \theta_0)[\Delta\mathbf{u}, \Delta\theta] &= (2a + 4b - d_1)\mathbf{I} + (-2a + c_1 + d_1)\text{tr}(\boldsymbol{\varepsilon})\mathbf{I} + (4a + 4b)\boldsymbol{\varepsilon} \\
&\quad - 3\beta(\theta - \theta_0)(c_2 + d_2)\mathbf{I}.
\end{aligned} \tag{D.10}$$

Comparing the resulting Cauchy stress with the Cauchy stress from theory of linear thermoelasticity, given by

$$\sigma_{\text{lin}} = \lambda\text{tr}(\boldsymbol{\varepsilon})\mathbf{I} + 2\mu\boldsymbol{\varepsilon} - \beta(\theta - \theta_0)(3\lambda + 2\mu)\mathbf{I}, \tag{D.11}$$

leads to following restrictions

$$d_1 = 2(a + 2b), \quad -2a + c_1 + d_1 = \lambda, \quad 4(a + b) = 2\mu, \quad \lambda + \frac{2}{3}\mu = K = c_2 + d_2, \tag{D.12}$$

for consistency of the suggested Helmholtz free energy density function with the linear theory where  $\lambda$  and  $\mu$  are the Lamé parameters and  $K$  is the bulk modulus.



# E Appendix to Chapter 6<sup>1</sup>

## E.1 Proof of directionality property

The objective of this section is to prove that the definition of the discrete derivatives of the internal energy  $u(C, G, C, D)$  satisfy the directionality property in equation (6.35). For that, let us denote the expression on the left-hand side of the directionality property in (6.35) as  $\mathcal{T}$ , namely

$$\begin{aligned} \mathcal{T} = & D_C u : (C_{n+1} - C_n) + D_G u : (G_{n+1} - G_n) \\ & + D_C u (C_{n+1} - C_n) + D_D u \cdot (D_{n+1} - D_n). \end{aligned} \quad (\text{E.1})$$

Substitution of the expressions for  $D_C u$  (6.37),  $D_G u$  (6.39),  $D_C u$  (6.40) and  $D_D u$  (6.41) into (E.1) leads to

$$\begin{aligned} \mathcal{T} = & \frac{1}{2} u (C_{n+1}, G_{n+1}, C_{n+1}, D_{n+1}) - \frac{1}{2} u (C_n, G_{n+1}, C_{n+1}, D_{n+1}) \\ & + \frac{1}{2} u (C_{n+1}, G_n, C_n, D_n) - \frac{1}{2} u (C_n, G_n, C_n, D_n) \\ & + \frac{1}{2} u (C_n, G_{n+1}, C_{n+1}, D_{n+1}) - \frac{1}{2} u (C_n, G_n, C_{n+1}, D_{n+1}) \\ & + \frac{1}{2} u (C_{n+1}, G_{n+1}, C_n, D_n) - \frac{1}{2} u (C_{n+1}, G_n, C_n, D_n) \\ & + \frac{1}{2} u (C_n, G_n, C_{n+1}, D_{n+1}) - \frac{1}{2} u (C_n, G_n, C_n, D_{n+1}) \\ & + \frac{1}{2} u (C_{n+1}, G_{n+1}, C_{n+1}, D_n) - \frac{1}{2} u (C_{n+1}, G_{n+1}, C_n, D_n) \\ & + \frac{1}{2} u (C_n, G_n, C_n, D_{n+1}) - \frac{1}{2} u (C_n, G_n, C_n, D_n) \\ & + \frac{1}{2} u (C_{n+1}, G_{n+1}, C_{n+1}, D_{n+1}) - \frac{1}{2} u (C_{n+1}, G_{n+1}, C_{n+1}, D_n) \\ = & \Delta u, \end{aligned} \quad (\text{E.2})$$

---

<sup>1</sup> This chapter is based on the appendix given in [133].

which proves that the definition of the discrete derivatives satisfy the directionality property.

## E.2 Definition of the discrete derivatives in the limit

The objective of this section is to prove that the definition of the directional derivatives satisfies the condition stated in (6.36), namely that they are well defined in the limit  $\|\Delta\mathbf{C}\| \rightarrow 0$ ,  $\|\Delta\mathbf{G}\| \rightarrow 0$ ,  $|\Delta C| \rightarrow 0$  and  $\|\Delta\mathbf{D}\| \rightarrow 0$ . In particular, it will be proved in this Section that based on the definition of the discrete derivatives, these can be equivalently written as

$$D_{\pi^i} u = \partial_{\pi^i} u (\boldsymbol{\pi}_{n+1/2}) + \sum_{i=1}^4 O\left(\|\Delta\pi^i\|^2\right) + \sum_{j=1, j \neq i}^4 \sum_{k=j+1, k \neq 1}^4 O\left(\|\Delta\pi^j\| \|\Delta\pi^k\|\right), \quad (\text{E.3})$$

where  $\boldsymbol{\pi} = \{\mathbf{C}, \mathbf{G}, C, \mathbf{D}\} = \{\pi^1, \pi^2, \pi^3, \pi^4\}$ . We now prove that they are well defined in the limit. For that, let us carry out a Taylor series expansion of the four different evaluations of the internal energy  $u$  in equation (6.37) around  $\mathbf{C}_{n+1/2}$ . This enables to express them as

$$\begin{aligned} u(\mathbf{C}_{n+1}, \mathbf{G}_{n+1}, C_{n+1}, \mathbf{D}_{n+1}) &= u(\mathbf{C}_{n+1/2}, \mathbf{G}_{n+1}, C_{n+1}, \mathbf{D}_{n+1}) \\ &\quad + \partial_{\mathbf{C}} u(\mathbf{C}_{n+1/2}, \mathbf{G}_{n+1}, C_{n+1}, \mathbf{D}_{n+1}) : \left(\frac{1}{2}\Delta\mathbf{C}\right) \\ &\quad + \left(\frac{1}{2}\Delta\mathbf{C}\right) : \partial_{\mathbf{C}\mathbf{C}}^2 u(\mathbf{C}_{n+1/2}, \mathbf{G}_{n+1}, C_{n+1}, \mathbf{D}_{n+1}) : \left(\frac{1}{2}\Delta\mathbf{C}\right) \\ &\quad + O\left(\|\Delta\mathbf{C}\|^3\right), \end{aligned} \quad (\text{E.4})$$

$$\begin{aligned} u(\mathbf{C}_n, \mathbf{G}_{n+1}, C_{n+1}, \mathbf{D}_{n+1}) &= u(\mathbf{C}_{n+1/2}, \mathbf{G}_{n+1}, C_{n+1}, \mathbf{D}_{n+1}) \\ &\quad - \partial_{\mathbf{C}} u(\mathbf{C}_{n+1/2}, \mathbf{G}_{n+1}, C_{n+1}, \mathbf{D}_{n+1}) : \left(\frac{1}{2}\Delta\mathbf{C}\right) \\ &\quad + \left(\frac{1}{2}\Delta\mathbf{C}\right) : \partial_{\mathbf{C}\mathbf{C}}^2 u(\mathbf{C}_{n+1/2}, \mathbf{G}_{n+1}, C_{n+1}, \mathbf{D}_{n+1}) : \left(\frac{1}{2}\Delta\mathbf{C}\right) \\ &\quad + O\left(\|\Delta\mathbf{C}\|^3\right), \end{aligned} \quad (\text{E.5})$$

$$\begin{aligned}
 u(\mathbf{C}_{n+1}, \mathbf{G}_n, C_n, \mathbf{D}_n) &= u(\mathbf{C}_{n+1/2}, \mathbf{G}_n, C_n, \mathbf{D}_n) \\
 &+ \partial_{\mathbf{C}} u(\mathbf{C}_{n+1/2}, \mathbf{G}_n, C_n, \mathbf{D}_n) : \left(\frac{1}{2}\Delta\mathbf{C}\right) \\
 &+ \left(\frac{1}{2}\Delta\mathbf{C}\right) : \partial_{\mathbf{C}\mathbf{C}}^2 u(\mathbf{C}_{n+1/2}, \mathbf{G}_n, C_n, \mathbf{D}_n) : \left(\frac{1}{2}\Delta\mathbf{C}\right) \\
 &+ O(\|\Delta\mathbf{C}\|^3),
 \end{aligned} \tag{E.6}$$

$$\begin{aligned}
 u(\mathbf{C}_n, \mathbf{G}_n, C_n, \mathbf{D}_n) &= u(\mathbf{C}_{n+1/2}, \mathbf{G}_n, C_n, \mathbf{D}_n) \\
 &- \partial_{\mathbf{C}} u(\mathbf{C}_{n+1/2}, \mathbf{G}_n, C_n, \mathbf{D}_n) : \left(\frac{1}{2}\Delta\mathbf{C}\right) \\
 &+ \left(\frac{1}{2}\Delta\mathbf{C}\right) : \partial_{\mathbf{C}\mathbf{C}}^2 u(\mathbf{C}_{n+1/2}, \mathbf{G}_n, C_n, \mathbf{D}_n) : \left(\frac{1}{2}\Delta\mathbf{C}\right) \\
 &+ O(\|\Delta\mathbf{C}\|^3).
 \end{aligned} \tag{E.7}$$

Introduction of above equations (E.4)-(E.7) into the last four terms on the right-hand side of equation (6.37) yields

$$\begin{aligned}
 &\frac{1}{2} \frac{u(\mathbf{C}_{n+1}, \mathbf{G}_{n+1}, C_{n+1}, \mathbf{D}_{n+1}) - u(\mathbf{C}_n, \mathbf{G}_{n+1}, C_{n+1}, \mathbf{D}_{n+1})}{\|\Delta\mathbf{C}\|^2} \Delta\mathbf{C} \\
 &+ \frac{1}{2} \frac{u(\mathbf{C}_{n+1}, \mathbf{G}_n, C_n, \mathbf{D}_n) - u(\mathbf{C}_n, \mathbf{G}_n, C_n, \mathbf{D}_n)}{\|\Delta\mathbf{C}\|^2} \Delta\mathbf{C} \\
 &- \frac{1}{2} \frac{\partial_{\mathbf{C}} u(\mathbf{C}_{n+1/2}, \mathbf{G}_{n+1}, C_{n+1}, \mathbf{D}_{n+1}) : \Delta\mathbf{C}}{\|\Delta\mathbf{C}\|^2} \Delta\mathbf{C} \\
 &- \frac{1}{2} \frac{\partial_{\mathbf{C}} u(\mathbf{C}_{n+1/2}, \mathbf{G}_n, C_n, \mathbf{D}_n) : \Delta\mathbf{C}}{\|\Delta\mathbf{C}\|^2} \Delta\mathbf{C} = O(\|\Delta\mathbf{C}\|^2).
 \end{aligned} \tag{E.8}$$

Introduction of the result in (E.8) into the expression for the directional derivative  $D_{\mathbf{C}}u$  in (6.37) leads to

$$D_{\mathbf{C}}u = \frac{1}{2}(\partial_{\mathbf{C}} u(\mathbf{C}_{n+1/2}, \mathbf{G}_{n+1}, C_{n+1}, \mathbf{D}_{n+1}) + \partial_{\mathbf{C}} u(\mathbf{C}_{n+1/2}, \mathbf{G}_n, C_n, \mathbf{D}_n)) + O(\|\Delta\mathbf{C}\|^2). \tag{E.9}$$

A Taylor series expansion on the two first terms on the right-hand side of above

equation (E.9) enables these to be expressed as

$$\begin{aligned}
\partial_{\mathbf{C}}u(\mathbf{C}_{n+1/2}, \mathbf{G}_{n+1}, \mathbf{C}_{n+1}, \mathbf{D}_{n+1}) &= \partial_{\mathbf{C}}u\left(\mathbf{C}_{n+1/2}, \mathbf{G}_{n+1/2}, \mathbf{C}_{n+1/2}, \mathbf{D}_{n+\frac{1}{2}}\right) \\
&\quad + \partial_{\mathbf{C}\mathbf{G}}^2u\left(\mathbf{C}_{n+1/2}, \mathbf{G}_{n+1/2}, \mathbf{C}_{n+1/2}, \mathbf{D}_{n+\frac{1}{2}}\right) : \left(\frac{1}{2}\Delta\mathbf{G}\right) \\
&\quad + \partial_{\mathbf{C}\mathbf{C}}^2u\left(\mathbf{C}_{n+1/2}, \mathbf{G}_{n+1/2}, \mathbf{C}_{n+1/2}, \mathbf{D}_{n+\frac{1}{2}}\right) \left(\frac{1}{2}\Delta\mathbf{C}\right) \\
&\quad + \partial_{\mathbf{C}\mathbf{D}}^2u\left(\mathbf{C}_{n+1/2}, \mathbf{G}_{n+1/2}, \mathbf{C}_{n+1/2}, \mathbf{D}_{n+\frac{1}{2}}\right) : \left(\frac{1}{2}\Delta\mathbf{D}\right) \\
&\quad + O\left(\|\Delta\mathbf{G}\|^2\right) + O\left(\Delta\mathbf{C}^2\right) + O\left(\|\Delta\mathbf{D}\|^2\right) \\
&\quad + O\left(\|\Delta\mathbf{G}\|\Delta\mathbf{C}\right) + O\left(\|\Delta\mathbf{G}\|\|\Delta\mathbf{D}\|\right) + O\left(\Delta\mathbf{C}\|\Delta\mathbf{D}\|\right),
\end{aligned} \tag{E.10}$$

and

$$\begin{aligned}
\partial_{\mathbf{C}}u(\mathbf{C}_{n+1/2}, \mathbf{G}_n, \mathbf{C}_n, \mathbf{D}_n) &= \partial_{\mathbf{C}}u\left(\mathbf{C}_{n+1/2}, \mathbf{G}_{n+1/2}, \mathbf{C}_{n+1/2}, \mathbf{D}_{n+\frac{1}{2}}\right) \\
&\quad - \partial_{\mathbf{C}\mathbf{G}}^2u\left(\mathbf{C}_{n+1/2}, \mathbf{G}_{n+1/2}, \mathbf{C}_{n+1/2}, \mathbf{D}_{n+\frac{1}{2}}\right) : \left(\frac{1}{2}\Delta\mathbf{G}\right) \\
&\quad - \partial_{\mathbf{C}\mathbf{C}}^2u\left(\mathbf{C}_{n+1/2}, \mathbf{G}_{n+1/2}, \mathbf{C}_{n+1/2}, \mathbf{D}_{n+\frac{1}{2}}\right) \left(\frac{1}{2}\Delta\mathbf{C}\right) \\
&\quad - \partial_{\mathbf{C}\mathbf{D}}^2u\left(\mathbf{C}_{n+1/2}, \mathbf{G}_{n+1/2}, \mathbf{C}_{n+1/2}, \mathbf{D}_{n+\frac{1}{2}}\right) : \left(\frac{1}{2}\Delta\mathbf{D}\right) \\
&\quad + O\left(\|\Delta\mathbf{G}\|^2\right) + O\left(\Delta\mathbf{C}^2\right) + O\left(\|\Delta\mathbf{D}\|^2\right) \\
&\quad + O\left(\|\Delta\mathbf{G}\|\Delta\mathbf{C}\right) + O\left(\|\Delta\mathbf{G}\|\|\Delta\mathbf{D}\|\right) + O\left(\Delta\mathbf{C}\|\Delta\mathbf{D}\|\right).
\end{aligned} \tag{E.11}$$

Insert (E.10) and (E.11) into (E.9) leads to the final expression for the discrete derivative  $\mathbf{D}_{\mathbf{C}}u$  (6.37) as

$$\begin{aligned}
\mathbf{D}_{\mathbf{C}}u &= \partial_{\mathbf{C}}u\left(\mathbf{C}_{n+1/2}, \mathbf{G}_{n+1/2}, \mathbf{C}_{n+1/2}, \mathbf{D}_{n+\frac{1}{2}}\right) \\
&\quad + O\left(\|\Delta\mathbf{C}\|^2\right) + O\left(\|\Delta\mathbf{G}\|^2\right) + O\left(\Delta\mathbf{C}^2\right) + O\left(\|\Delta\mathbf{D}\|^2\right) \\
&\quad + O\left(\|\Delta\mathbf{G}\|\Delta\mathbf{C}\right) + O\left(\|\Delta\mathbf{G}\|\|\Delta\mathbf{D}\|\right) + O\left(\Delta\mathbf{C}\|\Delta\mathbf{D}\|\right),
\end{aligned} \tag{E.12}$$

which proves condition (E.3). Proceeding similarly, it would be possible to generalise above result (E.12) to the discrete derivatives  $\mathbf{D}_{\mathbf{G}}u$  (6.39),  $\mathbf{D}_{\mathbf{C}}u$  (6.40) and  $\mathbf{D}_{\mathbf{D}}u$  (6.41), namely

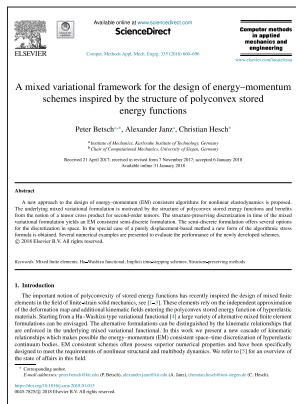
$$\begin{aligned}
\mathbf{D}_{\mathbf{G}}u &= \partial_{\mathbf{G}}u\left(\mathbf{C}_{n+1/2}, \mathbf{G}_{n+1/2}, \mathbf{C}_{n+1/2}, \mathbf{D}_{n+\frac{1}{2}}\right) \\
&\quad + O\left(\|\Delta\mathbf{C}\|^2\right) + O\left(\|\Delta\mathbf{G}\|^2\right) + O\left(\Delta\mathbf{C}^2\right) + O\left(\|\Delta\mathbf{D}\|^2\right) \\
&\quad + O\left(\|\Delta\mathbf{C}\|\Delta\mathbf{C}\right) + O\left(\|\Delta\mathbf{C}\|\|\Delta\mathbf{D}\|\right) + O\left(\Delta\mathbf{C}\|\Delta\mathbf{D}\|\right),
\end{aligned} \tag{E.13}$$

$$\begin{aligned}
 D_C u &= \partial_{C u} \left( C_{n+1/2}, G_{n+1/2}, C_{n+1/2}, D_{n+\frac{1}{2}} \right) \\
 &\quad + O \left( \|\Delta C\|^2 \right) + O \left( \|\Delta G\|^2 \right) + O \left( \Delta C^2 \right) + O \left( \|\Delta D\|^2 \right) \\
 &\quad + O \left( \|\Delta C\| \|\Delta G\| \right) + O \left( \|\Delta C\| \|\Delta D\| \right) + O \left( \|\Delta G\| \|\Delta D\| \right), \tag{E.14}
 \end{aligned}$$

$$\begin{aligned}
 D_D u &= \partial_{D u} \left( C_{n+1/2}, G_{n+1/2}, C_{n+1/2}, D_{n+\frac{1}{2}} \right) \\
 &\quad + O \left( \|\Delta C\|^2 \right) + O \left( \|\Delta G\|^2 \right) + O \left( \Delta C^2 \right) + O \left( \|\Delta D\|^2 \right) \tag{E.15} \\
 &\quad + O \left( \|\Delta C\| \|\Delta G\| \right) + O \left( \|\Delta C\| \Delta C \right) + O \left( \|\Delta G\| \Delta C \right).
 \end{aligned}$$



# Declaration of Authorship



**Citation:** P. Betsch, A. Janz and C. Hesch. A mixed variational framework for the design of energy-momentum schemes inspired by the structure of polyconvex stored energy functions. *Comput. Methods Appl. Mech. Engrg.*, 335:660–696, 2018.

**Declaration:** Alexander Janz (AJ) worked on the theory together with Peter Betsch (PB). The computational environment was partly provided by Christian Hesch (CH). AJ was responsible for the numerical implementation. Moreover, AJ performed the numerical verification of the newly developed formalism. Furthermore, AJ co-worked on the manuscript together with PB. Finally, the article was reviewed by all authors (AJ, PB, CH).



**Citation:** A. Janz, P. Betsch and M. Franke. Structure-preserving space-time discretization of a mixed formulation for quasi-incompressible large strain elasticity in principal stretches. *submitted to Int. J. Numer. Meth. Engng.*, 2018.

**Declaration:** AJ worked on the theory together with PB. AJ was responsible for the numerical implementation. Moreover, AJ performed the numerical verification of the newly developed formalism. Furthermore, AJ wrote the entire manuscript supported by PB and Marlon Franke (MF). Finally, the article was reviewed by all authors (AJ, PB, MF), where AJ was responsible for this process.

**Citation:** M. Franke, A. Janz, M. Schiebl and P. Betsch. An energy momentum consistent integration scheme using a polyconvexity-based framework for nonlinear thermo-elastodynamics. *Int. J. Numer. Meth. Engng.*, 115:549–577, 2018.

**Declaration:** AJ worked on the theory together with MF and Mark Schiebl (MS). AJ, MF and MS were responsible for the numerical implementation. Moreover, AJ, MF and MS performed the numerical verification of the newly developed formalism. Furthermore, AJ, MF and MS co-worked on the manuscript supported by PB. Finally, the article was reviewed by all authors (AJ, MF, MS, PB).

WILEY

**RESEARCH ARTICLE**

**An energy momentum consistent integration scheme using a polyconvexity-based framework for nonlinear thermo-elastodynamics**

M. Franke<sup>1</sup>, A. Janz<sup>1</sup>, M. Schiebl<sup>1</sup> & P. Betsch<sup>1</sup>

**Correspondence:** M. Franke, Institute of Mechanics, Karlsruhe Institute of Technology, Karlsruhe, Germany. Email: franke@kit.edu

**Summary**

The present contribution provides a new approach to the design of energy momentum consistent integrators schemes to the field of nonlinear thermo-elastodynamics. The method is inspired by the structure of polyconvex energy density functions and benefits from a lower order projection that greatly simplifies the algebra. Furthermore, a projection-based work form is used, which facilitates the design of a time-stepping time-stepping scheme for coupled thermoelastic problems. This approach is motivated by the general question for nonlocality sensitive nonlocality sensitive (NEN) framework for open systems. In contrast to complex projection-based discrete formulations, a new form of an algorithmic time-integration is proposed. The present discretization relies on finite element computations for the displacements and the temperature. The superior performance of the proposed formulation is shown within representative quasi-static and fully transient numerical examples.

**KEYWORDS**

finite element method, nonlinear thermo-elastodynamics, polyconvexity-based framework, time-stepping, time-stepping, time-stepping

**1 | INTRODUCTION**

The present contribution aims for the consistent discretization of nonlinear thermo-elastodynamics. The emphasis of this paper is on both theoretical and numerical aspects. In recent decades, thermomechanical constitutive models have been subjected to extensive modifications, see, for example, Eringen and Suhubi<sup>1</sup> and Eringen and Gendron<sup>2</sup>, as well as authors by Holzapfel and Grottel<sup>3</sup> and Grottel and Holzapfel<sup>4</sup>. Classically, the hyperelasticity framework is used to describe the behavior of the chosen material model, see, for example, Holzapfel<sup>5</sup>. The consistent linearization has led to the linearized constitutive equations.

In contrast to the current approach, the present contribution is based on the concept of 'low' and 'high' order, where the 'low' order is the energy, a convex function of the deformation gradient, the volume, and the temperature and the 'high' order is the momentum balance and the temperature. The present contribution is based on the concept of 'low' and 'high' order, where the 'low' order is the energy, a convex function of the deformation gradient, the volume, and the temperature and the 'high' order is the momentum balance and the temperature. The present contribution is based on the concept of 'low' and 'high' order, where the 'low' order is the energy, a convex function of the deformation gradient, the volume, and the temperature and the 'high' order is the momentum balance and the temperature.

**Citation:** R. Ortigosa, M. Franke, A. Janz, A.J. Gil and P. Betsch. An energy–momentum time integration scheme based on a convex multi-variable framework for non-linear electro-elastodynamics. *Comput. Methods Appl. Mech. Engrg.*, 339:1–35, 2018.

**Declaration:** AJ worked mainly on the theory together with Rogelio Ortigosa (RO) and MF. AJ was responsible for the numerical implementation. Moreover, AJ performed the numerical verification of the newly developed formalism. Furthermore, AJ, RO, and MF co-worked on the manuscript supported by Antonio J. Gil (AJG) and PB. Finally, the article was reviewed by all authors (AJ, RO, MF, AJG, PB).

WILEY

**RESEARCH ARTICLE**

**An energy–momentum time integration scheme based on a convex multi-variable framework for non-linear electro-elastodynamics**

R. Ortigosa<sup>1</sup>, M. Franke<sup>2</sup>, A. Janz<sup>2</sup>, A.J. Gil<sup>1</sup>, P. Betsch<sup>1</sup>

**Correspondence:** R. Ortigosa, Institute of Mechanics, Karlsruhe Institute of Technology, Karlsruhe, Germany. Email: ortigosa@kit.edu

**Summary**

The present contribution provides a new approach to the design of energy momentum consistent integrators schemes to the field of nonlinear electro-elastodynamics. The method is inspired by the structure of polyconvex energy density functions and benefits from a lower order projection that greatly simplifies the algebra. Furthermore, a projection-based work form is used, which facilitates the design of a time-stepping time-stepping scheme for coupled electro-thermoelastic problems. This approach is motivated by the general question for nonlocality sensitive nonlocality sensitive (NEN) framework for open systems. In contrast to complex projection-based discrete formulations, a new form of an algorithmic time-integration is proposed. The present discretization relies on finite element computations for the displacements and the temperature. The superior performance of the proposed formulation is shown within representative quasi-static and fully transient numerical examples.

**KEYWORDS**

finite element method, nonlinear thermo-elastodynamics, polyconvexity-based framework, time-stepping, time-stepping, time-stepping

**1 | INTRODUCTION**

The present contribution aims for the consistent discretization of nonlinear electro-elastodynamics. The emphasis of this paper is on both theoretical and numerical aspects. In recent decades, thermomechanical constitutive models have been subjected to extensive modifications, see, for example, Eringen and Suhubi<sup>1</sup> and Eringen and Gendron<sup>2</sup>, as well as authors by Holzapfel and Grottel<sup>3</sup> and Grottel and Holzapfel<sup>4</sup>. Classically, the hyperelasticity framework is used to describe the behavior of the chosen material model, see, for example, Holzapfel<sup>5</sup>. The consistent linearization has led to the linearized constitutive equations.

In contrast to the current approach, the present contribution is based on the concept of 'low' and 'high' order, where the 'low' order is the energy, a convex function of the deformation gradient, the volume, and the temperature and the 'high' order is the momentum balance and the temperature. The present contribution is based on the concept of 'low' and 'high' order, where the 'low' order is the energy, a convex function of the deformation gradient, the volume, and the temperature and the 'high' order is the momentum balance and the temperature.

# Publications and talks

## Publications

### Peer-reviewed

- M. Franke, R. Ortigosa, A. Janz, A.J. Gil, and P. Betsch. A mixed variational framework for the design of energy-momentum integration schemes based on convex multi-variable electro-elastodynamics. *Computer Methods in Applied Mechanics and Engineering*, submitted for publication, 2019.
- A. Janz, P. Betsch, and M. Franke. Structure-preserving space-time discretization of a mixed formulation for quasi-incompressible large strain elasticity in principal stretches. *International Journal for Numerical Methods in Engineering*, submitted for publication, 2018.
- R. Ortigosa, M. Franke, A. Janz, A. Gil, and P. Betsch. An energy-momentum time integration scheme based on a convex multi-variable framework for nonlinear electro-elastodynamics. *Computer Methods in Applied Mechanics and Engineering*, 339:1–35, 2018.
- P. Betsch, A. Janz, and C. Hesch. A mixed variational framework for the design of energy-momentum schemes inspired by the structure of polyconvex stored energy functions. *Computer Methods in Applied Mechanics and Engineering*, 335: 660–696, 2018.
- M. Franke, A. Janz, M. Schiebl, and P. Betsch. An energy momentum consistent integration scheme using a polyconvexity-based framework for nonlinear thermo-elastodynamics. *International Journal for Numerical Methods in Engineering*, 115:549–577, 2018.

- C. Hesch, A.J. Gil, R. Ortigosa, M. Dittmann, C. Bilgen, P. Betsch, M. Franke, A. Janz, and K. Weinberg. A framework for polyconvex large strain phase-field methods to fracture. *Computer Methods in Applied Mechanics and Engineering*, 317: 649–683, 2017.
- P. Betsch and A. Janz. An energy-momentum consistent method for transient simulations with mixed finite elements developed in the framework of geometrically exact shells. *International Journal for Numerical Methods in Engineering*, 108 (5):423–455, 2016.
- P. Betsch, C. Becker, M. Franke, Y. Yang, and A. Janz. A comparison of DAE integrators in the context of benchmark problems for flexible multibody dynamics. *Journal of Mechanical Science and Technology*, 29(7):2653–2661, 2015.

## Other publications

- A. Janz, P. Betsch, M. Franke, R. Ortigosa and A.J. Gil. A mixed variational framework for non-linear electro-elastodynamics. In R. Owen, R. de Borst, J. Reese, and C. Pearce, editors, *Proceedings of the 6th. European Conference on Computational Mechanics (ECCM 6)*, pages 3849–3860, Glasgow, Scotland, UK, 11 June - 15 June 2018.
- A. Janz, P. Betsch, M. Franke, and R. Ortigosa. Energy-momentum consistent time integration scheme for non-linear electro-elastodynamics. *PAMM*, submitted for publication, 2018.
- M. Franke, A. Janz, M. Schiebl, R. Ortigosa, and P. Betsch. Polyconvexity inspired frameworks and structure-preserving integrators for multi-field problems. *PAMM*, submitted for publication, 2018.
- A. Janz, P. Betsch, and C. Hesch. An algorithmic stress formula for energy conserving time integration in a mixed framework for polyconvex large strain elasticity. *PAMM*, 17(1):313–314, 2017.
- P. Betsch, M. Franke, and A. Janz. Polyconvexity and the design of mixed finite elements. in *Proceedings of the ECCOMAS Thematic Conference on Modern Finite Element Technologies (MFET) 2017*, Physikzentrum Bad Honnef, Germany, 2017.

- A. Janz, P. Betsch, and C. Hesch. Mixed integrators for structure-preserving simulations in nonlinear structural dynamics. In M. Papadrakakis, V. Papadopoulos, G. Stefanou, and V. Plevris, editors, *Proceedings of the VII European Congress on Computational Methods in Applied Sciences and Engineering*, pages 1736–1764, Crete Island, Greece, 5 June - 10 June 2016.
- A. Janz, P. Betsch, and C. Hesch. Structure-preserving space-time discretization of nonlinear structural dynamics based on a mixed variational formulation. *PAMM*, 16(1):205–206, 2016.
- P. Betsch and A. Janz. Energy-momentum conserving discretization of mixed shell elements for large deformation problems. *PAMM*, 15(1):205–206, 2015.

## Conference talks

- A. Janz and P. Betsch. Structure-preserving integrators for discrete mechanical systems subject to general holonomic constraints. *90th Annual Meeting of the International Association of Applied Mathematics and Mechanics (GAMM)*, Vienna, Austria, 18 February - 22 February 2019.
- A. Janz, P. Betsch, M. Franke, R. Ortigosa, and A.J. Gil. A mixed variational framework for structure-preserving space-time discretization for non-linear electro-elastodynamics. *13th World Congress in Computational Mechanics*, New York City, NY, USA, July 2018.
- A. Janz, P. Betsch, M. Franke, R. Ortigosa, and A.J. Gil. A mixed variational framework for non-linear electro-elastodynamics. *6th European Conferences on Computational Mechanics (ECCM 6) and 7th European Conference on Computational Fluid Dynamics (ECFD 7)*, Glasgow, UK, 11 June - 15 June 2018.
- A. Janz, P. Betsch, M. Franke, R. Ortigosa, and A.J. Gil. Energy-momentum consistent time integration scheme for non-linear electro-elastodynamics. *89th Annual Meeting of the International Association of Applied Mathematics and Mechanics (GAMM)*, Munich, Germany, 19 March - 23 March 2018.
- A. Janz and P. Betsch. Structure-preserving space-time discretization for continuum dynamics in a mixed framework for polyconvex large strain elasticity. *3rd*

*International Conference on Computational Models for Solids and Fluids - ECCOMAS MSF 2017, Ljubljana, Slovenia, 20 September - 22 September 2017.*

- M. Franke, P. Betsch and A. Janz. Polyconvexity and the design of mixed finite elements. *ECCOMAS Thematic Conference on Modern Finite Element Technologies (MFET) 2017, Physikzentrum Bad Honnef, Germany, 21 August - 23 August 2017.*
- A. Janz and P. Betsch. Energy-momentum consistent time integration schemes based on a polyconvex framework for non-linear (thermal) -elastodynamics. *Zienkiewicz Centre for Computational Engineering Seminar Series, Swansea, Wales, July 2017.*
- A. Janz, P. Betsch and C. Hesch. An algorithmic stress formula for energy conserving time integration in a mixed framework for polyconvex large strain elasticity. *88th Annual Meeting of the International Association of Applied Mathematics and Mechanics (GAMM), Weimar, Germany, 06 March - 10 March 2017.*
- A. Janz, P. Betsch and C. Hesch. Mixed integrators for structure-preserving simulations in nonlinear structural dynamics. *VII European Congress on Computational Methods in Applied Sciences and Engineering, Crete Island, Greece, 5 June - 10 June, 2016.*
- A. Janz, P. Betsch and C. Hesch. Structure-preserving space-time discretization of nonlinear structural dynamics based on a mixed variational formulation. *87th Annual Meeting of the International Association of Applied Mathematics and Mechanics (GAMM), Braunschweig, Germany, 07 March - 11 March, 2016.*
- A. Janz and P. Betsch. Structure-preserving integration with mixed finite elements. *86th Annual Meeting of the International Association of Applied Mathematics and Mechanics (GAMM), Lecce, Italy, 23 March - 27 March, 2015.*

# Bibliography

- [1] F. Armero. On the locking and stability of finite elements in finite deformation plane strain problems. *Computers and Structures*, 75(3):261 – 290, 2000.
- [2] F. Armero. Assumed strain finite element methods for conserving temporal integrations in non-linear solid dynamics. *International Journal for Numerical Methods in Engineering*, 74(12):1795–1847, 2008.
- [3] F. Armero and E. Petöcz. Formulation and analysis of conserving algorithms for frictionless dynamic contact/impact problems. *Computer Methods in Applied Mechanics and Engineering*, 158:269–300, 1998.
- [4] F. Armero and I. Romero. On the formulation of high-frequency dissipative time-stepping algorithms for nonlinear dynamics. Part II: Second-order methods. *Computer Methods in Applied Mechanics and Engineering*, 190:6783–6824, 2001.
- [5] F. Armero and I. Romero. Energy-dissipative momentum-conserving time-stepping algorithms for the dynamics of nonlinear Cosserat rods. *Computational Mechanics*, 31:3–26, 2003.
- [6] F. Armero and C. Zambrana-Rojas. Volume-preserving energy-momentum schemes for isochoric multiplicative plasticity. *Computer Methods in Applied Mechanics and Engineering*, 196(41-44):4130–4159, 2007.
- [7] J. M. Ball. Convexity conditions and existence theorems in nonlinear elasticity. *Archive for Rational Mechanics and Analysis*, 63(4):337–403, 1976.
- [8] J. M. Ball. *Geometry, Mechanics and Dynamics*, chapter Some open problems in Elasticity, pages 3–59. Springer, 2002.
- [9] M. Bartelt, J. Dietzsch, and M. Groß. Efficient implementation of energy conservation for higher order finite elements with variational integrators. *Mathematics and Computers in Simulation*, 150:83 – 121, 2018.

- [10] K.-J. Bathe. Conserving energy and momentum in nonlinear dynamics: A simple implicit time integration scheme. *Computers and Structures*, 85(7-8):437–445, 2007.
- [11] O.A. Bauchau and C.L. Bottasso. On the design of energy preserving and decaying schemes for flexible, nonlinear multi-body systems. *Computer Methods in Applied Mechanics and Engineering*, 169(1-2):61–79, 1999.
- [12] T. Belytschko, W.K. Liu, and B. Moran. *Nonlinear Finite Elements for Continua and Structures*. John Wiley & Sons, 2000.
- [13] P. Betsch, editor. *Structure-preserving Integrators in Nonlinear Structural Dynamics and Flexible Multibody Dynamics*, volume 565 of *CISM Courses and Lectures*. Springer-Verlag, 2016.
- [14] P. Betsch and C. Becker. Conservation of generalized momentum maps in mechanical optimal control problems with symmetry. *International Journal for Numerical Methods in Engineering*, 111(2):144–175, 2017.
- [15] P. Betsch and A. Janz. An energy-momentum consistent method for transient simulations with mixed finite elements developed in the framework of geometrically exact shells. *International Journal for Numerical Methods in Engineering*, 108(5):423–455, 2016.
- [16] P. Betsch and N. Sanger. A nonlinear finite element framework for flexible multi-body dynamics: Rotationless formulation and energy-momentum conserving discretization. In Carlo L. Bottasso, editor, *Multibody Dynamics: Computational Methods and Applications*, volume 12 of *Computational Methods in Applied Sciences*, pages 119–141. Springer-Verlag, 2009.
- [17] P. Betsch and M. Schiebl. Generic-based formulation and discretization of initial boundary value problems for finite strain thermoelasticity. *Computer Methods in Applied Mechanics and Engineering*, submitted for publication, 2018.
- [18] P. Betsch and P. Steinmann. Conservation properties of a time FE method. Part III: Mechanical systems with holonomic constraints. *International Journal for Numerical Methods in Engineering*, 53:2271–2304, 2002.
- [19] P. Betsch and P. Steinmann. A DAE approach to flexible multibody dynamics. *Multibody System Dynamics*, 8:367–391, 2002.

- 
- [20] P. Betsch, C. Hesch, N. Sanger, and S. Uhlar. Variational integrators and energy-momentum schemes for flexible multibody dynamics. *Journal of Computational and Nonlinear Dynamics*, 5(3):031001/1–11, 2010.
- [21] P. Betsch, R. Siebert, and N. Sanger. Natural coordinates in the optimal control of multibody systems. *Journal of Computational and Nonlinear Dynamics*, 7(1): 011009/1–8, 2012.
- [22] P. Betsch, C. Becker, M. Franke, Y. Yang, and A. Janz. A comparison of dae integrators in the context of benchmark problems for flexible multibody dynamics. *Journal of Mechanical Science and Technology*, 29(7):2653–2661, 2015.
- [23] P. Betsch, A. Janz, and C. Hesch. A mixed variational framework for the design of energy-momentum schemes inspired by the structure of polyconvex stored energy functions. *Computer Methods in Applied Mechanics and Engineering*, 335: 660–696, 2018.
- [24] D. Boffi, F. Brezzi, and M. Fortin. *Mixed finite element methods and applications*. Springer-Verlag, 2013.
- [25] J. Bonet, A.J. Gil, C.H. Lee, M. Aguirre, and R. Ortigosa. A first order hyperbolic framework for large strain computational solid dynamics. part i: Total lagrangian isothermal elasticity. *Computer Methods in Applied Mechanics and Engineering*, 283:689 – 732, 2015.
- [26] J. Bonet, A.J. Gil, and R. Ortigosa. A computational framework for polyconvex large strain elasticity. *Computer Methods in Applied Mechanics and Engineering*, 283:1061–1094, 2015.
- [27] J. Bonet, A.J. Gil, and R. Ortigosa. On a tensor cross product based formulation of large strain solid mechanics. *International Journal of Solids and Structures*, 84: 49–63, 2016.
- [28] C.L. Bottasso and A. Croce. Optimal control of multibody systems using an energy preserving direct transcription method. *Multibody System Dynamics*, 12 (1):17–45, 2004.
- [29] C.L. Bottasso, M. Borri, and L. Trainelli. Integration of elastic multibody systems by invariant conserving/dissipating algorithms. II. Numerical schemes and applications. *Computer Methods in Applied Mechanics and Engineering*, 190: 3701–3733, 2001.

- [30] B. Brank, J. Korelc, and A. Ibrahimbegović. Dynamics and time-stepping schemes for elastic shells undergoing finite rotations. *Computers and Structures*, 81(12):1193–1210, 2003.
- [31] R. Bustamante. Transversely isotropic non-linear electro-active elastomers. *Acta Mechanica*, 206(3-4):237–259, 2009. ISSN 0001-5970.
- [32] R. Bustamante and J. Merodio. Constitutive structure in coupled non-linear electro-elasticity: Invariant descriptions and constitutive restrictions. *International Journal of Non-Linear Mechanics*, 46(10):1315 – 1323, 2011.
- [33] S. Chiba, M. Waki, T. Wada, Y. Hirakawa, K. Masuda, and T. Ikoma. Consistent ocean wave energy harvesting using electroactive polymer (dielectric elastomer) artificial muscle generators. *Applied Energy*, 104(0):497–502, 2013.
- [34] J. Chung and G.M. Hulbert. A time integration algorithm for structural dynamics with improved numerical dissipation: The generalized- $\alpha$  method. *Journal of Applied Mechanics*, 60:371–375, 1993.
- [35] P.G. Ciarlet. *Mathematical Elasticity*, volume I: Three-dimensional elasticity. North-Holland, 1988.
- [36] S. Conde-Martín. *Energy-entropy-momentum time integration methods for coupled smooth dissipative problems*. PhD thesis, Caminos, 2016.
- [37] M.A. Crisfield and G. Jelenić. Energy/momentum conserving time integration procedures with finite elements and large rotations. In J. Ambrósio and M. Kleiber, editors, *NATO-ARW on Comp. Aspects of Nonlin. Struct. Sys. with Large Rigid Body Motion*, pages 181–200, Pultusk, Poland, July 2-7, 2000.
- [38] R. de Boer. *Vektor- und Tensorrechnung für Ingenieure*. Springer-Verlag, Berlin, 1982.
- [39] R. de Boer. *Theory of porous media*. Springer-Verlag, 2000.
- [40] S. Demoulini, D.M.A. Stuart, and A.E. Tzavaras. A variational approximation scheme for three-dimensional elastodynamics. *Archive for Rational Mechanics and Analysis*, 157(4):325–344, 2001.
- [41] M. Dittmann, M. Franke, I. Temizer, and C. Hesch. Isogeometric Analysis and thermomechanical Mortar contact problems. *Computer Methods in Applied Mechanics and Engineering*, 274:192–212, 2014.

- 
- [42] A. Dorfmann and R. W. Ogden. Nonlinear electroelasticity. *Acta Mechanica*, 174 (3-4):167–183, 2005.
- [43] P.J. Flory. Thermodynamic relations for high elastic materials. *Trans Faraday Society*, 57:829–838, 1961.
- [44] M. Franke, A. Janz, M. Schiebl, and P. Betsch. An energy momentum consistent integration scheme using a polyconvexity-based framework for nonlinear thermo-elastodynamics. *International Journal for Numerical Methods in Engineering*, 115:549–577, 2018.
- [45] M. Franke, R. Ortigosa, A. Janz, A.J. Gil, and P. Betsch. A mixed variational framework for the design of energy-momentum integration schemes based on convex multi-variable electro-elastodynamics. *Computer Methods in Applied Mechanics and Engineering*, submitted for publication, 2019.
- [46] J. C. García Orden. Energy and symmetry-preserving formulation of nonlinear constraints and potential forces in multibody dynamics. *Nonlinear Dynamics*, 95 (1):823–837, 2019.
- [47] A. J. Gil and R. Ortigosa. A new framework for large strain electromechanics based on convex multi-variable strain energies: variational formulation and material characterisation. *Computer Methods in Applied Mechanics and Engineering*, 302:293–328, 2016.
- [48] S. Glaser and F. Armero. On the formulation of enhanced strain finite elements in finite deformations. *Engineering Computations*, 14(7):759–791, 1997.
- [49] J.M. Goicolea and J. C. García Orden. Dynamic analysis of rigid and deformable multibody systems with penalty methods and energy-momentum schemes. *Computer Methods in Applied Mechanics and Engineering*, 188:789–804, 2000.
- [50] O. Gonzalez. *Design and analysis of conserving integrators for nonlinear Hamiltonian systems with symmetry*. PhD thesis, Stanford University, 1996.
- [51] O. Gonzalez. Time integration and discrete Hamiltonian systems. *Journal of Nonlinear Science*, 6:449–467, 1996.
- [52] O. Gonzalez. Exact energy and momentum conserving algorithms for general models in nonlinear elasticity. *Computer Methods in Applied Mechanics and Engineering*, 190(13-14):1763–1783, 2000.

- [53] O. Gonzalez and A.M. Stuart. *A First Course in Continuum Mechanics*. Cambridge University Press, 2008.
- [54] B. Göttlicher and K. Schweizerhof. Analysis of flexible structures with occasionally rigid parts under transient loading. *Computers and Structures*, 83(25-26): 2035–2051, 2005.
- [55] D. Greenspan. Conservative numerical methods for  $\ddot{x} = f(x)$ . *Journal of Computational Physics*, 56:28–41, 1984.
- [56] M. Grmela and H.C. Öttinger. Dynamics and thermodynamics of complex fluids. I. development of a general formalism. *Physical Review E*, 56(6):6620, 1997.
- [57] M. Groß and P. Betsch. Energy-momentum consistent finite element discretization of dynamic finite viscoelasticity. *International Journal for Numerical Methods in Engineering*, 81:1341–1386, 2010.
- [58] M. Groß and P. Betsch. Galerkin-based energy-momentum consistent time-stepping algorithms for classical nonlinear thermo-elastodynamics. *Mathematics and Computers in Simulation*, 82(4):718–770, 2011.
- [59] M. Groß and J. Dietzsch. Variational-based energy-momentum schemes of higher-order for elastic fiber-reinforced continua. *Computer Methods in Applied Mechanics and Engineering*, 320:509–542, 2017.
- [60] M. Groß, P. Betsch, and P. Steinmann. Conservation properties of a time FE method. Part IV: Higher order energy and momentum conserving schemes. *International Journal for Numerical Methods in Engineering*, 63:1849–1897, 2005.
- [61] J. Haider, C.H. Lee, A.J. Gil, and J. Bonet. A first-order hyperbolic framework for large strain computational solid dynamics: An upwind cell centred total lagrangian scheme. *International Journal for Numerical Methods in Engineering*, 109(3):407–456, 2017.
- [62] S. Hartmann and P. Neff. Polyconvexity of generalized polynomial-type hyperelastic strain energy functions for near-incompressibility. *International Journal of Solids and Structures*, 40:2767–2791, 2003.
- [63] C. Hesch and P. Betsch. A mortar method for energy-momentum conserving schemes in frictionless dynamic contact problems. *International Journal for Numerical Methods in Engineering*, 77(10):1468–1500, 2009.

- 
- [64] C. Hesch and P. Betsch. Transient three-dimensional domain decomposition problems: Frame-indifferent mortar constraints and conserving integration. *International Journal for Numerical Methods in Engineering*, 82(3):329–358, 2010.
- [65] C. Hesch and P. Betsch. Energy-momentum consistent algorithms for dynamic thermomechanical problems – application to mortar domain decomposition problems. *International Journal for Numerical Methods in Engineering*, 86(11):1277–1302, 2011.
- [66] C. Hesch, A.J. Gil, R. Ortigosa, M. Dittmann, C. Bilgen, P. Betsch, M. Franke, A. Janz, and K. Weinberg. A framework for polyconvex large strain phase-field methods to fracture. *Computer Methods in Applied Mechanics and Engineering*, 317: 649–683, 2017.
- [67] H.M. Hilber, T.J.R. Hughes, and R.L. Taylor. Improved numerical dissipation for time integration algorithms in structural dynamics. *Earthquake Engineering and Structural Dynamics*, 5:283–292, 1977.
- [68] G.A. Holzapfel. *Nonlinear Solid Mechanics*. John Wiley & Sons, 2001.
- [69] G.A. Holzapfel and J.C. Simo. Entropy elasticity of isotropic rubber-like solids at finite strains. *Computer Methods in Applied Mechanics and Engineering*, 132: 17–44, 1996.
- [70] J.C. Houbolt. A recurrence matrix solution for the dynamic response of elastic aircraft. *Journal of Aeronautical Science*, 17:540–550, 1950.
- [71] T.J.R. Hughes. *The Finite Element Method*. Dover Publications, 2000.
- [72] T.J.R. Hughes, T.K. Caughey, and W.K. Liu. Finite-element methods for nonlinear elastodynamics which conserve energy. *Journal of Applied Mechanics*, 45: 366–370, 1978.
- [73] M. Hütter and B. Svendsen. On the formulation of continuum thermodynamic models for solids as general equations for non-equilibrium reversible-irreversible coupling. *Journal of Elasticity*, 104(1):357–368, 2011.
- [74] A. Ibrahimbegović, S. Mamouri, R.L. Taylor, and A.J. Chen. Finite element method in dynamics of flexible multibody systems: Modeling of holonomic constraints and energy conserving integration schemes. *Multibody System Dynamics*, 4(2-3):195–223, 2000.

- [75] M. Itskov and V. N. Khiêm. A polyconvex anisotropic free energy function for electro- and magneto-rheological elastomers. *Mathematics and Mechanics of Solids*, pages 1–12, 2014.
- [76] M. Jabareen. On the modeling of electromechanical coupling in electroactive polymers using the mixed finite element formulation. *Procedia {IUTAM}*, 12: 105–115, 2015. ISSN 2210-9838.
- [77] A. Janz and P. Betsch. Energy-momentum conserving discretization of mixed shell elements for large deformation problems. *PAMM*, 15(1):205–206, 2015.
- [78] A. Janz, P. Betsch, and C. Hesch. Structure-preserving space-time discretization of nonlinear structural dynamics based on a mixed variational formulation. *PAMM*, 16(1):205–206, 2016.
- [79] A. Janz, P. Betsch, and C. Hesch. Mixed integrators for structure-preserving simulations in nonlinear structural dynamics. In M. Papadrakakis, V. Papadopoulos, G. Stefanou, and V. Plevris, editors, *Proceedings of the VII European Congress on Computational Methods in Applied Sciences and Engineering*, pages 1736–1764, Crete Island, Greece, 5 June - 10 June 2016.
- [80] A. Janz, P. Betsch, and C. Hesch. An algorithmic stress formula for energy conserving time integration in a mixed framework for polyconvex large strain elasticity. *PAMM*, 17(1):313–314, 2017.
- [81] A. Janz, P. Betsch, and M. Franke. Structure-preserving space-time discretization of a mixed formulation for quasi-incompressible large strain elasticity in principal stretches. *International Journal for Numerical Methods in Engineering*, submitted for publication, 2018.
- [82] A. Janz, P. Betsch, M. Franke, and R. Ortigosa. Energy-momentum consistent time integration scheme for non-linear electro-elastodynamics. *PAMM*, submitted for publication, 2018.
- [83] A. Janz, P. Betsch, M. Franke, R. Ortigosa, and A.J. Gil. A mixed variational framework for non-linear electro-elastodynamics. In R. Owen, R. de Borst, J. Reese, and C. Pearce, editors, *Proceedings of the 6th European Conferences on Computational Mechanics (ECCM 6) and 7th European Conference on Computational Fluid Dynamics (ECFD 7)*, pages 3849–3860, Glasgow, Scotland, UK, 11 June - 15 June 2018.

- 
- [84] E.P. Kasper and R.L. Taylor. A mixed-enhanced strain method Part II: Geometrically nonlinear problems. *Computers and Structures*, 75:251–260, 2000.
- [85] M.W. Koch and S. Leyendecker. Energy momentum consistent force formulation for the optimal control of multibody systems. *Multibody System Dynamics*, 29: 381–401, 2013.
- [86] M.W. Koch, M. Ringkamp, and S. Leyendecker. Discrete Mechanics and Optimal Control (DMOCC) of Walking Gaits. *Journal of Computational and Nonlinear Dynamics*, 12, 2016.
- [87] G. Kofod, P. Sommer-Larsen, R. Kornbluh, and R. Pelrine. Actuation response of polyacrylate dielectric elastomers. *Journal of Intelligent Material Systems and Structures*, 14(12):787–793, 2003.
- [88] S. Krenk. The role of geometric stiffness in momentum and energy conserving time integration. *International Journal for Numerical Methods in Engineering*, 71(6): 631–651, 2007.
- [89] M. Krüger. *Energie-Entropie-konsistente Zeitintegratoren für die nichtlineare Thermo-viskoelastodynamik*. PhD thesis, University of Siegen, 2013.
- [90] M. Krüger, M. Groß, and P. Betsch. An energy-entropy-consistent time stepping scheme for nonlinear thermo-viscoelastic continua. *ZAMM*, 96(2):141–178, 2016.
- [91] D. Kuhl and M.A. Crisfield. Energy-conserving and decaying algorithms in non-linear structural mechanics. *International Journal for Numerical Methods in Engineering*, 45:569–599, 1999.
- [92] D. Kuhl and E. Ramm. Generalized energy-momentum method for non-linear adaptive shell dynamics. *Computer Methods in Applied Mechanics and Engineering*, 178:343–366, 1999.
- [93] D. Kuhl and E. Ramm. Time integration in the context of energy control and locking free finite elements. *Archives of Computational Methods in Engineering. State of the Art Reviews*, 7(3):299–332, 2000.
- [94] T.A. Laursen and V. Chawla. Design of energy conserving algorithms for frictionless dynamic contact problems. *International Journal for Numerical Methods in Engineering*, 40:863–886, 1997.

- [95] C.H. Lee, A.J. Gil, O.I. Hassan, J. Bonet, and S. Kulasegaram. A variationally consistent streamline upwind Petrov-Galerkin smooth particle hydrodynamics algorithm for large strain solid dynamics. *Computer Methods in Applied Mechanics and Engineering*, 318:514 – 536, 2017.
- [96] E. Lens and A. Cardona. An energy preserving/decaying scheme for nonlinearly constrained multibody systems. *Multibody System Dynamics*, 18(3):435–470, 2007.
- [97] E.V. Lens, A. Cardona, and M. Géradin. Energy preserving time integration for constrained multibody systems. *Multibody System Dynamics*, 11(1):41–61, 2004.
- [98] A. Lew, Marsden J.E., M. Ortiz, and M. West. Variational time integrators. *International Journal for Numerical Methods in Engineering*, 60:153–212, 2004.
- [99] A. Lew, Marsden J.E., M. Ortiz, and M. West. An overview of variational integrators. In *Finite Element Methods: 1970's and Beyond*, pages 98–115. CIMNE Barcelona, Spain, 2004.
- [100] S. Leyendecker, P. Betsch, and P. Steinmann. Objective energy-momentum conserving integration for the constrained dynamics of geometrically exact beams. *Computer Methods in Applied Mechanics and Engineering*, 195:2313–2333, 2006.
- [101] S. Leyendecker, P. Betsch, and P. Steinmann. The discrete null space method for the energy consistent integration of constrained mechanical systems. Part III: Flexible multibody dynamics. *Multibody System Dynamics*, 19(1-2):45–72, 2008.
- [102] S. Leyendecker, J.E. Marsden, and M. Ortiz. Variational integrators for constrained dynamical systems. *Z. Angew. Math. Mech. (ZAMM)*, 88(9):677–708, 2008.
- [103] S. Leyendecker, S. Ober-Blöbaum, J.E. Marsden, and M. Ortiz. Discrete mechanics and optimal control for constrained systems. *Optim. Control Appl. Meth.*, 31(6):505–528, 2010.
- [104] T. Li, C. Keplinger, R. Baumgartner, S. Bauer, W. Yang, and Z. Suo. Giant voltage-induced deformation in dielectric elastomers near the verge of snap-through instability. *Journal of the Mechanics and Physics of Solids*, 61(2):611–628, 2013.
- [105] A. Lion. A physically based method to represent the thermo-mechanical behaviour of elastomers. *Acta Mechanica*, 123(1):1–25, 1997.

- 
- [106] R.H. MacNeal and R.L. Harder. A proposed standard set of problems to test finite element accuracy. *Finite Elements in Analysis and Design*, 1:3–20, 1985.
- [107] J. E. Marsden and T. J. R. Hughes. *Mathematical foundations of elasticity*. Dover Civil and Mechanical Engineering, 1994.
- [108] J.E. Marsden and T.S. Ratiu. *Introduction to Mechanics and Symmetry*. Springer-Verlag, 1994.
- [109] J.E. Marsden and M. West. Discrete mechanics and variational integrators. *Acta Numerica*, 10:357–514, 2001.
- [110] R. M. McMeeking and C. M. Landis. Electrostatic forces and stored energy for deformable dielectric materials. *Journal of Applied Mechanics*, 72(4):581–590, 2008.
- [111] C. Miehe. Computation of isotropic tensor functions. *Communications in Numerical Methods and Engineering*, 9:889–896, 1993.
- [112] C. Miehe. On the representation of Prandtl-Reuss tensors within the framework of multiplicative elastoplasticity. *International Journal of Plasticity*, 6:609–621, 1994.
- [113] C. Miehe. Entropic thermoelasticity at finite strains. Aspects of the formulation and numerical implementation. *Computer Methods in Applied Mechanics and Engineering*, 120:243–269, 1995.
- [114] C. Miehe. Comparison of two algorithms for the computation of fourth-order isotropic tensor functions. *Computers and Structures*, 66:37–43, 1998.
- [115] C. Miehe and J. Schröder. Energy and momentum conserving elastodynamics of a non-linear brick-type mixed finite shell element. *International Journal for Numerical Methods in Engineering*, 50:1801–1823, 2001.
- [116] C. Miehe, D. Vallicotti, and D. Zäh. Computational structural and material stability analysis in finite electro-elasto-statics of electro-active materials. *International Journal for Numerical Methods in Engineering*, 102(10):1605–1637, 2015.
- [117] A. Mielke. Formulation of thermoelastic dissipative material behavior using generic. *Continuum Mechanics and Thermodynamics*, 23(3):233–256, 2011.

- [118] R. Mohr, A. Menzel, and P. Steinmann. Galerkin-based mechanical integrators for finite elastodynamics formulated in principal stretches – Pitfalls and remedies. *Computer Methods in Applied Mechanics and Engineering*, 197:4444–4466, 2008.
- [119] R. Mohr, A. Menzel, and P. Steinmann. A consistent time FE-method for large strain elasto-plasto-dynamics. *Computer Methods in Applied Mechanics and Engineering*, 197:3024–3044, 2008.
- [120] M. Mooney. A theory of large elastic deformation. *Journal of Applied Physics*, 11: 582 – 592, 1940.
- [121] K.N. Morman. The generalized strain measure with application to nonhomogeneous deformations in rubber-like solids. *Journal of Applied Mechanics*, 53: 726–728, 1986.
- [122] T. Netz and S. Hartmann. A monolithic finite element approach using high-order schemes in time and space applied to finite strain thermo-viscoelasticity. *Computers & Mathematics with Applications*, 70(7):1457–1480, 2015.
- [123] N.M. Newmark. A method of computation for structural dynamics. *Journal of the Engineering Mechanics Division ASCE*, 85:67–94, 1959.
- [124] S. Ober-Blöbaum, O. Junge, and J.E. Marsden. Discrete mechanics and optimal control: An analysis. *ESAIM: Control, Optimisation and Calculus of Variations*, 17 (2):322–352, 2011.
- [125] R.W. Ogden. Large deformation isotropic elasticity: on the correlation of theory and experiment for compressible rubberlike solids. *The Royal Society*, 328(1575): 567–583, 1972.
- [126] R.W. Ogden. *Non-Linear Elastic Deformations*. Ellis Horwood, Chichester, 1984.
- [127] A. O’Halloran, F. O’Malley, and P. McHugh. A review on dielectric elastomer actuators, technology, applications, and challenges. *Journal of Applied Physics*, 104(7), 2008.
- [128] R. Ortigosa and A. J. Gil. A new framework for large strain electromechanics based on convex multi-variable strain energies: Conservation laws, hyperbolicity and extension to electro-magneto-mechanics. *Computer Methods in Applied Mechanics and Engineering*, 309:202–242, 2016.

- 
- [129] R. Ortigosa and A. J. Gil. A new framework for large strain electromechanics based on convex multi-variable strain energies: Finite element discretisation and computational implementation. *Computer Methods in Applied Mechanics and Engineering*, 302:329–360, 2016.
- [130] R. Ortigosa and A. J. Gil. A computational framework for incompressible electromechanics based on convex multi-variable strain energies for geometrically exact shell theory. *Computer Methods in Applied Mechanics and Engineering*, 317: 792–816, 2017.
- [131] R. Ortigosa, A. J. Gil, and C. H. Lee. A computational framework for large strain nearly and truly incompressible electromechanics based on convex multi-variable strain energies. *Computer Methods in Applied Mechanics and Engineering*, 310:297–334, 2016.
- [132] R. Ortigosa, A.J. Gil, J. Bonet, and C. Hesch. A computational framework for polyconvex large strain elasticity for geometrically exact beam theory. *Computational Mechanics*, 57:277 – 303, 2016.
- [133] R. Ortigosa, M. Franke, A. Janz, A. Gil, and P. Betsch. An energy-momentum time integration scheme based on a convex multi-variable framework for nonlinear electro-elastodynamics. *Computer Methods in Applied Mechanics and Engineering*, 339:1–35, 2018.
- [134] H.C. Öttinger. *Beyond equilibrium thermodynamics*. John Wiley & Sons, 2005.
- [135] H.C. Öttinger and M. Grmela. Dynamics and thermodynamics of complex fluids. II. illustrations of a general formalism. *Physical Review E*, 56(6):6633, 1997.
- [136] K.C. Park. An improved stiffly stable method for direct integration of nonlinear structural dynamic equations. *Journal of Applied Mechanics*, 42:464–470, 1975.
- [137] R. Pelrine, R. Kornbluh, and J. Joseph. Electrostriction of polymer dielectrics with compliant electrodes as a means of actuation. *Sensors and Actuators A: Physical*, 64(1):77–85, 1998.
- [138] R. Pelrine, R. Kornbluh, Q. Pei, and J. Joseph. High-speed electrically actuated elastomers with strain greater than 100%. *Science*, 287(5454):836–839, 2000.
- [139] R. Pelrine, R. Kornbluh, Q. Pei, S. Stanford, S. Oh, J. Eckerle, M. Rosenthal, and K. Meijer. Dielectric elastomer artificial muscle actuators: toward biomimetic

- motion. In *Proc. SPIE 4695, Smart Structures and Materials 2002: Electroactive Polymer Actuators and Devices (EAPAD)*, volume 4695, pages 126–137, 2002.
- [140] R. Poya, A. J. Gil, R. Ortigosa, R. Sevilla, J. Bonet, and W. A. Wall. A curvilinear high order finite element framework for electromechanics: From linearised electro-elasticity to massively deformable dielectric elastomers. *Computer Methods in Applied Mechanics and Engineering*, 329:75–117, 2018.
- [141] A. Raoult. Non-polyconvexity of the stored energy function of a Saint Venant-Kirchhoff material. *Aplikace matematiky*, 31(6):417–419, 1986.
- [142] S. Reese and S. Govindjee. Theoretical and Numerical Aspects in the Thermo-Viscoelastic Material Behaviour of Rubber-Like Polymers. *Mechanics of Time-Dependent Materials*, 1:357–396, 1998.
- [143] I. Romero. Thermodynamically consistent time-stepping algorithms for nonlinear thermomechanical systems. *International journal for numerical methods in engineering*, 79(6):706–732, 2009.
- [144] I. Romero. Algorithms for coupled problems that preserve symmetries and the laws of thermodynamics: Part I: Monolithic integrators and their application to finite strain thermoelasticity. *Computer Methods in Applied Mechanics and Engineering*, 199:1841–1858, 2010.
- [145] I. Romero. An analysis of the stress formula for energy-momentum methods in nonlinear elastodynamics. *Computational Mechanics*, 50(5):603–610, 2012.
- [146] I. Romero and F. Armero. Numerical integration of the stiff dynamics of geometrically exact shells: an energy-dissipative momentum-conserving scheme. *International Journal for Numerical Methods in Engineering*, 54:1043–1086, 2002.
- [147] I. Romero and F. Armero. An objective finite element approximation of the kinematics of geometrically exact rods and its use in the formulation of an energy-momentum conserving scheme in dynamics. *International Journal for Numerical Methods in Engineering*, 54:1683–1716, 2002.
- [148] T. Schlögl and S. Leyendecker. Electrostatic–viscoelastic finite element model of dielectric actuators. *Computer Methods in Applied Mechanics and Engineering*, 299: 421 – 439, 2016.

- 
- [149] J. Schröder, P. Wriggers, and D. Balzani. A new mixed finite element based on different approximations of the minors of deformation tensors. *Computer Methods in Applied Mechanics and Engineering*, 200(49-52):3583–3600, 2011.
- [150] M. H. Siboni and P. P. Castañeda. Fiber-constrained, dielectric-elastomer composites: Finite-strain response and stability analysis. *Journal of the Mechanics and Physics of Solids*, 68(0):211–238, 2014.
- [151] M. H. Siboni, R. Avazmohammadi, and P. P. Castañeda. Electromechanical instabilities in fiber-constrained, dielectric-elastomer composites subjected to all-around dead-loading. *Mathematics and Mechanics of Solids*, 2014.
- [152] J.C. Simo and F. Armero. Geometrically non-linear enhanced strain mixed methods and the method of incompatible modes. *International Journal for Numerical Methods in Engineering*, 33:1413–1449, 1992.
- [153] J.C. Simo and N. Tarnow. The discrete energy-momentum method. Conserving algorithms for nonlinear elastodynamics. *Zeitschrift für angewandte Mathematik und Physik (ZAMP)*, 43:757–792, 1992.
- [154] J.C. Simo and N. Tarnow. A new energy and momentum conserving algorithm for the nonlinear dynamics of shells. *International Journal for Numerical Methods in Engineering*, 37:2527–2549, 1994.
- [155] J.C. Simo and R.L. Taylor. Quasi-incompressible finite elasticity in principal stretches. Continuum basis and numerical algorithms. *Computer Methods in Applied Mechanics and Engineering*, 85:273–310, 1991.
- [156] J.C. Simo and K.K. Wong. Unconditionally stable algorithms for rigid body dynamics that exactly preserve energy and momentum. *International Journal for Numerical Methods in Engineering*, 31:19–52, 1991.
- [157] J.C. Simo, R.L. Taylor, and K.S. Pister. Variational and projection methods for the volume constraint in finite deformation elasto-plasticity. *Computer Methods in Applied Mechanics and Engineering*, 51:177–208, 1985.
- [158] J.C. Simo, M.S. Rifai, and D.D. Fox. On a stress resultant geometrically exact shell model. Part VI: Conserving algorithms for non-linear dynamics. *International Journal for Numerical Methods in Engineering*, 34:117–164, 1992.

- [159] J.C. Simo, N. Tarnow, and K.K. Wong. Exact energy-momentum conserving algorithms and symplectic schemes for nonlinear dynamics. *Computer Methods in Applied Mechanics and Engineering*, 100:63–116, 1992.
- [160] J.C. Simo, F. Armero, and R.L. Taylor. Improved versions of assumed enhanced strain tri-linear elements for 3D finite deformation problems. *Computer Methods in Applied Mechanics and Engineering*, 110:359–386, 1993.
- [161] S. Skatulla, C. Sansour, and A. Arockiarajan. A multiplicative approach for non-linear electro-elasticity. *Computer Methods in Applied Mechanics and Engineering*, 245-246(0), 2012.
- [162] G. Strang. *Lineare Algebra*. Springer-Verlag, 1998.
- [163] Z. Suo, X. Zhao, and W. H. Greene. A nonlinear field theory of deformable dielectrics. *Journal of the Mechanics and Physics of Solids*, 56(2):467–486, 2008.
- [164] T.C.T. Ting. Determination of  $\mathbf{C}^{1/2}$ ,  $\mathbf{C}^{-1/2}$  and more general isotropic functions of  $\mathbf{C}$ . *Journal of Elasticity*, 15:319–323, 1985.
- [165] F. Vogel, R. Bustamante, and P. Steinmann. On some mixed variational principles in electro-elastostatics. *International Journal of Non-Linear Mechanics*, 47(2): 341–354, 2012.
- [166] D. K. Vu and P. Steinmann. A 2-D coupled BEM-FEM simulation of electro-elastostatics at large strain. *Computer Methods in Applied Mechanics and Engineering*, 199(17-20):1124–1133, 2010.
- [167] D. K. Vu and P. Steinmann. On 3-D coupled BEM-FEM simulation of nonlinear electro-elastostatics. *Computer Methods in Applied Mechanics and Engineering*, 201-204(0):82–90, 2012.
- [168] D. K. Vu, P. Steinmann, and G. Possart. Numerical modelling of non-linear electroelasticity. *International Journal for Numerical Methods in Engineering*, 70(6): 685–704, 2007.
- [169] W. Wagner and F. Gruttmann. A robust non-linear mixed hybrid quadrilateral shell element. *International Journal for Numerical Methods in Engineering*, 64:635–666, 2005.
- [170] K. Washizu. *Variational Methods in Elasticity & Plasticity*. Pergamon Press, 3rd edition, 1982.

- [171] T. Wenger, S. Ober-Blöbaum, and S. Leyendecker. Construction and analysis of higher order variational integrators for dynamical systems with holonomic constraints. *Advances in Computational Mathematics*, 43:1163–1195, 2017.
- [172] M. West. *Variational integrators*. PhD Dissertation, California Institute of Technology, Pasadena, California, 2004.
- [173] E.L. Wilson. A computer program for dynamic stress analysis of underground structures. Technical report, University of California at Berkeley, 1968.
- [174] P. Wriggers. *Nonlinear Finite Element Methods*. Springer Berlin Heidelberg, 2008.
- [175] O.C. Zienkiewicz and R.L. Taylor. *The Finite Element Method for Solid and Structural Mechanics*. Elsevier Butterworth-Heinemann, 6th edition, 2005.



# Schriftenreihe des Instituts für Mechanik

## ISSN 2363-4936

Hrsg. von: Prof. Dr.-Ing. habil. Peter Betsch, Prof. Dr.-Ing. habil. Thomas Seelig

---

- Band 1    Marlon Franke  
**Discretisation techniques for large deformation computational contact elastodynamics.** 2014  
ISBN 978-3-7315-0278-4
- Band 2    Philipp Hempel  
**Constitutive modeling of amorphous thermoplastic polymers with special emphasis on manufacturing processes.** 2016  
ISBN 978-3-7315-0550-1
- Band 3    Martin Helbig  
**Mehrskalenmodellierung von Schädigung in gummimodifizierten thermoplastischen Kunststoffen.** 2017  
ISBN 978-3-7315-0571-6
- Band 4    Maik Dittmann  
**Isogeometric analysis and hierarchical refinement for multi-field contact problems.** 2017  
ISBN 978-3-7315-0616-4
- Band 5    Yinping Yang  
**Numerical methods for the inverse dynamics simulation of underactuated mechanical systems.** 2017  
ISBN 978-3-7315-0626-3
- Band 6    Alexander Janz  
**Structure-preserving space-time discretization in a mixed framework for multi-field problems in large strain elasticity.** 2019  
ISBN 978-3-7315-0926-4

# Band 6

Schriftenreihe des Instituts für Mechanik  
Karlsruher Institut für Technologie (KIT)

HERAUSGEBER

Prof. Dr.-Ing. habil. Peter Betsch

Prof. Dr.-Ing. habil. Thomas Seelig



ISSN 2363-4936

ISBN 978-3-7315-0926-4